



Durham E-Theses

Classical and quantum mechanics with chaos

Borgan, Sharry

How to cite:

Borgan, Sharry (1999) *Classical and quantum mechanics with chaos*, Durham theses, Durham University. Available at Durham E-Theses Online: <http://etheses.dur.ac.uk/4968/>

Use policy

The full-text may be used and/or reproduced, and given to third parties in any format or medium, without prior permission or charge, for personal research or study, educational, or not-for-profit purposes provided that:

- a full bibliographic reference is made to the original source
- a [link](#) is made to the metadata record in Durham E-Theses
- the full-text is not changed in any way

The full-text must not be sold in any format or medium without the formal permission of the copyright holders.

Please consult the [full Durham E-Theses policy](#) for further details.



University of Durham
Department of Mathematical Sciences
Durham DH1 3LE
England

Classical and quantum mechanics with chaos

by

Sharry Borgan

A thesis presented for the degree
of Doctor of Philosophy

The copyright of this thesis rests
with the author. No quotation
from it should be published
without the written consent of the
author and information derived
from it should be acknowledged.



19 JUL 2000

December 1999

Abstract

Classical and quantum mechanics with chaos

Sharry Borgan

This thesis is concerned with the study, classically and quantum mechanically, of the square billiard with particular attention to chaos in both cases.

Classically, we show that the rotating square billiard has two regular limits with a mixture of order and chaos between, depending on an energy parameter, E . This parameter ranges from $-2\omega^2$ to ∞ , where ω is the angular rotation, corresponding to the two integrable limits. The rotating square billiard has simple enough geometry to permit us to elucidate that the mechanism for chaos with rotation or curved trajectories is not flyaway, as previously suggested, but rather the accumulation of angular dispersion from a rotating line. Furthermore, we find periodic cycles which have asymmetric trajectories, below the value of E at which phase space becomes disjointed. These trajectories exhibit both left and right hand curvatures due to the fine balance between Centrifugal and Coriolis forces.

Quantum mechanically, we compare the spectral analysis results for the square billiard with three different theoretical distribution functions. A new feature in the study is the correspondence we find, by utilising the Berry-Robnik parameter q , between classical E and a quantum rotation parameter ω . The parameter q gives the ratio of chaotic quantum phase volume which we can link to the ratio of chaotic phase volume found classically for varying values of E . We find good correspondence, in particular, the different values of q as ω is varied reflect the births and subsequent destructions of the different periodic cycles.

We also study wave packet dynamics, necessitating the adaptation of a one dimensional unitary integration method to the two dimensional square billiard. In concluding we suggest how this work may be used, with the aid of the chaotic phase volumes calculated, in future directions for research work.

Declaration

This thesis is the result of research carried out between October 1995 and December 1999. The work presented in this thesis has not been submitted in fulfilment of any other degree or professional qualification.

No claim of originality is made for Chapters 1 and 2 and Appendices A, B and C. Elsewhere any work that is not original is referenced.

Chapter 3 is the basis for [1] and Chapter 4 for [2].

Copyright ©1999 by S. Borgan.

The copyright of this thesis rests with the author. No quotation from it should be published without his prior consent and any information derived from it should be acknowledged.

Acknowledgements

It is a great pleasure to thank my supervisor, Dr. R. C. Johnson, for always being extremely helpful and available.

I would like to thank every member of the Mathematical Sciences Department, including those who have left during my time here, for making my period of study an enjoyable one. In particular, I express my gratitude to the following:

Dr. D. S. Berman

Dr. J. F. Blowey

Dr. A. W. Craig

Dr. P. S. Craig

Dr. B. M. A. G. Piette

Dr. A. F. Ware

Prof. W. J. Zakrzewski

for the help and encouragement they have given me.

I am specially grateful to the late Prof. E. J. Squires for accepting my application for entry to the department.

The Department's five-a-side football team has been a source of great pleasure. I was fortunate to find a team in which my standard of football was not out of place. I thank all past and present members, in particular, James Blowey and Simon Shaw.

Dedicated

to

Eileen,

Gary

and

Laura.

Contents

1	Introduction	9
2	Review of classical and quantum dynamics	13
2.1	Classical dynamics	13
2.1.1	Types of motion	13
2.1.2	Integrable systems	14
2.1.2.1	Poincaré surface of section	17
2.1.3	Chaotic systems	18
2.1.4	Quasi-integrable systems	20
2.1.5	Pseudo-integrable systems	21
2.1.6	Discrete area-preserving maps of the plane	22
2.2	Quantum dynamics	24
2.2.1	Phase space surfaces and semiclassical wavefunctions	24
2.2.2	Wigner's function	27
2.2.3	Regular and irregular quantum states	30
2.2.4	Scars	32
2.2.5	Energy spectra	34
2.2.5.1	A simple example	34
2.2.5.2	Fluctuations	35
2.2.5.3	Random matrix theories	39
2.2.5.4	Gaussian ensembles	40
2.2.5.5	Fluctuation properties	43
3	Classical dynamics in the \mathcal{B}_\square	46
3.1	General rotating billiards	46
3.1.1	Equations of motion	46
3.2	The square billiard, \mathcal{B}_\square	48
3.2.1	Defining \mathcal{B}_\square	48
3.2.2	Phase space for \mathcal{B}_\square	49

3.3	Periodic cycles of the rotating \mathcal{B}_\square	51
3.3.1	The bounce map, \mathbf{B}	51
3.3.2	The Jacobian, \mathbf{J} , and Stability, \mathbf{S} , matrices	52
3.4	The stationary \mathcal{B}_\square	55
3.5	The slowly rotating \mathcal{B}_\square	61
3.6	Poincaré maps, cycles and trajectories	62
3.6.1	Periodic cycles with type I trajectories	63
3.6.2	Periodic cycles with type II trajectories	72
3.6.3	Periodic cycles with type III trajectories	76
3.6.3.1	Trajectory curvatures	81
3.7	Flyaway and adiabatic skipping	82
3.8	Lyapunov exponents	85
3.9	Chaotic phase volume	90
4	Spectral analysis for the \mathcal{B}_\square	95
4.1	Dimensionless form of the Hamiltonian operator	95
4.2	The Hamiltonian matrix	96
4.3	Unfolding the energy spectrum	98
4.4	Theoretical level spacing distribution functions	101
4.4.1	The Bohigas, Giannoni and Schmit (BGS) conjecture	101
4.4.2	Mixed systems	102
4.5	Level spacing distributions for the \mathcal{B}_\square	109
4.5.1	Nearest Neighbour Spacing Distribution (NNSD)	109
4.5.2	Integral Transition Distributions (ITD)	114
4.6	Spectral rigidity	118
4.7	Other statistics	121
5	Wave packet dynamics in the \mathcal{B}_\square	122
5.1	Dimensionless form of the Schrödinger equation	123
5.2	Numerical integration techniques	123
5.2.1	Euler's method	124
5.2.2	Runge-Kutta method	124
5.2.3	Unitary numerical integration technique	125
5.3	Initial and boundary conditions	127
5.4	Numerical simulations	129
5.4.1	Stationary table with initially stationary particle	129
5.4.2	Stationary table with initially moving particle	135
5.4.3	Rotating table with initially stationary particle	138

5.4.4	Rotating table with initially moving particle	141
6	Conclusions	145
6.1	Classical dynamics	145
6.2	Quantum dynamics	148
6.3	And there's more	149
A	KAM Theorem	150
B	Derivation of the equations of motion	158
C	Lagrangian for a rotating billiard	160
D	Energy conservation	163
E	Bounce maps	164
F	Elements of the Jacobian, J, matrix	166
G	Bounce maps for the stationary \mathcal{B}_\square	172
H	Unitary numerical integration technique	175

List of Figures

2.1	A 2-torus Σ in 4-dimensional phase space	15
2.2	Torus $I(\mathbf{q}, \mathbf{p})$	16
2.3	Poincaré surface of section	18
2.4	The Sinai billiard	19
2.5	Nonisolated orbits in the Sinai and stadium billiards	19
2.6	Isolated orbits in the Sinai and stadium billiards	20
2.7	Discrete map M	22
2.8	Iterates (q_n, p_n) of (q_0, p_0)	24
2.9	Σ as a function of $\mathbf{p}(\mathbf{q})$	24
2.10	Σ with $\mathbf{p}(\mathbf{q})$ multivalued	26
2.11	Σ for a regular system	30
2.12	Σ for an irregular system	31
2.13	Nodal lines for the stadium and circle billiards	31
2.14	Schematic plot of the overlap function in time (a) and in energy (b) .	32
2.15	An unstable periodic orbit of the stadium and a contour plot of the probability distribution for the corresponding eigenstate	33
2.16	A membrane	34
2.17	Interval for Wigner's argument	37
3.1	The square billiard	48
3.2	Circle of exclusion for $E = -1$	49
3.3	Phase space for \mathcal{B}_\square	51
3.4	Tessellation of the z -plane	57
3.5	$E=10^8$: Trajectories followed for 100 bounces; (a): $\mathbf{X} = (0.5, X_2 : \tau = \sqrt{3})$, (b): $\mathbf{X} = (0.5, X_2 : \tau = 1)$, (c): $\mathbf{X} = (0.5, X_2 : \tau = \sqrt{3})$ and (d): Phase portrait on a 8×8 grid for 1000 bounces	58
3.6	$E=10^8$; Trajectories followed for 100 bounces (a): \mathbf{X}_{2+} ; (b): \mathbf{X}_{6+} ; (c): \mathbf{X}_{8+} ; (d): \mathbf{X}_{10+}	60
3.7	Phase portraits for (a): $E = 10^7$; (b): $E = 10^6$; (c): $E = 10^5$; (d): $E = 10^4$	64

3.8	Phase portrait: $E = 10^3$; 8×8 grid, followed for 250 bounces	65
3.9	Phase portraits constructed by following orbits initiated from single \mathbf{X} -values near cycles at $E = 10^8$; (a): Fixed point; (b): 4-cycle; (c): 6-cycle; (d): 8-cycle. Trajectories; (e -f).	66
3.10	$E = 10^8$: (a - b): Trajectories corresponding to cycles indicated . (c -f): Trajectories showing B_{11}	67
3.11	Phase portraits showing the change in phase space with decreasing E ; (a): $E = 800$, (b): $E = 600$, (c): $E = 400$, (d): $E = 200$, (e): $E = 30$, (f): $E = 20$	68
3.12	Phase portraits showing the change in phase space with decreasing E ; (a): $E = 18.414$, (b): $E = 10$, (c): $E = 5$, (d): $E = 2.6$, (e): $E = 2.4$, (f): $E = 2.1$	69
3.13	$E = 2.4$: a 4-cycle at $\mathbf{X} = (0.5, 0.62)$: (a): Phase portrait, (b): Trajectory and at $\mathbf{X} = (0.7, 0.6)$: (c): Phase portrait, (d): Trajectory. Changes in the X_2 values of \mathbf{X}_+ for (e): $E = 2$ to 100 and (f): $E = 1.15$ to 2	70
3.14	Change in the curvature of the trajectories for \mathbf{X}_+ at (a): $E = 100$, (b): $E = 50$, (c): $E = 10$, (d): $E = 5$, (e): $E = 4$, (f): $E = 3$, (g): $E = 2$ and (h): $E = 1.1706$	71
3.15	Plot showing the eigenvalues of \mathbf{X}_+ moving round the unit circle for the range $E = 2$ to 50	72
3.16	Phase portraits showing the symmetric 2-cycle at: (a): $E = 2$, (b): $E = 1.8$, (c): $E = 1.6$ and (d): $E = 1$	73
3.17	(a): Phase portrait of the symmetric 2-cycle from $\mathbf{X}=(0.2, 0.655)$; (b): Trajectory of the 2-cycle from $\mathbf{X}=(0.2, 0.655)$; (c): Phase portrait of the symmetric 10-cycle from the 5-bifurcation; (d): Trajectory of the symmetric 10-cycle from the 5-bifurcation	74
3.18	Phase portraits(a, c, e and g) and trajectories(b, d, f and h) for the 3-,4-,5- and 6-cycles respectively.	75
3.19	Phase portraits; (a): Symmetric 2-cycle at $E = 1.17066$ and (b): Symmetric 3-cycle at $E = 0.3$	76
3.20	Phase portrait at $E = -1$ showing disjointed phase space.	76
3.21	Phase portrait at $E = -1.8$. Inset: 2-cycle and its trajectory.	77
3.22	Phase portrait at $E = -1.9$. Inset: 3-cycle and its trajectory.	78
3.23	Phase portraits; (a): at $E = -1.95$; Inset: 10-cycle and its trajectory. (b): at $E = -1.97$; Inset: 4-cycle and its trajectory.	79
3.24	Phase portraits; (a): at $E = -1.995$, (b): at $E = -1.998$	80

3.25	$E = -0.5, X_1 = 0.5$: Trajectory curvatures for various values of X_2 .	82
3.26	Phase portraits: (a): $E = 60$, (b): $E = 0$; Trajectories showing flyaway at $E = 0$ (c - f)	84
3.27	$E = 10^3$: Lyapunov exponents v no. of bounces for six different initial \mathbf{X} values	87
3.28	Bounces on a rotating line	88
3.29	Plot of Lyapunov exponents v E for range: $E = 0$ to 10^3 and $\mathbf{X} = (0.4, 0.4)$	89
3.30	Plot of Lyapunov exponents v E for range: $E = 10^3$ to 10^5 and $\mathbf{X} = (0.4, 0.4)$	89
3.31	Phase portraits at $E = 1200$ from (a): $\mathbf{X} = (0.5, 0.5)$ and (b) : $(0.2, 0.2)$.	91
3.32	Phase portraits at $E = 1100$ from (a): $\mathbf{X} = (0.5, 0.5)$ and (b) : $(0.2, 0.2)$.	92
3.33	Phase portraits at $E = 1000$ from (a): $\mathbf{X} = (0.5, 0.5)$ and (b) : $(0.2, 0.2)$.	92
3.34	Phase portraits at $E = 500$ from (a): $\mathbf{X} = (0.5, 0.5)$ and (b) : $(0.2, 0.2)$.	93
3.35	Ratio of chaotic phase space volume for (a): $E = 1000$ to 2, (b): $E = 2$ to -1 and (c): $E = -1.5$ to -2	94
4.1	Plot of the staircase function, $N(e_i)$, and some fitted curves	99
4.2	The unfolded energy spectrum, $N(x_i)$, versus ω	100
4.3	Magnification of portions of figure 4.2	100
4.4	Poisson and Wigner distributions	101
4.5	Brody (a) and Berry-Robnik (b) distribution functions interpolating between the Poisson and Wigner distributions	107
4.6	Lopac-Brant-Paar distribution function for various values of the parameters q and β	108
4.7	Histograms and the three fitted theoretical distributions for $\omega = 100, 300, 500, 700, 900, 1100$	110
4.8	Variation of the LBP parameter q and classical E with ω	111
4.9	Comparison of chaotic phase volumes obtained classically and quantum mechanically.	113
4.10	Comparison of chaotic phase volumes obtained classically and quantum mechanically.	114
4.11	Theoretical Integral Distributions: (a) Brody; (b) Berry-Robnik; (c) LBP ($q=0$); (d) LBP ($q=1$).	116
4.12	The theoretical Integral LBP distributions fitted to the Integral Transition distributions for $\omega = 100, 300, 500, 700, 900, 1100$.	117
4.13	Dependence of $\bar{\Delta}_3$ on L .	120

4.14	Dependence of $\bar{\Delta}_3(5)$ on ω	120
5.1	Unitarity of the Unitary Integration Method	126
5.2	Mesh plot at $t = 90$ showing oscillations at the $x = 1 $ boundaries . .	130
5.3	Mesh and contour plots of the Probability Densities: $\omega = 0$, $\mathbf{r}=(0, 0)$; (a,b): $t = 0$, (c,d): $t = 20$, and (e,f): $t = 40$	131
5.4	Mesh and contour plots of the Probability Densities: $\omega = 0$, $\mathbf{r}=(0, 0)$; (a,b): $t = 60$, (c,d): $t = 80$, and (e,f): $t = 100$	132
5.5	Mesh and contour plots of the Probability Densities: $\omega = 0$, $\mathbf{r}=(0, 0)$; (a,b): $t = 120$, (c,d): $t = 140$, and (e,f): $t = 160$	133
5.6	Mesh and contour plots of the Probability Densities: $\omega = 0$, $\mathbf{r}=(-0.5, 0)$; (a,b): $t = 0$, (c,d): $t = 100$, and (e,f): $t = 1000$	134
5.7	Plot of Expectation Values	135
5.8	Mesh and contour plots of the Probability Densities: $\omega = 0$, $K_r = 30\pi$, $\mathbf{r}=(0.5, -0.5)$; (a,b): $t = 0$, (c,d): $t = 20$, and (e,f): $t = 40$	136
5.9	Mesh and contour plots of the Probability Densities: $\omega = 0$, $K_r = 30\pi$, $\mathbf{r}=(0.5, -0.5)$; (a,b): $t = 60$, (c,d): $t = 80$, and (e,f): $t = 100$. . .	137
5.10	Plot of Expectation values for $\omega = 0, 1, 10$ and 100	138
5.11	Contour plots of the Probability Densities: $\mathbf{r}=(0.5, -0.5)$; (a,c,e): $t = 0, 20, 40$ ($\omega = 10$) and (b,d,f): $t = 0, 20, 40$ ($\omega = 0$).	139
5.12	Contour plots of the Probability Densities: $\mathbf{r}=(0.5, -0.5)$; (a,c,e): $t = 60, 80, 100$ ($\omega = 10$) and (b,d,f): $t = 60, 80, 100$ ($\omega = 0$).	140
5.13	Expectation values for $\omega = 0, 20, 40, 60, 80, 100$	141
5.14	Expectation values for $\omega = 0, 200, 400, 600, 800, 1000$	141
5.15	Expectation values at $\omega = 0, 1200, 1400, 1600, 1800, 2000$ and Contour plots at $\omega = 1400$	142
5.16	Contour plots of the Probability Densities: $\mathbf{r}=(0.5, -0.5)$; (a,c,e): $t = 0, 20, 40$ ($\omega = 30$) and (b,d,f): $t = 0, 20, 40$ ($\omega = 0$).	143
5.17	Contour plots of the Probability Densities: $\mathbf{r}=(0.5, -0.5)$; (a,c,e): $t = 60, 80, 100$ ($\omega = 30$) and (b,d,f): $t = 60, 80, 100$ ($\omega = 0$).	144

List of Tables

2.1	Space-time symmetries	40
3.1	Bounces from $\mathbf{X} = (0.5, 0.5), (0.2, 0.2)$ for $E = 1200, 1100, 1000$ and 500	90
4.1	Relationship between the LBP distribution and other distributions. .	107
4.2	Fitted parameters β, q for figure 4.7	109
4.3	Fitted parameters q, E for figure 4.8	112
4.4	Correspondence for some values of E and ω	114
5.1	Fixed initial conditions for all subsequent plots.	129

Chapter 1

Introduction

It is now well established that there are two radically different types of motion in classical Hamiltonian mechanics: the regular motion of integrable systems and the chaotic motion of non-integrable systems. The harmonic oscillator being an example of the former whilst a system as simple as a periodically driven pendulum an example of the latter. With the recognition of unpredictable causality in the case of chaotic motion, the explicit study of systems having this property has become an integral part of mathematics. Its evolution has led to the study of abstract dynamical systems which have resulted, amongst other things, in:

- (i) a classification scheme of solutions of classical dynamical systems, ordered according to increasing complexity;
- (ii) diagnostic tools to define, and to discover complexity;
- (iii) new models which exhibit particular complex behaviour without diluting it with unessential features.

The basic lesson for Physicists has been that extreme instabilities in motion manifest themselves in phase space through the proliferation of finer and finer structures; these allow a probabilistic imitation of the causal motion. The mechanism which produces these effects is crucially linked to:

- (i) the exponential divergence of the trajectories in phase space;
- (ii) the Poincaré recurrence engendered by the compactness of the phase space.

The question of importance is how much of this can be utilised if we use quantum theory as the basic dynamical description. All the important results of classical dynamics are statements referring to properties in phase space which simply does not exist in quantum mechanics, and there is no unique, or even best substitute for it.

Thus we do not know how to transfer to quantum theory the classical ideas essential in describing chaotic behaviour. One observation can however be made immediately. If classically chaotic behaviour manifests itself through the ever increasing complexity of the motion, expressed through the ever increasing fine structure of the evolving phase fluid, then this manifestation of chaos will not work. For no classical structure within one phase cell makes sense according to the rules of quantum theory. This feature arises from the non-commutability of canonically conjugate observables which also denies the existence of the phase space. In addition, it gives rise to the difficulty that knowing the time evolution of the p and q operators tells us very little about the time evolution of functions of these operators. This leads to the most fundamental question faced: on what observables, by what means can one in general detect that in the classical limit the dynamical system has certain properties. Because of this difficulty we are unable to answer some subsidiary questions which arise naturally:

- (i) What is the classification scheme of dynamical systems, and their solutions in quantum mechanics?
- (ii) According to what features should this scheme be organised?
- (iii) What corresponds in the quantal description to the classical notions of stability, or, inversely, to the sensitive dependence on initial data. For example, is there a quantity analogous to the Lyapunov exponent?
- (iv) Is there anything analogous to the deterministic, yet not predictable features of classical dynamics in the quantal description?
- (v) If the classical properties and diagnostic tools are of such little aid, how do they acquire their significance in the classical limit?
- (vi) What is the general, time-dependent correspondence principle?

A new question, not raised in classical theory, enters in quantum mechanics. The nature of the quantum system is described by its Hamiltonian operator, or equivalently by its spectrum and eigenfunctions with their degeneracy. If the classical system is chaotic, its phase space is compact, hence the spectrum is discrete. All that can be known about the system is then given by two infinite sets of numbers; the eigenvalues and their degeneracies, and an infinite set of eigenfunctions which form a complete orthonormal set. The relevant question now is: where in these numbers and functions is the information hidden that in the classical limit the system exhibits chaotic behaviour?

As the general theory of quantum chaos is in its early stages, analytic results being few and far between, we are forced to expend a great deal of numerical labour dealing with special cases. The hope is that with the aid of sufficient numerical results a coherent theory of quantum chaos will emerge. There is, however, a scarcity of good special cases to study. The ideal situation would be to investigate actual physical systems. These are de facto quantal and the results can be confronted with experimental evidence. However, actual physical systems suffer from the handicap that their behaviour (in the classical limit) is seldom purely chaotic, but diluted by other properties, irrelevant to putative chaotic behaviour. Most examples are furnished by atomic and molecular physics.

Because of this one looks at models. A good model in this context has the property that if you remove from those it features which lead to chaotic behaviour, the model ceases to exist, instead of just turning into a simple integrable system. Such models are the classical maps which are either associated with actual physical systems (via the Poincaré section map for example) or are caricatures, embodying only the essential features, and cannot be conceived as stroboscopic pictures of a continuous time evolution.

The quantal versions of these maps, however, are lacking some useful properties:

- (i) If the classical map comes from a continuous time evolution its quantal version can be written down. However, while one can reconstruct from the map the continuous time evolution in the classical case, such a reconstruction is not known in the quantal version.
- (ii) If the map is not a stroboscopic picture, no real rule of quantisation is known. Also, for time-dependent Hamiltonian systems the configuration space must be at least two dimensional to get a non-trivial model. Thus, the simplest Hamiltonian models are either non-autonomous and one dimensional or autonomous and two dimensional. If the Hamiltonian is time-dependent its future is arbitrary unless it is time-periodic.

A crude classification of models is consequently:

- (i) Real physical systems, described by quantum theory.
- (ii) Periodic, one dimensional Hamiltonian systems, or maps derived from them, which are amenable to quantisation.
- (iii) Two dimensional autonomous Hamiltonian systems, or maps derived from them, which are amenable to quantisation.

- (iv) Measure-preserving maps with no Hamiltonian, which require quantisation individually by special techniques.

A great amount of numerical research has been carried out with a variety of models, particularly billiards, some of these are mentioned in the ensuing chapters. This thesis follows in this vein with the study of a very simple system; a square billiard, \mathcal{B}_\square , with which we attempt to address some of the issues discussed so far.

The contents of the thesis are split into five parts. In Chapter 2 we review briefly classical and quantum dynamics of Hamiltonian systems in general. In Chapter 3 we study the classical dynamics of \mathcal{B}_\square . We investigate the periodic cycles in the whole permissible range of the energy parameter, E , Lyapunov exponents and chaotic phase volume. In Chapter 4 we carry out spectral analysis for the \mathcal{B}_\square paying particular attention to a link between the quantal and classical dynamics. In Chapter 5 we study the wave packet dynamics in the \mathcal{B}_\square , using a unitary numerical integration technique. We compare the motion of the expectation values with the appropriate classical trajectories. In Chapter 6 we discuss the work of Chapters 3, 4 and 5, what we have learned and further research that could be carried out.

Chapter 2

Review of classical and quantum dynamics

In this chapter we review briefly classical and quantum dynamics of Hamiltonian systems in general and where appropriate billiards in particular. The review is based on [3–7, 9, 11–13, 15–18, 30, 45, 47, 102, 103]

2.1 Classical dynamics

2.1.1 Types of motion

In Hamiltonian motion, that is motion governed by Newton's equations without dissipation, we encounter two types of motion:

- (1) Regular motion: exemplified by the one-dimensional oscillator which in its physical realization as a pendulum is the epitome of predictability. Another example is the elliptical orbits of the planets when mutual perturbations are ignored.
- (2) Irregular motion: exemplified by the classical motion of colliding molecules in a gas. If the molecules are confined to a plane, transformed to hard discs and all held fixed except one, then that one executes a motion with two degrees of freedom idealising a pinball machine. Such motion is unpredictable in the sense that neighbouring trajectories separate exponentially, resulting in a sensitivity to initial conditions.

The distinction between regularity and irregularity is embodied in the geometry of typical trajectories in the system's phase space over infinitely long times. For N freedoms this is the $2N$ -dimensional space \mathbf{q}, \mathbf{p} where $\mathbf{q} = (q_1 \dots q_N)$ are the coordinates and $\mathbf{p} = (p_1 \dots p_N)$ are the momenta.

There is a hierarchy of types of motion, increasingly chaotic; integrable \rightarrow quasi-integral \rightarrow ergodic \rightarrow mixing \rightarrow K-system \rightarrow B-system. An important class of

discontinuous Hamiltonians with $N = 2$ is the planar billiards which have Hamiltonian:

$$\begin{aligned} H(x, y, p_x, p_y) &= \frac{1}{2} (p_x^2 + p_y^2) \quad \text{inside a boundary } B \text{ in } \mathbf{q} \text{ space} \\ &= \infty \quad \text{outside } B. \end{aligned} \quad (2.1)$$

Motion consists of straight line segments joined by specular reflections at B and the nature of orbits is very sensitive to the form of B .

2.1.2 Integrable systems

The simplest situation corresponding to the regular case is fully integrable. Here there exist N constants of motion in the form of functions $C_i(\mathbf{q}, \mathbf{p})$ ($1 \leq i \leq N$) in phase space, assumed to be in involution. One of the constants is the Hamiltonian itself if it is time-independent. If the C_i are independent of one another, their existence restricts motion to a surface Σ in phase space with dimensionality $N (= 2N - N)$. Arnol'd gives a clear formulation and proof of a theorem that states that if the C_i are "smooth enough", then

- (i) Σ is an N -dimensional torus,
- (ii) the motion can be "integrated", that is the trajectories $\mathbf{q}(t)$ and $\mathbf{p}(t)$ can be determined by elimination and integration.

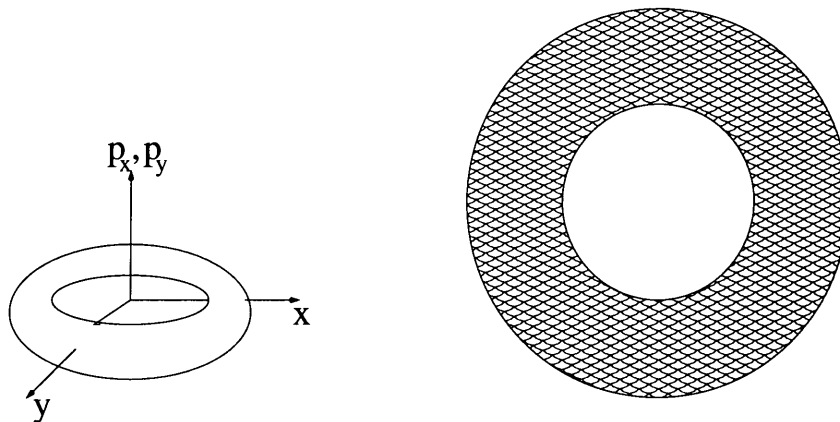
Examples of integrable systems are:

- (1) Stationary harmonic and anharmonic oscillators with $N = 1$ and mass μ , whose Hamiltonian is

$$H = \frac{p^2}{2\mu} + V(q), \quad (2.2)$$

where $V(q)$ is a potential well. The energy $E = H(q, p)$ is conserved, and since $N = 1$ this constant of motion suffices to make the system integrable. The "1-tori" on which motion occurs in phase space are simply closed contours of H .

- (2) All separable systems are integrable as they decouple into N one-dimensional systems.
 - (i) In particular, a particle moving in the plane, $N = 2$, under a central potential $V(r)$ is integrable. The two constants of motion being E and the angular momentum L . Each choice of E and L labels a 2-torus in

Figure 2.1: A 2-torus Σ in 4-dimensional phase space

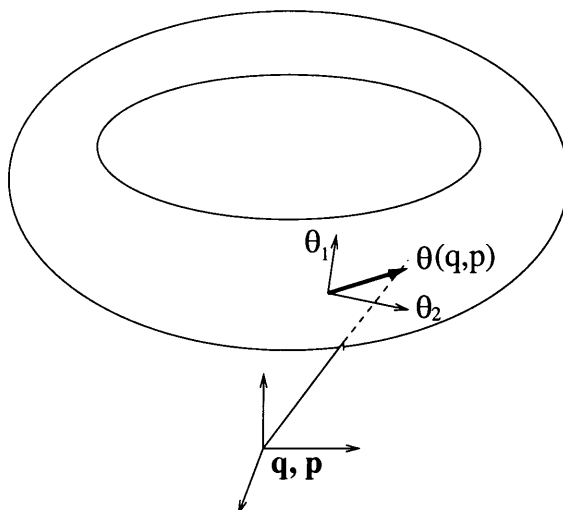
the 4-dimensional phase space (figure 2.1). The trajectory winds around Σ and typically fills Σ as $t \rightarrow \infty$. When projected “down” \mathbf{p} onto to the coordinate plane, (x, y) , the trajectory is enveloped by a caustic in the form of two circles at the radii of closest approach and furthest recession from the centre of force. Caustics are the singularities of the projection of Σ .

- (ii) Billiards such as
- (a) the circular billiard where the outer circle corresponds to the boundary B and is not a caustic.
 - (b) The rectangular billiard which is separable with p_x^2 and q_x^2 conserved, there are no caustics because the projection of Σ coincide with B .
 - (c) The ellipse billiard where orbits repeatedly touch an ellipse or hyperbola confocal with B .

The existence of tori throughout the phase space of an integrable system motivates the introduction of an alternate set of coordinates and momenta known as action-angle variables. The actions $\mathbf{I} = \{I_1 \dots I_N\}$ are particular combinations of the C_i which label the tori Σ , defined as

$$I_i = \frac{1}{2\pi} \oint_{\gamma_i} \mathbf{p} \cdot d\mathbf{q}, \quad (2.3)$$

where the γ_i is the i^{th} irreducible circuit of the torus. Letting \mathbf{I} be the conjugate momenta of new phase variables then the conjugate coordinates are the angles $\boldsymbol{\theta} = \{\theta_1 \dots \theta_N\}$. Any point \mathbf{q}, \mathbf{p} lies on a torus labelled by $\mathbf{I}(\mathbf{q}, \mathbf{p})$, and $\boldsymbol{\theta}(\mathbf{q}, \mathbf{p})$ locates the position of \mathbf{q}, \mathbf{p} on this torus (figure 2.2 on the following page). The variables $\boldsymbol{\theta}, \mathbf{I}$ and \mathbf{q}, \mathbf{p} are related by a canonical transformation: Let the torus Σ

Figure 2.2: Torus $\mathbf{I}(\mathbf{q}, \mathbf{p})$

labelled by \mathbf{I} be defined by a multivalued function with branches $\mathbf{p}_j(\mathbf{q}; \mathbf{I})$ in the phase. Then the generating function of the transformation is $\mathbf{S}(\mathbf{q}, \mathbf{I})$ with branches

$$\mathbf{S}_j(\mathbf{q}; \mathbf{I}) = \int_{\mathbf{q}_0}^{\mathbf{q}} \mathbf{p}_j(\mathbf{q}'; \mathbf{I}) \cdot d\mathbf{q}' \quad (2.4)$$

where \mathbf{q}_0 is an arbitrary point “beneath” Σ . This gives the transformation

$$\mathbf{S}_j(\mathbf{q}; \mathbf{I}) = \int_{\mathbf{q}_0}^{\mathbf{q}} \mathbf{p}_j(\mathbf{q}'; \mathbf{I}) \cdot d\mathbf{q}'. \quad (2.5)$$

From which follows that each angle variable θ_i changes by 2π during the corresponding circuit γ_i of Σ . The fact that \mathbf{S} is locally single-valued implies that tori have the “Lagrangian” property

$$\frac{\partial p_i}{\partial q_j} = \frac{\partial p_j}{\partial q_i}. \quad (2.6)$$

Because there are only N independent constants of motion, each member of the original set C_i is expressible in terms of N \mathbf{I}_i 's. In particular, the Hamiltonian is conserved and expressible as $H = H(\mathbf{I})$. By one of Hamilton's equations, this means that the angle variables change at a constant rate;

$$\theta = \omega t + \theta_0, \quad (2.7)$$

where $\omega = \{\omega_1 \dots \omega_N\}$ are the frequencies, given by

$$\omega(\mathbf{I}) = \nabla_{\mathbf{r}} H(\mathbf{I}). \quad (2.8)$$

The components ω_i give the rate at which a trajectory winds round Σ in directions labelled by the angles θ_i .

In the general case, all ω_i will be mutually incommensurable and the orbit will eventually fill Σ densely. But if all ω_i are rationally dependent;

$$\omega = \mathbf{M}\omega_0, \quad (2.9)$$

where $\mathbf{M} = \{M_1 \dots M_N\}$ is a lattice vector then each orbit on Σ will be closed.

2.1.2.1 Poincaré surface of section

In general there is no simple way to tell if a system is integrable or not. For systems with two degrees of freedom it can be checked numerically by constructing a Poincaré surface of section. Consider a conservative system, for such systems the energy is conserved and the Hamiltonian is then an isolating integral of the motion:

$$H(p_1, p_2, q_1, q_2) = E, \quad (2.10)$$

where the energy, E , is constant and restricts trajectories to be on a three dimension surface in the four dimension phase space. From equation 2.10 we can write $p_2 = p_2(p_1, q_1, q_2, E)$ and if the system has a second isolating integral,

$$I_2(p_1, p_2, q_1, q_2) = C_2, \quad (2.11)$$

where C_2 is a constant, then it too defines a three dimension surface in the four dimension phase space. Once the initial conditions are given, E and C_2 are fixed and the trajectory is constrained to the intersection of the surfaces defined by equations 2.10 and 2.11.

Combining equations 2.10 and 2.11 we can write $p_1 = p_1(q_1, q_2, E, C_2)$ and if we consider the surface, $q_0 = 0$, the trajectory lies on a one dimensional curve. Generally, it is not known if I_2 exists but its existence can be checked by solving Hamilton's equations ,

$$\frac{dp_i}{dt} = -\frac{\partial H}{\partial q_i} \quad \text{and} \quad \frac{dq_i}{dt} = \frac{\partial H}{\partial p_i}, \quad (2.12)$$

for $(i = 1, 2)$, numerically and then plotting p_2 and q_2 each time $q_1 = 0$ and $p_1 \geq 0$, as shown by figure 2.3(a) on the next page. If a system is integrable, the trajectory will appear as a series of points (a mapping) which lie on a one dimensional curve (figure 2.3(b) on the following page). If the system is non-integrable, the trajectory will appear as a scatter of points limited to a finite area due to energy conservation (figure 2.3(c) on the next page).

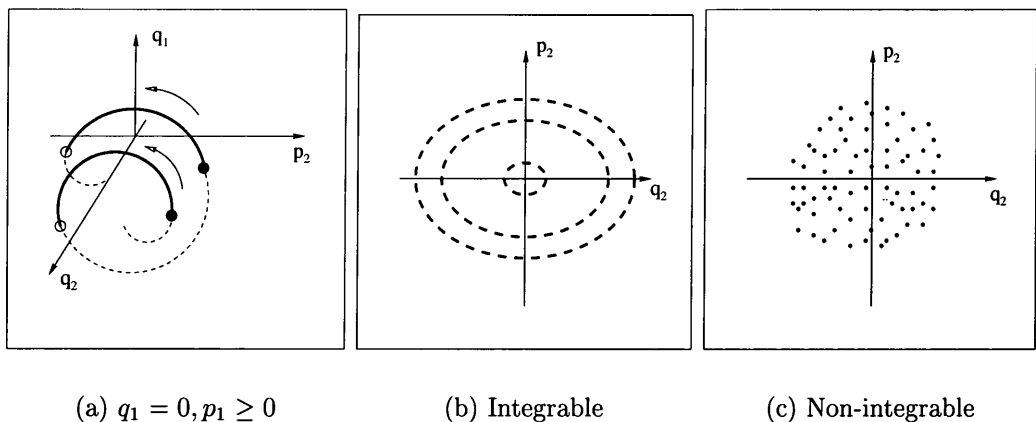


Figure 2.3: Poincaré surface of section

2.1.3 Chaotic systems

Integrable systems are in fact rare, amongst Hamiltonian systems, “almost all” are non-integrable in the sense that there are no global constants of motion other than H . An important class of non-integrable systems is one with the property of ergodicity: almost all orbits eventually explore almost all points in a $2N - 1$ dimensional energy surface defined by $H(\mathbf{q}, \mathbf{p}) = \text{constant}$, instead of being confined to an N -torus as with an integrable system.

The case $N = 1$ is degenerate because $2N - 1 = N$ and orbits are trivially ergodic as well as integrable. Examples of ergodic systems with $N = 2$ are:

1. The Sinai billiard which is the billiard motion of a particle moving on the coordinate torus x, y (square with opposite sides identified) containing a circular reflecting obstacle with radius R (figure 2.4 on the following page). If $R > 0$ then it is ergodic. Ergodicity is the consequence of exponential chaos which in turn results from the defocussing of particle that hit the disc.
2. The stadium of Bunimovich, consisting of two semicircles with radius R joined by parallel straight lines with length L , is ergodic for $L > 0$. The semicircles cause a convergence of beams of trajectories but this is outweighed by the subsequent divergences before the next reflection.

In these ergodic billiards, a typical orbit passes through almost every point within B with almost every direction if followed long enough. The energy surface thus explored is 3-dimensional ($2N - 1$) in contrast to the 2-torus explored when there is an additional constant of motion. Not every orbit is typical; it is possible to have one-parameter families of nonisolated orbits, (figure 2.5 on the next page),

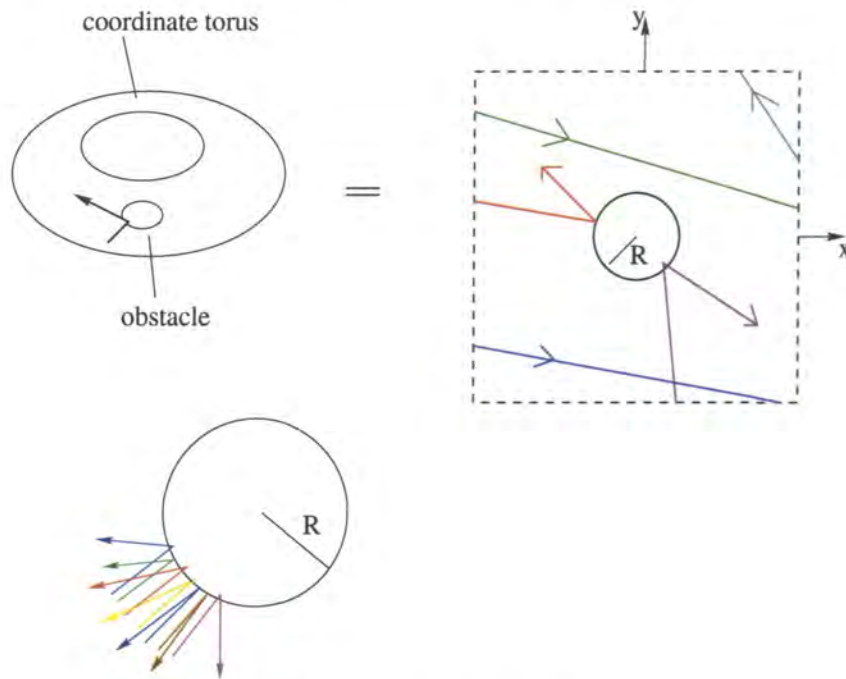


Figure 2.4: The Sinai billiard

although these do not fill tori. But vastly more numerous are the isolated closed orbits (figure 2.6 on the following page).

These closed orbits, isolated and nonisolated alike, are unstable; the slightest error in position or momentum gives an orbit separating rapidly (exponentially, for isolated orbits) from the closed one and eventually exploring all the energy surface. By contrast, the closed orbits in an integrable system are only linearly unstable and a perturbed orbit merely fills a nearby torus.

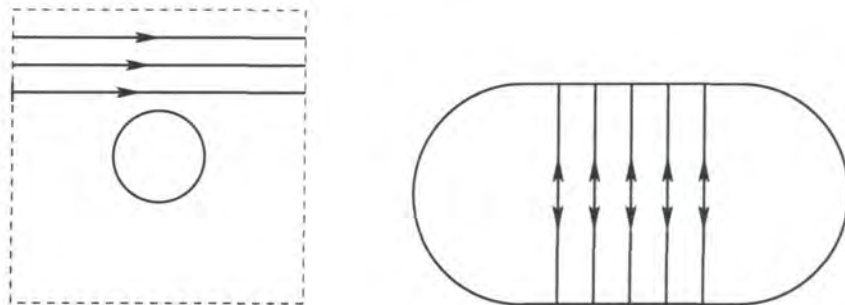


Figure 2.5: Nonisolated orbits in the Sinai and stadium billiards

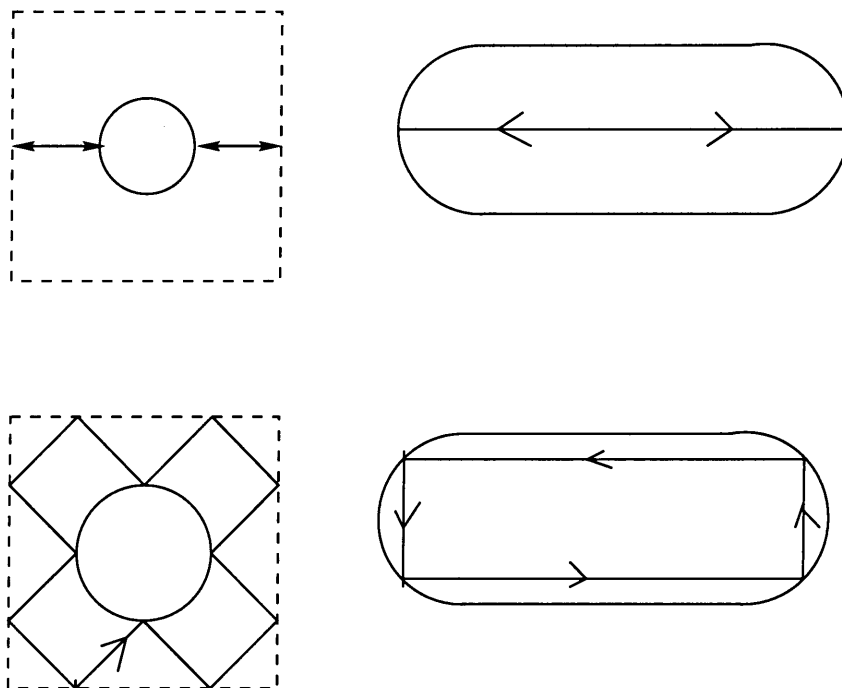


Figure 2.6: Isolated orbits in the Sinai and stadium billiards

2.1.4 Quasi-integrable systems

These are systems which are neither integrable nor ergodic, typically (excluding billiards) having smooth Hamiltonians of the form:

$$H(\mathbf{q}, \mathbf{p}) = H_0(\mathbf{q}, \mathbf{p}) + \epsilon H_1(\mathbf{q}, \mathbf{p}), \quad (2.13)$$

where H_0 is integrable and ϵ is a small parameter that turns on a generic perturbation H_1 . When $\epsilon = 0$, all trajectories lie on tori filling phase space. The answer to what happens to these tori when $\epsilon \neq 0$ is given by the celebrated KAM theorem (reviewed in Appendix A on page 150). This theorem basically says that under perturbation, most tori survive though distorted. Therefore the motion is not ergodic. But for almost all H_1 , some tori are destroyed, so the motion is not integrable either.

The destroyed tori form a set of finite measure growing with ϵ , they are centred on those unperturbed tori whose frequencies ω_i are incommensurable (that is whose orbits are closed). Motion near the unstable orbits is chaotic and fills regions with dimensionality $2N - 1$. Near the stable closed orbits, most trajectories lie on “higher-order” tori, but these, like the original “parent” tori, have gaps near sites where “rational” tori would be, and the whole structure repeats in microcosm, recursively down to infinitely fine scales.

The Solar System is quasi-integrable. Planets unperturbed by their neighbours

move integrably in Kepler ellipses. Including the perturbation results in a Hamiltonian of the form given by equation 2.13 on the page before. The effect can be seen in the asteroids, which correspond, in effect, to an ensemble of zero-mass “test particles”. Most move in approximately elliptical orbits, in spite of being perturbed by Jupiter, but there are gaps in the asteroid belt where orbital motion would be commensurate (resonant) with Jupiter’s; these gaps correspond to the destroyed tori. There are similar gaps in Saturn’s rings, which may correspond to resonant perturbation of the orbits of ring particles by the satellite Mimas.

As for billiards, Lazutkin [8] has proved a theorem analogous to the KAM theorem but more general in that it is nonperturbative. If B is convex and smooth enough, some orbits (of positive measure) will envelop caustics, that is, there will be some tori in phase space. The sufficient condition for smoothness is that B ’s radius of curvature as a function of arc length must possess 553 continuous derivatives.

Berry [30] illustrates Lazutkin’s theorem with computations indicating quasi-integrable behaviour, that is, some tori, some chaos for a family of oval billiards. Bennetin and Strelcyn [47] study a generalisation of the stadium made from four circular arcs, which has discontinuous curvature but nevertheless displays quasi-integrability.

2.1.5 Pseudo-integrable systems

Even if N constants of motion, independent and in involution, exist so that each orbit is restricted to a N -dimensional surface Σ in phase space it is not always the case that Σ is a torus. For billiards whose boundary is a polygon with angles which are rational multiples of π (apart from integrable ones: rectangle and equilateral, $30^\circ - 60^\circ - 90^\circ$ and $45^\circ - 45^\circ - 90^\circ$ triangles) Σ is not a torus but a multiply-handled sphere (that is, genus $g > 1$).

An example of such a system is the square torus billiard which resembles Sinai’s billiard except that the reflecting disc is replaced by square. The squares, v_x^2 and v_y^2 , of the velocity components are separately conserved and at most four directions are available to each trajectory $(v_x, v_y; -v_x, v_y; v_x, -v_y; -v_x, -v_y)$. Then the phase space surface Σ consists of four sheets and the “sewing” together of which shows that Σ is in fact a five-handled sphere.

KAM theorem does not apply to these; the reason being, for example, in the case of the square torus billiard that certain vector fields on Σ , constructed from v_x^2 and v_y^2 , possess singularities at the vortices of the reflecting square.

2.1.6 Discrete area-preserving maps of the plane

The distinction between regular and irregular motion is very clearly exhibited by discrete maps M in the phase plane where variables are a coordinate q and a momenta p . Under M (figure 2.7) each point (q_{n+1}, p_{n+1}) is a deterministic function of (q_n, p_n) :

$$\begin{aligned} M : q_{n+1} &= q_{n+1}(q_n, p_n) \\ p_{n+1} &= p_{n+1}(q_n, p_n). \end{aligned} \quad (2.14)$$

Area-preservation is ensured by requiring

$$\det \begin{bmatrix} \frac{\partial q_{n+1}}{\partial q_n} & \frac{\partial q_{n+1}}{\partial p_n} \\ \frac{\partial p_{n+1}}{\partial q_n} & \frac{\partial p_{n+1}}{\partial p_n} \end{bmatrix} \approx \frac{\partial (q_{n+1}, p_{n+1})}{\partial (q_n, p_n)} = 1. \quad (2.15)$$

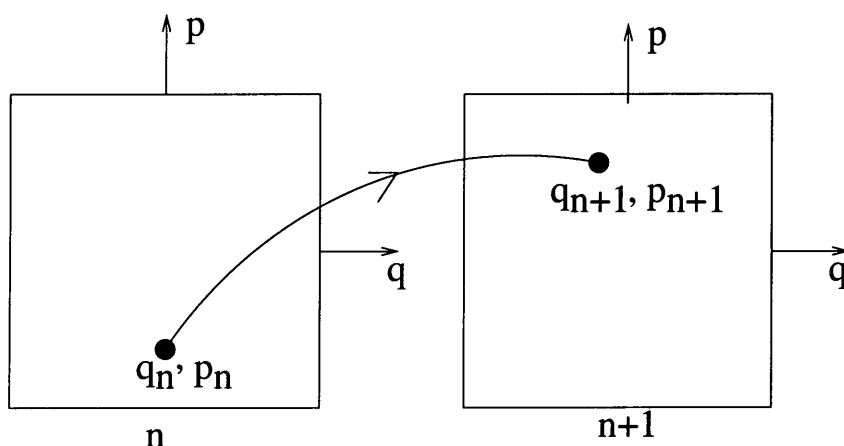


Figure 2.7: Discrete map M

M can be regarded as an abstract dynamical system whose evolution takes place in discrete time steps according to “Hamilton’s equations” (equation 2.14) with equation 2.15 replacing Liouville’s theorem on conservation of phase-space volume. However, these maps also arise from continuous time dynamical systems in two ways:

- (1) With $N = 2$ and a time-independent Hamiltonian where q and p are coordinates on a “surface of section” through the three dimensional energy surface. M is determined by the succession of points q_n, p_n in which a trajectory intersects the surface of section. For billiards a convenient surface of section is given by successive bounces at B , and variables for which M is area-preserving are $q = \text{arclength around } B$ and $p = \text{cosine of angle made by emerging trajectory with forward tangent to } B$.

(2) With $N = 1$ and a Hamiltonian periodic in time,

$$H(q, p, t + T) = H(q, p, t). \quad (2.16)$$

Then M is defined by a “stroboscopic phase portrait”, that is, by jumps of points q, p between snapshots of the motion at intervals T ,

$$q_n \equiv q(nT), \quad p_n \equiv p(nT) \quad (2.17)$$

and the motion between snapshots is ignored.

In terms of M , regularity or irregularity depends on the manner in which iterates (q_n, p_n) of some initial point (q_0, p_0) are distributed as $n \rightarrow \infty$. There are three possibilities:

(1) Iterates may be on a zero-dimensional set in the plane, (figure 2.8(a) on the following page), by forming a closed orbit, that is, a fixed point of some finite power N of M :

$$q_{n+N} = q_n, \quad p_{n+N} = p_n \quad (2.18)$$

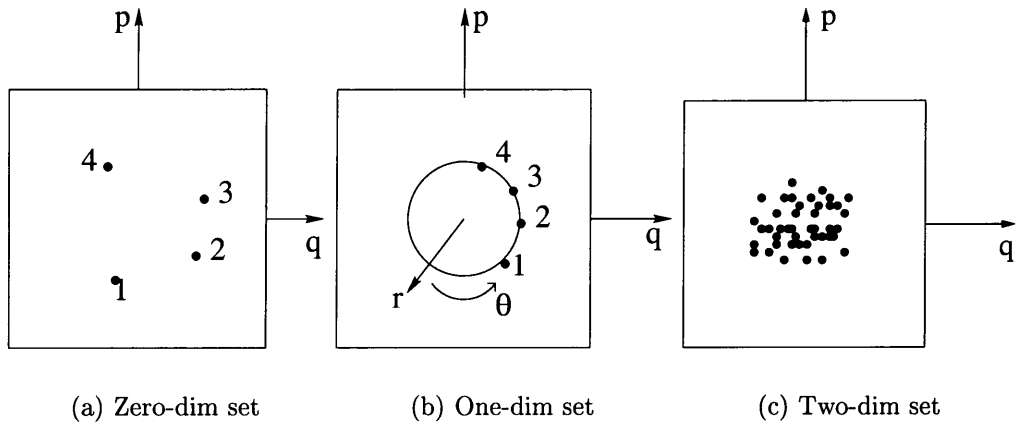
(2) Iteration may fill a one dimensional set in the plane, (figure 2.8(b) on the next page), an invariant curve which maps onto itself although its individual points do not. An example is the twist map;

$$M : r_{n+1} = r_n, \quad \theta_{n+1} = \theta_n + 2\pi\alpha(r_n). \quad (2.19)$$

Here the invariant curves are circles. If the “rotation number” α is irrational, iterates eventually fill the circle, while if $\alpha = M/N$ (M, N mutually prime finite integers) the iterates form a closed orbit with period N .

(3) Iterates may fill a two dimensional set in the plane, (figure 2.8(c) on the following page), a so-called chaotic area.

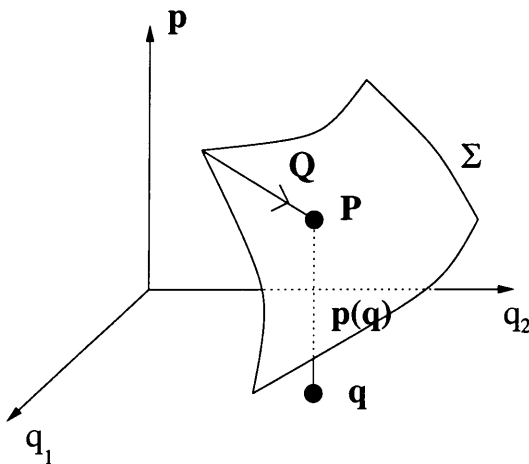
Integrable maps are those like figure 2.8(b) on the next page, where all points lie on invariant curves which are the analogues of tori and in the “surface of section” interpretation are precisely sections of 2-tori. Their existence implies a “constant of motion” in the form of a function $f(q, p)$ whose contours are the invariant curves and whose value is unchanged under M (for the twist map, $f = q^2 + p^2$).


 Figure 2.8: Iterates (q_n, p_n) of (q_0, p_0)

2.2 Quantum dynamics

2.2.1 Phase space surfaces and semiclassical wavefunctions

An important semiclassical concept was developed by Keller [9] which associates wave functions $\psi(\mathbf{q})$ and N -dimensional surfaces Σ in $2N$ -dimensional phase space \mathbf{q}, \mathbf{p} . Locally, Σ can be written as a function $\mathbf{p}(\mathbf{q})$, (figure 2.9), and corresponds to a N -parameter ensemble of states (points) in classical phase space.


 Figure 2.9: Σ as a function of $\mathbf{p}(\mathbf{q})$

$$\begin{aligned}
 (\mathbf{q}, \mathbf{p}) &\leftarrow S(\mathbf{q}, \mathbf{p}) \rightarrow (\mathbf{Q}, \mathbf{P}) \\
 \mathbf{p} &= \nabla_{\mathbf{q}} S, \quad \mathbf{Q} = \nabla_{\mathbf{P}} S
 \end{aligned}
 \tag{2.20}$$

which imply that Σ has the ‘‘Lagrangian’’ property, (equation 2.6 on page 16). We want to associate with Σ a wave

$$\psi(\mathbf{q}) = a(\mathbf{q}) e^{ib(\mathbf{q})},
 \tag{2.21}$$

A density on Σ is defined in which these states are distributed uniformly in some coordinate $\mathbf{Q} = \{Q_1 \dots Q_N\}$. This can be accomplished by imagining an N -parameter family of surfaces filling phase space near Σ , labelled by $\mathbf{P} = \{P_1 \dots P_N\}$ and then regarding \mathbf{Q}, \mathbf{P} as alternative phase space variables in a canonical form \mathbf{q}, \mathbf{p} . This is specified by a generating function $S(\mathbf{q}, \mathbf{p})$ by

there is a natural choice for the wave equation based on two physical principles, one each for $a(\mathbf{q})$ and $b(\mathbf{q})$:

- (1) For the amplitude $a(\mathbf{q})$ we require that the wave intensity $|\omega|^2$ is proportional to the density of points in classical \mathbf{q} -space. This is obtained by projecting the density on Σ and using equation 2.20 on the preceding page, in terms of the Jacobian determinant

$$a^2(\mathbf{q}) = K \left| \frac{d\mathbf{Q}}{d\mathbf{q}} \right| = K \det \left| \frac{\partial^2 S}{\partial \mathbf{q}_i \partial \mathbf{P}_j} \right|, \quad (2.22)$$

where K is a constant.

- (2) For the phase $b(\mathbf{q})$ we use de Broglie's rule relating the classical momentum $\mathbf{p}(\mathbf{q})$ to the wave vector $\mathbf{k}(\mathbf{q})$ of a locally plane wave, so that, in terms of the phase difference between two points separated by $\delta\mathbf{q}$,

$$b(\mathbf{q} + \delta\mathbf{q}) - b(\mathbf{q}) = \nabla b \cdot \delta\mathbf{q} = \mathbf{k} \cdot \delta\mathbf{q} = \frac{\mathbf{p} \cdot \delta\mathbf{q}}{\hbar}, \quad (2.23)$$

thereby introducing Planck's constant \hbar . Thus

$$\nabla b(\mathbf{q}) = \frac{\mathbf{p}(\mathbf{q})}{\hbar} \quad \text{and} \quad (2.24)$$

$$b(\mathbf{q}) = \frac{1}{\hbar} \int_{\mathbf{q}_0}^{\mathbf{q}} \mathbf{p}(\mathbf{q}') \cdot d\mathbf{q}' = \frac{S(\mathbf{q}; \mathbf{P})}{\hbar}, \quad (2.25)$$

again using equation 2.20 on the page before, where \mathbf{q}_0 is a fixed position where S is defined to vanish. The Lagrangian property makes S a (locally) single valued function of \mathbf{q} so this phase is uniquely defined locally, independent of the integration path between \mathbf{q}_0 and \mathbf{q} .

The plane wave associated with the surface Σ labelled by \mathbf{P} so constructed is

$$\psi(\mathbf{q}) = K \left| \det \frac{\partial^2 S(\mathbf{q}; \mathbf{P})}{\partial q_i \partial q_j} \right|^{1/2} \exp \left(\frac{i}{\hbar} S(\mathbf{q}; \mathbf{P}) \right). \quad (2.26)$$

This association is useful if ψ is regarded as an initial quantum state and letting it evolve according to the Schrödinger equation under dynamics governed by a Hamiltonian H . After time t , ψ will have evolved into a new wave ψ' and Σ will have evolved into a new surface Σ' by virtue of the classical Hamiltonian motion of each of its points. Dirac [12] has shown that solving the time-dependent Schrödinger equation asymptotically, that is, to lowest order in \hbar , that the ψ' can be constructed from Σ' by equation 2.26.

The above procedure is well defined only if $\mathbf{p}(\mathbf{q})$ is single valued. If Σ is curved in such a way that a fibre drawn “upwards” from \mathbf{q} intersects it at several momenta $\mathbf{p}_i(\mathbf{q})$, (figure 2.10), then it is natural to invoke the principle of superposition and extend the association by writing $\psi(\mathbf{q})$ as a sum of terms like equation 2.26 on the page before, one for each branch of $\mathbf{p}_i(\mathbf{q})$.

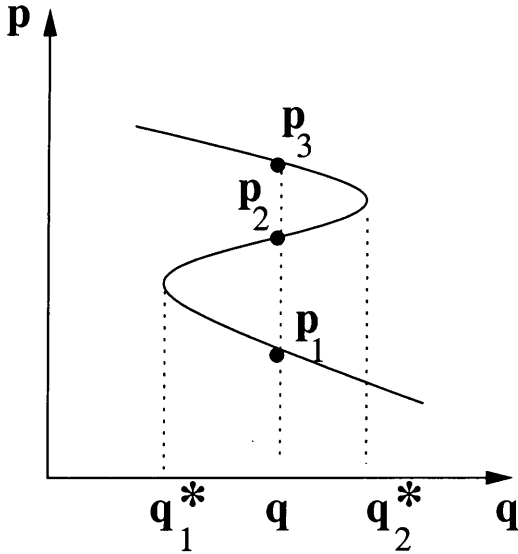


Figure 2.10: Σ with $\mathbf{p}(\mathbf{q})$ multivalued

How these contributions are to be joined at caustics, where the projection of Σ “down” onto \mathbf{q} is singular (for example at the points \mathbf{q}_1^* and \mathbf{q}_2^*) poses two difficulties: firstly, it is not clear how to relate the phases of the different contributions. Secondly equation 2.26 on the preceding page has the undesired property that it becomes infinite on caustics, because of the divergence of the “projection” Jacobian $d\mathbf{Q}/d\mathbf{q}$ (equation 2.22 on the page before) determining the amplitude $a(\mathbf{q})$.

Both difficulties can be overcome by Maslov’s procedure [10] of requiring the association between waves and phase space surfaces to hold for momenta as well as position coordinates. Therefore the semiclassical momentum wave functions $\bar{\psi}(\mathbf{p})$ will be given by a formula like equation 2.26 on the preceding page with Σ specified by the function $\mathbf{q}(\mathbf{p}; \mathbf{P})$ and the generating function $\bar{S}(\mathbf{p}; \mathbf{P})$ constructed from the line integral $\int \mathbf{q} \cdot d\mathbf{p}$ rather than $\int \mathbf{p} \cdot d\mathbf{q}$. Now, Σ is a smooth surface and so cannot have points where the projection is singular in both \mathbf{q} and \mathbf{p} , so when problems near \mathbf{q} -caustics are encountered its momentum analogue is well behaved.

For the N -torus it is always possible to return to any original point \mathbf{q} in N essentially different ways, corresponding to the irreducible circuits γ_i of Σ . There is no global action function S which is single valued on Σ , because around γ_i there must be a change $\Delta_i S$ given by

$$\Delta_i S = \oint_{\gamma_i} \mathbf{p} \cdot d\mathbf{q}, \quad (2.27)$$

and equal to the sum of the areas of the projections of γ_i onto the N qp planes. During such a circuit, the phase of the wave constructed by equation 2.26 on the page before will change by $\Delta_i S/\hbar$ plus a multiple α_i of $-\pi/2$ equal to the number of caustics encountered during γ_i . But the wave function $\psi(\mathbf{q})$ must be single valued

under continuation, implying

$$\frac{1}{\hbar} \oint_{\gamma_i} \mathbf{p}_i \cdot d\mathbf{q}_i - \frac{1}{2} \alpha_i \pi = 2m_i \pi \quad (1 \leq i \leq N), \quad \text{that is,} \quad (2.28)$$

$$\frac{1}{2\pi} \oint_{\gamma_i} \mathbf{p}_i \cdot d\mathbf{q}_i = \left(m_i + \frac{1}{4} \alpha_i \right) \hbar, \quad (2.29)$$

where m_i are integers.

This is a set of N quantum conditions on the geometry of Σ . A typical torus will not satisfy these conditions, but Σ is embedded in an N -parameter family labelled by \mathbf{P} and if (as is true semiclassically) \hbar is small compared with $\Delta_i S$ it will always be possible close to any given Σ to find a surface for which equation 2.29 is satisfied and ψ is a single valued semiclassical wave function. The numbers α_i are the Maslov indices and depend on how Σ is embedded in phase space.

The wave ψ thus obtained, based on a quantised torus Σ , will not in general be an eigenfunction of the Hamiltonian H , because it will change with time as Σ deforms under H . Only when Σ is an invariant torus of motion under H will the surface remain fixed as its individual points \mathbf{q}, \mathbf{p} wind around it, and then ψ will be an energy eigenfunction, labelled by N quantum numbers m_i .

2.2.2 Wigner's function

The procedure outlined in the previous subsection for constructing energy eigenfunctions can succeed only if tori exist, that is, if the motion is regular as in integrable systems or throughout most of the phase space as in quasi-integrable systems. For irregular and in particular ergodic motion, no tori exist and Maslov's method fails completely. Wigner [13] introduced a phase space distribution function $\mathbf{W}(\mathbf{q}, \mathbf{p})$ corresponding to a quantum state $\psi(\mathbf{q})$ defined by the N -fold integral

$$\mathbf{W}(\mathbf{q}, \mathbf{p}) = \frac{1}{(2\pi\hbar)^N} \int \dots \int d^N \mathbf{X} \exp\left(-i\mathbf{p} \cdot \frac{\mathbf{X}}{\hbar}\right) \psi^*\left(\mathbf{q} - \frac{\mathbf{X}}{2}\right) \psi\left(\mathbf{q} + \frac{\mathbf{X}}{2}\right), \quad (2.30)$$

namely the Fourier transform of the product ψ and ψ^* at positions separated by \mathbf{X} . \mathbf{W} is a quantal generalization of the classical density of points in phase space. It is possible to generalize other classical functions to get phase space representations of quantal operators [14] but Wigner's function is particularly well suited as it is in phase space that the distinction between classical regular and irregular motion manifests itself most clearly. So the hope is that the analogous quantal distinctions will be revealed with corresponding clarity in the form of $\mathbf{W}(\mathbf{q}, \mathbf{p})$. This idea was developed by Berry and Balazs [17, 18].

Despite appearances, $\mathbf{W}(\mathbf{q}, \mathbf{p})$ has complete formal symmetry in \mathbf{q} and \mathbf{p} . It contains all the information about the quantum state. In particular, the coordinate probability density is obtained by projection “down” \mathbf{p} onto \mathbf{q} :

$$|\psi(\mathbf{q})|^2 = \int \dots \int d^N \mathbf{p} \mathbf{W}(\mathbf{q}, \mathbf{p}), \quad (2.31)$$

and the momentum probability density is obtained by projection “across” \mathbf{q} onto \mathbf{p} :

$$|\bar{\psi}(\mathbf{p})|^2 = \int \dots \int d^N \mathbf{q} \mathbf{W}(\mathbf{q}, \mathbf{p}). \quad (2.32)$$

To see what $\mathbf{W}(\mathbf{q}, \mathbf{p})$ looks like for a semiclassical state of the form given by equation 2.26 on page 25 associated with a surface Σ we substitute equation 2.26 into equation 2.30 on the page before:

$$\begin{aligned} \mathbf{W}(\mathbf{q}, \mathbf{p}) &= \frac{K^2}{(2\pi\hbar)^N} \int \dots \int d^N \mathbf{X} \left| \det \left(\frac{\partial^2 S(\mathbf{q} + \frac{\mathbf{X}}{2}; \mathbf{P})}{\partial \mathbf{q}_i \partial \mathbf{P}_j} \right) \det \left(\frac{\partial^2 S(\mathbf{q} - \frac{\mathbf{X}}{2}; \mathbf{P})}{\partial \mathbf{q}_i \partial \mathbf{P}_j} \right) \right|^{\frac{1}{2}} \\ &\times \exp \left(\frac{i}{\hbar} \left[\int_{\mathbf{q} - \frac{\mathbf{X}}{2}}^{\mathbf{q} + \frac{\mathbf{X}}{2}} \mathbf{p}(\mathbf{q}', \mathbf{P}) \cdot d\mathbf{q}' - \mathbf{p} \cdot \mathbf{X} \right] \right). \end{aligned} \quad (2.33)$$

As $\hbar \rightarrow 0$, the integrand oscillates rapidly and is dominated by the region near $\mathbf{X} = 0$. Expanding the phase for small \mathbf{X} gives

$$\int_{\mathbf{q} - \frac{\mathbf{X}}{2}}^{\mathbf{q} + \frac{\mathbf{X}}{2}} \mathbf{p}(\mathbf{q}', \mathbf{P}) \cdot d\mathbf{q}' \approx \mathbf{X} \cdot \mathbf{p}(\mathbf{q}, \mathbf{P}). \quad (2.34)$$

On setting $\mathbf{X} = 0$ in the determinants, the integral can be evaluated to give the purely classical result

$$\mathbf{W}(\mathbf{q}, \mathbf{p}) \approx K^2 \left| \det \frac{\partial^2 S(\mathbf{q}; \mathbf{P})}{\partial \mathbf{q}_i \partial \mathbf{q}_j} \right| \delta[\mathbf{p} - \mathbf{p}(\mathbf{q}, \mathbf{P})] \quad (2.35)$$

In this approximation, therefore, \mathbf{W} is nonzero only on the surface Σ employed in the construction of ψ . This can be expressed alternatively if we define Σ as the member \mathbf{P}^* of the N -parameter family of surfaces labelled by \mathbf{P} , and use the fact that

$$\left| \det \frac{\partial^2 S(\mathbf{q}; \mathbf{P})}{\partial \mathbf{q}_i \partial \mathbf{P}_j} \right| = \left| \frac{\partial \mathbf{P}}{\partial \mathbf{P}} \right| \quad (2.36)$$

to change the variables in the delta function in equation 2.35. This gives

$$\mathbf{W}(\mathbf{q}, \mathbf{p}) \approx K^2 \delta[\mathbf{P}(\mathbf{q}, \mathbf{p}) - \mathbf{P}^*], \quad (2.37)$$

where $\mathbf{P}(\mathbf{q}, \mathbf{p})$ is the label of the particular surface that passes through \mathbf{q}, \mathbf{p} . From this representation it is clear that \mathbf{W} is of uniform strength in the variable \mathbf{Q} conjugate to \mathbf{P} .

Applying equation 2.37 on the preceding page to the energy eigenstates of a system for which some orbits trace out phase space tori, which must satisfy the quantization conditions (equation 2.29 on page 27) which according to equation 2.3 on page 15 restricts the action variables to

$$\mathbf{I}_{\mathbf{m}} = \left(\mathbf{m} + \frac{\boldsymbol{\alpha}}{4} \right) \hbar \quad (2.38)$$

where $\mathbf{m} = \{m_1 \dots m_N\}$ is the set of quantum numbers and $\boldsymbol{\alpha} = \{\alpha_1 \dots \alpha_N\}$ are the Maslov indices. Then the Wigner function $\mathbf{W}_{\mathbf{m}}$ representing the state labelled by \mathbf{m} is given by equation 2.37 on the page before as the following correctly normalized expression

$$\mathbf{W}_{\mathbf{m}}(\mathbf{q}, \mathbf{p}) \approx \frac{1}{(2\pi)^N} \delta[\mathbf{I}(\mathbf{q}, \mathbf{p}) - \mathbf{I}_{\mathbf{m}}], \quad (2.39)$$

where $\mathbf{I}(\mathbf{q}, \mathbf{p})$ is the action of the torus passing through \mathbf{q}, \mathbf{p} . The N -dimensional delta function for an eigenstate is concentrated on the region that an orbit explores over infinite time, that is, on the torus.

Extending this idea to the case where motion is irregular and so not confined to tori results in the "semiclassical eigenfunction hypothesis":

Each semiclassical eigenstate has a Wigner function concentrated on the region explored by a typical orbit over infinite times.

Berry [18] realized that this plausible hypothesis has powerful predictive force: For an ergodic system, whose orbits fill whole energy surfaces in phase space, each quantum state corresponds to one energy surface, selected by a quantum condition. The hypothesis gives for the correctly normalized Wigner function representing an eigenstate with energy E ,

$$\mathbf{W}(\mathbf{q}, \mathbf{p}) \approx \frac{\delta[E - H(\mathbf{q}, \mathbf{p})]}{\int \dots \int d_q^N d_p^N \delta[E - H(\mathbf{q}, \mathbf{p})]}. \quad (2.40)$$

In contrast to equation 2.39, this is a one-dimensional delta function, reflecting the fact that \mathbf{W} is spread over a much larger region of phase space.

The prediction of different morphologies for \mathbf{W} is supported by computations of Hutchinson and Wyatt [19] for a Hamiltonian with $N = 2$ corresponding to motion of a particle in a potential giving predominantly regular motion at low energies and irregular motion at high energies.

2.2.3 Regular and irregular quantum states

Using the “integrable” (equation 2.39 on the preceding page) or the “ergodic” (equation 2.40 on the page before) together with the definition (equation 2.30 on page 27) it is possible to obtain morphological information about two aspects of $\psi(\mathbf{q})$: its local average strength and its pattern of local oscillations.

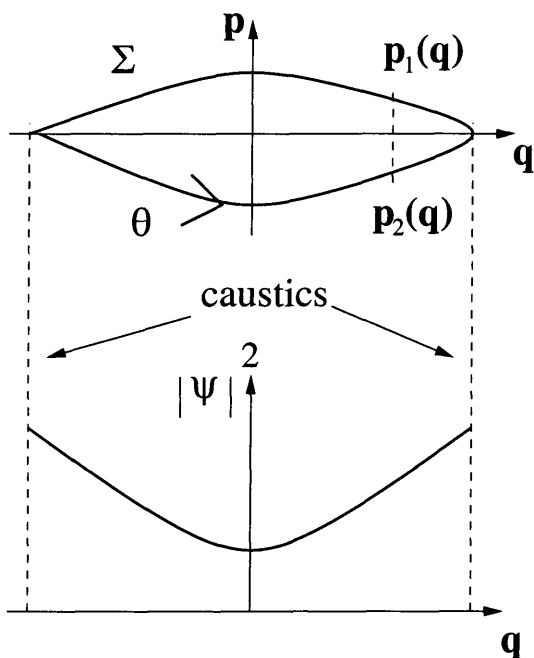


Figure 2.11: Σ for a regular system

Firstly, the probability density $|\psi(\mathbf{q})|^2$ obtained according to equation 2.31 on page 28 by projecting “down” \mathbf{p} . For a system with tori, equation 2.39 on the preceding page simply gives the particular case of equation 2.22 on page 25 appropriate for this form of Σ , (figure 2.11), namely the sum over branches

$$|\psi(\mathbf{q})|^2 \approx \frac{1}{(2\pi)^N} \sum_i \left| \frac{d\theta}{dq}(\mathbf{q}, \mathbf{p}_i(\mathbf{q})) \right|. \quad (2.41)$$

As previously mentioned, there are caustics at the singularities of the projection of the torus onto \mathbf{q} , that is, on local boundaries of the region explored by the orbit in \mathbf{q} -space.

In general the caustics have various morphologies classified as singularities and become very complicated as N increases.

On the other hand, for an ergodic system equation 2.40 on the preceding page gives

$$|\psi(\mathbf{q})|^2 \approx \int \dots \int d^N \delta[E - H(\mathbf{q}, \mathbf{p})], \quad (2.42)$$

that is, the projection of the energy surface. Berry [18] evaluated this for the case of a Hamiltonian

$$H(\mathbf{q}, \mathbf{p}) = \frac{|\mathbf{p}|^2}{2\mu} + V(\mathbf{q}), \quad (2.43)$$

with $V(\mathbf{q})$ corresponding to ergodic motion to get the result

$$|\psi(\mathbf{q})|^2 \sim [E - V(\mathbf{q})]^{\frac{N}{2}-1} \Theta[E - V(\mathbf{q})], \quad (2.44)$$

where the step function confines $|\psi|^2$ to the classically allowed part of \mathbf{q} -space. For $N > 1$ the result shows that $|\psi(\mathbf{q})|^2$ does not diverge on the boundary of the

classical region: instead, it displays anticaustics. Geometrically, this unexpected result is made plausible by a one-dimensional analogy in which instead of projecting a closed curve as in figure 2.11 on the page before we project the patch of phase space enclosed by the curve (figure 2.12).

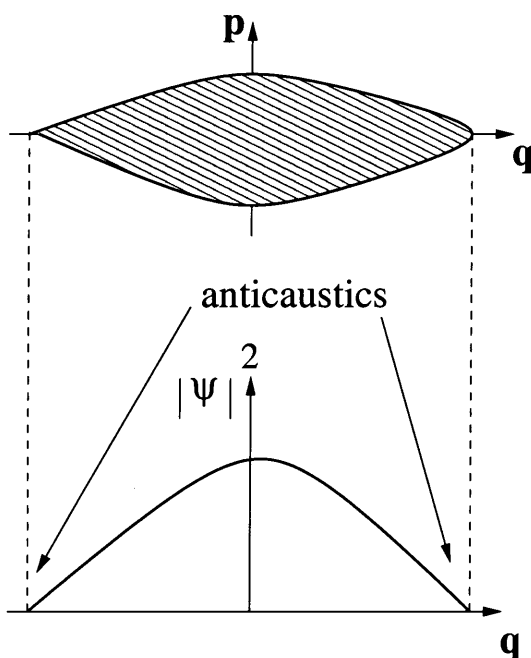


Figure 2.12: Σ for an irregular system

of wave functions.

It implies that as $\hbar \rightarrow 0$ wave functions separate into two universality classes, associated with regular and irregular classical motion. In the regular case, ψ is associated with tori, and has vivid anisotropic interference oscillations rising to high intensity $|\psi|^2$ on caustics.

In the irregular case, where ψ is associated with chaotic regions in phase space and has a random pattern of oscillations (isotropic for ergodic systems) with anticaustics at classical boundaries.

This means that for irregular states an unfamiliar structure is predicted and computations by McDonald and Kaufman [51] confirm this for the desymmetrized stadium which is classically ergodic so quantal eigenstates should be irregular. Figure 2.13 is an illustration of the sort of nodal lines obtained showing them to wander

As to what sort of semiclassical $|\text{wave function}|^2$ is being calculated by this procedure involving the purely classical Wigner functions (equations 2.39 and 2.40 on page 29): The probable answer is that it is the limit $\hbar \rightarrow 0$ of the probability density $|\psi|_{\text{sm}}^2$ which has been smoothed over a distance Δ in each direction in \mathbf{q} -space, where Δ vanishes as $\hbar \rightarrow 0$ more slowly than \hbar , so that oscillatory detail on the scale of the de Broglie wavelength is smoothed away.

The idea underlying the semiclassical eigenfunction hypothesis has led to predictions concerning the morphology

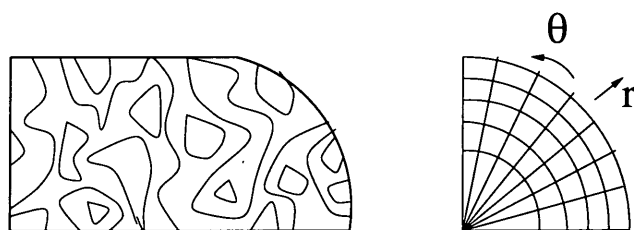


Figure 2.13: Nodal lines for the stadium and circle billiards

irregularly with no systematic well defined direction. For comparison the nodal lines for an eigenfunction of a circle is shown, which form a regular pattern because the circle is an integrable billiard.

2.2.4 Scars

Heller, O'Connor and Gehlan [23] studied the eigenstates of the Stadium billiard, discovering that each eigenstate has an intensity pattern showing what they termed scars, that is, narrow line at regions with an enhanced intensity which stands out clearly and appears to be coming from classical periodic orbits.

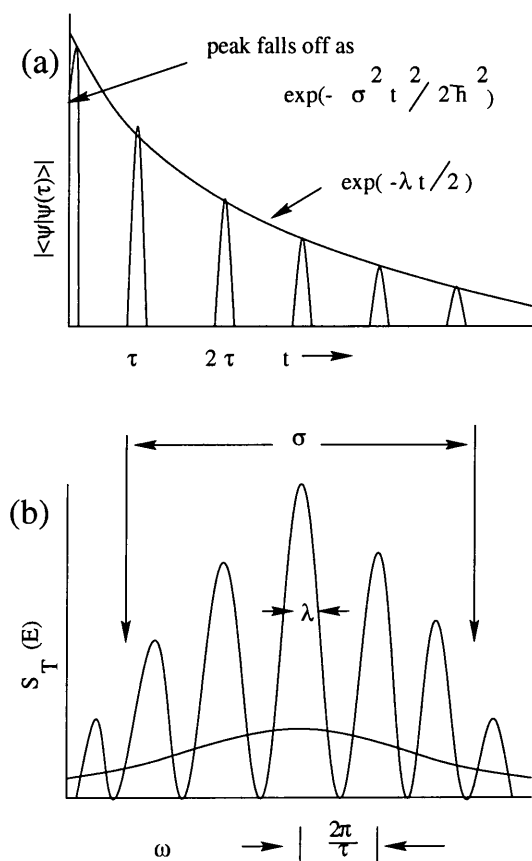


Figure 2.14: Schematic plot of the overlap function in time (a) and in energy (b)

The stability of an unstable periodic orbit can be characterized by a frequency ω and a Lyapunov exponent λ . The distance of neighbouring trajectories from the periodic orbit increases with time t as $\exp(\lambda t)$ and scars of a periodic orbit will appear if $\lambda < \omega$. Heller's argument [24] for criterion can be explained with the aid of figure 2.14.

A Gaussian wave packet

$$\psi(q, t) = \exp \left[\frac{i}{\hbar} \left\{ \alpha_t (q - q_t)^2 + p_t (q - q_t) + \gamma_t \right\} \right] \quad (2.45)$$

where α_t is a complex symmetric matrix with dimensions corresponding to the degrees of freedom and λ_t is a complex phase, is launched along a classical periodic orbit at time $t = 0$.

The overlap

$$\langle \psi | \psi(t) \rangle = \int dq \psi^\dagger(q, 0) \psi(q, t) \quad (2.46)$$

has the appearance of figure 2.14(a) as a function of time: tight Gaussian peaks repeat at intervals corresponding to the period of the orbit $\tau = 2\pi/\omega$, but they decay exponentially with half the Lyapunov exponent λ . The Fourier spectrum of

the overlap

$$S_T(E) = \frac{1}{2\pi} \int dt \exp\left(\frac{iEt}{\hbar}\right) \langle \psi(0) | \psi(t) \rangle \quad (2.47)$$

extended over the finite interval $-T$ to $+T$, has the complementary shape given in figure 2.14(b).

If the original wave packet $\psi(q, 0)$ is expanded in the eigenstates ϕ_n of the system, the function $S_T(E)$ is further resolved into narrow peaks of widths \hbar/T , each corresponding to an energy level E_n ; the height of the peak gives the intensity I_n with which ϕ_n is participating in $\psi(q, 0)$; of course, these intensities add up to 1. Since they are concentrated in bands of width $\hbar\lambda$, which occur at intervals of $\hbar\omega$, the intensities are enhanced by a factor ω/λ compared to a completely random distribution. We find, therefore, a privileged set of eigenstates that have a marked preference for the particular periodic orbit along which the initial Gaussian wave packet is launched. The privilege becomes the more exclusive the larger the ratio ω/λ . An illustration of the scarring is shown in figure 2.15 for the stadium billiard.

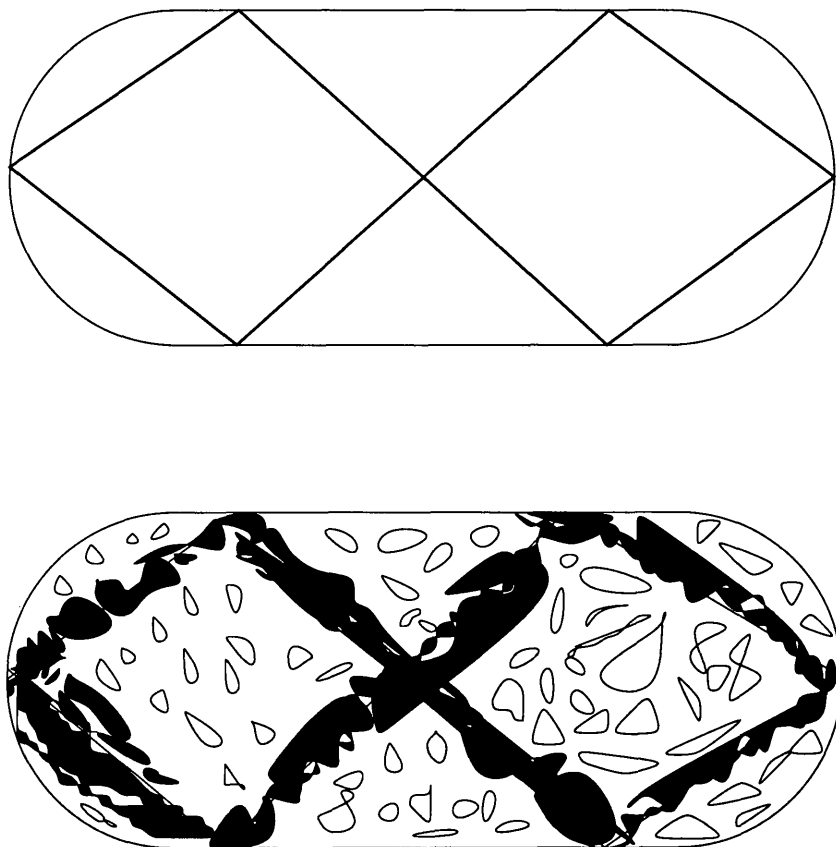


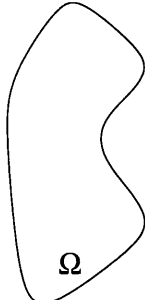
Figure 2.15: An unstable periodic orbit of the stadium (top) and a contour plot (bottom) of the probability distribution for the corresponding eigenstate

2.2.5 Energy spectra

Whilst the previous subsections have been concerned with connecting classical dynamics of a system with the wave functions of the equivalent quantum system. We now consider the relationship between classical dynamics and the energy spectra, that is, the set of eigenvalues of the Hamiltonian of the system. This is intimately related to random matrix theories (RMT), but, before discussion of RMT we need an understanding of energy spectra, fluctuations, spacing distributions and correlations.

2.2.5.1 A simple example

In order to get some flavour about general ideas and concepts to come we begin by considering the vibrations of a membrane (the drum): A membrane is a perfectly flexible and infinitely thin lamina of solid matter of uniform material and thickness which is stretched in all directions by a tension so great as to remain unaltered during its vibrations. Of interest is the investigation of the transverse vibrations of membranes of different shapes, whose boundaries are fixed.


 One considers then (figure 2.16) a membrane stretched over an area Ω included within a fixed, closed plane boundary Γ . Taking the plane of the membrane as that of $x - y$ and letting ψ denote the small displacement perpendicular to its original plane then ψ obeys the wave equation

$$\frac{\partial^2 \psi}{\partial t^2} = c^2 \nabla^2 \psi, \quad (2.48)$$

where c is a constant, with dimensions of velocity, depending on the physical properties of the membrane and on the tension. Of special interest are the solutions of the form

$$\psi(x, y; t) = \psi(x, y) e^{i\omega t} \quad (2.49)$$

for, being harmonic in time with frequency ω , they represent the pure tones the membrane is capable of producing. These special solutions are the normal modes and are found by substituting equation 2.49 into equation 2.48 whereupon it is found that ψ must satisfy the eigenvalue equation

$$\nabla^2 \psi = -\frac{\omega^2}{c^2} \psi = -\kappa^2 \psi = -E \psi \quad (2.50)$$

with the condition that ψ must vanish on the boundary Γ , and ω is a frequency, κ is a wave number and E is an energy. It possess an infinite number of eigenvalues E_n

which are real and non-negative and have no accumulation point. One has therefore

$$0 \leq E_1 \leq E_2 \leq E_3 \dots, \quad \lim_{n \rightarrow \infty} E_n = \infty. \quad (2.51)$$

We are interested in properties of the sequence of eigenvalues. For instance, on what characteristics of the boundary depends the number of modes per unit energy (or unit frequency), that is, what is the density of eigenmodes.

In quantum physics, equation 2.50 represents the time-independent Schrödinger equation for a free particle of mass m moving in the interior of a box with infinite walls, with $\hbar\kappa = \sqrt{2mE}$, where E is the kinetic energy.

Now consider the number $N(E)$ of eigenvalues which are less than or equal to E . The function $N(E)$ is an infinite staircase, which increases by one each time one “crosses” an eigenvalue. We are interested in extracting a smoothed eigenvalue distribution $N_{av}(E)$, that is, the smoothed function giving the number of eigenvalues less than or equal to E in order to study the fluctuations or oscillations of the eigenvalue distribution around the averaged value $N_{av}(E)$. The function $N_{av}(E)$ can be written

$$N_{av}(E) = \frac{\sigma}{4\pi} E \mp \frac{\gamma}{4\pi} \sqrt{E} + K + O\left(E^{-\eta/2} \ln \sqrt{E}\right), \quad (2.52)$$

where $0 \leq \eta \leq 1$, σ is the surface of the area Ω (Weyl’s term) and γ is the perimeter of the boundary Γ (– and + sign for the Dirichlet and Neumann conditions respectively). K is a constant term containing complex information on the geometrical and topological properties of the domain. The geometrical features contributing to the constant term are:

(i) Curvature contributions

$$\frac{1}{12} \int_{\Gamma} k(l) dl, \quad (2.53)$$

where $k(l)$ denotes the local curvature.

(ii) Corner contributions: for a square (or rectangle) it is $4 \times 1/48$.

The topological features concern the connectivity of the surface; for a multiply connected drum containing r holes, the contribution is $(1 - r)/6$.

2.2.5.2 Fluctuations

For a dynamical system, one obtains the discrete set of eigenvalues of the Hamiltonian which give the staircase function $N(\zeta)$. Then as in the previous subsection

this is separated into a smooth part $N_{av}(\zeta)$ and a fluctuating part $N_{fl}(\zeta)$

$$N(\zeta) = N_{av}(\zeta) + N_{fl}(\zeta). \quad (2.54)$$

Before study of the fluctuations is possible it is necessary to get rid of the $N_{av}(\zeta)$ in order to compare the fluctuation patterns of different systems whose corresponding average behaviour $N_{av}(\zeta)$ are not the same. For that purpose, one “unfolds” the original spectrum to obtain a new spectrum $\{x_i\}$ (this procedure is given in Chapter 4). The effect is that for the new sequence $\{x_i\}$, $N_{av}(x) = x$, that is, the sequence $\{x_i\}$ on the average has a constant mean spacing (or a constant density) equal to unity;

$$N_{av}(\zeta) = \int_0^\zeta \rho_{av}(\zeta') d\zeta' = \int_0^x dx' = x = \hat{N}_{av}(x), \quad (2.55)$$

where $\rho_{av}(\zeta)$ is the average density of $\{\zeta_i\}$.

So after unfolding, we study quantities related to

$$\hat{N}(x) = \hat{N}_{av}(x) + \hat{N}_{fl}(x) = x + \hat{N}_{fl}(x). \quad (2.56)$$

For the fluctuation properties of sequences $\{x_i\}$ two situations arise:

- (i) The system is known to be, from a statistical point of view, translational invariant or stationary, that is, the fluctuation properties are the same irrespective of which region of the spectrum of the sequence is being considered.
- (ii) The system is not stationary but the asymptotic properties of the spectrum are of interest.

Two limiting types of system are encountered:

- (i) Poisson systems: Take a random variable s whose probability density $p(x)$ is e^{-x} and construct a sequence $\{x_i\}$

$$x_1 = 0, \quad x_{i+1} = x_i + s_i \quad i = 1, 2, 3, \dots, \quad (2.57)$$

where s_i are outcomes of independent trials of the variable s . The resulting spectrum is a Poisson spectrum, which is obviously stationary. For instance, the counting rate of a decaying source forms a Poisson spectrum, the time being measured in units of the mean life of the source. In this type of spectrum we find a large probability of small spacings, occurrence of some large spacings and no correlations between spacings. The knowledge of a stretch of the spectrum puts no restrictions on the behaviour of the spectrum beyond the interval considered, irrespective of the form of $p(x)$ chosen. Thus we have complete randomness.

- (ii) Picket fence systems: The sequence $\{x_i\}$ is fluctuation free, for example, $\zeta_k = k^2$ ($k = 1, 2 \dots$) then $N_{av}(\zeta) = \sqrt{\zeta}$ and $x_k = k$, a sequence of equally spaced points or picket fence. This spectrum qualifies as absolutely rigid in the sense that there is no departure at all from uniformity. Once the position of one level x_i is known, the position of any other level is determined. The correlations between spacings are maximum and it shows perfect short and long range order. Thus we have no randomness at all.

In the intermediate cases small probability of small and large spacings is encountered, with the former being usually referred to in the literature as the phenomenon of level repulsion. Here the degree of spectral rigidity is governed by the nature and strength of the correlations between spacings.

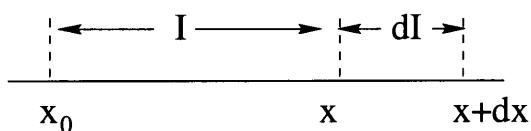


Figure 2.17: Interval for Wigner's argument

A simple heuristic argument due to Wigner that illustrates the presence or absence of level repulsion is as follows: Consider the probability $p(x) dx$ that, given a level at x_0 , the next level is in the small interval (figure 2.17)

$$dI = [x_0 + x, x_0 + x + dx].$$

It can be represented as the product of two factors

$$p(x) dx = p_r(\text{one level in } dI/\text{no level in } I) \times p_r(\text{no level in } I), \tag{2.58}$$

where p_r means probability and $p_r(a/b)$ is the conditional probability of having a if b is true. One has

$$p_r(\text{no level in } I) = \int_x^\infty p(x') dx' \quad \text{and} \tag{2.59}$$

$$p_r(\text{one level in } dI/\text{no level in } I) = \mu(x) dx, \quad \text{therefore} \tag{2.60}$$

$$p(x) = \mu(x) \int_x^\infty p(x') dx', \tag{2.61}$$

which can be solved to give

$$p(x) = C \mu(x) \exp\left(-\int_0^x \mu(x') dx'\right). \tag{2.62}$$

Now for a Poisson sequence $\mu(x)$ is independent of x and one obtains ($\int p(x) dx = \int xp(x) dx = 1$)

$$p(x) e^{-x} \quad x \geq 0. \tag{2.63}$$

A linear level repulsion can be introduced by assuming $\mu(x) = \beta$, then

$$p_W(x) = \frac{\pi}{2} x e^{-\frac{\pi}{4} x^2} \quad x \geq 0. \quad (2.64)$$

The result (equation 2.64) for the spacing distribution, $p(x)$, is known in the literature of random matrices as the Wigner surmise and it explicitly shows the level repulsion or tendency to avoid clustering of levels. Indeed, $p(x=0) = 0$ in contrast to the Poisson case, for which the corresponding spacing distribution (equation 2.63) is maximum at the origin.

The spacing distribution $p(x)$ contains no information about spacing correlations. A simple measure of spacing correlations is the correlation coefficient C between, for instance, two adjacent spacings. Let $\{x_i\}$ be the sequence of levels and s_i the spacings $s_i = x_{i+1} - x_i$, C is given by

$$C = \frac{\sum_i (s_i - 1)(s_{i+1} - 1)}{\sum_i (s_i - 1)^2}, \quad (2.65)$$

where we assume the mean spacing equal to unity. For a Poisson spectrum $C = 0$.

A convenient variable often used is Mehta's spectral rigidity, $\Delta_3(L)$ [20] which measures, given an interval $[\alpha, \alpha + L]$ of length L , the least squares deviation of the staircase $\hat{N}(x)$ from the best straight line fitting it:

$$\Delta_3(\alpha; L) = \left(\frac{1}{L}\right) \min_{A,B} \int_{\alpha}^{\alpha+L} [\hat{N}(x) - Ax - B]^2 dx. \quad (2.66)$$

We are dealing with spectra for which the average part $\hat{N}_{av}(x)$ of $\hat{N}(x)$ is a straight line $y = x$. However, when considering a given interval $[\alpha, \alpha + L]$, the best straight line fitting $\hat{N}(x)$ will not just be $y = x$ but another (presumably close lying) straight line $Ax + B$ which is determined by equation 2.66. The value of $\Delta_3(L)$ for $L \gtrsim 1$ for a picket fence is $1/12$ whereas the average $\langle \Delta_3(L) \rangle$ of $\Delta_3(\alpha; L)$ (take many non overlapping adjacent segments of length L of the spectrum, compute the value of Δ_3 for each segment and perform the average) for a Poisson spectrum is $L/15$. The departure of the average value of $\Delta_3(L)$ from the linear increase with L characteristic of the Poisson spectrum gives, in intermediate situations between Poisson and picket fence, information on the correlation between spacings and the spectral rigidity or spectral stiffness.

Another useful variable is the number statistic $n(L)$: given an interval $[\alpha, \alpha + L]$ of length L , it counts the number of levels contained in the interval. The average value of $n(L)$ is L , if the mean spacing is unity. There are also higher moments or cumulants of $n(L)$:

- (i) $\Sigma^2(L)$, variance,
- (ii) $\gamma_1(L)$, skewness.
- (iii) $\gamma_2(L)$, excess.

If the spectrum is stiff, the variance of $n(L)$ is small whereas for a non-rigid or compressible spectrum it is comparatively large.

2.2.5.3 Random matrix theories

Random matrix theories have their origin in the following physical problem: In the low energy region of the excitation spectrum of a nucleus, the level density $\rho(E)$ is small and one expects to describe most of the states in a detailed way using nuclear models. However, due to the rapid increase of the levels with the excitation energy E

$$\rho(E) \simeq \frac{c}{(E - \Delta)^{5/4}} \exp\left(a\sqrt{E - \Delta}\right) \quad (2.67)$$

where c, Δ and a are constants for a given nucleus, by the time one reaches the region, for instance, of the neutron threshold ($E \sim 6MeV$), the number of levels is so high that one must give up a description of microscopic detail, a description of the individual levels.

Dyson [22] made a resume of the situation which ends with

“... What is required is a new kind of statistical mechanics, in which we renounce exact knowledge not of the state of a system but of the nature of the system itself. We picture a complex nucleus as a “black box” in which a large number of particles are interacting according to unknown laws. The problem is then to define in a mathematically precise way an ensemble of systems in which all possible laws of interest are equally probable.”

The appropriate language to define an ensemble of systems is provided by random matrix theory [21]. One considers the Hamiltonian matrix H as an $N \times N$ stochastic matrix and the question is to specify the probability density $\rho(H) dH$. This is shown in the next Subsubsection.

Time reversal invariance	Angular momentum	Rotation invariance	Hamiltonian matrix	Canonical group	β
yes	Integer $\frac{1}{2}$ -Odd-Integer	- yes	Real Symmetric	Orthogonal	1
yes	$\frac{1}{2}$ -Odd-Integer	no	Real Quarternion	Symplectic	4
no	-	-	Complex Hermitian	Unitary	2

Table 2.1: Space-time symmetries

2.2.5.4 Gaussian ensembles

The underlying space-time symmetries obeyed by the system put important restrictions on the admissible matrix ensembles. these are shown in table 2.1

In order to introduce a proper invariant measure dH in the space of matrices one can proceed as follows. A metric is defined in the matrix space to which H belongs by expressing

$$ds^2 = \text{Tr} \delta H \delta H^\dagger \quad (2.68)$$

in terms of the independent variables x_μ of H , as

$$ds^2 = \sum_{\mu, \nu}^M g_{\mu\nu=1} \delta x_\mu \delta x_\nu, \quad (2.69)$$

where M is the number of independent variables (matrix elements). The basic measure dH is then induced by this matrix, namely

$$dH = (\det g_{\mu\nu})^{1/2} \prod_{\mu=1}^M dx_\mu. \quad (2.70)$$

For ($\beta = 1$) real symmetric matrices H ($H^* = H^T$) there are $N(N + 1)/2$ independent variables and one has

$$ds^2 = \sum_{1 \leq i \leq N} (\delta H_{ii})^2 + 2 \sum_{1 \leq i < j \leq N} (\delta H_{ij})^2 \quad (2.71)$$

so that

$$dH = 2^{N(N-1)/4} \prod_{1 \leq i \leq N} dH_{ii} \prod_{1 \leq i < j \leq N} dH_{ij}. \quad (2.72)$$

For the case ($\beta = 2$) of Hermitian matrices H ($= H^\dagger$) one has N^2 independent variables. Writing $H = H' + iH''$ where $H' = H'^T$, $H'' = H''^* = H''^T$, one has

$$ds^2 = \sum_{1 \leq i \leq N} (\delta H'_{ii})^2 + 2 \sum_{1 \leq i < j \leq N} [(\delta H'_{ij})^2 + (\delta H''_{ij})^2] \quad (2.73)$$

so that

$$dH = 2^{N(N-1)/2} \prod_{1 \leq i \leq N} dH'_{ii} \prod_{1 \leq i < j \leq N} dH'_{ij} dH''_{ij}. \quad (2.74)$$

Gaussian orthogonal ensembles (GOE) in the space of real symmetric matrices is defined by demanding two requirements:

- (1) The ensemble is invariant under every orthogonal transformation

$$H' = W^T H W, \quad (2.75)$$

where W is any real orthogonal matrix, that is, the probability $\wp(H) dH$ that a matrix H will be in the volume element dH (equation 2.72 on the preceding page) is invariant under orthogonal transformations

$$\wp(H') dH' = \wp(H) dH. \quad (2.76)$$

- (2) The various elements H_{ij} ($i \leq j$) are independent random variables.

The first requirement is made so that all states behave in the same way and the second one is for the purpose of simplicity.

Similarly, the Gaussian Unitary Ensemble (GUE) in the space of Hermitian matrices is defined by the properties

- (1*) The ensemble is invariant under every unitary transformation

$$H' = U^T H U, \quad (2.77)$$

where U is any real unitary matrix, that is, the probability $\wp(H) dH$ that a matrix H will be in the volume element dH (equation 2.74) is invariant under unitary transformations

$$\wp(H') dH' = \wp(H) dH. \quad (2.78)$$

- (2*) The various elements H'_{ij} ($i \leq j$), H''_{ij} ($i \leq j$) are independent random variables, that is, $\wp(H)$ is a product of N^2 functions.

These two requirements (1 and 2 or 1* and 2*) determine uniquely the ensembles. The function $\wp(H)$ can be written

$$\wp(H) = K_{N\beta} \exp \left\{ -\frac{\text{Tr}(H^2)}{4\sigma^2} \right\}, \quad (2.79)$$

where $K_{N\beta}$ is a normalisation constant (N is the dimensionality of the matrix and $\beta = 1, 2, 4$ labels the different cases) and σ is a scale factor. In equation 2.79 on the preceding page

$$\text{Tr}H^2 = \sum_{1 \leq i \leq N} H_{ii}^2 + 2 \sum_{1 \leq i < j \leq N} H_{ij}^2 \quad \text{for } \beta = 1 \quad (2.80)$$

$$\text{Tr}H^2 = \sum_{1 \leq i \leq N} H_{ii}^2 + 2 \sum_{1 \leq i < j \leq N} (H_{ij}'^2 + H_{ij}''^2) \quad \text{for } \beta = 2. \quad (2.81)$$

For the GOE one therefore has that each matrix element H_{ij} is distributed normally (that is, Gaussian distributed) with zero mean

$$\bar{H}_{ij} = 0 \quad i \leq j \quad (2.82)$$

and variance

$$\bar{H}_{ij}^2 = (1 + \delta_{ij}\sigma^2) \quad i \leq j. \quad (2.83)$$

where for any quantity W , \bar{W} is its ensemble average. For the GUE one also has normal distribution of the different variables with

$$\bar{H}'_{ii} = \bar{H}''_{ii} = 0, \quad \bar{H}'_{ii}{}^2 = 2\sigma^2 \quad i = j \quad (2.84)$$

and

$$\bar{H}'_{ij} = \bar{H}''_{ij} = 0, \quad \bar{H}'_{ij}{}^2 = \bar{H}''_{ij}{}^2 = \sigma^2 \quad i < j. \quad (2.85)$$

Making use of the invariance properties, the joint probability density of the eigenvalues E_i can be extracted from equation 2.79 on the page before:

$$P_{N\beta}(E_1, E_2, \dots, E_N) = C_{N\beta} \exp \left\{ -\frac{1}{4\sigma^2} \sum E_i^2 \right\} \prod |E_i - E_j|^\beta, \quad (2.86)$$

where $C_{N\beta}$ is a normalisation constant determined by

$$\int P_{N\beta}(E_1, E_2, \dots, E_N) dE_1 dE_2 \dots E_N = 1. \quad (2.87)$$

$P_{N\beta}(E_1, E_2, \dots, E_N) dE_1 dE_2 \dots E_N$ gives the probability, regardless of labelling, of having one eigenvalue at E_1 , another at E_2, \dots another at E_N within each of the intervals $[E_j, E_{j+1}]$. Equation 2.86 contains all the information concerning the eigenvalue distribution and the correlations among eigenvalues. By performing suitable integrations, one can in principle derive all the quantities related to eigenvalues which are of interest.

By integrating Equation 2.86 on the page before over all variables but one, one finds, in the limit of large N for the three cases $\beta = 1, 2, 4$, the ensemble averaged eigenvalue density $\bar{\rho}(E)$

$$\begin{aligned}\bar{\rho}(E) &= \int \dots \int P_{N\beta}(E, E_2 \dots E_N) dE_2 \dots dE_N \\ &= \begin{cases} \frac{1}{2\pi} \frac{1}{N\sigma^2} \sqrt{4N\sigma^2 - E^2} & \text{for } |E| \leq 2\sqrt{N\sigma^2} \\ 0 & \text{for } |E| \geq 2\sqrt{N\sigma^2} \end{cases} \quad (2.88)\end{aligned}$$

which, from equation 2.87 on the preceding page, is normalised to unity.

2.2.5.5 Fluctuation properties

Once the global behaviour of the eigenvalues has been established (the ensemble averaged eigenvalue density $\bar{\rho}(E)$) level fluctuations or departures of the spectrum from its average behaviour can be investigated. One introduces the k -level correlation functions $\tilde{R}_k(E_1, E_2 \dots E_k)$ defined by

$$\tilde{R}_k(E_1, E_2 \dots E_k) = \frac{N!}{(N-k)!} \int \dots \int P_N(E_1, \dots, E_N) dE_{k+1} \dots dE_N \quad (i \leq k \leq N), \quad (2.89)$$

where P_N is given by equation 2.86 on the page before. It follows that $\tilde{R}_1 = N\bar{\rho}(E_1)$, where $\bar{\rho}(E_1)$ is given by equation 2.88 and $\tilde{R}_N = N!P_N$. $\tilde{R}_k(E_1, E_2 \dots E_k) dE_1 \dots E_k$ is the probability of finding one level, regardless of labelling, within each of the intervals $[E_j, E_j + dE_j]$. To get rid of $\bar{\rho}(E)$, one introduces a new set of k -level correlation functions $R_k(x_1, \dots x_k)$ (unfolding) and one considers the case of interest $N \gg k \geq 1$

$$R_k(x_1, \dots x_k) = \lim_{N \rightarrow \infty} \frac{\tilde{R}_k(E_1, \dots, E_k)}{\tilde{R}_1(E_1) \dots \tilde{R}_k(E_k)}. \quad (2.90)$$

The fluctuation properties of the levels are completely characterized by the set of functions $R_k(x_1, \dots x_k)$.

From R_k one obtains the k -level cluster functions Y_k by subtracting out the lower-order correlation terms

$$Y_k(x_1, \dots, x_G) = \sum_G (-1)^{k-m} (m-1)! \prod_{j=1}^m R_{G_j}(x_t, \text{ with } t \in G_j). \quad (2.91)$$

Here G stands for any division of the indices $[1, 2, \dots k]$ into subgroups $[G_1, G_2 \dots G_m]$.

For instance

$$\begin{aligned}
 k = 1 \quad m = 1 \quad [(1)] \text{ and} \\
 Y_1(x_1) = R_1(x_1) = 0
 \end{aligned} \tag{2.92}$$

$$\begin{aligned}
 k = 2 \quad m = 1 \quad [(1, 2)] \\
 m = 2 \quad [(1)(2)] \text{ and} \\
 Y_2(x_1, x_2) = -R_2(x_1 x_2) + R_1(x_1) R_1(x_2)
 \end{aligned} \tag{2.93}$$

The advantage of the cluster functions is that they have the property of vanishing when one (or several) of the separations $|x_i - x_j|$ becomes large. The function Y_k describes the correlation properties of a single cluster of k levels, isolated from more trivial effects of lower-order correlations.

An alternative way to characterise fluctuations is to deal with spacing distributions and related quantities. In equation 2.89 on the page before instead of integrating from $-\infty$ to ∞ without any restrictions one integrates some of the variables outside the interval $[\alpha, \alpha + l]$ whereas the others are integrated inside it. Assume that the unfolding (mapping $E \rightarrow x$) has been performed. One defines ($N \gg k \geq 0$)

$$E(k; L) = \lim_{N \rightarrow \infty} \frac{N!}{(N-k)!} \int_{in} \dots \int dx_1 \dots dx_k \int_{out} dx_{k+1} \dots dx_N P_N(x_1, \dots, x_N). \tag{2.94}$$

If the system is stationary $E(k; L)$ will be independent of α . $E(k; L)$ is the probability that in a sequence $\{x_i\}$ of levels with mean spacing unity an interval of length L taken at random contains exactly k levels. A useful aspect of the functions $E(k; L)$ is that they are very directly connected to the spacing distributions

$$p(k; L) = \left(\frac{d^2}{dL^2} \right) \sum_{j=0}^k (k-j+1) E(j; L). \tag{2.95}$$

In particular for the nearest-neighbour spacing distribution $p(x)$

$$p(x) \equiv p(0; x) = \frac{d^2}{dx^2} E(0, x). \tag{2.96}$$

The probability $F(k; L)$ that in a sequence $\{x_i\}$ of levels with mean spacing unity an interval $[x_\alpha, x_\alpha + L]$ of length L which starts at a level x_α contains exactly k levels is also given in terms of the function $E(k; L)$:

$$F(k; L) = -\frac{d}{dL} \sum_{j=0}^k E(j; L) \tag{2.97}$$

and, in particular

$$F(0, L) = -\frac{d}{dL}E(0; L). \quad (2.98)$$

When comparing a theoretical model with experiment, due to the limited number of high quality data, it is impossible to make a complete comparison between the set of k -level cluster functions Y_k and the corresponding quantities extracted from experiment. It is convenient to work with integrated quantities like

$$y_k(L) = \int_0^L \dots \int_0^L Y_k(x_1, \dots, x_k) dx_1 \dots dx_k. \quad (2.99)$$

Chapter 3

Classical dynamics in the \mathcal{B}_\square

3.1 General rotating billiards

The trajectory of a particle of mass m moving freely on a plane table within a closed wall that reflects perfectly at each impact, while the system rotates steadily about a fixed perpendicular axis, is curved between impacts and upon reflection the particle loses or gains momentum instantaneously. This means that the energy of the particle is not conserved in the laboratory frame, thus constructing a conserved Hamiltonian is not feasible.

Construction of a conserved Hamiltonian is possible by making the standard transformation to a rotating frame with the same angular speed, ω , as the rotating boundary. In this rotating frame the equation of motion can be neatly written using the parametrisation of the (x, y) co-ordinates of the particle by the complex variable $z = x + iy$.

3.1.1 Equations of motion

The equations of motion in the rotating frame are derived in Appendix B on page 158. With the billiard rotating about the z -axis, the particle confined to the plane and our aforementioned parametrisation the conditions are:

$$\mathbf{r} = x\hat{\mathbf{i}} + y\hat{\mathbf{j}}, \quad \boldsymbol{\omega} = \omega\hat{\mathbf{k}} \quad \text{and} \quad z = x + iy \quad (3.1)$$

Then with a little algebraic manipulation equation B.4 on page 158 leads to the concise equation of motion:

$$\ddot{z} + 2i\omega\dot{z} - \omega^2 z = 0 \quad (3.2)$$

in agreement with [25]. It has the general solution:

$$z(t) = (a + bt)e^{-i\omega t} \quad (3.3)$$

Where $a = z(0)$ and b are complex constants, this equation represents free-particle motion with a superposed anticlockwise rotation (choosing $\omega > 0$). Upon differentiating we obtain the velocity of the particle at an arbitrary time t :

$$\dot{z}(t) = be^{-i\omega t} - i\omega(a + bt)e^{-i\omega t} = be^{-i\omega t} - i\omega z(t) \quad (3.4)$$

Which leads to $b = \dot{z}(0) + i\omega z(0)$ and hence

$$z(t) = [z(0) + (\dot{z}(0) + i\omega z(0))t]e^{-i\omega t} \quad (3.5)$$

$$\dot{z}(t) = [\dot{z}(0) - i\omega(\dot{z}(0) + i\omega z(0))t]e^{-i\omega t} \quad (3.6)$$

The motion described by equation 3.2 on the preceding page is in fact that of charged particle in a stationary frame with Lorentz force, \mathbf{F} :

$$\mathbf{F} = \omega^2 z - 2i\omega \dot{z} \quad (3.7)$$

That is, that arising from a constant magnetic field of magnitude 2 perpendicular to the plane and a linear electric field radially outwards. This is the connection between rotating billiards and [26].

The equation of motion, (3.2 on the page before), in the rotating frame can also be derived from the Lagrangian for a rotating frame. This is shown in Appendix C on page 160 to be

$$\mathcal{L} = \frac{1}{2}\{(\dot{x}^2 + \dot{y}^2) + \omega^2(x^2 + y^2)\} + \omega(xy - y\dot{x}) \text{ or} \quad (3.8)$$

$$\mathcal{L} = |\dot{z}|^2 + |\omega z|^2 + i\omega(\dot{z}z - z\dot{z}) \quad (3.9)$$

in keeping with [25].

The form of the Hamiltonian can be seen directly from equation C.17 on page 162 or alternatively by expressing the velocity, \mathbf{v} , in equation C.15 on page 161 in terms of the momentum, \mathbf{p} , by equation C.14 on page 161:

$$H = \frac{m|\mathbf{v}|^2}{2} - \boldsymbol{\omega} \cdot \mathbf{r} \wedge \mathbf{p} \quad (3.10)$$

or by using the conditions given by equation 3.1 on the preceding page:

$$H = \frac{1}{2m}(p_x^2 + p_y^2) - \omega(xp_y - yp_x) = |\dot{z}|^2 - |\omega z|^2 = \text{constant} \quad (3.11)$$

Then Hamilton's equations of motion are:

$$\dot{x} = \frac{\partial H}{\partial p_x} = p_x + \omega y, \quad \dot{y} = \frac{\partial H}{\partial p_y} = p_y - \omega x \quad (3.12)$$

$$\dot{p}_x = -\frac{\partial H}{\partial x} = \omega p_y, \quad \dot{p}_y = -\frac{\partial H}{\partial y} = -\omega p_x \quad (3.13)$$

Hence a suitable conserved Hamiltonian for a rotating billiard is:

$$H = \frac{1}{2m}(p_x^2 + p_y^2) - \omega(xp_y - yp_x) + U(x, y) \quad (3.14)$$

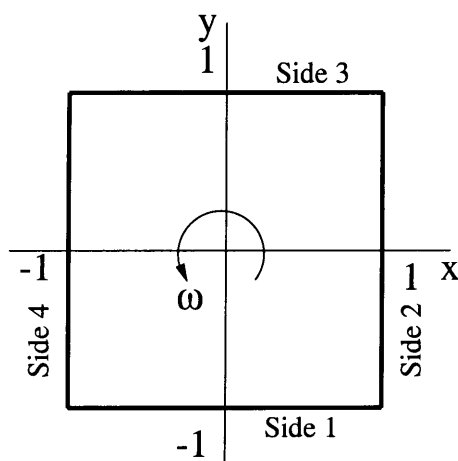
Where U is the infinite potential well:

$$U = \begin{cases} 0 & \text{inside boundary} \\ \infty & \text{outside boundary} \end{cases} \quad (3.15)$$

In the rotating frame the boundary appears stationary; thus the particle is specularly reflected in this frame, justifying equation 3.15 to be the correct potential to use. This means that H is conserved in the rotating frame even though the particle is gaining and losing momentum in the laboratory frame and the rotating frame. So the rotating frame is the natural one to choose in the study of rotating billiards. That energy is indeed conserved in the rotating frame is shown in Appendix D on page 163.

3.2 The square billiard, \mathcal{B}_\square

3.2.1 Defining \mathcal{B}_\square



We now take the ball to be confined to the square, $|x| \leq 1$ and $|y| \leq 1$, by perfectly reflecting walls, i.e. \mathcal{B}_\square , which rotates with constant angular speed about its centre of symmetry, with sides 1-4 as shown in figure 3.1. For the \mathcal{B}_\square rotating anticlockwise we have that:

$$\text{A bounce on side 1 gives } \dot{z} = \dot{x} - i\dot{y} \rightarrow \dot{z}' = \dot{x} + i\dot{y} = \dot{\bar{z}}$$

$$\text{A bounce on side 2 gives } \dot{z} = \dot{x} + i\dot{y} \rightarrow \dot{z}' = -\dot{x} + i\dot{y} = -\dot{\bar{z}}$$

$$\text{A bounce on side 3 gives } \dot{z} = -\dot{x} + i\dot{y} \rightarrow \dot{z}' = -\dot{x} - i\dot{y} = \dot{\bar{z}}$$

$$\text{A bounce on side 4 gives } \dot{z} = -\dot{x} - i\dot{y} \rightarrow \dot{z}' = \dot{x} - i\dot{y} = -\dot{\bar{z}}$$

The same bounce conditions are also obtained for the \mathcal{B}_\square rotating clockwise, hence our bounce condition is simply $\dot{z} \rightarrow \dot{\bar{z}}$ on sides $|y| = 1$ and $\dot{z} \rightarrow -\dot{\bar{z}}$ on sides

$|x| = 1$. Bounces do not change z or $|\dot{z}|$, so conserve energy, but merely reverse the ball's normal component of velocity, which is either $\Re(\dot{z})$ or $\Im(\dot{z})$.

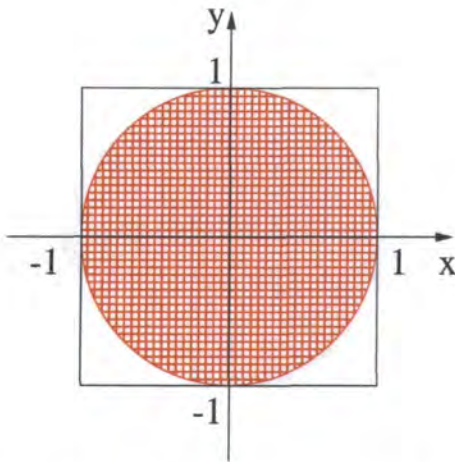


Figure 3.2: Circle of exclusion for $E = -1$ those of [25, 27].

With $\omega > 0$ then generally, and always for $E > 0$, the Coriolis acceleration keeps trajectories curving to the right; this will be expanded upon in a later section.

Also from equation D.7 on page 163 we see that high E corresponds to small ω and vice-versa, very large E means large \dot{z} and relatively little rotation and so from equation 3.3 on page 46 the motion is close to the straight line transits expected on a stationary table. At lower values of E the influence of the rotation increases and the ball's trajectories are expected to be increasingly curved. In addition equation D.7 on page 163 shows that the velocity of the ball reaches zero at a finite radius $|z| = \sqrt{-E}/\omega$ and for $-2 < E/\omega^2 < -1$ it is permitted to move only in one of the corners of the table as shown in figure 3.2.

3.2.2 Phase space for \mathcal{B}_\square

The nature of billiard ball motion at any given value of E is revealed by a Poincaré section, recording the position and conjugate momentum of each bounce at the boundary [28]. Rather than use position-angle variables [25–27] we use the conjugate variables (X_1, X_2) which lead to helpful simplifications. The position X_1 normalised to $0 \leq X_1 \leq 1$ is defined as the fractional distance of impact along the wall struck, in the positive (anticlockwise) sense around \mathcal{B}_\square . Then we have

$$X_1 = \frac{1 \mp x}{2} \quad \text{on sides } y = \pm 1 \quad (3.16)$$

$$X_1 = \frac{1 \pm y}{2} \quad \text{on sides } x \pm 1 \quad (3.17)$$

This also recognises the symmetry of the system, folding the four sides together [29].

Choosing table size 2×2 specifies length units, and we take a unit-mass ball. Then the motion is characterised by the energy parameter $E = 2\mathcal{E}/\omega^2$, where \mathcal{E} is given by equation D.7 on page 163, i.e.,

$$\mathcal{E} = \frac{1}{2} (|\dot{z}|^2 - |\omega z|^2).$$

Fixing ω and using variable E , which ranges continuously from $-2\omega^2$ to $+\infty$, eases the comparison of our results with

The momentum variable X_2 is a similarly normalised momentum component canonically conjugate to X_1 . With the Lagrangian given by equation 3.9 on page 47 the momenta conjugate to (x, y) are (p_x, p_y) given by:

$$p_x = \frac{\partial \mathcal{L}}{\partial \dot{x}} = \dot{x} - \omega y \quad (3.18)$$

$$p_y = \frac{\partial \mathcal{L}}{\partial \dot{y}} = \dot{y} + \omega x \quad (3.19)$$

Then for example on side 1 ($y = -1$), using equation D.7 on page 163, we have:

$$\begin{aligned} E &= \dot{x}^2 + \dot{y}^2 - \omega^2(x^2 + y^2) \geq \dot{x}^2 - \omega^2(x^2 + 1) \\ &\geq (p_x - \omega)^2 - \omega^2(x^2 + 1) \quad \text{using (D.9)} \end{aligned} \quad (3.20)$$

Which leads to

$$p_x \leq \omega \pm \sqrt{E + \omega^2(x^2 + 1)} \quad (3.21)$$

So p_x has the range

$$\omega - \sqrt{E + \omega^2(x^2 + 1)} \leq p_x \leq \omega + \sqrt{E + \omega^2(x^2 + 1)} \quad (3.22)$$

Hence an appropriate choice for X_2 on side 1 is:

$$X_2 = \frac{1}{2} \left(1 + \frac{\dot{x}}{\sqrt{E + 2\omega^2}} \right) \quad (3.23)$$

Similarly

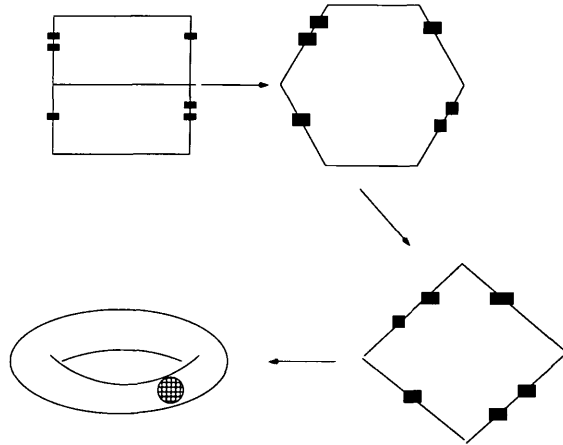
$$X_2 = \frac{1}{2} \left(1 + \frac{\dot{y}}{\sqrt{E + 2\omega^2}} \right) \quad \text{on side 2} \quad (3.24)$$

$$X_2 = \frac{1}{2} \left(1 - \frac{\dot{x}}{\sqrt{E + 2\omega^2}} \right) \quad \text{on side 3} \quad (3.25)$$

$$X_2 = \frac{1}{2} \left(1 - \frac{\dot{y}}{\sqrt{E + 2\omega^2}} \right) \quad \text{on side 4} \quad (3.26)$$

Phase portraits of orbits are then made by plotting $\mathbf{X} = (X_1, X_2)$ in the Cartesian plane.

Figure 3.8 on page 65 shows the symmetry in phase space, that is, the folding of the sides; diagonally opposite halves of the lines $X_1 = 0$ and $X_1 = 1$ are connected, so phase space in fact is always connected. By a topological deformation of the square we see that phase space is in fact a punctured torus, due to the corners, as shown in figure 3.3 on the following page.

Figure 3.3: Phase space for \mathcal{B}_\square

3.3 Periodic cycles of the rotating \mathcal{B}_\square

The fixed points and periodic cycles (n -cycles) of a Hamiltonian system are of the outmost importance in the study of its dynamics. The bifurcations of the n -cycles in two dimensional Hamiltonian systems are much richer and varied than the corresponding ones in the more understood one dimensional dissipative systems.

3.3.1 The bounce map, \mathbf{B}

Consider the trajectory between two successive collisions with the boundary of \mathcal{B}_\square , occurring at $\mathbf{X} = (X_1, X_2)$ and $\mathbf{X}' = (X'_1, X'_2)$, then the bounce map is defined as:

$$\mathbf{B} : (X_1, X_2) \rightarrow (X'_1, X'_2) \quad (3.27)$$

The equations involved in determining \mathbf{B} are in fact transcendental, thus the time, T , taken between successive collisions cannot be obtained in closed form. T can be determined either numerically or by employing the Newton-Raphson method, we have used both methods obtaining identical results.

The set of points (X_1^i, X_2^i) for $i = 1 \dots n$, which satisfy $\mathbf{B}^n(X_1^i, X_2^i) = (X_1, X_2)$ are defined to be an n -cycle of the bounce map. In particular the case $n = 1$ is a fixed point. We, in fact, require four bounce maps B_{11}, B_{12}, B_{13} and B_{14} in order to represent bounces from side 1 to sides 1, 2, 3 and 4. These four maps are sufficient to deal with all possibilities due to the symmetry of the \mathcal{B}_\square . The expressions for these bounce maps are given in Appendix E on page 164.

3.3.2 The Jacobian, \mathbf{J} , and Stability, \mathbf{S} , matrices

The Jacobian matrix, \mathbf{J} , of \mathbf{B} is defined as:

$$\mathbf{J} = \begin{pmatrix} \frac{\partial X_1'}{\partial X_1} & \frac{\partial X_1'}{\partial X_2} \\ \frac{\partial X_2'}{\partial X_1} & \frac{\partial X_2'}{\partial X_2} \end{pmatrix} \quad (3.28)$$

The elements of \mathbf{J} for B_{11} , B_{12} , B_{13} , and B_{14} are given in Appendix F on page 166.

The Jacobian matrix allows us to compute Lyapunov exponents and to determine the stability of periodic orbits. For $\mathbf{X} = (X_1, X_2)$, the stability matrix, \mathbf{S} , is defined as:

$$\mathbf{S}_n(\mathbf{X}) = \mathbf{J}(\mathbf{B}^{n-1}(\mathbf{X})) \cdots \mathbf{J}(\mathbf{B}(\mathbf{X}))\mathbf{J}(\mathbf{X}) \quad (3.29)$$

An orbit, then consists of the succession of number pairs $\{X_1^{(n)}, X_2^{(n)}\}$ corresponding to the n^{th} bounce, and is generated by specifying an initial state $\{X_1^{(0)}, X_2^{(0)}\}$. This discrete dynamics is a mapping, \mathbf{S} , of the phase space with co-ordinates X_1, X_2 and symbolised by:

$$\begin{pmatrix} X_1^{(n+1)} \\ X_2^{(n+1)} \end{pmatrix} = \mathbf{S} \begin{pmatrix} X_1^{(n)} \\ X_2^{(n)} \end{pmatrix} \quad (3.30)$$

Since X_1 and X_2 are conjugate \mathbf{S} is area preserving:

$$\frac{\partial(X_1^{(1)}, X_2^{(1)})}{\partial(X_1^{(0)}, X_2^{(0)})} = \det \left\{ \begin{array}{cc} \frac{\partial X_1^{(1)}}{\partial X_1^{(0)}} & \frac{\partial X_1^{(1)}}{\partial X_2^{(0)}} \\ \frac{\partial X_2^{(1)}}{\partial X_1^{(0)}} & \frac{\partial X_2^{(1)}}{\partial X_2^{(0)}} \end{array} \right\} = 1 \quad (3.31)$$

There are three ways in which the orbit generated by infinitely many iterations of \mathbf{S} can be explored in phase space [30];

1. A finite set of N points $(X_1^{(0)}, X_2^{(0)})$, $(X_1^{(1)}, X_2^{(1)}) \cdots (X_1^{(N-1)}, X_2^{(N-1)})$ may be encountered repeatedly corresponding to orbits that close after N bounces. Such a closed orbit satisfies

$$\begin{pmatrix} X_1^{(n+N)} \\ X_2^{(n+N)} \end{pmatrix} = \mathbf{S}^{(N)} \begin{pmatrix} X_1^{(n)} \\ X_2^{(n)} \end{pmatrix} = \begin{pmatrix} X_1^{(n)} \\ X_2^{(n)} \end{pmatrix} \quad (3.32)$$

So that each of its N points is a fixed point of the mapping $\mathbf{S}^{(N)}$.

2. The iterates of $(X_1^{(0)}, X_2^{(0)})$ may fill a smooth curve in phase space, called an invariant curve because the whole curve maps unto itself under \mathbf{S} (although its individual points do not map unto themselves). This behaviour occurs, for

example, if the dynamics is integrable in the sense that there exists a constant of motion in the form of a function $F(X_1, X_2)$ satisfying

$$F(X_1^{(1)}, X_2^{(1)}) = F(X_1^{(0)}, X_2^{(0)})$$

in which case the invariant curves are the contours of $F(X_1, X_2)$

3. The iterates of $(X_1^{(0)}, X_2^{(0)})$ may fill an area of phase space. This happens when the orbit, unrestricted by the existence of any conserved quantity, evolves in a chaotic manner whose detail is sensitively dependent on the values of $X_1^{(0)}$ and $X_2^{(0)}$

The closed orbits, which satisfy equation 3.32 on the page before, may be stable or unstable in the sense that an orbit starting at $(X_1^{(0)} + \delta X_1^{(0)}, X_2^{(0)} + \delta X_2^{(0)})$ where $\delta X_1^{(0)}$ and $\delta X_2^{(0)}$ are small, may after many bounces remain near the closed orbit or may deviate increasingly from it. After N iterations, when $X_1^{(0)}$ and $X_2^{(0)}$ have returned to their initial values, the deviations $\delta X_1^{(N)}$ and $\delta X_2^{(N)}$ of the nearby orbit will be

$$\begin{pmatrix} \delta X_1^{(N)} \\ \delta X_2^{(N)} \end{pmatrix} = \mathbf{S}^{(N)} \begin{pmatrix} \delta X_1^{(0)} \\ \delta X_2^{(0)} \end{pmatrix} \quad (3.33)$$

Orbital stability depends on the eigenvalues of $\mathbf{S}^{(N)}$, [31], which are the Floquet multipliers for the linear difference equations in the periodic tangent space. These are λ_{\pm} given in terms of the trace of $\mathbf{S}^{(N)}$ by

$$\lambda_{\pm} = \frac{1}{2} \left\{ \text{Tr} \mathbf{S}^{(N)} \pm \left[(\text{Tr} \mathbf{S}^{(N)})^2 - 4 \right]^{1/2} \right\} \quad (3.34)$$

After j traversals of the closed orbit (i.e. Nj iterations of \mathbf{S}) the deviations given by $(\delta X_1^{(Nj)}, \delta X_2^{(Nj)})$ can be written as a linear combination of λ_{\pm}^j times eigenvectors of $\mathbf{S}^{(N)}$,

$$\begin{pmatrix} \delta X_1^{(Nj)} \\ \delta X_2^{(Nj)} \end{pmatrix} = A \lambda_+^j \begin{pmatrix} \delta X_1^{(+)} \\ \delta X_2^{(+)} \end{pmatrix} + B \lambda_-^j \begin{pmatrix} \delta X_1^{(-)} \\ \delta X_2^{(-)} \end{pmatrix} \quad (3.35)$$

There are three possibilities [30];

1.

$$\text{If } |\text{Tr} \mathbf{S}^{(N)}| < 2 \quad (\text{stable}) \quad (3.36)$$

it follows from equation 3.34 that λ_{\pm} are complex conjugates on the unit circle, so that

$$\lambda_{\pm}^j = e^{\pm ij\beta} \quad (3.37)$$

where β is a 'stability angle'. In this case the deviations given by equation 3.35 on the page before oscillate about zero as j increases, and remain bounded, so that the orbit is stable, provided λ is not a small root of unity (generically it is sufficient to exclude the cases $\lambda^k = 1$, $k \leq 4$, though the case $\lambda = \pm i$ can be stable or unstable).

2.

$$\text{If } |\text{Tr}\mathbf{S}^{(N)}| > 2 \quad (\text{unstable}) \quad (3.38)$$

it follows from equation 3.34 on the preceding page that λ_{\pm} are real and reciprocals of each other, so that

$$\lambda_{\pm}^j = e^{\pm j\gamma} \quad (3.39)$$

where γ is an 'instability exponent'. In this case the positive exponent guarantees that almost all deviations grow exponentially so that the orbit is unstable.

3.

$$\text{If } |\text{Tr}\mathbf{S}^{(N)}| = 2 \quad (\text{neutral}) \quad (3.40)$$

both eigenvalues are $+1$ or -1 and deviations grow linearly so that in this case the orbit has neutral stability.

An equivalent quantity to $\text{Tr}\mathbf{S}$ is the residue [32], \mathcal{R} , of an orbit defined by

$$\mathcal{R} = \frac{1}{4}(2 - \text{Tr}\mathbf{S}),$$

the eigenvalues and \mathcal{R} are related by:

$$\lambda_{\pm} = 1 - 2\mathcal{R} \pm 2[\mathcal{R}(\mathcal{R} - 1)]^{\frac{1}{2}}$$

Since the trace of a product is invariant under cyclic permutations of the factors, the residue of an orbit is independent of the point at which we evaluate \mathbf{S} .

When $0 < \mathcal{R} < 1$ the eigenvalues are complex with magnitude unity (except for $\mathcal{R} = 3/4$, and sometimes $\mathcal{R} = 1/2$, corresponding to $\lambda^3 = 1$ and $\lambda^4 = 1$). Under this condition, tangent space orbits, continued over many periods, rotate about the origin on ellipses (thus the name 'elliptic' orbit) at a rate ν rotations/period, given by

$$\mathcal{R} = \sin^2(\pi\nu)$$

When $\mathcal{R} < 0$ or $\mathcal{R} > 1$, the tangent space lies on hyperbolae, alternating between corresponding branches if $\mathcal{R} > 1$ ("hyperbolic with reflection" or "inversion hyperbolic"), and staying on one branch if $\mathcal{R} < 0$ ("ordinary hyperbolic"). Then the periodic orbit is said to be unstable since all the tangent space orbits march off to infinity, except those lying on the eigenvectors of \mathbf{S} with an eigenvalue less than one.

In the special cases $\mathcal{R} = 0, 1, 3/4, 1/2$ corresponding to low order resonances $\lambda^k = 1, k = 1, 2, 3, 4$ the linearisation of \mathbf{B} is not sufficient to describe the behaviour of nearby points. As the energy is varied, a periodic orbit will, in general, move and its residue will change. Whenever the residue passes through one of the values

$$\mathcal{R}_{m,n} = \sin^2(\pi m/n), \quad m, n \text{ co-prime integers}$$

one or more cycles of n times the original period with residue near 0 are born or absorbed by the periodic orbit. If these daughter orbits have intervals (in energy) of stability, they will in turn bifurcate.

3.4 The stationary \mathcal{B}_\square

The stationary \mathcal{B}_\square with $E = \infty$ (or equivalently $\omega = 0$) is of course integrable and so the time taken, T , between successive bounces can be ascertained from geometrical considerations of the \mathcal{B}_\square . Alternatively, we can substitute $\omega = 0$ into the relevant equations in Appendix E on page 164 and obtain the stationary bounce map, \mathbf{B}_∞ , and thus the related Jacobian and Stability matrices. Here of course the component B_{11} of \mathbf{B} does not exist as it is a purely rotational phenomenon. The substitution is done in Appendix G on page 172 and the bounce map, $\mathbf{B}_\infty : \mathbf{X} \rightarrow \mathbf{X}'$, is given by

$$\begin{aligned} (X_1, X_2) &\rightarrow \left(\frac{(1 - X_1)}{\tau}, \frac{1}{2} + \frac{(X_2 - \frac{1}{2})}{\tau} \right) && \text{for } B_{12} \\ &\rightarrow (1 - X_1 - \tau, 1 - X_2) && \text{for } B_{13} \\ &\rightarrow \left(1 + \frac{X_1}{\tau}, \frac{1}{2} - \frac{(X_2 - \frac{1}{2})}{\tau} \right) && \text{for } B_{14} \end{aligned} \quad (3.41)$$

Where $\tau \equiv \frac{(X_2 - \frac{1}{2})}{\sqrt{X_2(1 - X_2)}}$ is the cotangent of the angle between trajectory vector and positive sense of initial wall [29].

We can take τ to be $\tau = |(v_p)|/(v_i)$, where v_p is the velocity perpendicular to initial wall and v_i is the velocity along positive sense of initial wall in order to explore

the relationship between τ and τ' , its value after a bounce:

$$\begin{aligned}\tau &= \frac{\dot{y}}{\dot{x}} && \text{Initially side 1} \\ \tau' &= \frac{\dot{x}}{\dot{y}} = \frac{1}{\tau} && \text{Bounce between adjacent walls} \\ \tau' &= \frac{\dot{y}}{-\dot{x}} = -\tau && \text{Bounce between opposite walls}\end{aligned}\tag{3.42}$$

Hence under the three parts of \mathbf{B}_∞ we have

$$\begin{aligned}\tau' &\rightarrow \frac{1}{\tau} && \text{for } B_{12} \text{ and } B_{14} \\ \tau' &\rightarrow -\tau && \text{for } B_{13}\end{aligned}\tag{3.43}$$

This allows us to determine that there are three and only three fixed points of the stationary \mathcal{B}_\square as follows; for B_{12} and B_{14} , by equation 3.43, the only possible values for τ are, respectively, 1 and -1 which both constrain X_1 to be $\frac{1}{2}$, by equation 3.41 on the preceding page. For B_{13} the only possible value is zero which again constrains X_1 to be $\frac{1}{2}$. Thus the three fixed points of \mathbf{B}_∞ are:

$$\begin{aligned}\mathbf{X} &= \mathbf{X}_0 = \left(\frac{1}{2}, \frac{1}{2}\right) \\ \mathbf{X} &= \mathbf{X}_\pm = \left(\frac{1}{2}, \frac{1}{2} \pm \frac{\sqrt{2}}{4}\right)\end{aligned}\tag{3.44}$$

corresponding respectively to bounces straight across from a side's centre, and to circuits of central 45° bounces with the ball touring the \mathcal{B}_\square in \pm sense.

The orbits of the stationary \mathcal{B}_\square are closed or not depending on the rationality of τ , being closed if the initial value of X_2 is chosen such that τ is rational, equal to p/q in lowest terms, then an orbit is a cycle of \mathbf{B}_∞ . Its order is $n = 2(|p| + |q|)$ at most, counting τ (including zero) with denominator $q = 1$. This can be seen by tessellating the z -plane [33] with squares generated by repeated reflections in edges. Then an orbit is represented by a single infinite straight line produced from any transit of the original square. This line encounters $2|p| + 2|q|$ boundaries before reaching a repeat of its initial point in proper orientation. Figure 3.4 on the next page shows such a tessellation with $\tau = \frac{p}{q} = \frac{3}{1}$ where it can be seen that $n = 2(3 + 1) = 8$.

The folding together of sides in the definition of \mathbf{B} reduces n in isolated cases, for example, when $\tau \pm 1$ (45° bounces). The case for $\tau = 1$ is shown in figure 3.4 on the following page where $\tau' = 1/\tau = 1$ so $X'_2 = X_2$ and the equivalence of the 4 sides reduces n from 4 to 1.

These two orbits are shown on figures 3.5(a) and 3.5(b) on page 58 where the ball is initially at $(X_1, X_2) = (\frac{1}{2}, \frac{1}{2} + \frac{3\sqrt{10}}{20}), (\frac{1}{2}, \frac{1}{2} + \frac{\sqrt{2}}{4})$ corresponding to $\tau = 3, 1$

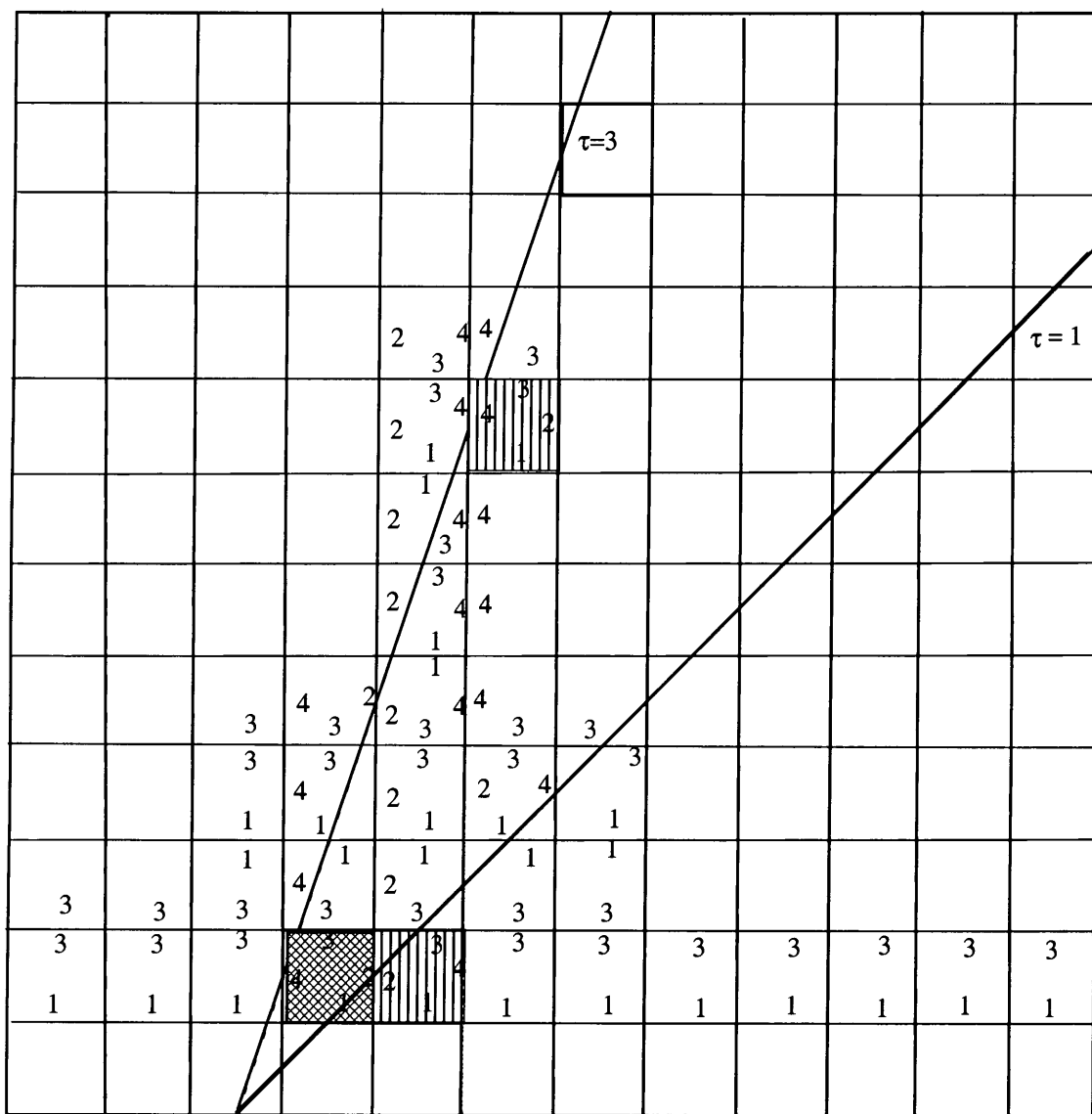
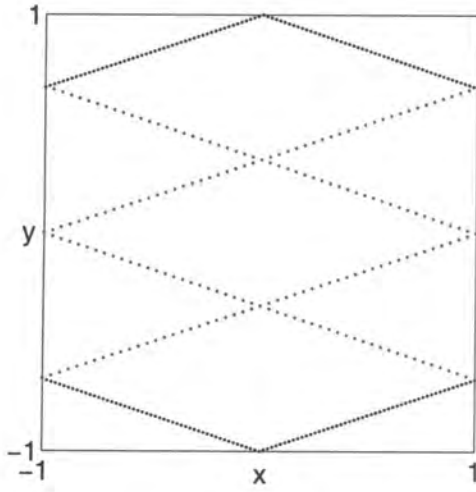
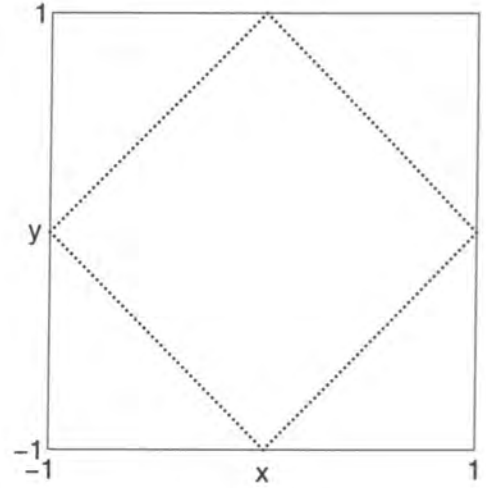
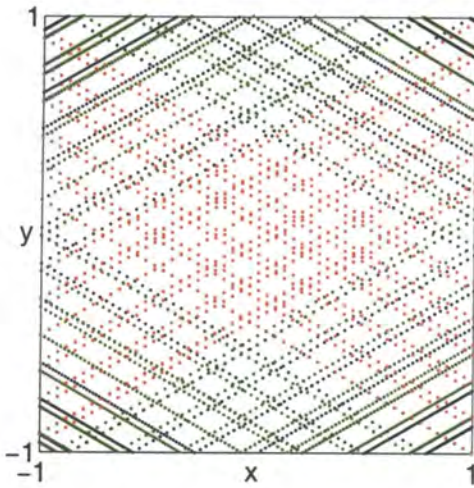
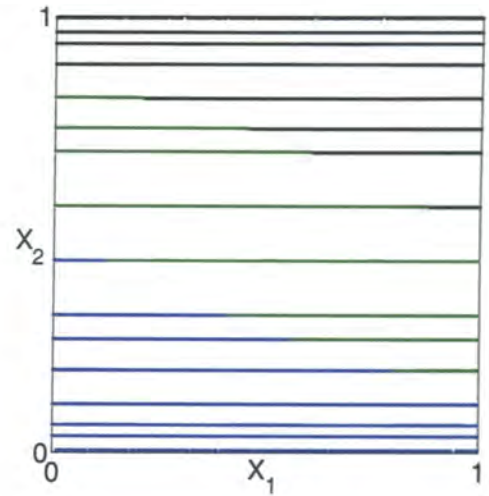


Figure 3.4: Tesselation of the z -plane

respectively. On the other hand figure 3.5(c) on the following page shows an orbit for initially $(X_1, X_2) = (\frac{1}{2}, \frac{1}{2} + \frac{\sqrt{3}}{4})$ corresponding to $\tau = \sqrt{3}$. As can be observed the orbit is not closed in this instance. Figure 3.5(d) on the next page is a phase portrait, with $E = 10^8$ and ω set to unity, in the canonical variables $\mathbf{X} = (X_1, X_2)$. It is a superposition of 64 orbits initialised from a square grid $\{\mathbf{X} = ((2i - 1)/16, (2j - 1)/16); i, j = 1, \dots, 8\}$. Each orbit is followed for 1000 bounces, for which X_2 is plotted vertically against X_1 horizontally. The Poincaré map for the stationary \mathcal{B}_\square is very regular consisting of almost horizontal invariant bands. As there is symmetry ($X_2 \rightarrow 1 - X_2$) in pairs among the 8 initial X_2 values used for the phase portrait then there are $(8 \times 4)/2 = 16$ bands each covered twice. From equations G.1 - G.3 on page 174 it follows that the three components, J_{12}, J_{13} and J_{14} of the Jacobian


 (a) Trajectory: $\mathbf{X} = (0.5, X_2 : \tau = 3)$

 (b) Trajectory: $\mathbf{X} = (0.5, X_2 : \tau = 1)$

 (c) Trajectory: $\mathbf{X} = (0.5, X_2 : \tau = \sqrt{3})$


(d) Phase portrait as explained in the text

Figure 3.5: $E=10^8$: (a), (b) and (c): Trajectories followed for 100 bounces. (d): Phase portrait on a 8×8 grid for 1000 bounces constructed as explained in the text. (Colour coding - red: B_{11} black: B_{12} green: B_{13} blue: B_{14})

for the stationary \mathcal{B}_\square , \mathbf{J}_∞ , are given by

$$J_{12} = \begin{pmatrix} -\frac{1}{\tau} & -\frac{(1-X_1)}{(X_2-\frac{1}{2})} \left(\tau + \frac{1}{\tau} \right) \\ 0 & -\tau \end{pmatrix} \quad (3.45)$$

$$J_{13} = \begin{pmatrix} -1 & -\frac{1}{\sqrt{X_2(1-X_2)}}(1+\tau^2) \\ 0 & -1 \end{pmatrix} \quad (3.46)$$

$$J_{14} = \begin{pmatrix} \frac{1}{\tau} & \frac{X_1}{(X_2-\frac{1}{2})}(\tau+\frac{1}{\tau}) \\ 0 & \tau \end{pmatrix} \quad (3.47)$$

The zero entries in the component Jacobian matrices appear because the boundary is a polygon and away from the corners a small change in X_1 has no effect on X_2' .

In principle the stability of all the n -cycles of the stationary \mathcal{B}_\square can be analysed using \mathbf{J}_∞ , but the simplest cases of all are the three fixed points, \mathbf{J}_∞ then reduces to (with $*$ replacing $0, \pm$)

$$J_* = \begin{pmatrix} -1 & -A \\ 0 & -1 \end{pmatrix} \quad (3.48)$$

Where $A = 2$ for \mathbf{X}_0 and $2\sqrt{2}$ for \mathbf{X}_\pm , the diagonal entries are simple due to the particular values $\tau = 0, \pm 1$ for the fixed points. By equation 3.34 on page 53, the matrix (equation 3.48) has double eigenvalue (-1) , hence each zero-rotation fixed point is neutrally stable.

For all higher cycles of \mathbf{B}_∞ similar analysis can be applied. Let \mathbf{X}_* now denote the n -cyclic point and \mathbf{J}_* be a product of n derivative matrices, one for each bounce. Each of the n factors is J_{1i} ; $i = 2, 3, 4$ and so upper triangular and hence so is the product of any such n factors. J_{1i} has diagonal elements both equal to -1 for $i = 3$ and equal to $\mp \frac{1}{\tau}$ and $\mp \tau$ for $i = 2, 4$ respectively.

Using the tessellation procedure or by considering equations 3.45 - 3.47 it can be concluded that for the n -cycle analogue of equation 3.48 we have

$$J_* = \begin{pmatrix} \pm 1 & -A \\ 0 & \pm 1 \end{pmatrix} \quad (3.49)$$

Where upper or lower sign must be taken together. The calculation of the upper entry $-A$ is now non-trivial since it depends in a far more complicated way on exact \mathbf{X} -values for each bounce. However, for every cycle \mathbf{J}_* has trace of magnitude 2 so its eigenvalues are both either $+1$ or -1 and hence, like the fixed points, all the higher cycles are neutrally stable.

Figure 3.5(a) on the page before is an example of a 4-cycle, ($\mathbf{X}_{4+} = (0.5, X_2 : \tau = 3)$) and figure 3.6 on the following page shows the following cycles: 3.5(a) is a 2-cycle ($\mathbf{X}_{2+} = (0.25, X_2 : \tau = 1)$), 3.5(b) is a 6-cycle ($\mathbf{X}_{6+} = (0.5, X_2 : \tau = 2)$), 3.5(c) is an 8-cycle ($\mathbf{X}_{8+} = (0.5, X_2 : \tau = 7)$) and 3.5(d) is a 10-cycle ($\mathbf{X}_{10+} = (0.5, X_2 : \tau = 4)$).

All these cycles of course have their counterparts, with the ball touring the \mathcal{B}_\square in a clockwise direction, \mathbf{X}_{i-} , with $X_1 \rightarrow 1 - X_1; \tau \rightarrow -\tau$.

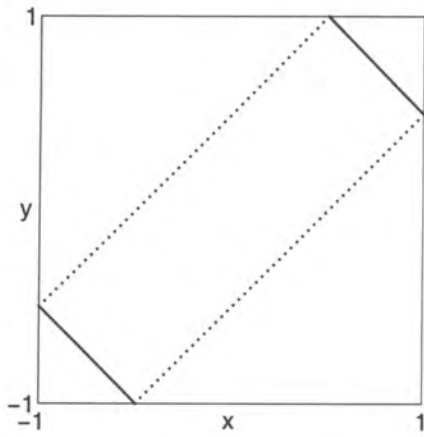
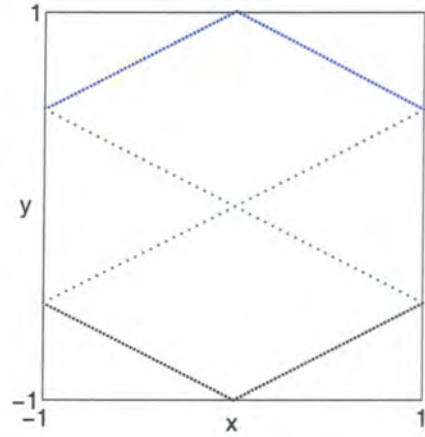
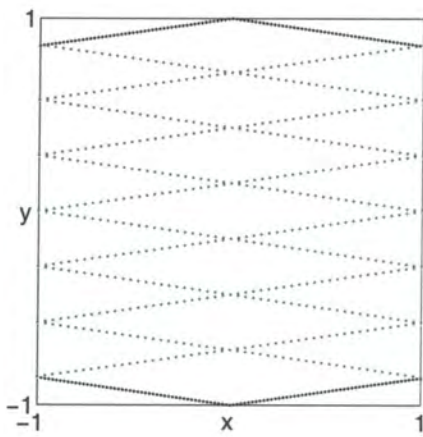
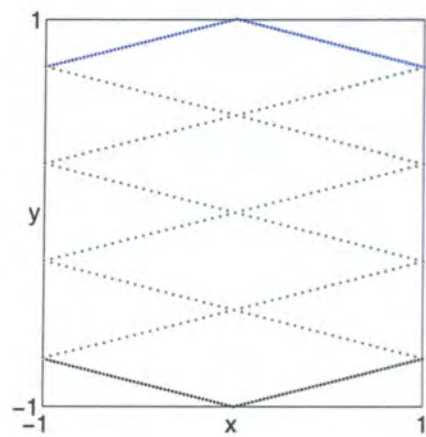
(a) $\mathbf{X}_{2+} = (0.25, X_2 : \tau = 1)$ (b) $\mathbf{X}_{6+} = (0.5, X_2 : \tau = 2)$ (c) $\mathbf{X}_{8+} = (0.5, X_2 : \tau = 7)$ (d) $\mathbf{X}_{10+} = (0.5, X_2 : \tau = 4)$

Figure 3.6: $E=10^8$; Trajectories followed for 100 bounces. (Colour coding - red: B_{11} black: B_{12} green: B_{13} blue: B_{14})

3.5 The slowly rotating \mathcal{B}_\square

For the rotating \mathcal{B}_\square , having obtained the time taken, T , for successive bounces numerically the elements of the components of the Jacobian matrices are obtained from equations F.1 - F.16 on page 171. We can deduce the likely fates of the fixed points by looking at when rotation just commences, that is, with ω very small and T is also seen to be very small so that ω , T and the product ωT can be limited to first order. Then with the approximations $\cos(\omega T) = 1$ and $\sin(\omega T) = \omega T$ we obtain

$$\left. \begin{aligned} 1 &= A|_{\substack{\omega \ll 1 \\ T \ll 1}} = 2X_1 - 1 + \sqrt{E}(2X_2 - 1)T \\ \Rightarrow T &= \frac{-2(1-X_1)}{\sqrt{E}(2X_2-1)} \\ \Rightarrow \frac{\partial T}{\partial X_1} &= \frac{2}{\sqrt{E}(2X_2-1)} \\ \Rightarrow \frac{\partial T}{\partial X_2} &= \frac{4(1-X_1)}{\sqrt{E}(2X_2-1)^2} \end{aligned} \right\} \text{For } B_{12} \quad (3.50)$$

$$\left. \begin{aligned} 1 &= B|_{\substack{\omega \ll 1 \\ T \ll 1}} = -1 + 2\sqrt{EX_2(1-X_2)}T \\ \Rightarrow T &= \frac{1}{\sqrt{EX_2(1-X_2)}} \\ \Rightarrow \frac{\partial T}{\partial X_1} &= 0 \\ \Rightarrow \frac{\partial T}{\partial X_2} &= \frac{(1-2X_2)}{2X_2(X_2-1)\sqrt{EX_2(1-X_2)}} \end{aligned} \right\} \text{For } B_{13} \quad (3.51)$$

$$\left. \begin{aligned} -1 &= A|_{\substack{\omega \ll 1 \\ T \ll 1}} = 2X_1 - 1 + \sqrt{E}(2X_2 - 1)T \\ \Rightarrow T &= \frac{-2X_1}{\sqrt{E}(2X_2-1)} \\ \Rightarrow \frac{\partial T}{\partial X_1} &= \frac{-2}{\sqrt{E}(2X_2-1)} \\ \Rightarrow \frac{\partial T}{\partial X_2} &= \frac{4X_1}{\sqrt{E}(2X_2-1)^2} \end{aligned} \right\} \text{For } B_{14} \quad (3.52)$$

Since we are discussing very small rotations here the curvature is insufficient to permit B_{11} . Substituting the expressions for the various $\frac{\partial T}{\partial X_i}$ from the above equations into equations F.1 on page 166 to F.16 on page 171 it can be seen that for very large but finite E , that is as rotation commences, to first order the Jacobian, \mathbf{J} , for all cycles including the fixed points has the form:

$$\begin{pmatrix} \pm 1 + \delta_1 & -A \\ \epsilon & \pm 1 + \delta_2 \end{pmatrix} \quad (3.53)$$

and thus by equation 3.29 on page 52 so does the Stability matrix, \mathbf{S} . The unitary condition (equation 3.31 on page 52) of course still applies so we have:

$$\begin{aligned} (\pm 1 + \delta_1)(\pm 1 + \delta_2) + A\epsilon &= 1 && \text{giving} \\ \delta_1 + \delta_2 &= \mp A\epsilon && \text{and so} \\ \text{Tr}\mathbf{J} &\sim \pm 2 \mp A\epsilon && \text{as } \epsilon \rightarrow 0 \end{aligned} \quad (3.54)$$

where again upper and lower signs must be taken together, so

$$\begin{aligned} \text{If } \epsilon = \frac{\partial X_2'}{\partial X_1} > 0 & \text{ then } |\text{Tr}\mathbf{J}| < 2 \\ \text{If } \epsilon = \frac{\partial X_2'}{\partial X_1} < 0 & \text{ then } |\text{Tr}\mathbf{J}| > 2 \end{aligned} \quad (3.55)$$

Hence by equation 3.55 the sign of ϵ determines the stability of the perturbed cycles, and in general $\epsilon \neq 0$ (as any change in X_1 changes X_2' due to the rotation) so neutral stability is destroyed.

Consideration of the orbits curving to the right as in the rotating \mathcal{B}_\square shows that for anticlockwise and clockwise tours we must have $\epsilon > 0$ and $\epsilon < 0$ respectively, and for bounces straight across $\epsilon = 0$. Hence the fixed points \mathbf{X}_+ and \mathbf{X}_- become elliptic and inversion hyperbolic as rotation commences whilst the fate of \mathbf{X}_0 is determined by higher order effects. The fate of all the other cyclic points of \mathbf{B}_∞ cannot be determined so simply and we must resort to numerical simulations.

3.6 Poincaré maps, cycles and trajectories

For the range $-2 < E \leq \infty$ we have encountered three different types of trajectories, which we shall call types *I*, *II* and *III*:

1. Type *I* trajectories

These are trajectories which are associated with the stationary \mathcal{B}_\square . As the E -values decrease these show increasing curvature, the energy range for which type I trajectories are found is $1 \lesssim E \leq \infty$.

2. Type *II* trajectories

These trajectories demonstrate a feature of the rotating \mathcal{B}_\square not connected to any structure at $E = \infty$. They are symmetric trajectories of order $4k$, where k is the number of successive bounces on the same side (that is, B_{11}) of the \mathcal{B}_\square . These are observed for $-0.5 \lesssim E \lesssim 2$.

3. Type *III* trajectories

For $-2 < E \leq -1$ phase space is disjointed, hence trajectories of type *I* or

\mathcal{I} are not possible. However, we have found numerous periodic cycles in this energy range which have asymmetric trajectories confined to the corners of the \mathcal{B}_\square . These cycles demonstrate the approach to integrability in the limit $E \rightarrow -2$ and are found for $-2 < E \lesssim -1.8$.

3.6.1 Periodic cycles with type I trajectories

Poincaré maps for $E = 10^7, 10^6, 10^5$ and 10^4 are shown in figure 3.7 on the next page. These and all other phase portraits, unless otherwise indicated, are produced from an 8×8 grid of initial positions and directions. The ball is followed from each of the initial 64 possibilities for 250 bounces. As shown, with a decrease in E the invariant curves approximated at $E = 10^8$, (figure 3.5(d) on page 58), break up and chaos appears, this is in keeping with other studies with changes in the appropriate parameter for the dynamical system under consideration. Some examples are [25–27,30,31,33–42]. By $E = 10^5$, (figure 3.7(c) on the next page) there is a clear indication of growing disorder in phase space suggesting that instability is the generic fate of cycles of the $E = \infty$ map. By $E = 10^4$, (figure 3.7(d) on the following page), phase space consists of numerous cycles embedded in a sea of chaos.

We choose the map at $E = 10^3$, (figure 3.8 on page 65), for a more detailed examination of phase space at these high E -values: The stable fixed point, \mathbf{X}_+ is now centred near $X_2 = 0.85$ and the eigenvalues of its \mathbf{J} -matrix have moved to $-0.9144 \pm 0.4048i$ round the unit circle from -1 at $E = \infty$. En-route they pass through the simple roots of unity, and \mathbf{X}_+ is correspondingly surrounded by alternate stable and unstable cycles, giving island chains in the sea of chaos.

Figure 3.9 on page 66 are phase portraits obtained by following orbits initiated from single \mathbf{X} -values near the centres of some of the prominent cycles in figure 3.8 on page 65 for a 1000 bounces; figure 3.9(a): the fixed point, \mathbf{X}_+ , figure 3.9(b) : a 4-cycle, figure 3.9(c): a 6-cycle and figure 3.9(d): an 8-cycle. The corresponding trajectories are shown in figure 3.10 on page 67, at this E -value there is no noticeable curvature in the trajectories.

Careful examination of figure 3.8 on page 65 reveals a few red dots, at very high X_2 values, corresponding to B_{11} even at this relatively high E -value. For B_{11} we must of course have trajectories with some curvature, figure 3.10 on page 67 show this to be the case for 4 chosen values of \mathbf{X} . Figures 3.11 on page 68 and 3.12 on page 69 show the change in the structure of phase space as the E is decreased down to $E = 2.1$. The X_2 values of the cycles are decreasing and we see various bifurcations leading to births and absorptions of cycles.

By $E = 200$, (figure 3.11(d) on page 68), all the cycles except \mathbf{X}_+ have become

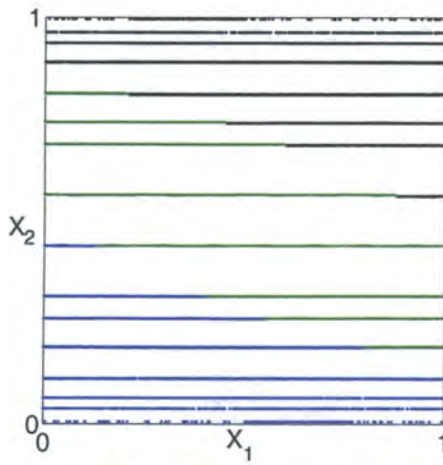
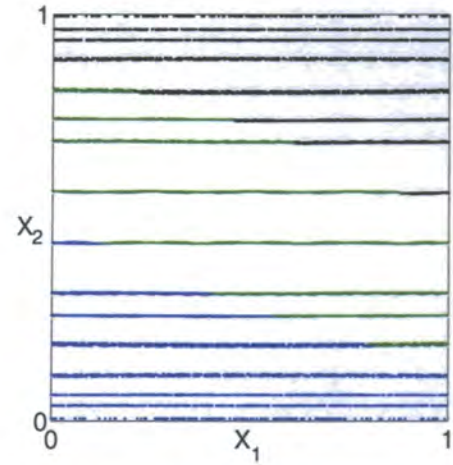
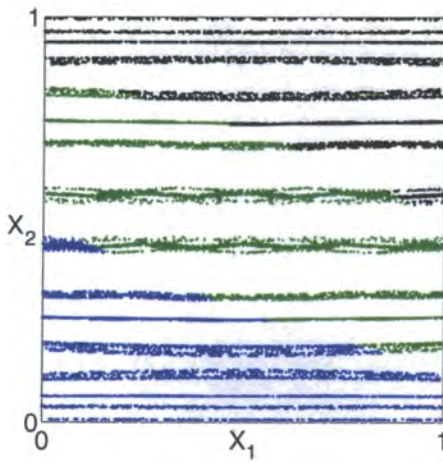
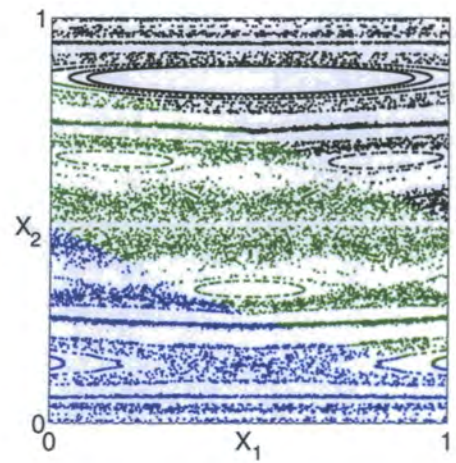

 (a) Phase portrait: $E = 10^7$

 (b) Phase portrait: $E = 10^6$

 (c) Phase portrait: $E = 10^5$

 (d) Phase portrait: $E = 10^4$

Figure 3.7: Phase portraits for $E = 10^7$ to $E = 10^4$. (Colour coding - red: B_{11} black: B_{12} green: B_{13} blue: B_{14})

unstable and disappeared. \mathbf{X}_+ has moved down to about $X_2 = 0.82$ and is isolated in a sea of chaos.

As E is further decreased the X_2 value of \mathbf{X}_+ decreases slowly and by $E = 30$, (shown in figure 3.11(e) on page 68), it has reached about $X_2 = 0.72$. It is at $E = 20$, (figure 3.11(f) on page 68), that the curvature of the phase boundary first becomes apparent. It increases to curve further with decreasing E -values until $E = -1$, as shown by figure 3.20 on page 76, when phase space “pinches off” into

two disjoint regions. All phase portraits drawn for $E \leq 20$ use only the initial points in the stated $n \times n$ grid lying inside the curved phase space boundary at that particular E -value. There is an interesting resonance at $E = 18.414$ when the eigenvalues of the \mathbf{J} -matrix of \mathbf{X}_+ are the cubic roots of unity. Thus we have a 3-bifurcation, and the elliptic shape of \mathbf{X}_+ is replaced by a structure consisting of hyperbolae, figure 3.12(a) on page 69 shows a magnification of \mathbf{X}_+ at $E = 18.414$. We were unable to produce phase portraits or trajectories of the unstable 3-cycle, presumably due to its transient nature.

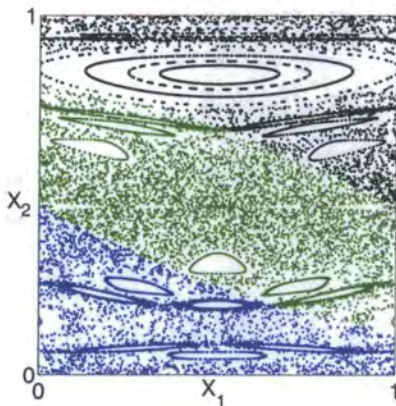


Figure 3.8: Phase portrait: $E = 10^3$. Figures 3.13(a) to 3.13(d) on page 70 show the phase portraits and trajectories for these two 4-cycles at $E = 2.4$ obtained from initial single \mathbf{X} values.

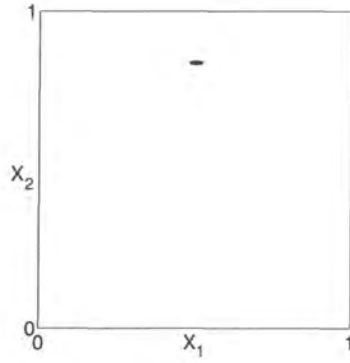
As E is further decreased the unstable 3-cycle bifurcates back to \mathbf{X}_+ , but its shape is now inverted as shown in figure 3.12(b) on page 69 for $E = 10$. Thereafter its X_2 value is decreasing rapidly, as can be seen from figures 3.12(c) to 3.12(f) on page 69, with decreasing E .

At $E = 2.6$ the eigenvalues of the \mathbf{J} -matrix of \mathbf{X}_+ are the 4th roots of unity giving rise to a 4-bifurcation resulting in a stable and an unstable 4-cycle as shown in figures 3.12(e) and 3.12(f) on page 69. Figures

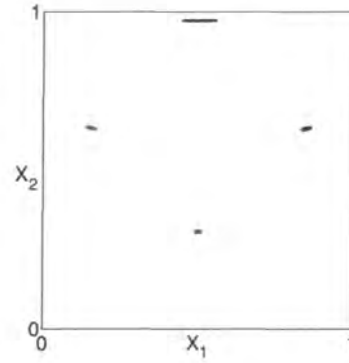
Figures 3.13(e) and 3.13(f) on page 70 are plots showing the change in the X_2 -values of \mathbf{X}_+ for the ranges $E = 2$ to 100 and $E = 1.15$ to 2. It would appear we have two almost straight lines connected by a curve between about $E = 10$ and $E = 20$. This suggests a dramatic change in the dynamics of the \mathcal{B}_\square , but rather disappointingly the phase portraits do not show any evidence of such a change. For $E > 20$ the line has a very small gradient whilst for $2 < E < 10$ it is approximately 0.04, increasing to more than 2 for $0 < E < 2$.

Figure 3.14 on page 71 shows the increasing curvature of the trajectories for \mathbf{X}_+ with decreasing E -values. The change in the curvatures for $50 \leq E \leq 100$ is not significant but for a small decrease in the E -value for $E \leq 10$ causes a considerable increase in the curvature of the trajectory.

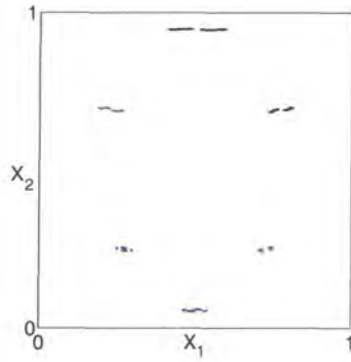
Hence after the curve in figure 3.13(e) on page 70 passes through the curved portion we have a considerable increase in both the rate at which the X_2 values of \mathbf{X}_+ decrease and curvature of the trajectories for \mathbf{X}_+ .



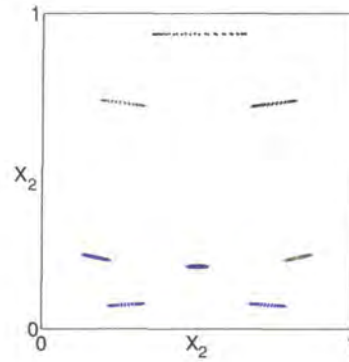
(a) $\mathbf{X}_+ = (0.5, 0.84)$



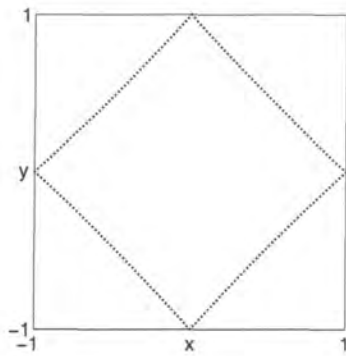
(b) $\mathbf{X}_{4+} = (0.5, 0.31)$



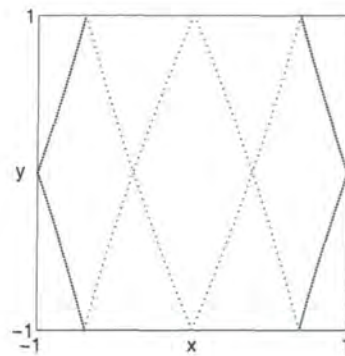
(c) $\mathbf{X}_{6+} = (0.5, 0.05)$



(d) $\mathbf{X}_{8+} = (0.5, 0.19)$

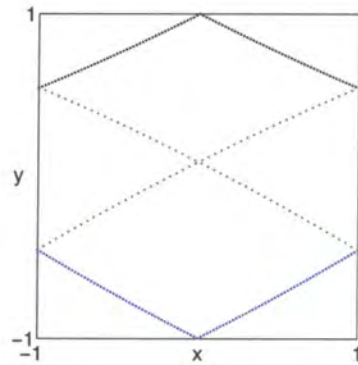


(e) Trajectory for figure 3.9(a)

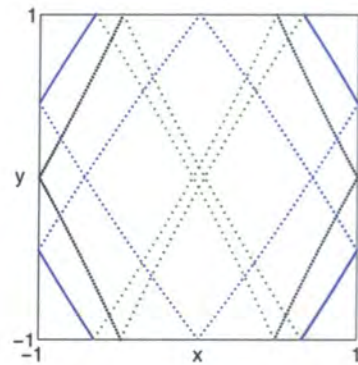


(f) Trajectory for figure 3.9(b)

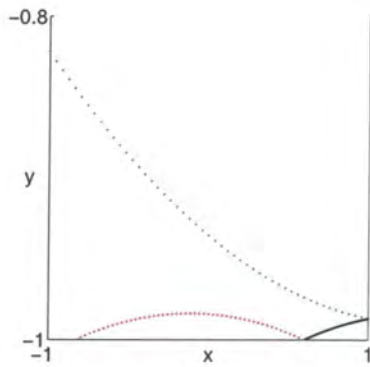
Figure 3.9: (a - d): Phase portraits constructed by following orbits initiated from single \mathbf{X} -values near cycles in figure 3.8 on the preceding page. (e -f): Trajectories as indicated. (Colour coding - red: B_{11} black: B_{12} green: B_{13} blue: B_{14})



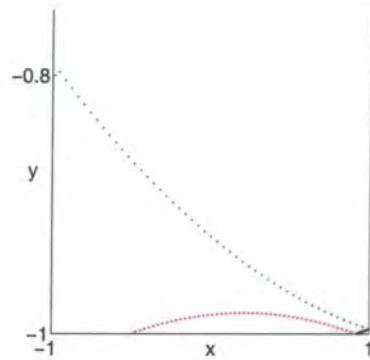
(a) Trajectory for figure 3.9(c)



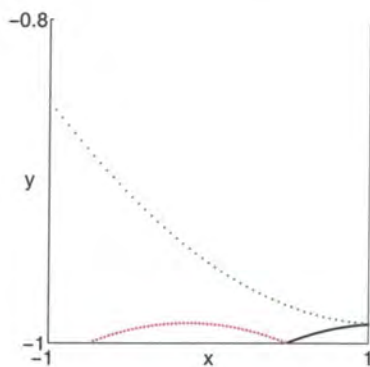
(b) Trajectory for figure 3.9(d)



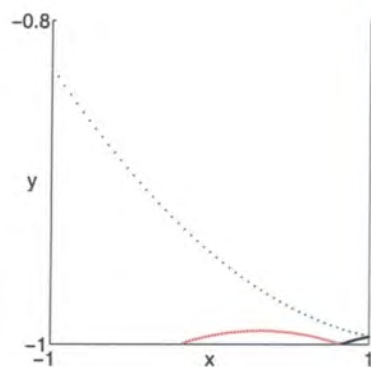
(c) $\mathbf{X} = (0.0876, 0.9994)$



(d) $\mathbf{X} = (0.2509, 0.9993)$

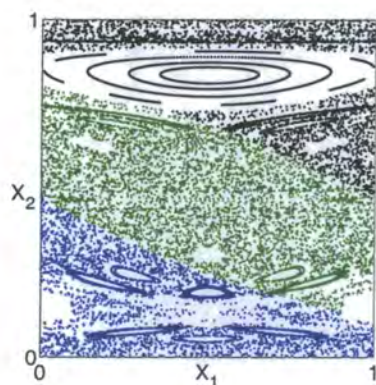


(e) $\mathbf{X} = (0.1217, 0.9995)$

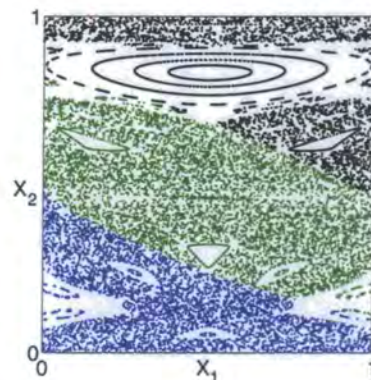


(f) $\mathbf{X} = (0.4065, 0.9994)$

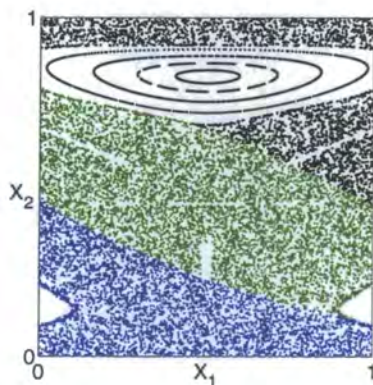
Figure 3.10: $E = 10^8$: (a - b): Trajectories corresponding to cycles in figures 3.9(c) and 3.9(d) on the preceding page . (c -f): Trajectories showing B_{11} in figure 3.8 on page 65. (Colour coding - red: B_{11} black: B_{12} green: B_{13} blue: B_{14})



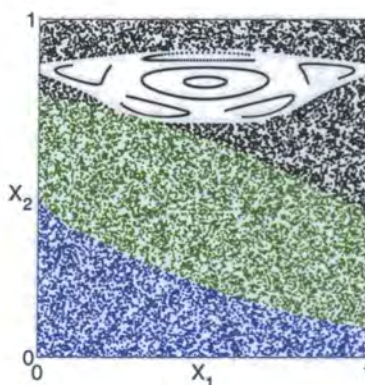
(a) Phase portrait at $E = 800$



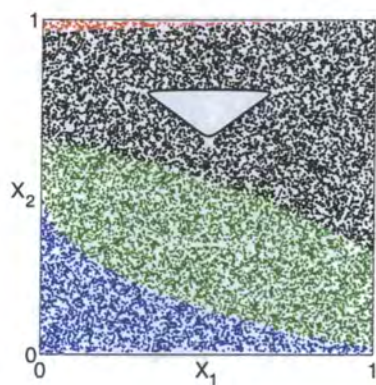
(b) Phase portrait at $E = 600$



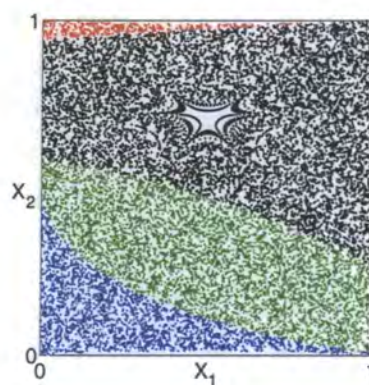
(c) Phase portrait at $E = 400$



(d) Phase portrait at $E = 200$

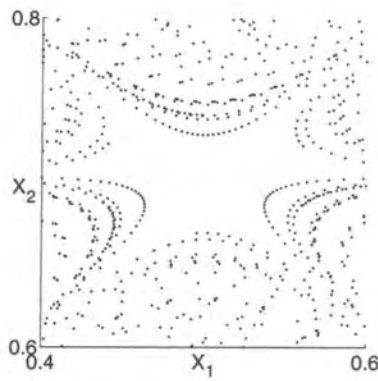


(e) Phase portrait at $E = 30$

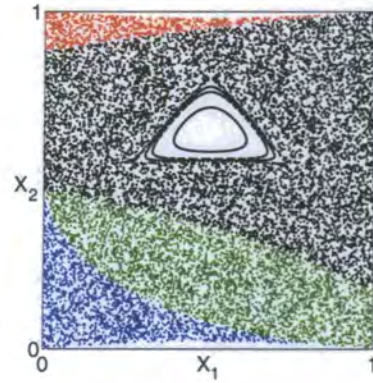


(f) Phase portrait at $E = 20$

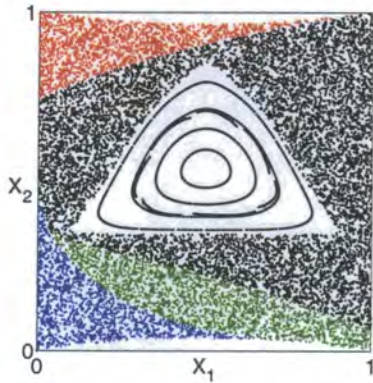
Figure 3.11: Phase portraits showing the change in phase space with decreasing E . (Colour coding - red: B_{11} black: B_{12} green: B_{13} blue: B_{14})



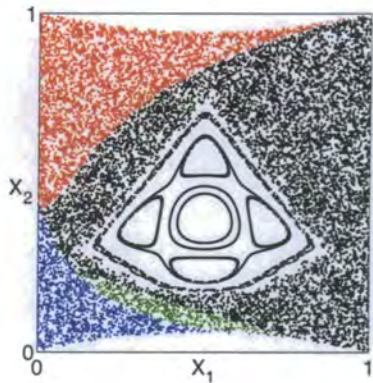
(a) Fixed point at $E = 18.414$



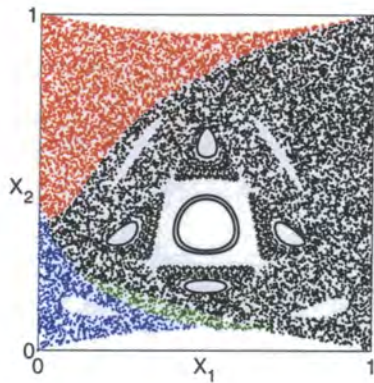
(b) Phase portrait at $E = 10$



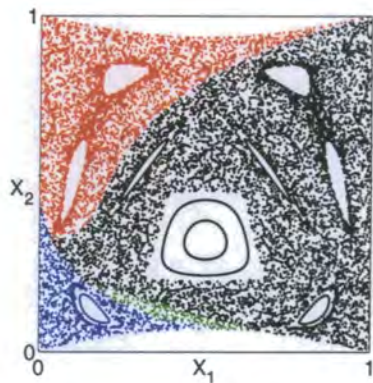
(c) Phase portrait at $E = 5$



(d) Phase portrait at $E = 2.6$

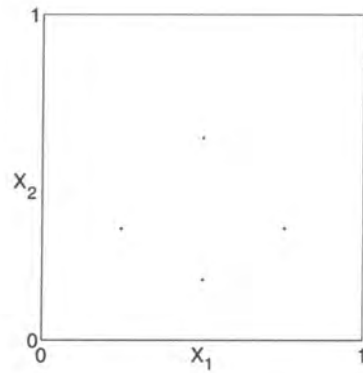


(e) Phase portrait at $E = 2.4$

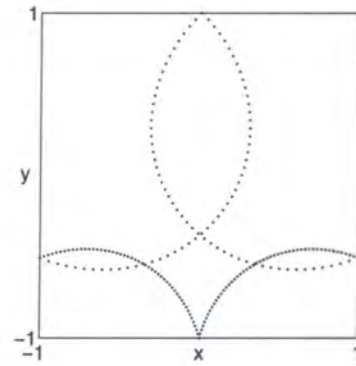


(f) Phase portrait at $E = 2.1$

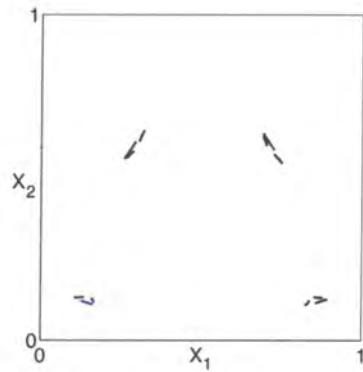
Figure 3.12: Phase portraits showing the change in phase space with decreasing E . (Colour coding - red: B_{11} black: B_{12} green: B_{13} blue: B_{14})



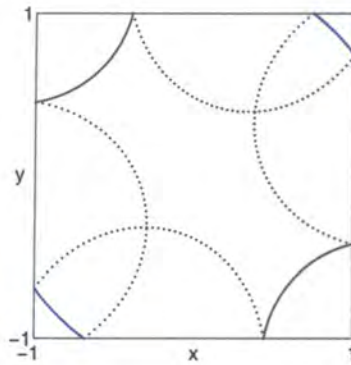
(a) 4-cycle at $\mathbf{X} = (0.5, 0.62)$



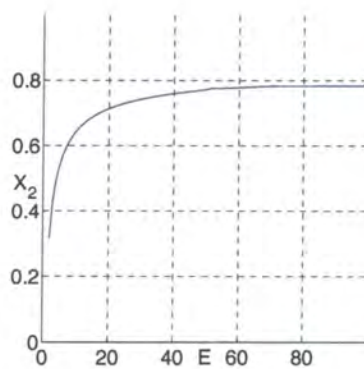
(b) Trajectory for 3.13(a)



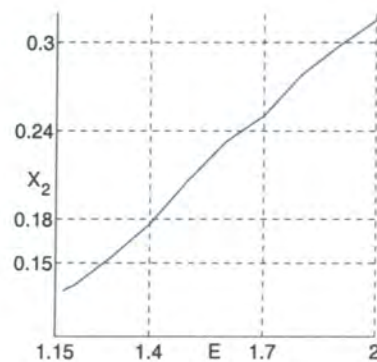
(c) 4-cycle at $\mathbf{X} = (0.7, 0.6)$



(d) Trajectory for 3.13(c)

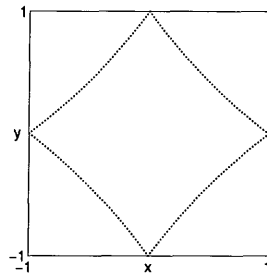


(e) $\mathbf{X}_+ : E = 2$ to 100

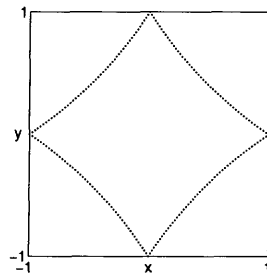


(f) $\mathbf{X}_+ : E = 1.5$ to 2

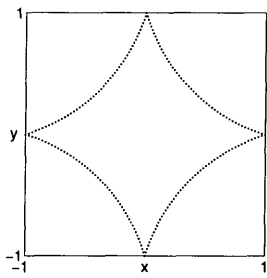
Figure 3.13: Phase portraits and trajectories for the 4-cycles embedded in figure 3.12(f) - (a) to (d) (Colour coding - red: B_{11} black: B_{12} green: B_{13} blue: B_{14}). Changes in the X_2 values of \mathbf{X}_+ with E - (e) and (f)



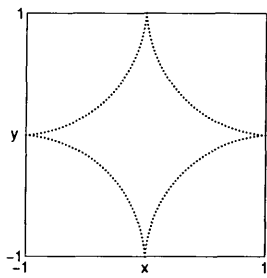
(a) $E = 100$



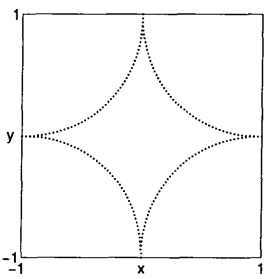
(b) $E = 50$



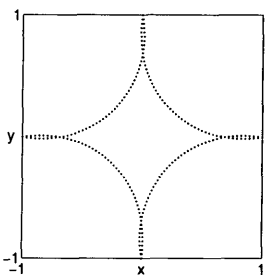
(c) $E = 10$



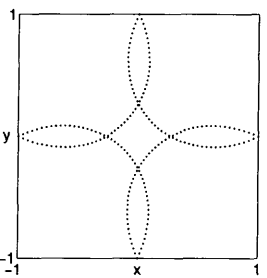
(d) $E = 5$



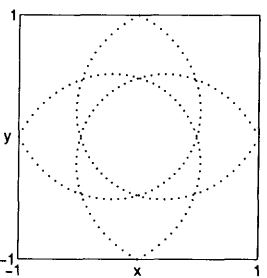
(e) $E = 4$



(f) $E = 3$



(g) $E = 2$



(h) $E = 1.1706$

Figure 3.14: Change in the curvature of the trajectories for \mathbf{X}_+ with decreasing E . (Colour coding - red: B_{11} black: B_{12} green: B_{13} blue: B_{14})

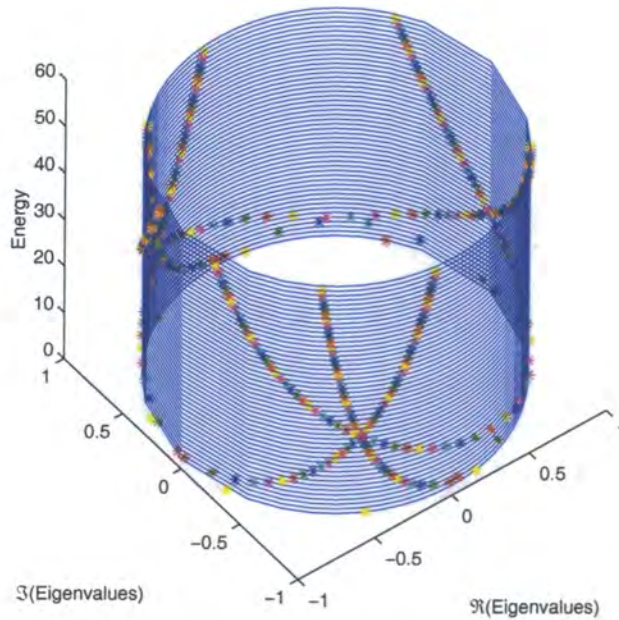


Figure 3.15: Plot showing the eigenvalues of \mathbf{X}_+ moving round the unit circle for the range $E = 2$ to 50

Figure 3.15 demonstrates that the eigenvalues of the \mathbf{J} -matrix of \mathbf{X}_+ for the range $2 \leq E \leq 50$ do indeed traverse the unit circle, as they must do.

3.6.2 Periodic cycles with type II trajectories

We have found periodic cycles with symmetric trajectories of order $4k$ for $k = 2, 3, 4, 5, 6$. The 2-cycle makes its first appearance at about $E = 2.1$, (figure 3.16 on the following page for $E = 2, 1.8, 1.6$ and 1). The phase portrait and trajectory for the 2-cycle are shown, respectively, in figures 3.17(a) and 3.17(b) on page 74 obtained from single initial \mathbf{X} values.

At $E = 1.6$ the eigenvalues of the \mathbf{J} -matrix for the 2-cycle are the 5th roots of unity giving a 5-bifurcation; the phase portrait and trajectory of the resulting 10-cycle are shown, respectively, in figures 3.17(c) and 3.17(d) on page 74.

The persistent \mathbf{X}_+ becomes unstable and vanishes at $E = 1.1706$, (figure 3.19(a) on page 76) and also at this value of E the 2-cycle has associated eigenvalues near a cube root of unity and its shape changes as in the case of resonance for \mathbf{X}_+ at $E = 20$, (figure 3.12(f) on page 69). Again due to the transient nature of the unstable 3-cycle produced by this 3-bifurcation we were unable to produce the corresponding phase portrait or closed trajectory from one initial \mathbf{X} value.

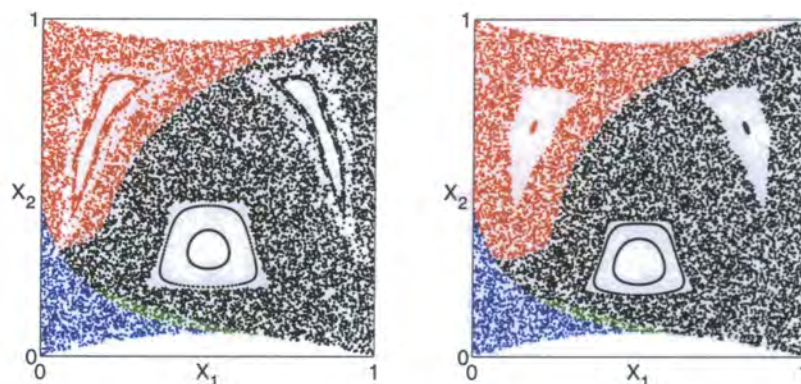
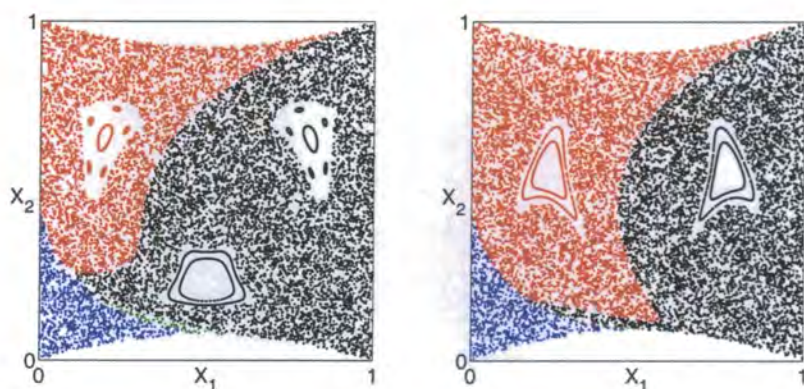
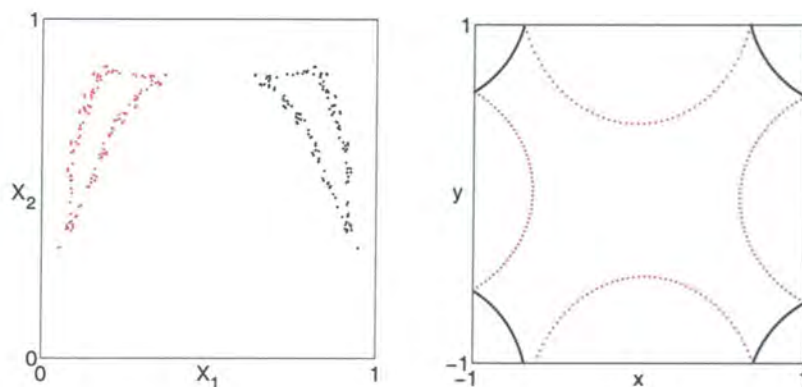
(a) Phase portrait at $E = 2$ (b) Phase portrait at $E = 1.8$ (c) Phase portrait at $E = 1.6$ (d) Phase portrait at $E = 1$

Figure 3.16: Phase portraits showing the symmetric 2-cycle (Colour coding - red: B_{11} black: B_{12} green: B_{13} blue: B_{14})

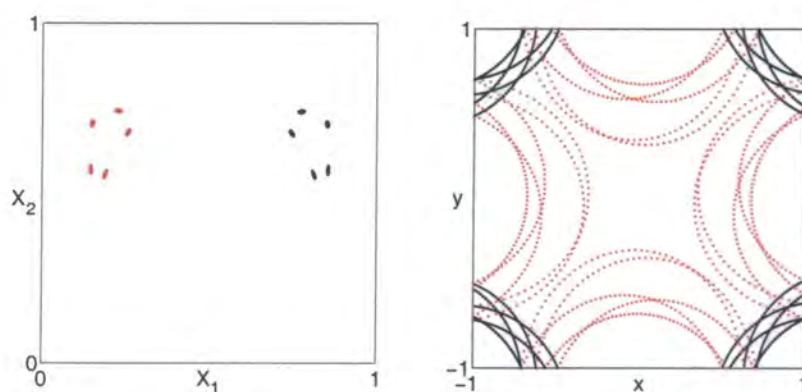
The 2-cycle is clearly evident until about $E = 0.7$ when it vanishes. The 3-cycle appears briefly at $E = 0.3$, (figure 3.19(b) on page 76), its phase portrait and trajectory are depicted, respectively, in figures 3.18(a) and 3.18(b) on page 75.

The 4, 5 and 6-cycles make very brief appearances at $E = -0.18$, -0.387 and -0.536 respectively. These can only be detected with many thousands of bounces so that the whole of phase space is completely covered with the exception of very small areas corresponding to the cycles. The required files are rather expensive in computer disc space so phase portraits at these energies are not included. However, confirmation of their existence is given by figures 3.18(c) to 3.18(h) on page 75 which are the phase portraits and trajectories for these cycles from single initial \mathbf{X} values.



(a) $E = 2$: Phase portrait of 2-cycle from $\mathbf{X}=(0.2, 0.655)$

(b) $E = 1.8$: Trajectory of the 2-cycle from $\mathbf{X}=(0.2, 0.655)$



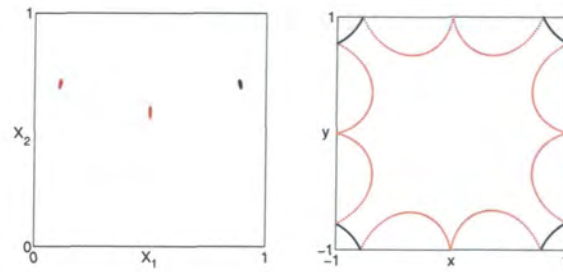
(c) Phase portrait of the 10-cycle from the 5-bifurcation

(d) Trajectory of the 10-cycle from the 5-bifurcation

Figure 3.17: Phase portraits and trajectories for symmetric 2-cycle and 10-cycle (from the 5-bifurcation). (Colour coding - red: B_{11} black: B_{12} green: B_{13} blue: B_{14})

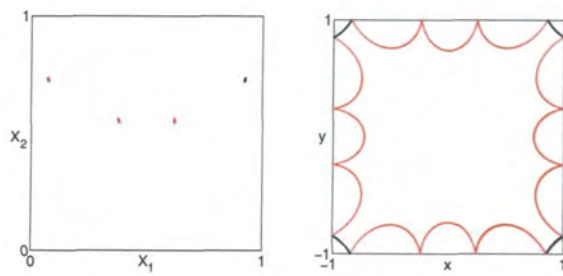
Figure 3.18(h) on the following page gives the impression that for the 6-cycle the ball actually hits the corners, but magnification of the corners verifies that this is not the case. In any event, the phase portrait (figure 3.18(g) on the next page) confirms that amongst the 6 bounces one is B_{12} .

One noticeable difference between the periodic cycles of this subsection and the previous one is that for any given E in the range $2 < E < -1$ there is at most one periodic cycle with a symmetric trajectory of order $4k$. Hence phase space alternates between having such a cycle and being completely chaotic.



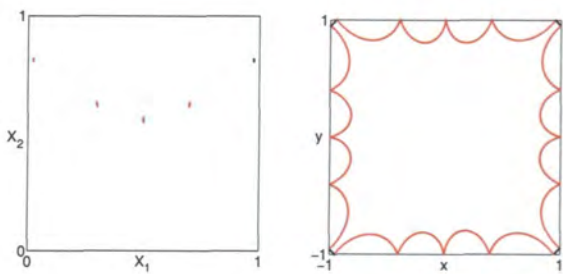
(a) and (b) 3-cycles

(b) at $E = 0.3$



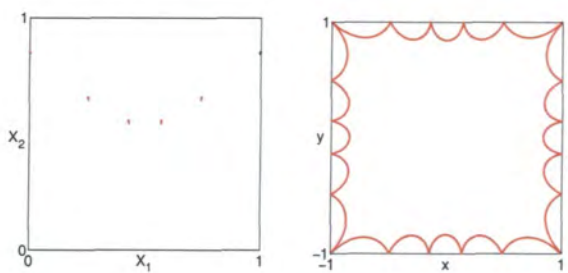
(c) and (d) 4-cycles

(d) at $E = -0.18$



(e) and (f) 5-cycles

(f) at $E = -0.387$



(g) and (h) 6-cycles

(h) at $E = -0.536$

Figure 3.18: Phase portraits and trajectories for the symmetric 3-,4-,5- and 6-cycles. (Colour coding - red: B_{11} black: B_{12} green: B_{13} blue: B_{14})

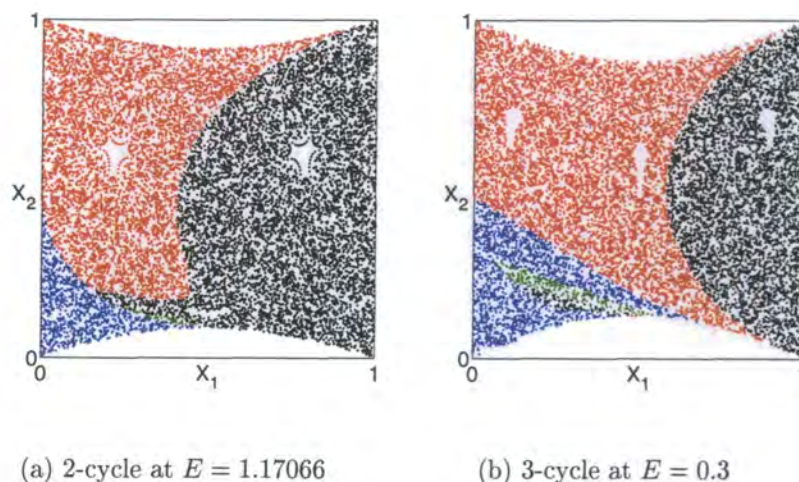


Figure 3.19: Phase portraits of the symmetric 2- and 3-cycles. (Colour coding - red: B_{11} black: B_{12} green: B_{13} blue: B_{14})

3.6.3 Periodic cycles with type III trajectories

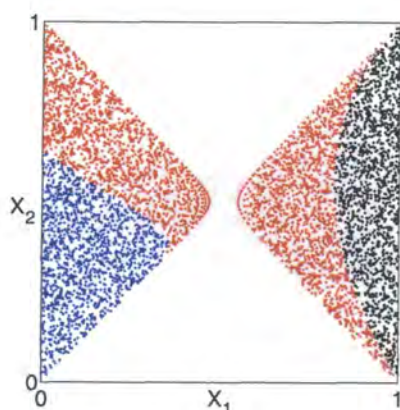


Figure 3.20: Phase portrait at $E = -1$ showing disjoint phase space.

From previous studies, [25–27,30,40,41,43,44], of polygon billiards the aforementioned periodic cycles were fully anticipated. However, no mention is made of periodic cycles below the energy when such cycles cannot exist, in the case of the \mathcal{B}_{\square} this is $E = -1$ when phase space becomes disjoint (figure 3.20).

But in the limit $E = -2$, the \mathcal{B}_{\square} must be integrable since the kinetic energy term in the Hamiltonian vanishes leaving only the "effective" potential energy term due to the rotation.

Our numerical simulations do show that as E is decreased from $E = -1$ towards the limit $E = -2$ the \mathcal{B}_{\square} tends to integrability.

Extremely exhaustive attempts at locating cycles in the range $-1.8 < E < -0.5$ bore no fruition, so we surmise that in this range the \mathcal{B}_{\square} is completely chaotic. The first cycle to appear is the 2-cycle at $E = -1.8$, the left portion of the phase portrait obtained from a 64×64 grid of points each followed for 250 bounces (as are

all subsequent phase portraits, unless otherwise stated) is depicted in figure 3.21. It is worth noting that the X_1 axes in this figure (and for all with lower values of E) is greatly expanded. Since the right portions of the phase portraits are disjoint and symmetrical, these will be omitted subsequently.

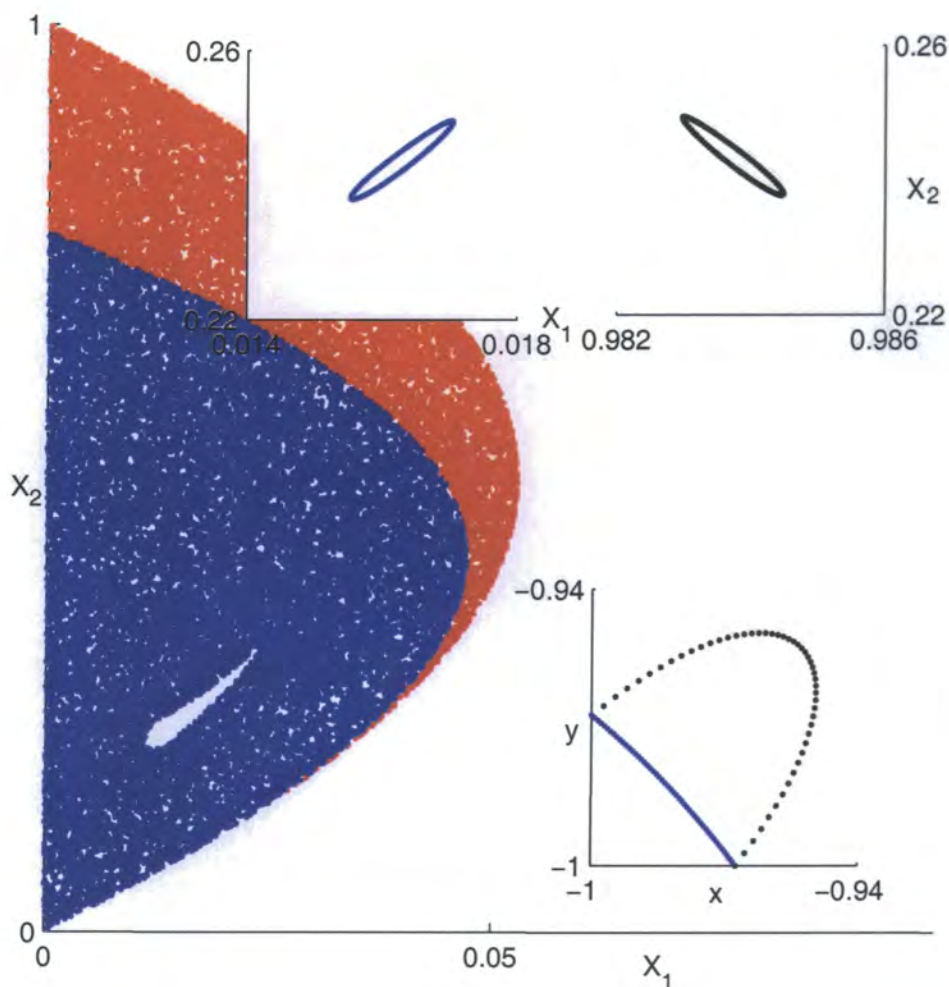


Figure 3.21: Phase portrait at $E = -1.8$. Inset: 2-cycle and its trajectory. (Colour coding - red: B_{11} black: B_{12} green: B_{13} blue: B_{14})

Inset is the phase portrait of the asymmetric 2-cycle from a single initial \mathbf{X} value and its corresponding trajectory.

It is the only cycle present until $E = -1.9$, figure 3.22 on the following page, when two 3-cycles appear (inset is the phase portrait and trajectory for one of them).

Figure 3.23(a) on page 79 is the phase portrait at $E = -1.95$ (from a $128 \times$

128 grid) which has a 10-cycle (resulting from a 5-birfucation of the the 2-cycle) embedded in it.

Figure 3.23(b) is a phase portrait for $E = -1.97$, where two 4-cycles have now appeared, inset is the phase portrait and trajectory for one of them.

Figure 3.24 on page 80 is a phase portrait for E approaching the limit $E = -2$ ($E = -1.998$ from a 2048×2048 grid for 50 bounces); as can be seen there is a growing number of cycles.

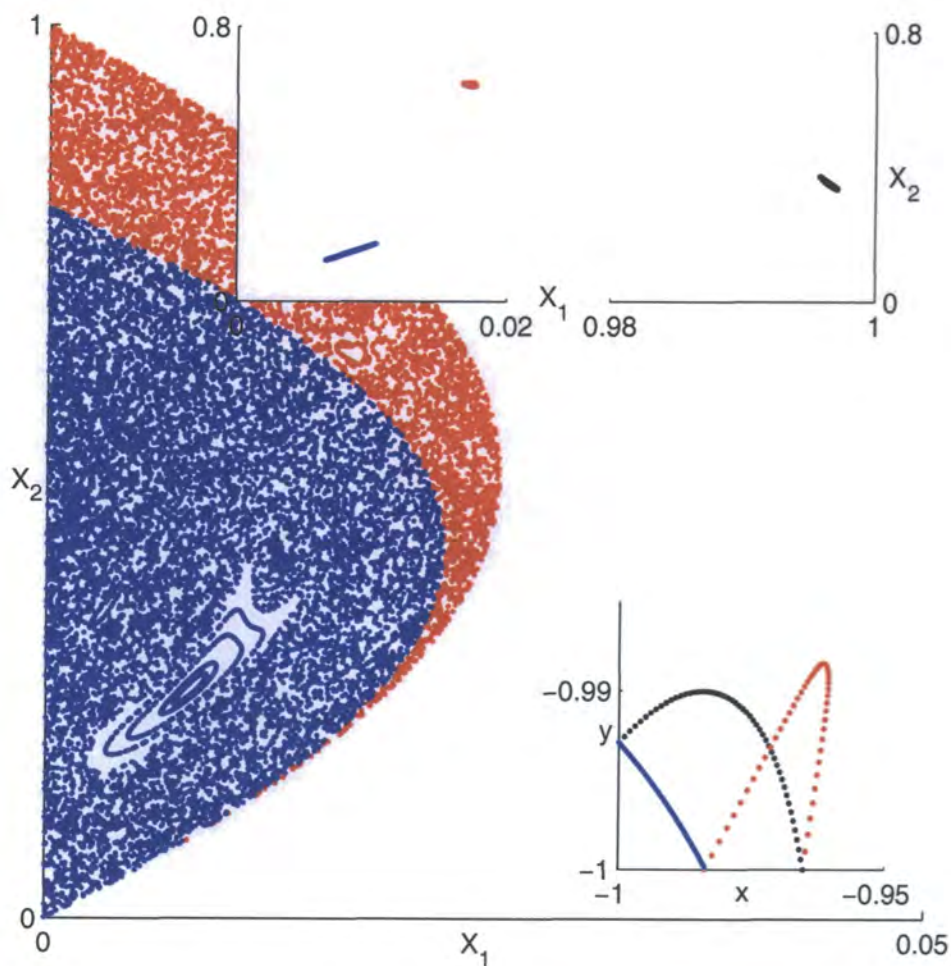
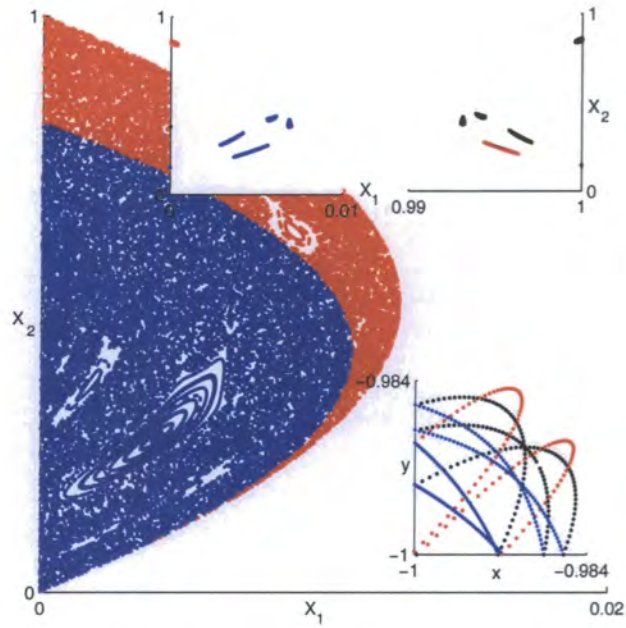
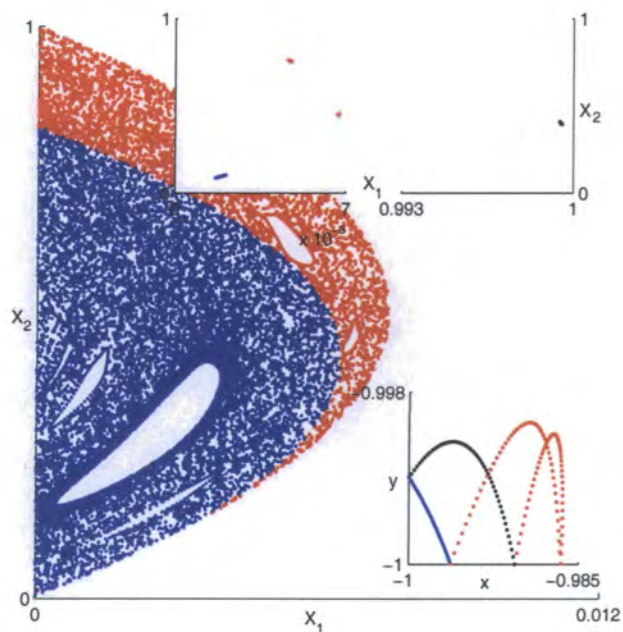


Figure 3.22: Phase portrait at $E = -1.9$. Inset: 3-cycle and its trajectory. (Colour coding - red: B_{11} black: B_{12} green: B_{13} blue: B_{14})

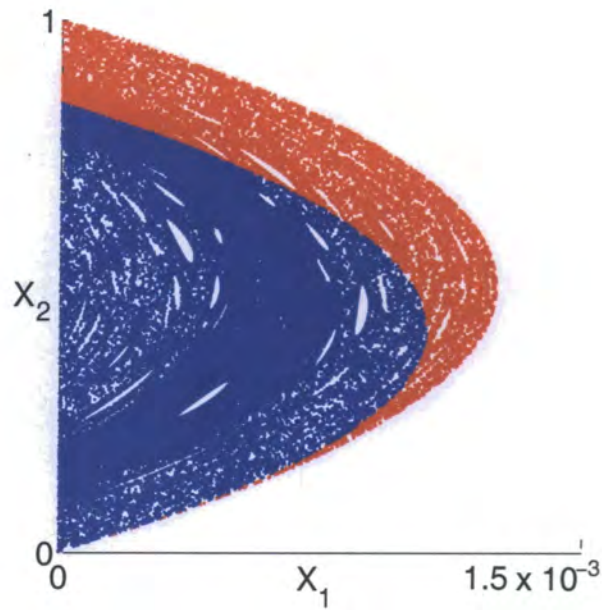


(a) Phase portrait at $E = -1.95$

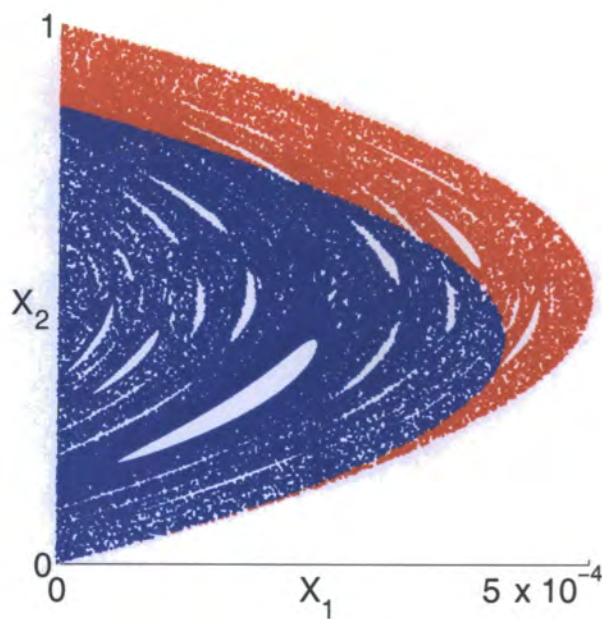


(b) Phase portrait at $E = -1.97$

Figure 3.23: Phase portraits at $E = -1.95$ and $E = -1.97$ (Colour coding - red: B_{11} black: B_{12} green: B_{13} blue: B_{14})



(a) Phase portrait at $E = -1.995$



(b) Phase portrait at $E = -1.998$

Figure 3.24: Phase portraits; (a): at $E = -1.995$, (b): at $E = -1.998$. (Colour coding - red: B_{11} black: B_{12} green: B_{13} blue: B_{14})

3.6.3.1 Trajectory curvatures

Figure 3.21 on page 77 affords our first example of a cycle exhibiting trajectory curvature to the left rather than to the right as has been the case for all the preceding cycles. Equation B.6 on page 158 shows that the effective force acting on a moving particle in a rotating frame of reference contains the following two forces:

- (1) Coriolis force which has magnitude $2m\omega|\dot{z}|$ and is directed perpendicular to both the direction of rotation and the direction of motion of the particle.
- (2) Centrifugal force which has magnitude $m\omega^2|z|$ and is directed perpendicular to the direction of rotation and radially outwards.

For $E > 0$ the Coriolis force dominates and keeps trajectory curvature to the right for the particle travelling both in the clockwise and anti-clockwise direction. However, for $E < 0$ the dominance of the forces is position dependent, the Centrifugal force being greater for:

$$\begin{aligned}
 |z|\omega^2 &> 2|\dot{z}|\omega \\
 |z|^2\omega^2 &> 4(2\mathcal{E} + |z|^2\omega^2) \quad (\text{using equation D.7 on page 163}) \\
 -3|z|^2\omega^2 &> 8\mathcal{E} \\
 -\frac{3|z|^2}{4} &> \frac{2\mathcal{E}}{\omega^2} = E \\
 |z|^2 &< -\frac{4E}{3}
 \end{aligned} \tag{3.56}$$

Recalling that for $E < 0$ there exists a circle of exclusion of radius $|z| = \sqrt{-E}$ then we have an annulus $\sqrt{-4E/3} < |z| \leq \sqrt{-E}$ within which trajectories exhibiting both left and right curvature are observed as illustrated by figure 3.25 on the next page.

Trajectories which do not enter the annulus, ($X_2 = 0.5, 0.22$), maintain their right curvature for their duration whilst those entering have curvature depending on their X_2 value relative to a critical X_2 . At $E = -0.5$ this critical X_2 , as shown in figure 3.25 on the following page, is 0.3 and it is the only value for which the trajectory encounters the circle of exclusion. The segment approaching the excluded region has the normal right curvature and at the point of contact we observe a cusp where the particle momentarily has zero velocity (the spacings between the dots is an indication of the velocity of the particle). Hence the Coriolis force is zero at that moment and the radial Centrifugal force acts to push the particle away imparting velocity to it, thus making the Coriolis force nonzero again which acts to maintain the right curvature. Trajectories with X_2 values higher than the critical

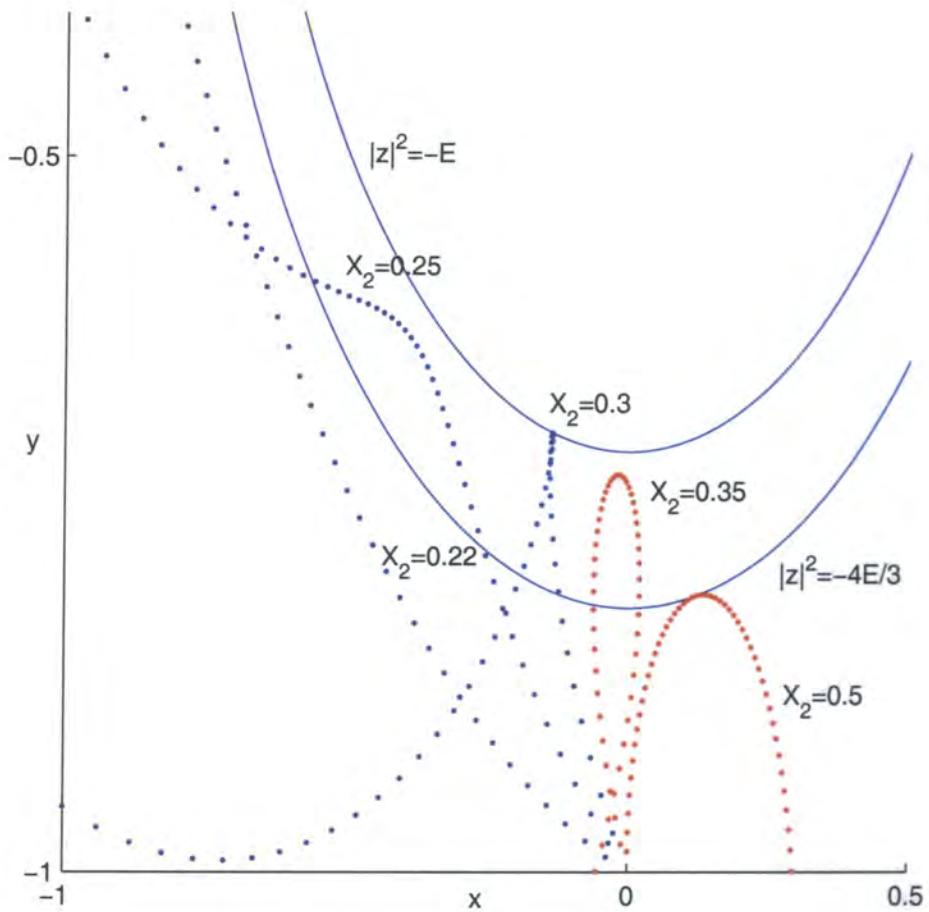


Figure 3.25: $E = -0.5, X_1 = 0.5$: Trajectory curvatures for various values of X_2 . (Colour coding - red: B_{11} black: B_{12} green: B_{13} blue: B_{14})

value, ($X_2 = 0.35$), maintain their right curvature. Those with lower X_2 values, ($X_2 = 0.25$), develop a kink for the duration of which the trajectory exhibits left curvature. Again the Coriolis force momentarily becomes zero but this time because the rate of change of $|z|$ becomes zero at which point the Centrifugal force causes the left curvature until the Coriolis force once more comes into play.

Since $|z|_{max} = \sqrt{2}$, for $E < -1.5$ all trajectories are in the annulus resulting in many trajectories which display left curvature for the whole of their duration.

3.7 Flyaway and adiabatic skipping

With trajectories curving to the right there exists the possibility that a trajectory may have a grazing bounce on the boundary to its left or with only slightly different initial values it merely skims it and curves away to impact with the adjacent bound-

ary. Flyaway is the term describing the difference between these two possibilities and was the mechanism identified by [26] in magnetic billiards as the originator of chaos.

Flyaway has also been proposed by [25,27,43,44] as the origin of chaos in rotating billiards, however, our simulations indicate that the contribution to disorder that flyaway makes in the \mathcal{B}_\square is negligible.

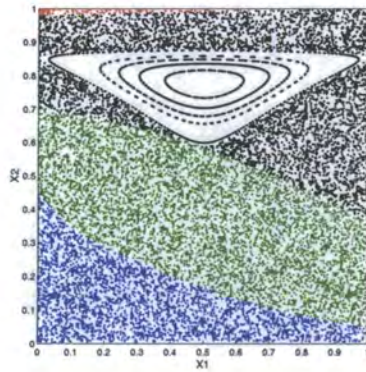
For the purpose of this discussion the phase portrait at $E = 60$, (figure 3.26(a) on the next page), is typical of phase portraits for those with, $E \geq 10$.

There is a clear separation of phase space for the four bounces, B_{11} , B_{12} , B_{13} and B_{14} , as displayed by the colour coding. This means that the set of slightly different initial conditions that can exhibit flyaway is restricted to the points lying in a very narrow band centred on one of the three curves separating the four colours.

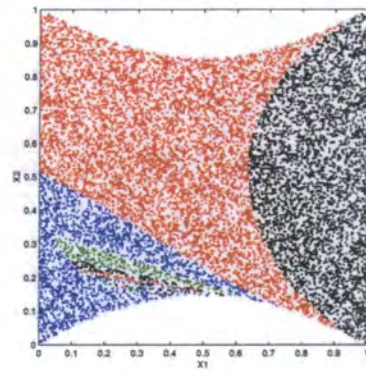
The phase portrait also reveals that only two sides of the \mathcal{B}_\square are accessible to a particular flyaway trajectory; that is B_{14} or B_{13} , B_{13} or B_{12} and B_{12} or B_{11} . Typically these phase portraits have 16,000 points and the total number of points within these three narrow bands is very small in comparison so their contribution to the disorder is insignificant.

As E is decreased below $E = 10$ three sides of the \mathcal{B}_\square becomes accessible and by $E = 0$, (figure 3.26(b) on the following page), all four sides are accessible for a limited set of initial \mathbf{X} values. We see that there is now embedded in the blue region of phase space small black, green and red subregions. It is in this region that small changes in initial \mathbf{X} values can give rise to B_{11} , B_{12} , B_{13} or B_{14} . Figures 3.26(c) to 3.26(f) on the next page show such trajectories where X_1 is fixed and X_2 is slightly varied. At these low values of E there is certainly increased disorder, but the volume of phase space involved is small, so again the contribution of flyaway to the chaos is insignificant. In any case, chaos has set in at a higher value of E .

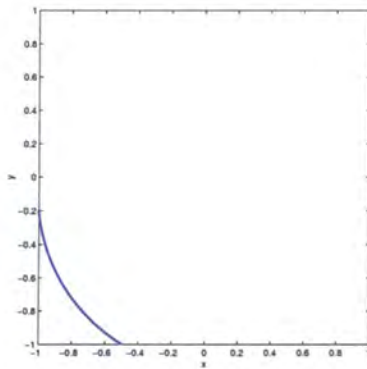
Adiabatic skipping is discussed in much detail in [44], in relation to the rotating circular billiard, and [26] for the magnetic billiard. Adiabatic skipping describes successive bounces on the boundary for which the distance apart is much less than the local radius of curvature of the trajectory. The curvature is considered as changing adiabatically and the short skips have a conserved function whose contours are invariant curves of the bounce map.



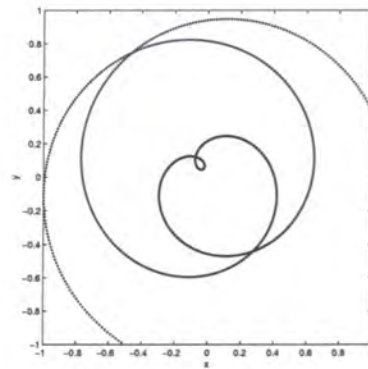
(a) Phase portrait: $E = 60$



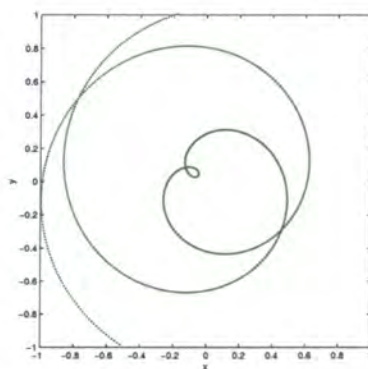
(b) Phase portrait: $E = 0$



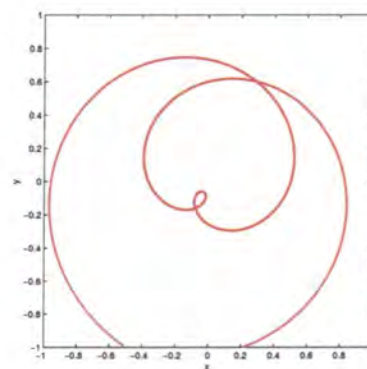
(c) $\mathbf{X} = (0.25, 0.165)$



(d) $\mathbf{X} = (0.25, 0.166)$



(e) $\mathbf{X} = (0.25, 0.167)$



(f) $\mathbf{X} = (0.25, 0.172)$

Figure 3.26: Phase portraits: (a): $E = 60$, (b): $E = 0$; Trajectories showing flyaway at $E = 0$ (c - f). (Colour coding - red: B_{11} black: B_{12} green: B_{13} blue: B_{14})

For the \mathcal{B}_\square adiabatic skipping is destroyed by the corners and as such does not exist. In a sense the \mathcal{B}_\square is a good system to study as the insignificance of flyaway and the absence of adiabatic skipping means that the dynamics observed is not obscured by these two mechanisms. Thus revealing the true mechanism to be the accumulation of angular dispersion from a rotating line as indicated in the next section.

3.8 Lyapunov exponents

In chaotic regions of phase space two initially nearby trajectories separate roughly exponentially with time whilst in quasiperiodic regions nearby trajectories separate roughly linearly with time [45]. The average rate of separation may be defined by [46]:

$$\gamma(t) = \frac{\ln(d(t)/d(t_0))}{(t - t_0)} \quad (3.57)$$

where d is the Euclidean distance between two initially nearby trajectories in their phase space.

If the trajectories are chaotic, then d will grow exponentially on the average and $\gamma(t)$ will approach some positive constant, if the trajectories are quasiperiodic, then d will grow linearly on the average and $\gamma(t)$ will approach zero as $\ln(t)/t$ and these two cases are readily distinguishable on a plot of $\log(\gamma(t))$ versus $\log(t)$.

For chaotic trajectories $\log(\gamma(t))$ will approach the logarithm of the Lyapunov exponent, $\Lambda(x)$, while for quasiperiodic trajectories $\log(\gamma(t))$ versus $\log(t)$ will follow a line with slope -1 . In any finite computation only an estimate of $\Lambda(x)$ can be given, which strictly speaking is only defined in the infinite time limit. It has been proven that for almost all initial conditions this limit can take at most n different values ($\Lambda(x)$'s) as the initial displacement is varied, where n is the dimension of the system. In fact, except for a set of measure zero, all initial displacements lead to the maximum $\Lambda(x)$.

We have used the usual method [47], which is an adaptation of the variational method for discrete maps, for calculating $\Lambda(\mathbf{x})$. This involves considering two nearby trajectories initially distance d_0 apart and measuring their separation, d_1 , after the first bounce. Then instead of continuing with these two trajectories, we change the second trajectory for one which is again a distance d_0 from the first trajectory but maintain the separation vector in the same direction. This procedure is repeated for many bounces.

Let d_i be the separation after the i^{th} bounce, then $\Lambda(\mathbf{X})$ can be written as:

$$\Lambda(\mathbf{X}) = \lim_{n \rightarrow \infty} \frac{1}{n} \sum_{i=1}^n \ln(d_i/d_0) \quad (3.58)$$

Our numerical results are in keeping with [47]; if $\Lambda_n(\mathbf{X})$ is the value of Λ before the limit is taken then

1. $\Lambda_n(\mathbf{X})$ is independent of \mathbf{X} .
2. $\Lambda_n(\mathbf{X})$ is independent of the length (for $d_0 < 10^{-5}$) and direction of the initial separation vector.
3. Small fluctuations in Λ are observed, approximately 5%, as it approaches its limiting value even after 10^5 bounces.

A better method for calculating $\Lambda_n(\mathbf{X})$ is, in fact, that found in [41] where we can make use of our Stability matrix, $\mathbf{S}_n(\mathbf{X})$, as given by eqn (3.29) in terms of which the Lyapunov exponents for our 2-dimensional system are given by:

$$\Lambda_{\pm}(\mathbf{X}) = \pm \lim_{n \rightarrow \infty} \frac{1}{n} \ln \|\text{Tr}(\mathbf{S}_n(\mathbf{X}))\| \quad (3.59)$$

or equivalently, for the maximum Λ ,

$$\Lambda(\mathbf{X}) = \lim_{n \rightarrow \infty} \frac{1}{2n} \ln[\text{Tr}(S_n^T(\mathbf{X}))S_n(\mathbf{X})] \quad (3.60)$$

The graphs in this section are obtained using this method, which has the advantage of quicker convergence to the limiting value (approximately 10^3 bounces compared to 10^5) and the absence of the fluctuations about the limiting value. The results obtained for relatively few bounces (~ 2000) are quite revealing, figure 3.27 on the following page is for $E = 10^3$ and at this high value it is possible to choose initial points such that they exhibit predominantly one of the four types of bounce, that is, B_{1i} ; $i = 1, 2, 3, 4$. One point is chosen for each i for both the chaotic and regular regions. As expected the three regular initial values all very quickly converge to zero, giving a check on the convergence. However, there is a clear distinction between the $\Lambda_n(\mathbf{X})$ values for the three initial chaotic points with $\Lambda_{B_{13}} < \Lambda_{B_{12}} < \Lambda_{B_{14}}$.

This is a clear indication that the origin of chaos in the rotating \mathcal{B}_{\square} is the ball bouncing of a rotating line: Consider for simplicity two parallel trajectories distance d_0 apart travelling towards the rotating line such that trajectory 1 impacts upon the line first, when it is in the vertical position, (figure 3.28 on page 88), at an angle θ . Let the line rotate through an angle of $\delta\theta$ before trajectory 2 impacts. Then simple trigonometry shows that the original parallel trajectories are traversing, after specular reflections, with a divergent angle of $2\delta\theta$.

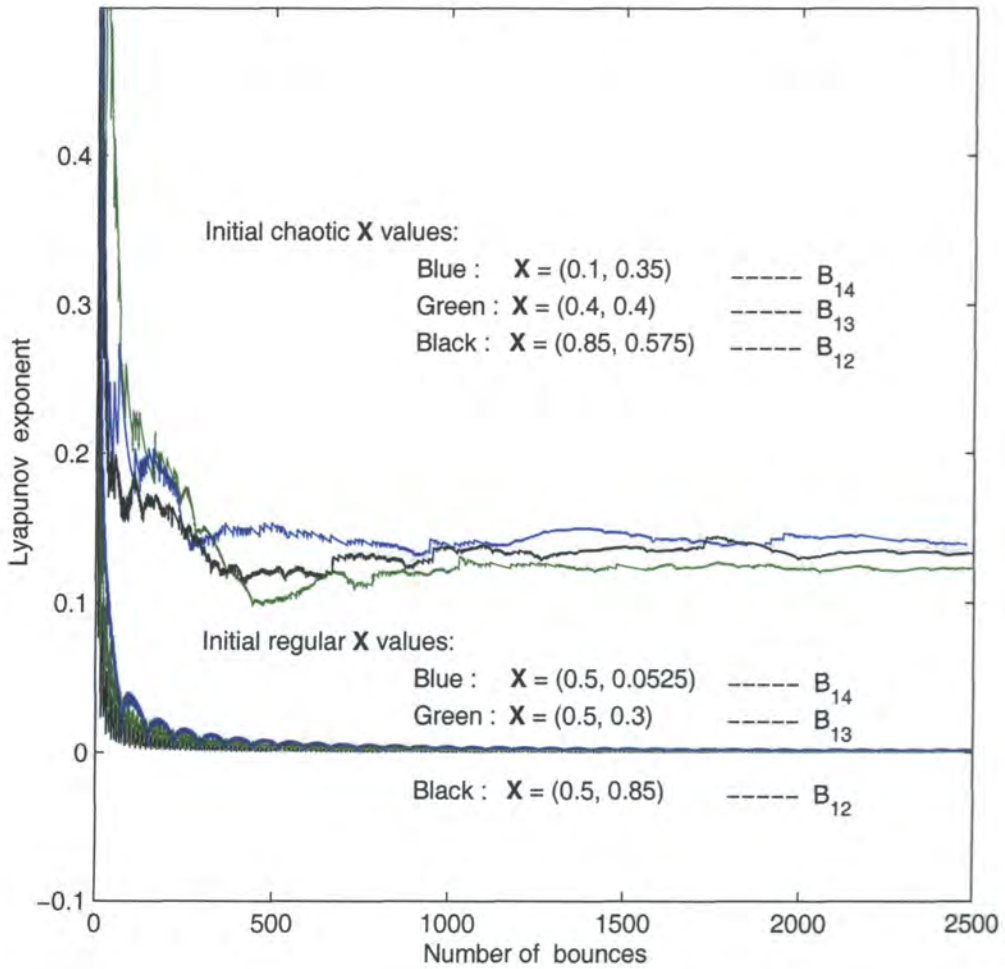


Figure 3.27: $E = 10^3$: Lyapunov exponents v no. of bounces for six different initial \mathbf{X} values

Figures 3.29 and 3.30 on page 89 are plots of the Lyapunov exponents versus E for one point for two different ranges of E . As expected there is a decrease in the value of the Lyapunov exponent with increasing E and this is consistent with the value tending to zero in the limit $E \rightarrow \infty$.

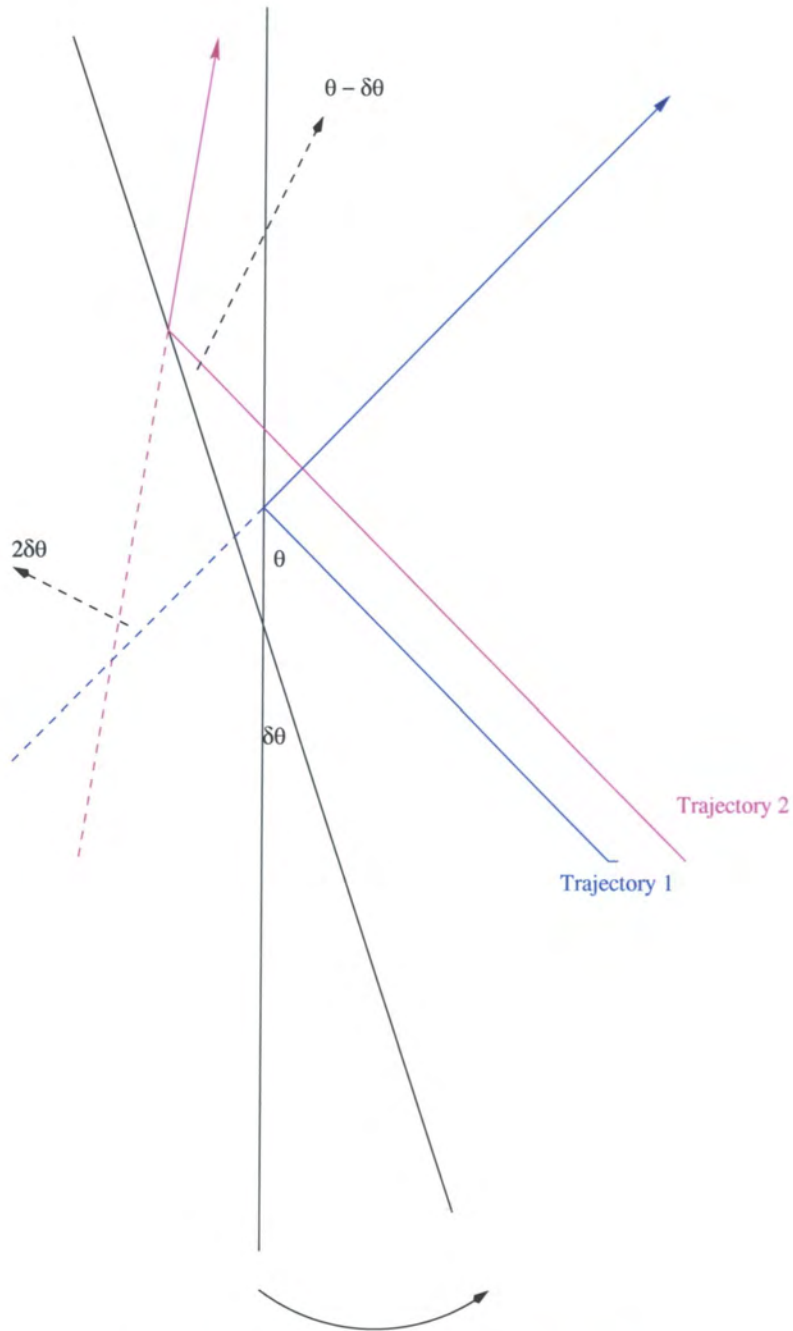


Figure 3.28: Bounces on a rotating line

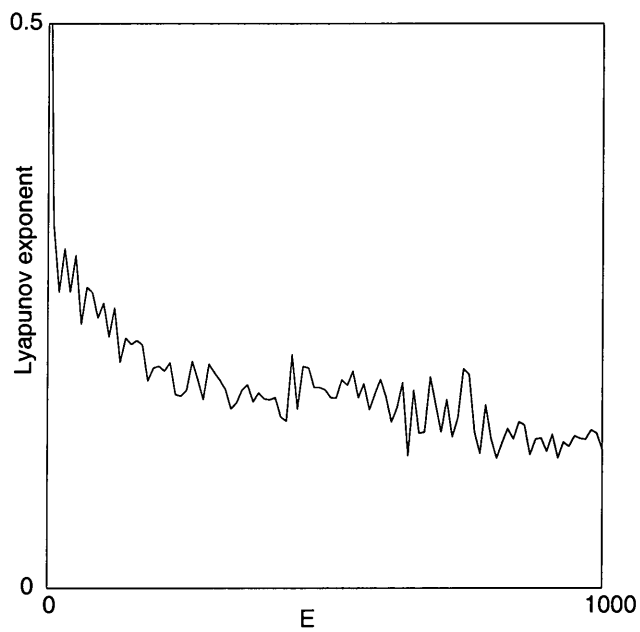


Figure 3.29: Lyapunov exponents v E for range: $E = 0$ to 10^3 and $\mathbf{X} = (0.4, 0.4)$

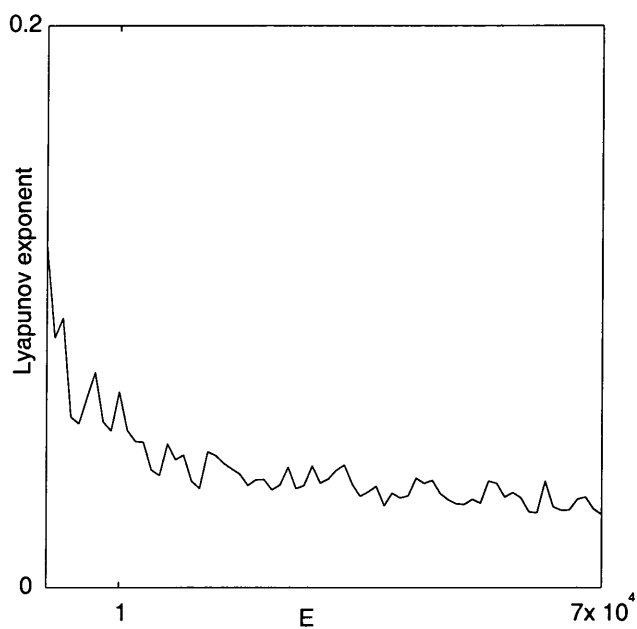


Figure 3.30: Lyapunov exponents v E for range: $E = 0$ to 10^5 and $\mathbf{X} = (0.4, 0.4)$

3.9 Chaotic phase volume

In this section we investigate the change in the ratio chaotic : available phase space for differing values of E , by ascertaining the proportion of chaotic phase space in phase plots generated from following an initial \mathbf{X} value for 10^5 bounces. This only makes sense, of course, if we begin at an E -value at which the phase plot produced is independent of the initial \mathbf{X} value. In the process of determining this E -level we see again that the mechanism for chaos is the accumulation of angular dispersion from a rotating line rather than flyaway. At $E = 1200$ the phase portraits produced from $\mathbf{X}_{(0.5,0.5)} = (0.5, 0.5)$ and $\mathbf{X}_{(0.2,0.2)} = (0.2, 0.2)$ are quite distinct, giving a central and an outer region respectively as shown in figure 3.31 on the next page.

Table 3.1 and figure 3.31 on the next page show that at $E = 1200$ the bounces are predominantly B_{13} and B_{14} for $\mathbf{X}_{(0.5,0.5)}$ and $\mathbf{X}_{(0.2,0.2)}$ respectively. At this relatively high E -value with an initial $\mathbf{X}_{(0.2,0.2)}$ for many successive bounces the \mathbf{X} value varies only slightly due to the small curvature of the trajectories resulting in about 54% of the bounces being B_{14} . Similarly, with an initial $\mathbf{X}_{(0.5,0.5)}$ we have about 60% of the bounces being B_{13} .

	B_{11}	B_{12}	B_{13}	B_{14}	Total
$E = 1200, \mathbf{X} = (0.5, 0.5)$	46	16566	57955	25434	100000
$E = 1200, \mathbf{X} = (0.2, 0.2)$	0	27779	18031	54190	100000
$E = 1100, \mathbf{X} = (0.5, 0.5)$	68	16276	60867	22789	100000
$E = 1100, \mathbf{X} = (0.2, 0.2)$	42	22753	37359	39846	100000
$E = 1000, \mathbf{X} = (0.5, 0.5)$	36	21703	39488	38773	100000
$E = 1000, \mathbf{X} = (0.2, 0.2)$	6	26778	22399	50817	100000
$E = 500, \mathbf{X} = (0.5, 0.5)$	102	18336	51066	30496	100000
$E = 500, \mathbf{X} = (0.2, 0.2)$	74	18314	51045	30547	100000

Table 3.1: Bounces from $\mathbf{X} = (0.5, 0.5), (0.2, 0.2)$ for $E = 1200, 1100, 1000$ and 500

The predominance of the two different types of bounces gives rise to two distinct phase portraits for the two different initial \mathbf{X} values. This difference is also apparent from differing LCE values for the two regions. Examination of figure 3.31(b) on the following page reveals that the possibilities for flyaway trajectories between B_{13}, B_{14} and B_{12}, B_{13} are rather quite small, but yet, apart from the fixed point at this E -value the whole of the available phase space is chaotic. This is a confirmation of our earlier suggestion of the mechanism for the chaotic behaviour being the accumulation of angular dispersion from a rotating line.

At $E = 1100$, (figure 3.32 on page 92) the curvature of the $\mathbf{X}_{(0.2,0.2)}$ trajectories, (figure 3.32(b) on page 92), have increased enough to allow a large number

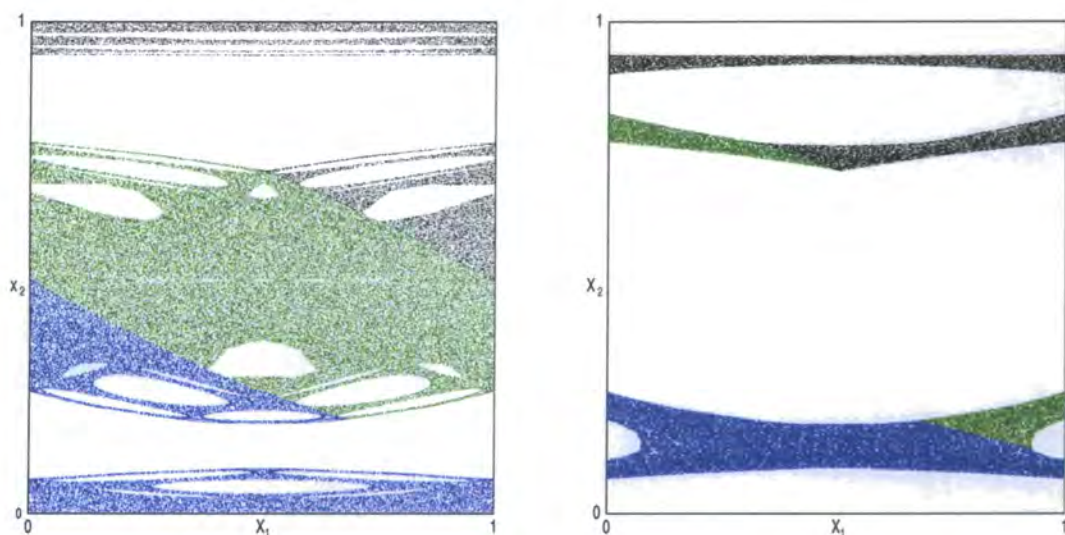
(a) $E = 1200$; $\mathbf{X} = (0.5, 0.5)$ (b) $E = 1200$; $\mathbf{X} = (0.2, 0.2)$

Figure 3.31: Phase portraits at $E = 1200$ from $\mathbf{X} = (0.5, 0.5)$ and $(0.2, 0.2)$. (Colour coding - red: B_{11} black: B_{12} green: B_{13} blue: B_{14})

of trajectories to escape from the outer region to the central region. The central region is structurally identical to that produced by $\mathbf{X}_{(0.5,0.5)}$, (figure 3.32(a) on the next page) but with a reduced density. However, the trajectory curvature is not sufficient enough to allow escape of $\mathbf{X}_{(0.5,0.5)}$ trajectories from the central region to the outer region so we still have distinct phase portraits from the two different initial \mathbf{X} values.

It is at $E = 1000$, (figure 3.33 on the following page) that we have structurally identical phase portraits, though the two regions are clearly distinguishable due to the different densities in the two phase portraits. So this E -value would seem to be a convenient starting point for obtaining the ratio of chaotic phase volume as the result obtained will be independent of the initial \mathbf{X} value. For completeness we have included the phase portraits obtained at $E = 500$, (figure 3.34 on page 93), from $\mathbf{X}_{(0.5,0.5)}$ and $\mathbf{X}_{(0.2,0.2)}$ where it can be seen, along with table 3.1 on the preceding page, that the phase portraits produced are completely independent of the initial \mathbf{X} value due to the high curvature of the trajectories.

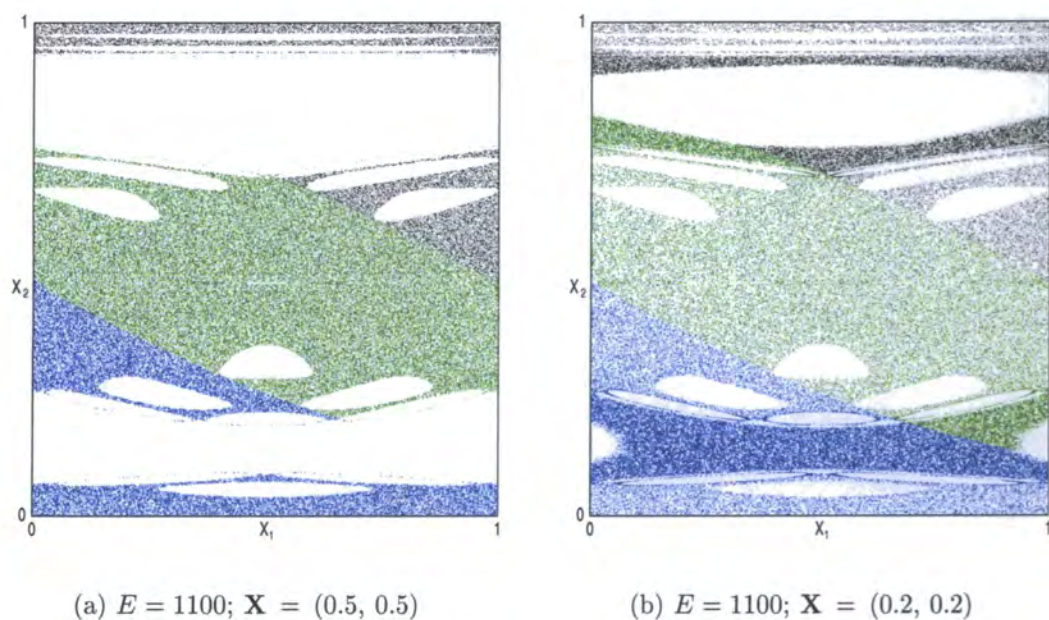


Figure 3.32: Phase portraits at $E = 1100$ from $\mathbf{X} = (0.5, 0.5)$ and $(0.2, 0.2)$. (Colour coding - red: B_{11} black: B_{12} green: B_{13} blue: B_{14})

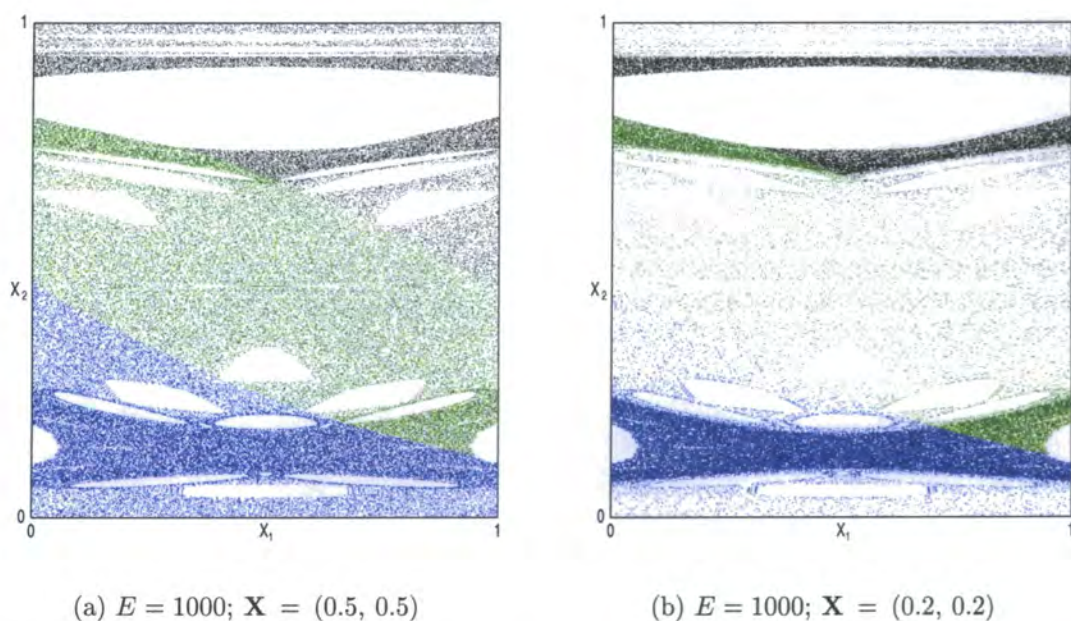


Figure 3.33: Phase portraits at $E = 1000$ from $\mathbf{X} = (0.5, 0.5)$ and $(0.2, 0.2)$. (Colour coding - red: B_{11} black: B_{12} green: B_{13} blue: B_{14})

The results obtained for the ratio of the chaotic phase volume with decreasing E are as anticipated, but it has been a useful exercise as they are a confirmation of the accuracy and validity of the phase portraits produced in the previous sections.

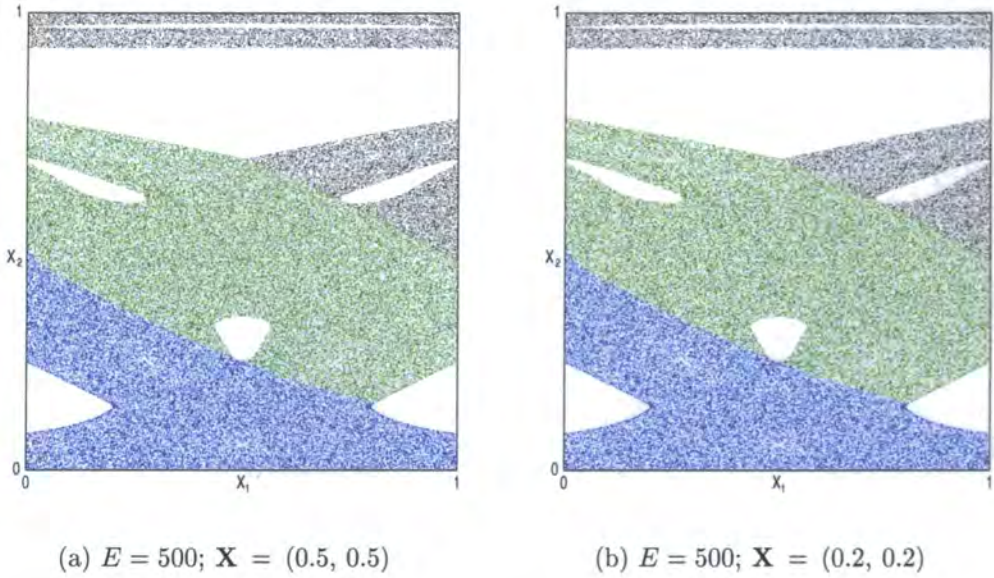


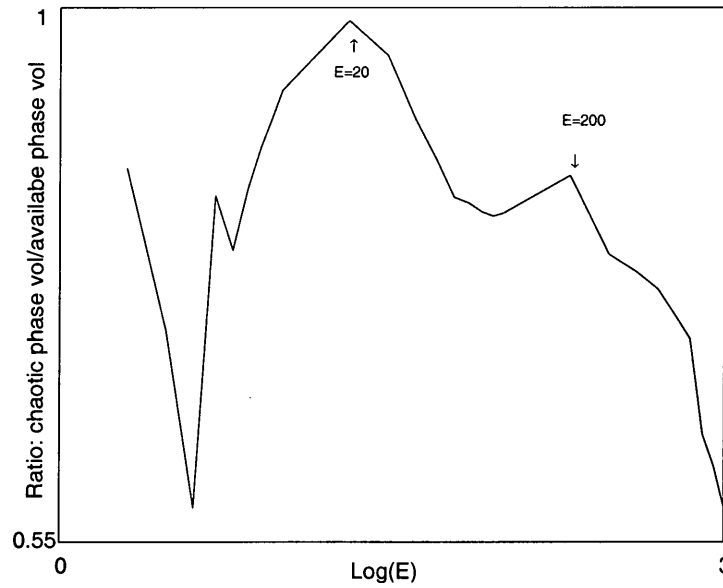
Figure 3.34: Phase portraits at $E = 500$ from $\mathbf{X} = (0.5, 0.5)$ and $(0.2, 0.2)$. (Colour coding - red: B_{11} black: B_{12} green: B_{13} blue: B_{14})

Figure 3.35(a) on the next page starts at $E = 1000$ and we see a monotonic increase in the ratio until about $E = 200$. This is due to the vanishing of the various cycles related to the stationary \mathcal{B}_\square as the E -value decreases. By about $E = 400$ all the cycles except the fixed point, \mathbf{X}_+ , have vanished and \mathbf{X}_+ is gradually decreasing in size until about $E = 200$.

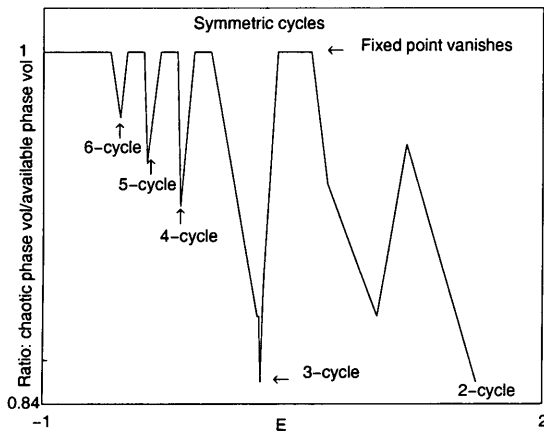
At this E -value the eigenvalues of the \mathbf{J} -matrix of \mathbf{X}_+ are the 5th roots of unity, thus we have a 5-bifurcation and the resulting birth of a 5-cycle results in a decrease in the ratio of chaotic phase volume. The 5-cycle is unstable and does not persist long leaving again only the gradually decreasing \mathbf{X}_+ .

Just below $E = 20$ the eigenvalues of the \mathbf{J} -matrix of \mathbf{X}_+ are the cubic roots of unity, the resulting unstable 3-cycle is very small and the \mathcal{B}_\square is almost totally chaotic. The 3-cycle bifurcates to an inverted \mathbf{X}_+ which is rapidly increasing in size and by $E = 2$ we have \mathbf{X}_+ along with a 4-cycle and the symmetric 2-cycle giving a ratio for the chaotic phase volume as low as that found at $E = 1000$.

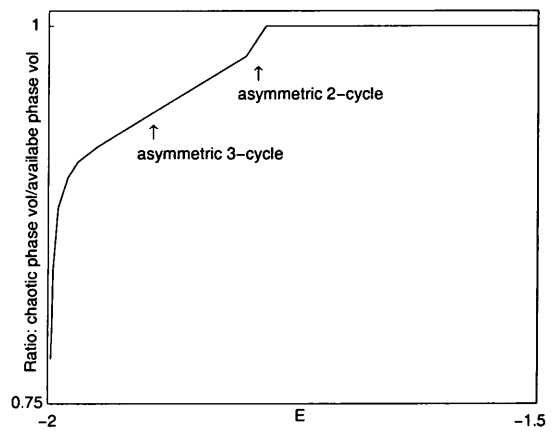
Figure 3.35(b) on the following page confirms the positions and relative sizes of the symmetric 2-, 3-, 4-, 5- and 6-cycles previously found and the presence of complete chaos between their occurrences. Figure 3.35(c) on the next page shows that after the last symmetric cycle has disappeared we have total chaos until the birth of the first asymmetric cycle at about $E = -1.8$, thereafter the chaotic phase volume ratio is decreasing due to the proliferation of cycles as \mathcal{B}_\square tends to integrability in the limit $E \rightarrow -2$.



(a) $E = 1000$ to 2



(b) $E = 2$ to -1



(c) $E = -1.5$ to -2

Figure 3.35: Ratio of chaotic phase space volume

Chapter 4

Spectral analysis for the \mathcal{B}_\square

4.1 Dimensionless form of the Hamiltonian operator

For computational purposes it is more convenient to deal with the dimensionless form of the Hamiltonian operator, which for the \mathcal{B}_\square is given by:

$$\hat{H} = -\frac{\hbar^2}{2m}\nabla^2 - \omega L_z = -\frac{\hbar^2}{2m}\left(\frac{\partial}{\partial x^2} + \frac{\partial}{\partial y^2}\right) + i\hbar\omega\left(x\frac{\partial}{\partial y} - y\frac{\partial}{\partial x}\right) \quad (4.1)$$

We have a characteristic length, say a , the length of the sides of the \mathcal{B}_\square , so $-a \leq x \leq a$ and $-a \leq y \leq a$.

Let $x = x'a$ and $y = y'a$ then $-1 \leq x \leq 1$ and $-1 \leq y \leq 1$.

A convenient characteristic time is \hbar/E_g , where E_g is the ground state energy of the stationary \mathcal{B}_\square (that is, the two dimensional infinite square well).

$$\text{Let } \hat{H} = \hat{H}' E_g \text{ and } \omega = \omega' \frac{E_g}{\hbar}$$

Where x', y', \hat{H}' and ω' are dimensionless quantities. Substitution, a little rearrangement and dropping the primes converts equation 4.1 to:

$$\hat{H} = -\frac{\hbar^2}{2ma^2 E_g}\left(\frac{\partial^2}{\partial x^2} + \frac{\partial^2}{\partial y^2}\right) + i\omega E_g\left(x\frac{\partial}{\partial y} - y\frac{\partial}{\partial x}\right) \quad (4.2)$$

The ground state energy for the two dimensional square well is

$$E_g = \frac{\pi^2 \hbar^2}{4ma^2} = 1 \Rightarrow \frac{\hbar^2}{2ma^2 E_g} = \frac{2}{\pi^2}$$

Substituting into equation 4.2 we obtain

$$\hat{H} = -\frac{2}{\pi^2}\left(\frac{\partial^2}{\partial x^2} + \frac{\partial^2}{\partial y^2}\right) + i\omega\left(x\frac{\partial}{\partial y} - y\frac{\partial}{\partial x}\right). \quad (4.3)$$

4.2 The Hamiltonian matrix

We require a wave function, ψ , such that $\psi = 0$, on $x, y = \pm 1$, so the appropriate normalised basis functions, ϕ , to use are

$$\begin{aligned} \phi(x, y) &= f_m(x) f_n(y) \\ \text{where } f_r(z) &= \text{trig}\left(\frac{r\pi}{2}z\right) \text{ for } r = 1, 2, 3, \dots \\ \text{and } \text{trig} &= \begin{cases} \cos & \text{for } r \text{ odd} \\ \sin & \text{for } r \text{ even.} \end{cases} \end{aligned} \quad (4.4)$$

For the stationary table, $\omega = 0$, we have

$$\begin{aligned} \langle mn | \hat{H}_{ij} | m'n' \rangle &= -\frac{2}{\pi^2} \int_{-1}^1 f_m^*(x) \frac{\partial^2}{\partial x^2} (f_{m'}(x)) dx \int_{-1}^1 f_n^*(y) \frac{\partial^2}{\partial y^2} (f_{n'}(y)) dy \\ &= \left(\frac{1}{2}(m'^2 + n'^2)\right) \int_{-1}^1 f_m^*(x) f_{m'}(x) dx \int_{-1}^1 f_n^*(y) f_{n'}(y) dy \\ &= \frac{1}{2} (m'^2 + n'^2) \delta_{mm'} \delta_{nn'}. \end{aligned} \quad (4.5)$$

For the rotating table, $\omega \neq 0$, we have with $\hat{L}_z = x \frac{\partial}{\partial y} - y \frac{\partial}{\partial x}$

$$\begin{aligned} i\omega \langle mn | \hat{L}_z | m'n' \rangle &= i\omega \left(\int_{-1}^1 x f_m^*(x) f_{m'}(x) dx \int_{-1}^1 f_n^*(y) \frac{\partial}{\partial y} (f_{n'}(y)) dy \right. \\ &\quad \left. - \int_{-1}^1 f_m^*(x) \frac{\partial}{\partial x} (f_{m'}(x)) dx \int_{-1}^1 y f_n^*(y) f_{n'}(y) dy \right) \\ &= i\omega (Q_{mm'} P_{nn'} - P_{mm'} Q_{nn'}) \end{aligned} \quad (4.6)$$

which is non-zero only when both $(m + m')$ and $(n + n')$ are odd, in which case Q_{rs} and P_{rs} are calculated to be:

$$\begin{aligned} Q_{rs} &= \frac{4}{\pi^2} (-1)^{\frac{r+s-1}{2}} \left(\frac{(r+s)^2 - (r-s)^2}{(r+s)^2 (r-s)^2} \right) \\ &= \frac{16}{\pi^2} (-1)^{\frac{r+s-1}{2}} \left(\frac{rs}{(r^2 - s^2)^2} \right). \end{aligned} \quad (4.7)$$

$$\begin{aligned} P_{rs} &= s (-1)^{\frac{r+s-1}{2}} \left(\frac{1}{r+s} + \frac{1}{r-s} \right) \\ &= 2 (-1)^{\frac{r+s-1}{2}} \frac{rs}{r^2 - s^2}. \end{aligned} \quad (4.8)$$

Using the above definitions of P_{rs} and Q_{rs} in equation 4.6 we find the expression for $i\omega \langle mn | \hat{L}_z | m'n' \rangle$ to be:

$$\begin{aligned} & \frac{32i\omega}{\pi^2} \left\{ (-1)^{\frac{m+m'-1}{2}} \frac{mm'}{(m^2 - m'^2)^2} (-1)^{\frac{n+n'-1}{2}} \frac{nn'}{n^2 - n'^2} \right. \\ & \quad \left. - (-1)^{\frac{n+n'-1}{2}} \frac{nn'}{(n^2 - n'^2)^2} (-1)^{\frac{m+m'-1}{2}} \frac{mm'}{m^2 - m'^2} \right\} \quad (4.9) \\ & = -\frac{32i\omega}{\pi^2} (-1)^\beta \frac{mm'n'n'}{(m^2 - m'^2)(n^2 - n'^2)} \left\{ \frac{1}{(m^2 - m'^2)} - \frac{1}{(n^2 - n'^2)} \right\} \end{aligned}$$

where $\beta = \frac{m + m' + n + n'}{2}$.

With the mappings $i \rightarrow m, n$ and $j \rightarrow m', n'$ We obtained the required matrix to be:

$$\begin{aligned} H_{ij} &= \langle j | \hat{H} | i \rangle \\ &= \begin{cases} \frac{1}{2} (m'^2 + n'^2) \delta_{mm'} \delta_{nn'} \\ i\omega \langle mn | \hat{L}_z | m'n' \rangle & \text{for } (m \pm m') \text{ and } (n \pm n') \text{ odd} \\ 0 & \text{otherwise} \end{cases} \quad (4.10) \end{aligned}$$

where $i\omega \langle mn | \hat{L}_z | m'n' \rangle$ is given by equation 4.9.

The eigenvalues we seek are the diagonal elements of the above Hamiltonian matrix, infinite in size, after it has been diagonalised. The eigenvalues so obtained are not in ascending order, since we expect high-lying levels to be the most affected as ω increases the matrix must first be re-ordered to ensure that high-lying levels are not calculated at the expense of low-lying levels.

Another difficulty is determining the required truncation of the infinite matrix to diagonalise; this has to be a compromise between computational cost and how well the eigenvalues of the truncated matrix converge to their true values in the infinite matrix case. We diagonalised matrices, in the range $0 \leq \omega \leq 2000$, for a variety of different sized pairs, N^2 and $(N + 1)^2$ and compared the eigenvalues obtained, rejecting those that had a relative error greater than 10%. We found for $N = 20$ that the eigenvalues obtained for $\omega \leq 1200$ fulfilled this requirement. For $N > 20$ the increase in the value of ω for which the requirement held was relatively little but the increase in computational cost rather high. Consequently, eigenvalues obtained for $N = 200$ and $\omega \leq 1200$ were used in subsequent spectral analysis.

4.3 Unfolding the energy spectrum

In order to make a comparison between the theory of spectral analysis and experimentally or numerically obtained spectra (and different dynamical systems), it is necessary first to “unfold” the spectrum. We do this following the prescription of [80]; from the spectral sequence, $\{e_1, e_2, \dots, e_n\}$, obtained by diagonalising the re-ordered Hamiltonian matrix we plot the staircase function, $N(e)$, which is the number of energy levels less than e . The staircase function, on the average, often lies on a curve, $F(e)$, which gives the average behaviour of the staircase function.

It is crucial that this decomposition of the spectrum into secular variations and fluctuations is carried out with the correct choice of $F(e)$ since all fluctuation measures depend very sensitively on this choice. Several ways of fitting such a curve to the staircase function are described in [76]. We are guided in our search for a suitable $F(e)$ by the semiclassical Weyl rule, [77, 78], for a stationary billiard, \mathcal{D} :

$$F(e) = \frac{A}{4\pi} \frac{2me}{\hbar^2} \pm \frac{L}{4\pi} \sqrt{\frac{2me}{\hbar^2}} + K \quad (4.11)$$

where the upper sign applies to the Neumann boundary condition and the lower sign to the Dirichlet boundary condition. A and L are the area and the length of the perimeter respectively, K is a number that carries information about the topological nature of \mathcal{D} and the curvature of its boundary. The second and third term depend on the boundary conditions, as well as on the shape.

We assume that the rotation causes a deviation from this but, nevertheless, $F(e)$ is a polynomial in e , so numerous polynomial fits were tried. Figure 4.1 on the next page is a plot of the staircase function and the closest three fits. Calculating the residuals for the three curves showed that the best fit was obtained from:

$$F(e) = a + be + c\sqrt{e} + de^2 \quad (4.12)$$

where the constants, (a, b, c, d) , are dependent upon ω . Since we have a square root term in the expression we must carry out a translation on the original spectral sequence to ensure every term is non-negative.

Having ascertained $F(e)$ we then map the original spectral sequence, that is, $\{e_1, e_2, \dots, e_n\}$, onto a new spectral sequence, $\{x_1, x_2, \dots, x_n\}$, by means of the mapping $x_i = a_1^{-1} [F(e_i) - a_0]$, where a_0 and a_1 are constants. The staircase function, $N(x)$, for this new sequence will have an average behaviour, $F'(x)$, which is simply a straight line. Therefore, this new sequence will have a constant average level spacing density, D , (the inverse slope of $F'(x)$) and by an appropriate choice of the constant terms the unfolding can be done so that average spacing, $D = 1$.

It is assumed that this “unfolding” procedure does not change the character of the fluctuations about the average but simply straightens out the average.

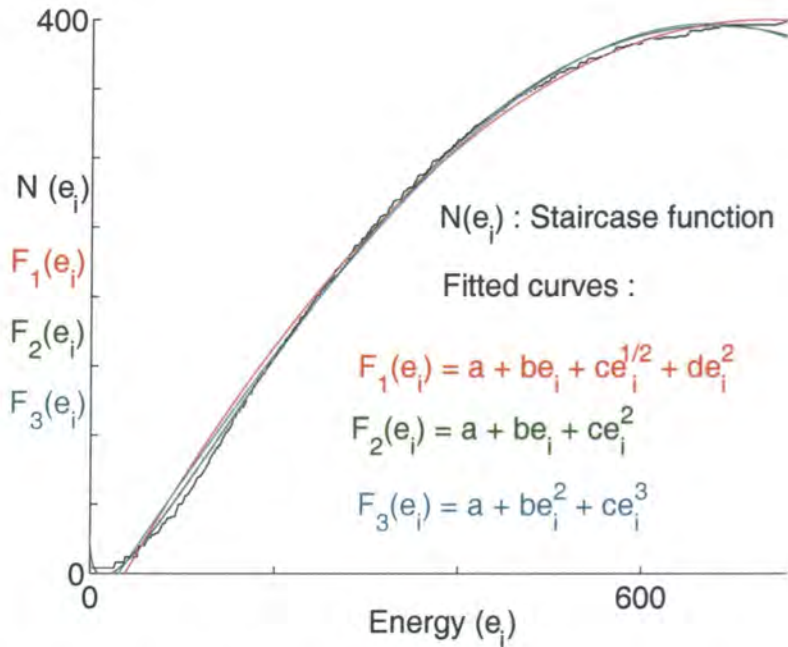


Figure 4.1: Plot of the staircase function, $N(e_i)$, and some fitted curves

Figure 4.2 on the following page is plot of the lower eigenvalues against the parameter ω in the range $0 \leq \omega < 10$. It demonstrates how quickly the degeneracies of the even parity states observed at $\omega = 0$, due to the symmetry of the stationary \mathcal{B}_\square , disappear as soon as rotation commences, i.e. $\omega \neq 0$. We did not encounter any accidental degeneracies (or diabolical points as termed by Berry, [79]), in this range of values. These are degeneracies not due the symmetries of the dynamical system under investigation but rather different values of parameters accidentally combining to give the same result.

For small ω and high energy there appear to be a number of apparent crossings in figure 4.2 on the next page but figure 4.3(a) on the following page shows that they are in fact avoided crossings with exceedingly narrow separations of the order of $e^{-c/\hbar}$, with c a constant. This is in keeping with Berry’s prediction, [94], from consideration of tunnelling between neighbouring tori. Thus this region of the spectrum appears to be regular.

For high ω and low energy the pattern of the spectrum in figure 4.2 on the next page has changed considerably; there are no apparent level crossings and the presence of avoided crossings is clearly shown by the colour coding and confirmed by figure 4.3(b) on the following page. This is the transition from the regular spectrum where there is a large probability of near degeneracies, that is, the probability

distribution $P(S) \rightarrow \text{constant}$ as $S \rightarrow 0$ (S is the spacing between adjacent levels) to a chaotic spectrum where there is level repulsion and hence little probability of degeneracies; $P(S) \rightarrow 0$ as $S \rightarrow 0$ [82]. Another interesting feature displayed by figure 4.3(b) is the exchange of slopes, $dx_i/d\omega$, between adjacent levels at avoided crossings; this is a manifestation of strong mixing between states and wavefunctions exchanging quantum numbers near each avoided crossing.

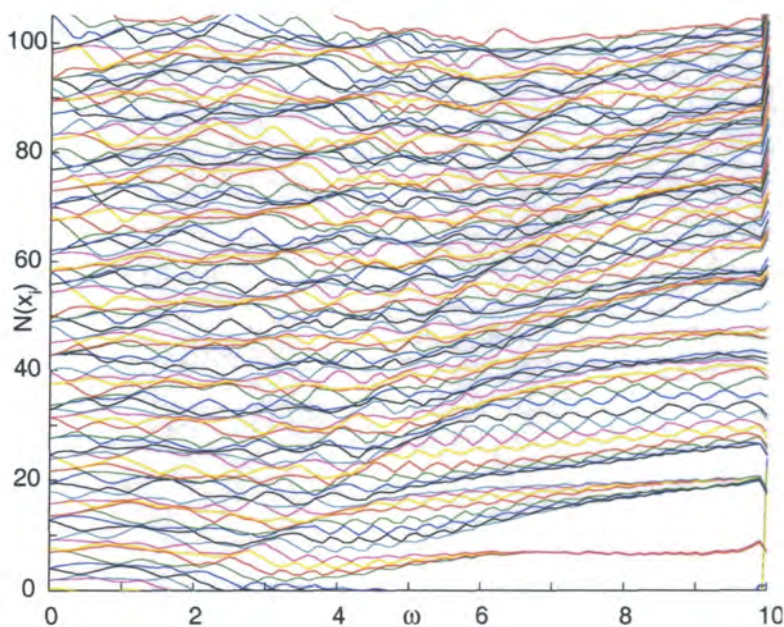
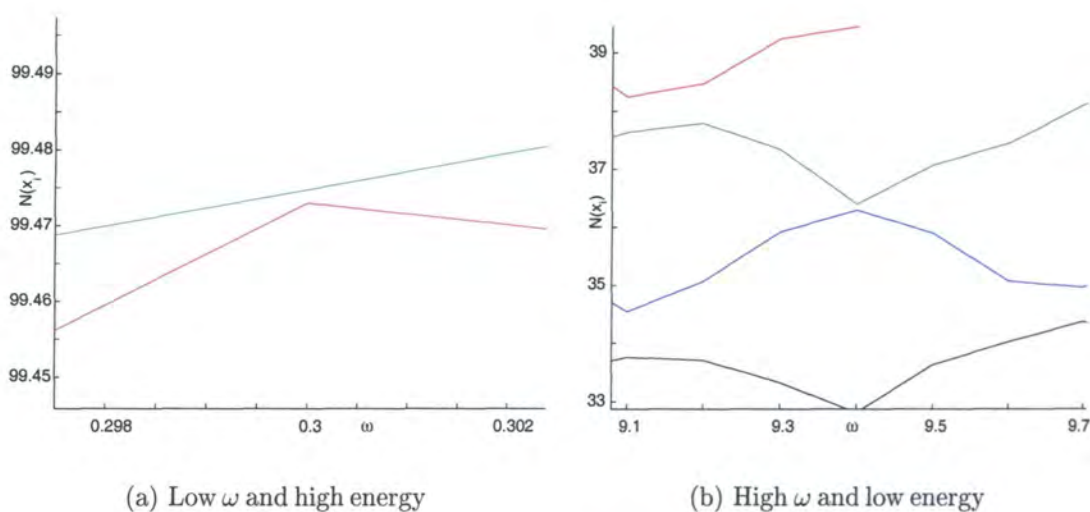


Figure 4.2: The unfolded energy spectrum, $N(x_i)$, versus ω



(a) Low ω and high energy

(b) High ω and low energy

Figure 4.3: Magnification of portions of figure 4.2

4.4 Theoretical level spacing distribution functions

4.4.1 The Bohigas, Giannoni and Schmit (BGS) conjecture

Taking into consideration the statistical properties of nuclear and atomic spectra [81] and results for two-dimensional quantum billiards [51, 82, 83] Bohigas, Giannoni and Schmit, [84], made the following conjecture:

- (1) For classically integrable systems with more than one degree of freedom, the nearest neighbour spacing distribution, (NNSD), $P(S)$ of the quantum energy levels should be Poisson-like and the spacings should not be correlated.
- (2) For classically chaotic systems with more than one degree of freedom the NNSD, $P(S)$ of the quantum energy levels should be Wigner-like.

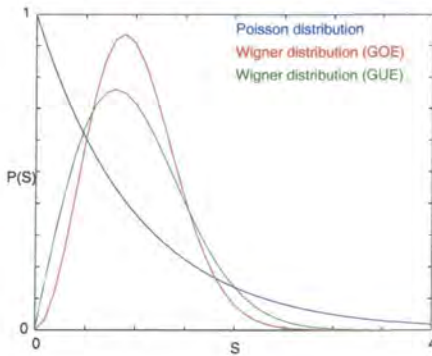


Figure 4.4: Distributions

In the latter case one has to distinguish between real symmetric [Gaussian orthogonal ensemble (GOE)] and complex Hermitian random matrices [Gaussian unitary ensemble (GUE)] [85].

The plots of these distributions are shown in figure 4.4, the relevant spacings are given by:

$$P(S) = \begin{cases} e^{-S} & \text{(Poisson)} \\ \frac{\pi}{2} S e^{-\left(\frac{\pi}{4}\right) S^2} & \text{(GOE)} \\ \frac{32}{\pi^2} S^2 e^{-\left(\frac{4}{\pi}\right) S^2} & \text{(GUE)} \end{cases} \quad (4.13)$$

GOE (GUE) fluctuations apply if the system is (not) time-reversal invariant.

This conjecture on the relation between the quantal energy level statistics and the regularity or chaos of the corresponding classical dynamics has been confirmed in a number of studies of low-dimensional systems, [30, 84, 86–90]. There are also semiclassical arguments [68, 82, 92] that support this conjecture.

However, this universality of the energy level statistics is broken in some dynamical systems, [91, 93], these are typically harmonic oscillator related systems. Nevertheless, it is generally accepted that the BGS conjecture expresses a generic property of quantal systems, in the sense of the definition of the word *generic* given by Berry, [94]: there may be exceptions, but they form a set of zero measure.



4.4.2 Mixed systems

Generally, in classical dynamical systems regularity and chaos co-exist with transition from the former to the latter governed by some parameter of the system. The Poisson and the Wigner distributions are the respective limiting cases and there exist many theoretical distribution functions to account for this transition. We consider only three of them:

(1) Brody distribution.

[95] extend Wigner's surmise for the NNSD in the GOE case (equation 4.13 on the page before) by means of the ansatz

$$P^B(S) = AS^\beta e^{-\alpha S^u}, \quad (4.14)$$

where A, α and u depend on β , the parameter which should measure the repulsion. For $\beta = 1$ we have again the Wigner surmise, and it is desirable that $\beta = 0$ should mean no repulsion at all, i.e. the Poisson distribution: hence we have that $u = 2$ and $u = 1$ for these two cases. The simplest supposition is then to take u linear in β so that $u = \beta + 1$. Since the mean of S is, by construction, 1 and $P^B(S)$ is normalized, [95] find that $A = (\beta + 1)\alpha$ so

$$P^B(S) = \alpha(\beta + 1) S^\beta e^{\{-\alpha S^{(\beta+1)}\}} \quad \text{with} \quad (4.15)$$

$$\alpha = \left[\Gamma\left(\frac{\beta + 2}{\beta + 1}\right) \right]^{(\beta+1)} \quad \text{where } \Gamma \text{ is the Gamma function.} \quad (4.16)$$

This distribution is only phenomenological and does not have a theoretical basis as a measure of underlying chaos in the system. However, there are strong indications supporting the idea that the parameter β reflects the degree of the level repulsion within a spectral sequence. Since it is an empirical parameter, it can be allowed to take on all the values $-1 < \beta \leq 1$, the negative values being appropriate if for small spacings the calculated distribution is steeper than the Poisson curve. Figure 4.5(a) on page 107 shows the interpolation between the Poisson and Wigner curves, being identical to the former and latter for $\beta = 0$ and $\beta = 1$ respectively.

(2) Berry-Robnik distribution [92].

For a bound quantum system with f freedoms, the number of energy levels in any narrow interval E to $E + \Delta E$ diverges as $\Delta E/\hbar^f$ in the semiclassical limit $\hbar \rightarrow 0$. It is then possible to regard $P(S)$ as one way of characterising the semiclassical spectrum at energy E . As to how $P(S)$ is related to the classical motion on the energy surface E has been studied for three special cases where in each $P(S)$ takes universal functional forms parametrised by the mean level density ρ which for a system with Hamiltonian $H(q_1 \dots q_f, p_1 \dots p_f)$ is given by

$$\rho = \frac{1}{(2\pi\hbar)^f} \int dq_1 \dots \int dq_f \int dp_1 \dots dp_f \delta(E - H(q_1 \dots p_f)). \quad (4.17)$$

- (a) The first special case is that of one dimensional systems where the phase plane contours are simple closed curves. The levels form, locally, a perfectly regular sequence and

$$P(S) = \delta(S - \rho^{-1}). \quad (4.18)$$

- (b) The second special case is that of multidimensional integrable systems, where trajectories wind smoothly round f -dimensional tori in the $2f$ -dimensional phase space. [82] have shown that levels are uncorrelated and so form a Poisson process whose level spacing distribution is

$$P(S) = \rho e^{-\rho S}. \quad (4.19)$$

- (c) The third special case is that of chaotic motion, where systems are ergodic and almost all orbits densely and unpredictably explore the $(2f - 1)$ -dimensional energy surface. For such systems, [84], $P(S)$ is closely approximated by the Wigner distribution

$$P(S) = \frac{\pi}{2} \rho^2 S e^{-\pi \rho^2 S^2/4}. \quad (4.20)$$

Generic cases do not conform to these three special cases: their phase space is mixed, in the sense that some orbits with energy E wind regularly round f -dimensional tori and others explore $(2f - 1)$ -dimensional regions chaotically. Underlying the basis of this distribution is the idea that each connected regular and irregular classical phase space region in ΔE gives rise to its own sequence of regular and irregular levels. For the i th such region, the level density ρ_i is proportional to the Liouville measure of the region and is given by an expression of the form of equation 4.17 and the level spacing distribution $P_i(S)$ is given by

equations 4.18 and 4.19 on the preceding page for regular and irregular regions respectively. In the semiclassical limit all these sequences are independent and the complete spectrum is obtained by their random superposition.

Consider N sequences of levels with mean densities ρ_i and spacing distributions $P_i(S)$, so that

$$\bar{S}_i = \int_0^\infty dS S P_i(S) = \rho_i^{-1}, \quad \text{where} \quad \int_0^\infty dS P_i(S) = 1. \quad (4.21)$$

The sequences are statistically independent, and we seek the spacing distribution $P(S)$ of the combined sequence obtained by superposing them. This combined sequence has mean level density

$$\rho = \sum_{i=1}^N \rho_i, \quad (4.22)$$

given in terms of the Hamiltonian by equation 4.17 on the page before.

$P(S)$ is calculated in terms of the probability that there is no level in the interval E to $E+S$, given that there is a level at E . This probability is $\int_S^\infty P(x) dx$ and is given as the sum of N independent contributions, the i th of which corresponds to E being a level of the i th sequence. Thus

$$\int_S^\infty dx P(x) = \sum_{i=1}^N \left(\frac{\rho_i}{\rho} \int_S^\infty dy P_i(y) \prod_{\substack{j=1 \\ j \neq i}}^N Q_j(S) \right) \quad (4.23)$$

where in each term the factor ρ_i/ρ is the probability that E belongs to the i th sequence, $\int_S^\infty P_i(y) dy$ is the probability that no further level of this sequence lies in the interval, and $Q_j(S)$ is the probability that no level of the j th sequence lies in the interval.

To find $Q_j(S)$, note that in

$$\{d\sigma P_j(\sigma) \sigma \rho_j\} \left\{ \left(1 - \frac{S}{\sigma}\right) \theta(\sigma - S) \right\} \quad (4.24)$$

the first factor is the probability that E , which is uncorrelated with the j th sequence, lies in a gap of length σ to $\sigma + d\sigma$ of that sequence; and the second factor is the probability of having no level of this sequence in an interval of length S inside this gap (θ denotes the unit step function). Integration over σ then gives $Q_j(S)$ as

$$Q_j(S) = \rho_j \int_S^\infty d\sigma P_j(\sigma) (\sigma - S). \quad (4.25)$$

Thus equation 4.23 on the preceding page becomes

$$\int_S^\infty dx P(x) = \frac{1}{\rho} \left(\prod_{k=1}^N \rho_k \right) \sum_{i=1}^N \left(\int_S^\infty dy P_i(y) \prod_{\substack{j=1 \\ j \neq i}}^N \int_S^\infty d\sigma P_j(\sigma) (\sigma - S) \right), \quad (4.26)$$

which takes a much simpler form by defining

$$Z_i(S) \equiv \int_S^\infty d\sigma \int_\sigma^\infty dx P(x) = \frac{1}{\rho} \prod_{i=1}^N \rho_i Z_i(S) \quad (4.27)$$

and integrating equation 4.26 over S , to give a factorized expression which embodies the statistical independence of the N sequences;

$$Z(S) \equiv \int_S^\infty d\sigma \int_\sigma^\infty dx P(x) = \frac{1}{\rho} \prod_{i=1}^N \rho_i Z_i(S). \quad (4.28)$$

In terms of this the level spacing distribution of the full spectrum is

$$P(S) = \frac{d^2 Z(S)}{dS^2}. \quad (4.29)$$

Physically it is obvious that the superposition of all the Poisson type level sequences corresponding to regular motion will produce a sequence which is itself a Poisson process, $P(S)$ being of the form of equation 4.20 on page 103 with ρ given by the sum of the level densities of the separate regular regions. This result follows from equation 4.28 because the factors $\rho_i Z_i$ corresponding to regular regions have, from equations 4.27 and 4.20 on page 103, the form $\rho_i Z_i = \exp(-\rho_i S)$. Denoting by ρ_1 the level density of all the regular sequences taken together, then the corresponding contribution to equation 4.28 is

$$Z_1(S) = \frac{e^{-\rho_1 S}}{\rho_1}. \quad (4.30)$$

The remaining phase space regions $i = 2, \dots, N$ are chaotic, and equations 4.27 and 4.21 on the preceding page give

$$Z_i(S) = \frac{1}{\rho_i} \operatorname{erfc} \left(\frac{\sqrt{\pi}}{2} \rho_i S \right) \quad (i \geq 2) \quad (4.31)$$

where

$$\operatorname{erfc} x \equiv \frac{2}{\sqrt{\pi}} \int_x^\infty dt e^{-t^2}. \quad (4.32)$$

The level spacing distribution is now obtained from equations 4.28 on the page before and 4.29 on the preceding page as

$$P(S) = \frac{1}{\rho} \frac{d^2}{dS^2} \left[e^{-\rho_1 S} \prod_{i=2}^N \operatorname{erfc} \left(\frac{\sqrt{\pi}}{2} \rho_i S \right) \right]. \quad (4.33)$$

The most important case of the above equation is when $N = 2$; normalising the energy scale to ensure that the mean density ρ , and thus the mean level spacing, are unity then ρ_1 is simply the fraction of the energy surface for which motion is regular. Defining $q = 1 - \rho_1$ as the fraction of the energy surface for which motion is chaotic, then $Z(S) = \exp(- (1 - q) S) \operatorname{erfc}(\sqrt{\pi} q S / 2)$ and 4.33 give the Berry-Robnik distribution:

$$P^{BR}(S) = e^{(q-1)S} \left[(1 - q)^2 \operatorname{erfc} \left(\frac{\pi}{2} q S \right) + \left(2q(1 - q) + \frac{\pi}{2} q^3 S \right) e^{-\frac{\pi}{4} q^2 S^2} \right]. \quad (4.34)$$

This distribution is quite different from the previous one, particularly, with respect to the vanishing of the probability of very small spacings in the Brody distribution for all values of β compared to $P^{BR}(0) = 1 - q^2$ in the Berry-Robnik distribution. Also the parameter q has a well defined physical meaning: quantitatively it is the fraction of phase space which is filled with chaotic trajectories. However, this distribution is exactly applicable only in the semiclassical limit and so will give erroneous results for the lowest-lying levels. Figure 4.5(b) on the following page shows the interpolation between the Poisson and Wigner curves, being identical to the former and latter for $q = 0$ and $q = 1$ respectively.

(3) Lopac-Brant-Paar distribution [96].

The LBP distribution is a generalisation of both the above distributions, having both the parameters, β, q :

$$P(S) = e^{-(1-q)S} (1 - q^2) Q \left[\frac{1}{(\beta + 1)}, \alpha q^{(\beta+1)} S^{(\beta+1)} \right] \quad (4.35)$$

$$+ e^{-(1-q)S} q \left[2(1 - q) + \alpha (\beta + 1) q^{(\beta+1)} S^\beta \right] e^{-\alpha q^{(\beta+1)} S^{(\beta+1)}}$$

Where α is defined by equation 4.16 on page 102 and Q denotes the incomplete Gamma function:

$$Q(a, x) = \frac{1}{\Gamma(a)} \int_x^\infty e^{-t} t^{(a-1)} dt. \quad (4.36)$$

The parameter β and q describe the transitions from the semiclassical to the quantal regime and integrability to chaos respectively [97], so that q retains its meaning as the chaotic fraction of phase space but is now applicable also to cases far from the semiclassical limit. The parameter β describes the degree of level repulsion in the given spectral sequence and is essentially connected with the localization of the underlying chaotic states [64].

Figure 4.6 on the following page is a graphical representation of the LBP distribution in its dependence on β and q ; table 4.1 shows its relationship with the other distributions.

β	q	Identical to
-	1	Brody distribution
1	-	Berry-Robnik distribution
All	0	Poisson distribution
1	1	Wigner (GOE) distribution

Table 4.1: Relationship between the LBP distribution and other distributions.

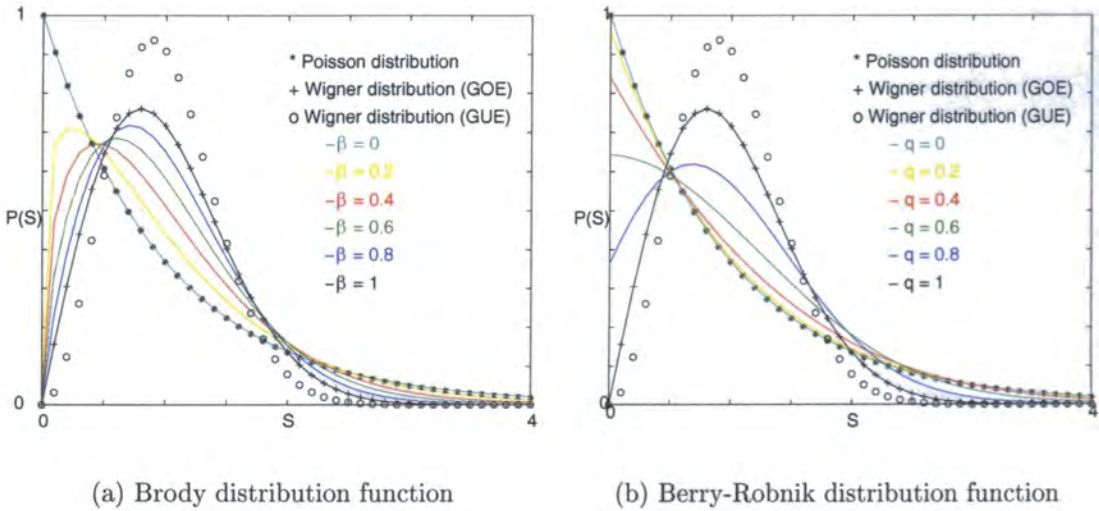


Figure 4.5: Brody and Berry-Robnik distribution functions interpolating between the Poisson and Wigner distributions

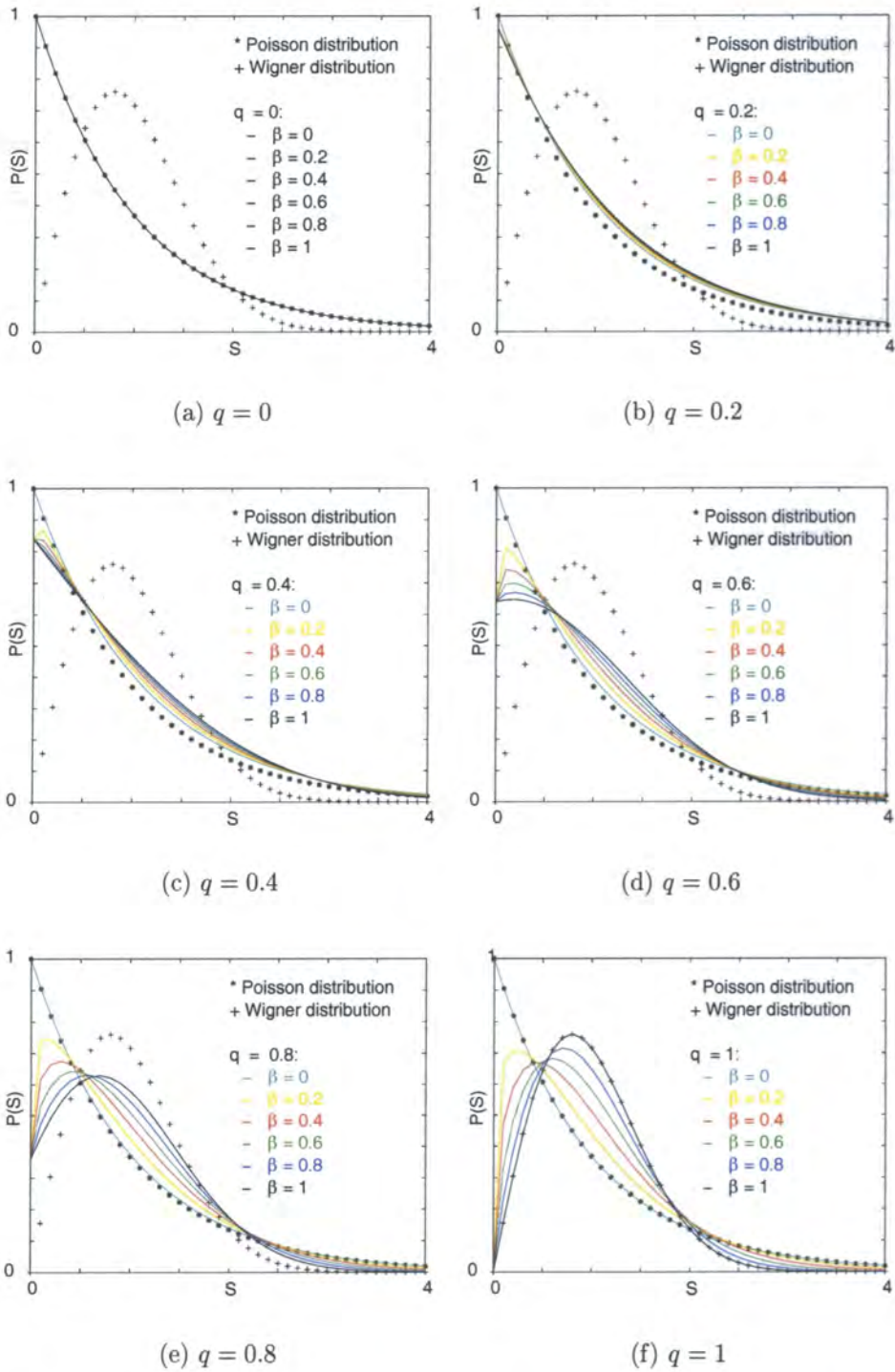


Figure 4.6: Lopac-Brant-Paar distribution function for various values of the parameters q and β

4.5 Level spacing distributions for the \mathcal{B}_\square

4.5.1 Nearest Neighbour Spacing Distribution (NNSD)

The NNSD is the probability that two neighbouring eigenvalues are a distance S apart and the unfolded spectrum is utilised to give the spacings:

$$S_i \equiv N(e_{i+1}) - N(e_i) \quad (4.37)$$

and then histogrammed (scaled to unity) to produce $P(S)$ to compare with the theoretical level spacing distributions of the previous section. An important property a spectrum must possess for comparisons to be meaningful is the stationarity of $P(S)$, that is, translation invariance. To check this we divided each spectrum produced from different values of ω into 4 equal subintervals and performed the statistics on each to ensure the same distribution ensued.

The bin size in the histogramming is important as we require a large bin to have enough eigenvalues to do statistics on but sufficiently small in order to get good resolution. We found unity (before scaling) fulfilled both requirements.

From the classical treatment of the \mathcal{B}_\square in Chapter 3 on page 46 we expect that as ω is increased from 0 the NNSD is accompanied by a transition from the Poisson to the Wigner (GOE) statistics and back to Poisson. Figure 4.7 on the next page shows the histograms and the fitted theoretical distributions for the cases $\omega = 100, 300, 500, 700, 900$ and 1100 and illustrates the applicability of the intermediate distributions for quantifying these transitions. Table 4.2 gives the fitted values of the parameters β, q for each distribution.

ω	Brody: β	Berry-Robnik: q	LPB: q	LPB: β	Classical E
100	0.05	0.23	0.2531	0.165	> 1000
300	0.275	0.5894	0.6874	0.5164	746
500	0.8081	0.9394	0.8918	0.9285	45.662
700	0.6807	0.8894	0.8882	0.8884	7.926
900	0.4807	0.7649	0.7816	0.8084	2.636
1100	0.3371	0.8171	0.9029	0.8793	1.056

Table 4.2: Fitted parameters β, q for figure 4.7

Apart from applicability to the complete spectrum a crucial criterion is the agreement at small spacings $S \approx 0$. Examination of figure 4.7 on the next page clearly shows that the LPB distribution is superior, consequently its value of q (recalling that it is the fraction of chaotic phase space) is used in ascertaining the classical value E , with the aid of figure 3.35(a) on page 94, given in table 4.2.

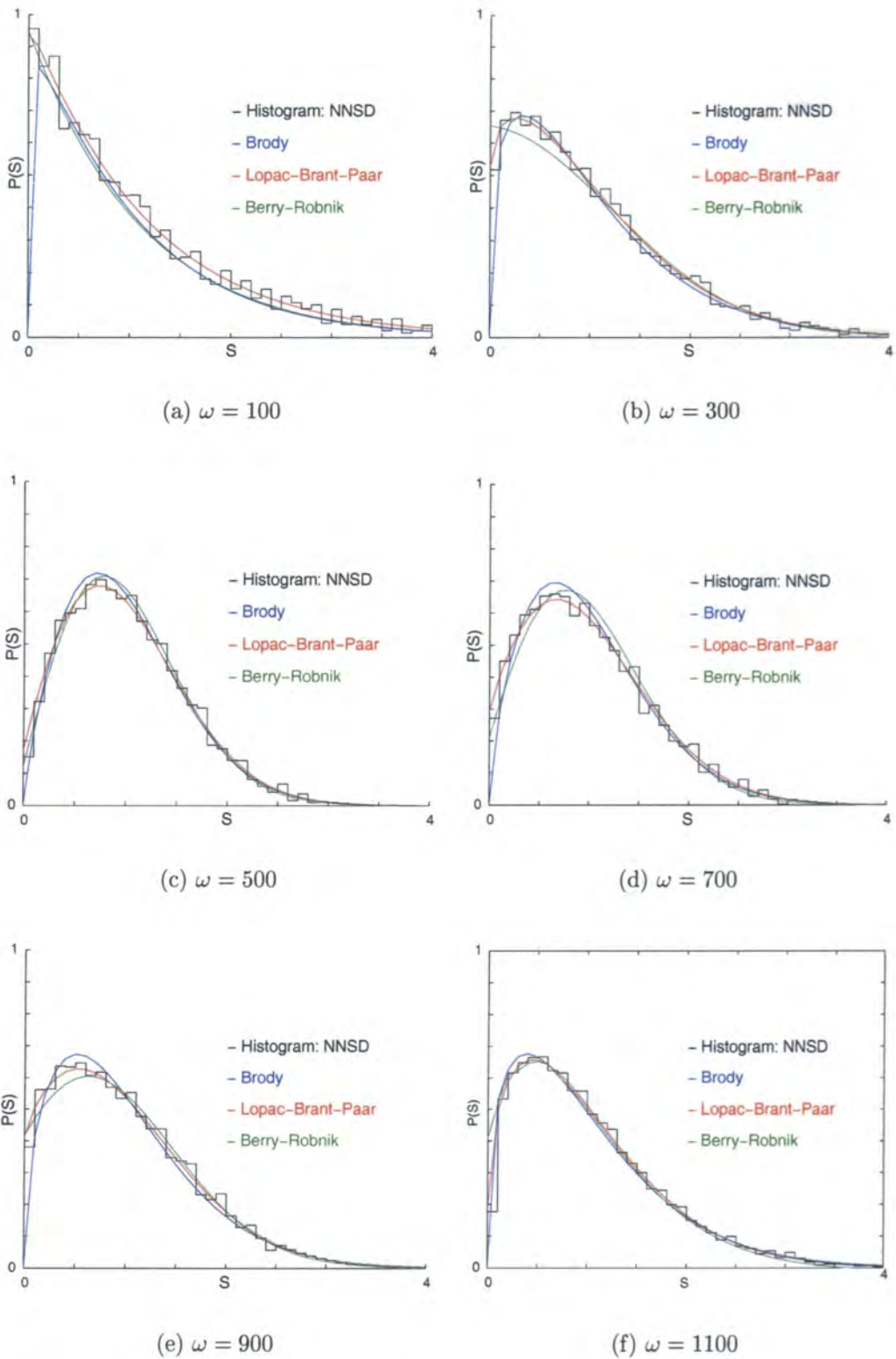
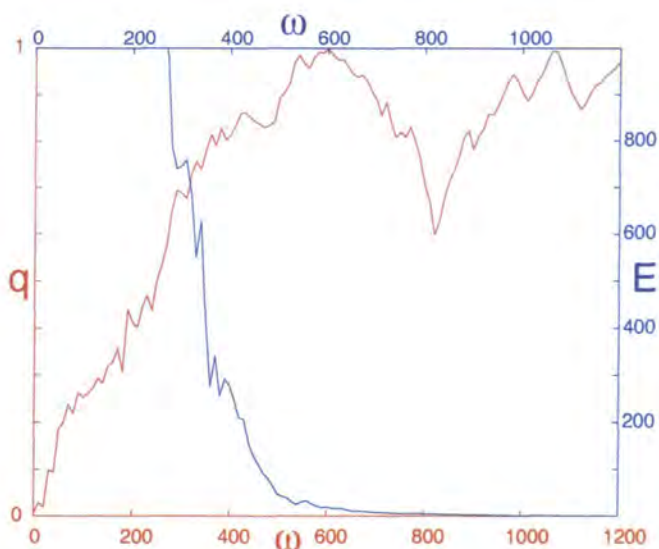
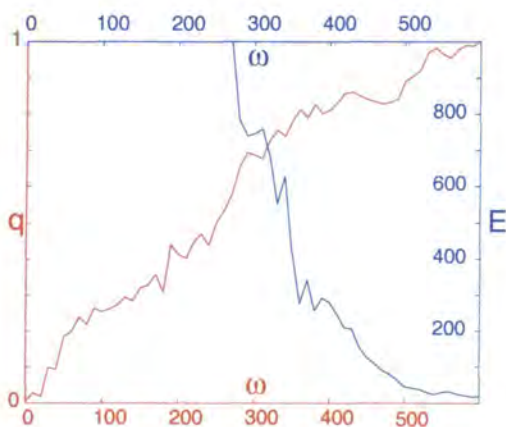


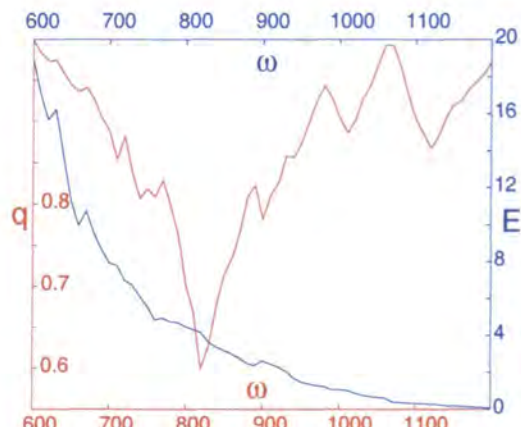
Figure 4.7: Histograms and the three fitted theoretical distributions for $\omega = 100, 300, 500, 700, 900, 1100$.



(a) $\omega = 0$ to 1200



(b) $\omega = 0$ to 600



(c) $\omega = 601$ to 1200

Figure 4.8: Variation of the LBP parameter q and classical E with ω

The parameter q is important as it allows contact between the quantal and classical dynamics in the \mathcal{B}_\square . Even just considering the six values of ω we see in the quantal analysis a reflection of the disappearance of the periodic cycles associated with the stationary \mathcal{B}_\square , cycles with type I trajectories, as E decreases through $E = 1000$ to the extent when only X_+ remains. Table 4.3 on the following page and figure 4.8 show the variation of the Lopac-Brant-Paar parameter q with ω with steps of 20 and 10 respectively.

As can be seen the values obtained for q reflect quite well the chaotic phase volume values obtained in Chapter 3 on page 46; for $\omega = 0 (E = \infty)$ we have $q = 0$

and as ω increases (E decreases) q slowly approaches 1 and then begins to decrease. This reflects the breaking up of the invariant tori associated with the stationary \mathcal{B}_\square , the appearance and the subsequent destruction of the periodic cycles with type I trajectories (except X_+). Finally we see the demise of X_+ and the birth and death of type II cycles discussed in Subsection 3.6.2 on page 72

Unfortunately, we do not see the birth and proliferation of the type III cycles of Subsection 3.6.3 on page 76 and the associated tendency towards integrability in the limit $E = -2$. The reason for this is that the eigenvalues produced by the high required value of ω are not accurate enough to justify statistics being performed upon them.

ω	q	E	ω	q	E	ω	q	E
20	0.02	> 1000	580	1.0	21	1140	0.91	0.22
40	0.09	> 1000	600	1.0	19	1160	0.93	0.17
60	0.19	> 1000	620	0.97	162	1180	0.95	0.12
80	0.22	> 1000	640	0.96	14	1200	0.97	0.06
100	0.25	> 1000	660	0.94	10			
120	0.27	> 1000	680	0.98	9.6			
140	0.28	> 1000	700	0.89	7.9			
160	0.33	> 1000	720	0.88	7			
180	0.31	> 1000	740	0.81	6.1			
200	0.41	> 1000	760	0.81	4.8			
220	0.45	> 1000	780	0.80	4.7			
240	0.44	> 1000	800	0.7	4.47			
260	0.53	> 1000	820	0.6	4.1			
280	0.65	786	840	0.68	3.37			
300	0.69	746	860	0.73	3			
320	0.73	683	880	0.81	2.49			
340	0.74	628	900	0.78	2.63			
360	0.81	276	920	0.82	2.3			
380	0.83	256	940	0.86	1.71			
400	0.81	278	960	0.9	1.38			
420	0.86	209	980	0.94	1.24			
440	0.85	153	1000	0.9	1			
460	0.83	110	1020	0.9	0.88			
480	0.83	81	1040	0.94	0.69			
500	0.89	46	1060	1	0.62			
520	0.92	38	1080	0.97	0.37			
540	0.98	24	1100	0.9	0.32			
560	0.96	32	1120	0.87	0.29			

Table 4.3: Fitted parameters q, E for figure 4.8

Recalling that the classical energy parameter E is in fact given by $E = \frac{\mathcal{E}}{\omega^2}$, it is constructive to compare the values of the ratio of chaotic phase volume obtained from the classical treatment with respect to E and the values of q obtained from the quantal treatment with respect to $\frac{1}{\omega^2}$ (figure 4.9). This is also another method of establishing the link between the classical energy parameter E and the quantal parameter ω . Figure 4.9 shows remarkable similarities between the plots in fig-

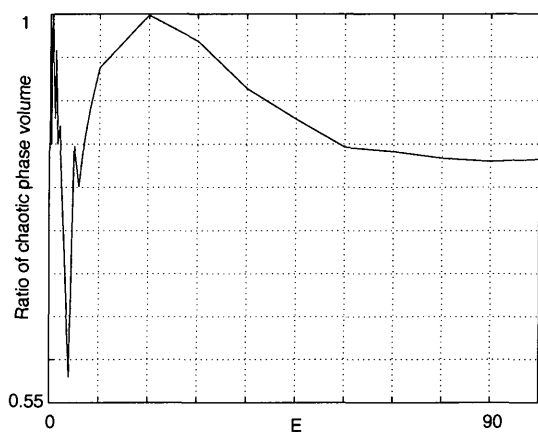
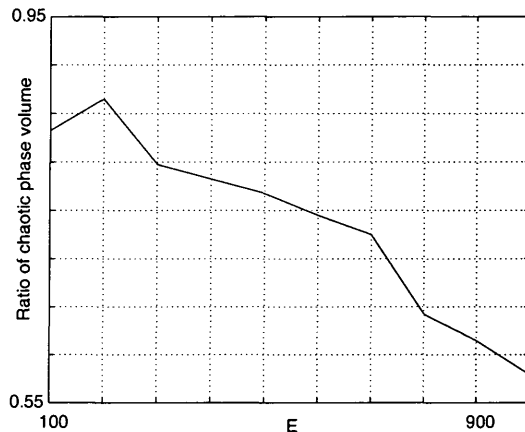
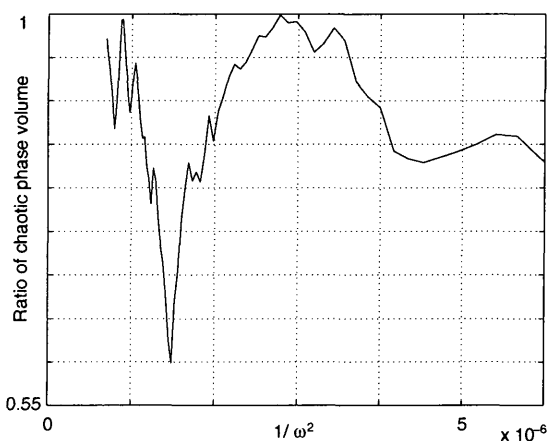
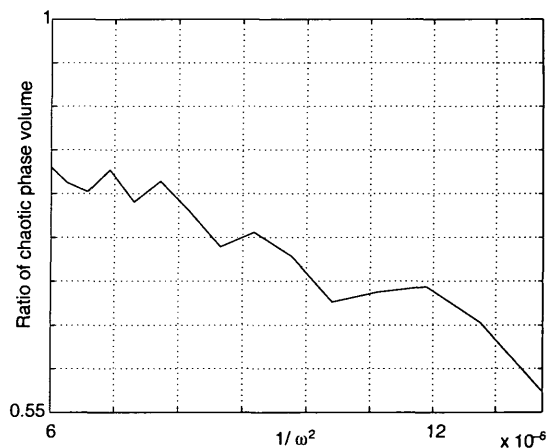

 (a) $E = 0$ to 100

 (b) $E = 100$ to 1000

 (c) $1/\omega^2 = 0$ to 6×10^{-6}

 (d) $1/\omega^2 = 6 \times 10^{-6}$ to 14×10^{-6}

Figure 4.9: Comparison of chaotic phase volumes obtained classically and quantum mechanically.

ures 4.9(a) and 4.9(c) and figures 4.9(b) and 4.9(d). The fact that these are not identical is unsurprising since the values of the chaotic phase volume are determined by two entirely different methods, each with its own inherent errors. Reading off the values of E and $\frac{1}{\omega^2}$ for the same value of the chaotic phase volume gives a direct

correspondence between the classical energy parameter E and the quantal rotation parameter ω . Some such values are given in table 4.4 and figure 4.10 continues the comparison of the chaotic phase volumes.

E	1	4.5	20	100	300	700	800	10^3	10^4	5×10^4	10^5
ω	1008	816	603	447	371	318	280	267	200	81	63

Table 4.4: Correspondence for some values of E and ω

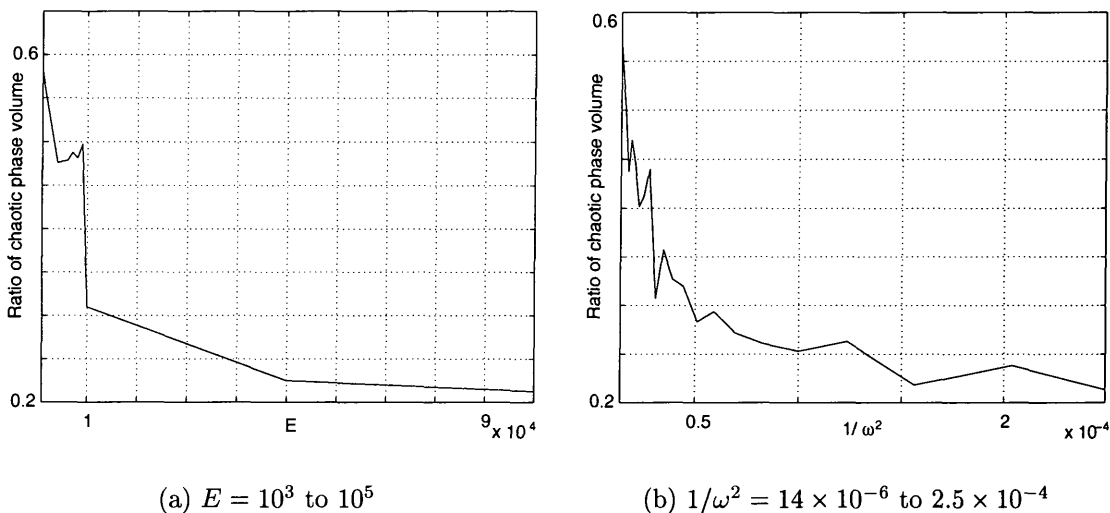


Figure 4.10: Further comparison of chaotic phase volumes obtained classically and quantum mechanically.

4.5.2 Integral Transition Distributions (ITD)

The integral transition distribution (or cumulative level-spacing distribution) [97], $W(S)$, gives the total number of energy levels (obtained from the unfolded spectra) below the level spacing S (scaled to unity). It has the advantage that it does not suffer from arbitrariness of binning as is the case for the probability distribution, $P(S)$. The two distributions are related by

$$W(S) = \int_0^S P(\sigma) d\sigma. \quad (4.38)$$

The limiting and transitional probability distributions now read as:

1. Integral Poisson distribution

$$W(S) = 1 - e^{-S}. \quad (4.39)$$

2. Integral Wigner (GOE) distribution

$$W(S) = 1 - e^{-\frac{\pi}{4}S^2}. \quad (4.40)$$

3. Integral Brody distribution

$$W(S) = 1 - e^{-\alpha S^{(\beta+1)}}. \quad (4.41)$$

4. Integral Berry-Robnik distribution

$$W(S) = 1 - e^{(q-1)S} \left\{ qe^{-\frac{\pi}{4}q^2S^2} + (1-q)\sqrt{\pi}\operatorname{erfc}\left(\frac{\sqrt{\pi}}{2}qS\right) \right\} \quad (4.42)$$

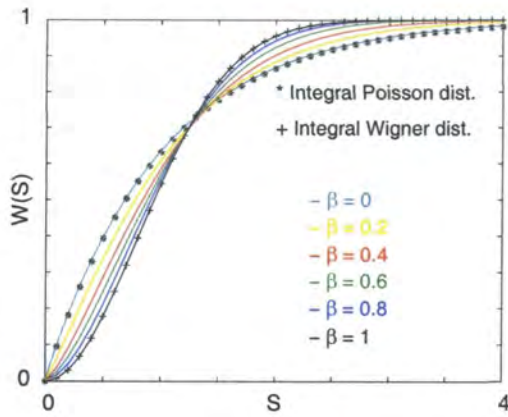
5. Integral Lopac-Brant-Paar distribution [96]

$$W(S) = 1 - e^{(q-1)S} \left\{ qe^{-\alpha q^{(\beta+1)}S^{(\beta+1)}} - (1-q)Q\left[\frac{1}{\beta+1}, \alpha q^{(\beta+1)}S^{(\beta+1)}\right] \right\}. \quad (4.43)$$

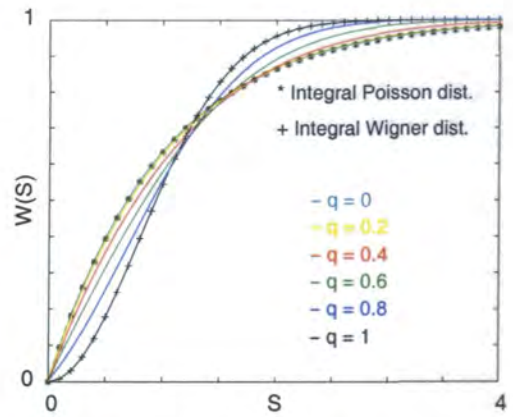
The same relationships hold between the integral transition distributions and the integral limiting cases as in the case of the probability distributions. Also, the three transitional distributions are again connected by table 4.1 on page 107.

Figure 4.11 on the following page shows the interpolation of the ITD between the limiting integral distributions for various values of the parameters q and β , in the case of the LBP distribution only the cases $q = 0, 1$ are shown.

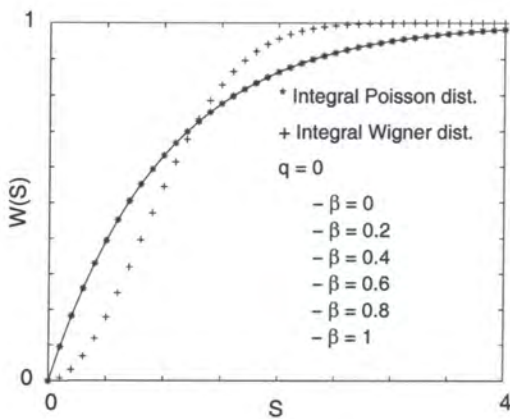
Again, we found that the LBP distribution gave a superior fitting to the \mathcal{B}_\square spectra, so, for the sake of clarity it is the only one shown in figure 4.12 on page 117. For $\omega = 100, 300, 500, 700, 900, 1100$ it confirms the results of the NNSD with regards to the transition from the Poisson to the Wigner and back towards the Poisson distribution with increasing values of ω .



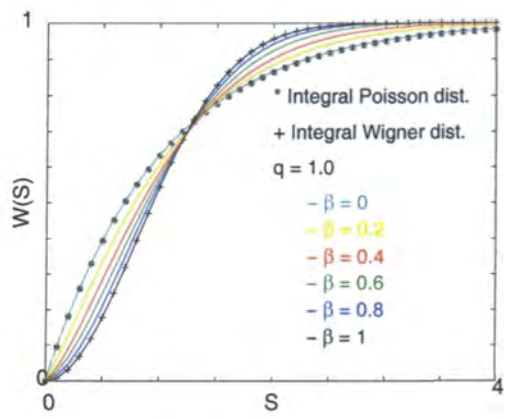
(a) Integral Brody Distribution.



(b) Integral Berry-Robnik Distribution.



(c) Integral LBP Distribution: $q=0$.



(d) Integral LBP Distribution: $q=1$.

Figure 4.11: Theoretical Integral Distributions interpolating between the Integral Poisson and Wigner Distributions.

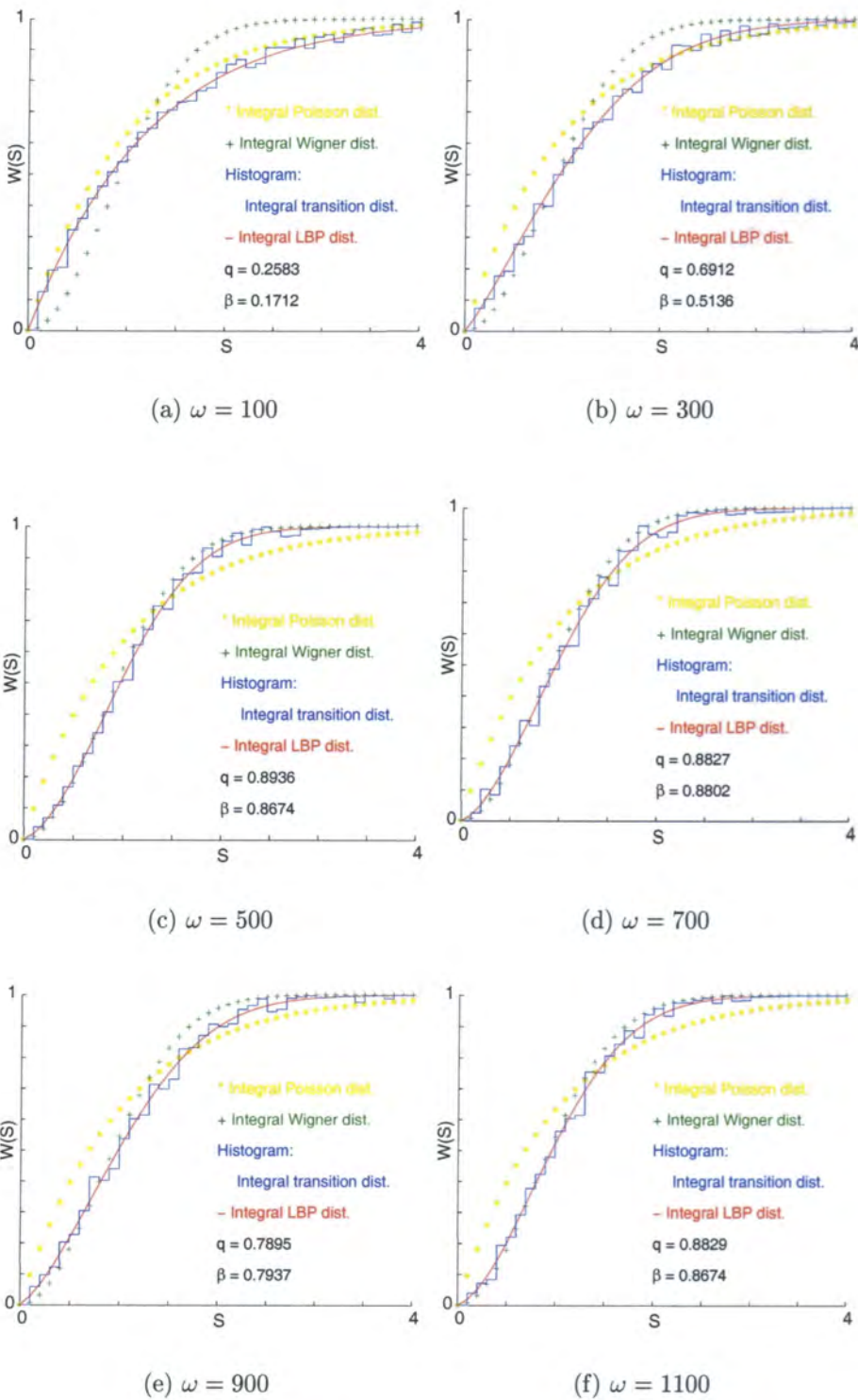


Figure 4.12: The theoretical Integral LBP distributions fitted to the Integral Transition distributions for $\omega = 100, 300, 500, 700, 900, 1100$.

4.6 Spectral rigidity

Whereas the NNSD method reveals correlations between the neighbouring levels, the Δ_3 statistics (spectral rigidity) accounts for the long range effects in the energy spectrum. Dyson and Mehta, [98], introduced three measures of rigidity, Δ_1, Δ_2 and Δ_3 -statistics, of which the latter has proven to be the best and is in common usage. Δ_3 has also been semiclassically derived by Berry, [68].

For calculation of Δ_3 we again need to carry out the unfolding procedure as detailed in Section 4.3 on page 98, with a slight difference; for a finite sequence of $n = 2m$ energy levels for the \mathcal{B}_\square with a range of energies ΔE , we rescale the levels so that they range from $-\frac{\Delta E}{2}$ to $\frac{\Delta E}{2}$ with unit average spacing. The staircase function for the level sequence, $N(x)$, now gives the number of levels between $-\frac{\Delta E}{2}$ and x .

The Δ_3 is defined, for a fixed interval $[\sigma, \sigma + L]$, as the least-squares deviation of the staircase function, $N(x)$, from the best straight line fitting it [84]:

$$\Delta_3(\sigma, L) = \frac{1}{L} \min_{A,B} \int_{\sigma}^{\sigma+L} [N(x) - Ax - B]^2 dx \quad (4.44)$$

A small value of $\Delta_3(L)$ indicates that the spectrum is stiff: given one eigenvalue one can predict the location of distant eigenvalues with some accuracy. A large value of $\Delta_3(L)$ means that such a prediction cannot be made with confidence. A GOE spectrum is much stiffer than a Poisson spectrum.

For a quantum spectrum for which the classical analogue is integrable $\bar{\Delta}_3(L)$ (the bar indicates ensemble average) is given by [98]

$$\bar{\Delta}_3(L) = \frac{L}{15}. \quad (4.45)$$

If the system is chaotic in the classical limit, Δ_3 starts with the slope (4.45) for small values of L , and for $L \gg 1$ asymptotically approaches the function [98]

$$\bar{\Delta}(L) = \frac{1}{\pi^2} [\ln(L) - 0.0687]. \quad (4.46)$$

Transition between the Poisson and GOE limits is observed as in the case of NNSD and the ITD.

To calculate Δ_3 for the \mathcal{B}_\square spectra, we used the numerically efficient formula [99]

$$\begin{aligned} \Delta_3(\sigma, L) = & \frac{n^2}{16} - \frac{1}{L^2} \left[\sum_{i=1}^n \tilde{x}_i \right]^2 + \frac{3n}{2L^2} \left[\sum_{i=1}^n \tilde{x}_i^2 \right] \\ & - \frac{3}{L^4} \left[\sum_{i=1}^n \tilde{x}_i^2 \right]^2 + \frac{1}{L} \left[\sum_{i=1}^n (n - 2i + 1) \tilde{x}_i \right], \end{aligned} \quad (4.47)$$

where $\tilde{x}_i = x_i - (\sigma + \frac{L}{2})$ are the shifted, unfolded eigenvalues and n is the number of levels in the interval $[\sigma, \sigma + L]$.

The spectral average $\bar{\Delta}_3(L)$, required for comparison with ensemble averages, is computed by

$$\bar{\Delta}_3(L) \equiv \frac{1}{N_\sigma} \sum_{\sigma} \Delta_3(\sigma, L), \quad (4.48)$$

where the σ 's are chosen such that successive intervals overlap by $\frac{L}{2}$ and N_σ counts the number of intervals.

Figure 4.13 on the next page shows the dependence of the calculated $\bar{\Delta}_3$ -statistics for the \mathcal{B}_\square for $\omega = 200, 400, 600, 800, 1000$ and 1200 on L along with the Poisson and Wigner dependence. For $\omega = 200$ the dependence is close to Poisson, moving away for $\omega = 400$ and lying very close to the Wigner(GOE) for $\omega = 600$. This is a reflection of the increase in the value of the parameter q and the decrease in the classical parameter E as shown in figure 4.8 on page 111. More interestingly it provides a concrete connection with the fate of the type I cycles discussed in Subsection 3.6.1 on page 63; as ω increases (E decreases) the invariant curves at $E = \infty$ break up and chaos appears. With further increase in ω all the cycles except X_+ , which is decreasing in size, become unstable and gradually disappear. By $\omega = 600$, corresponding to $E \approx 20$, X_+ , the only cycle now present, inverts its shape and occupies the minimum volume of phase space in its existence; at this point we have virtually total chaos.

As ω is further increased X_+ begins to grow reaching its maximum size at $\omega \approx 820, E \approx 4$; and in figure 4.13 on the following page the $\bar{\Delta}_3$ values are seen to lie between $\omega = 400$ and 200 . For ω between 820 and 1200 the variation in q reflects the changes in the chaotic phase volume due the eventual death of X_+ alongside the births and deaths of the type II cycles.

Figure 4.14 on the next page shows the variation of $\bar{\Delta}_3$ for one particular value of L , (5), with ω . It shows and confirms the results of the NNSD and ITD in its interpolation between the limiting statistics. It also mimics the classical results, namely, complete integrability at high E (low ω) towards complete chaos at low E (high ω) and back towards integrability at lower E (higher ω) and finally back towards complete chaos at even lower E (even higher ω).

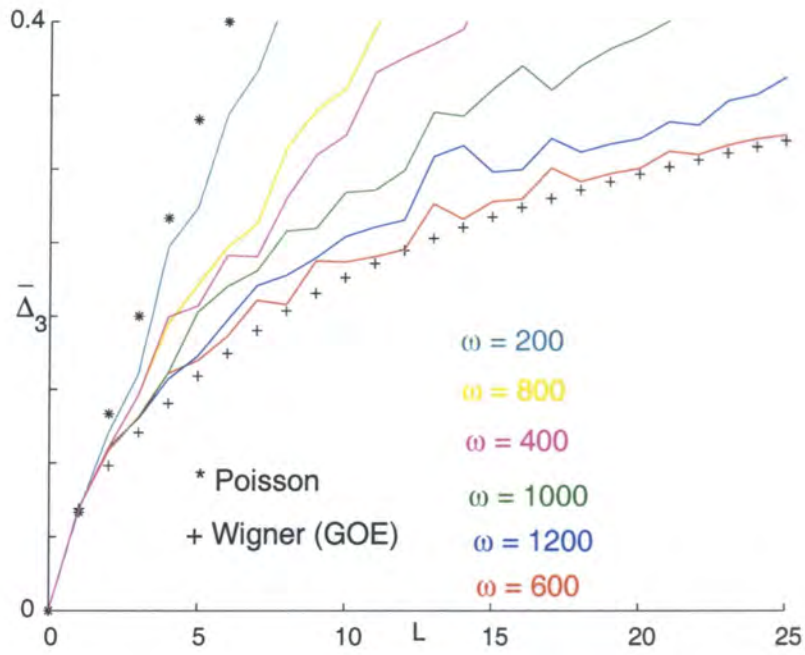


Figure 4.13: Dependence of $\bar{\Delta}_3$ on L .

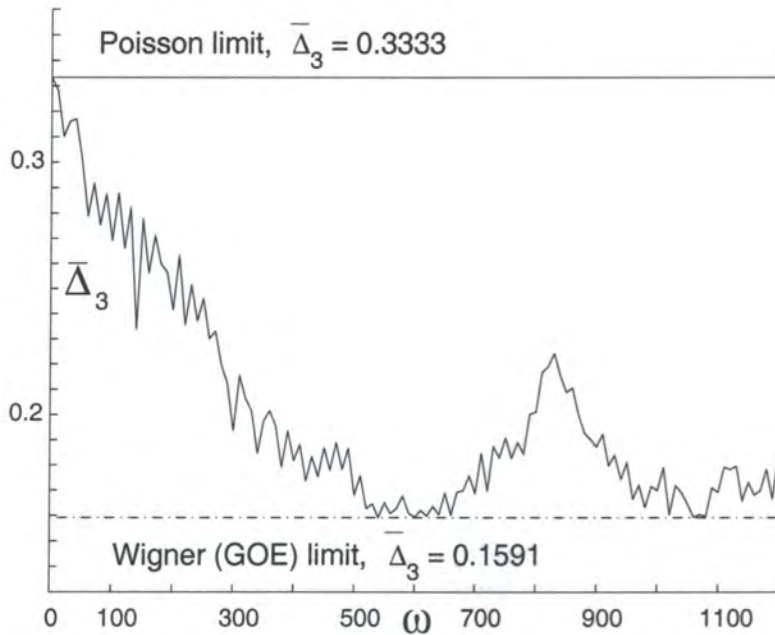


Figure 4.14: Dependence of $\bar{\Delta}_3(5)$ on ω

4.7 Other statistics

We have made preliminary investigations of three further statistics for the \mathcal{B}_\square but do not report on them as they merely confirm the earlier results, namely, demonstrate the interpolation between the Poisson and Wigner (GOE) limits but provide no further insights.

These are the cumulants of the number statistic $n(\sigma, L)$ which gives the number of levels in the energy interval $[\sigma, \sigma + L]$. They are defined as follows [89]:

1. The variance statistic

$$\Sigma^2(L) \equiv \langle [n(\sigma, L) - \langle n(L) \rangle]^2 \rangle. \quad (4.49)$$

2. The skewness statistic

$$\gamma_1(L) \equiv \frac{\langle [n(\sigma, L) - \langle n(L) \rangle]^3 \rangle}{\Sigma^3(L)}. \quad (4.50)$$

3. The excess (or kurtosis) statistic

$$\gamma_2(L) \equiv \frac{\langle [n(\sigma, L) - \langle n(L) \rangle]^4 \rangle}{\Sigma^4(L)} - 3. \quad (4.51)$$

Chapter 5

Wave packet dynamics in the \mathcal{B}_\square

In classical physics chaos can be characterised by the long-time behaviour of the dynamics, the most obvious property being a sensitive dependence on initial conditions. Time correlations of classical observables decay (possibly exponentially) for $t \rightarrow \infty$ when the system shares mixing property [48], reflecting a complete loss of information on the system. Integrable systems, however, show quasiperiodic time evolutions which result in nondecreasing time correlations. For bound conservative systems (such as the \mathcal{B}_\square) the quantum mechanical time evolution is almost periodic. This is due to the discrete spectrum of the time-evolution operator $U(t) = \exp(-i\hat{H}t/\hbar)$, where \hat{H} denotes the quantum Hamiltonian with discrete spectrum $E_n, n \in \mathbb{N}$. Thus the time-correlation function of two states ψ, φ from the quantum mechanical Hilbert space is:

$$\langle \psi, U(t)\varphi \rangle = \sum_{n=1}^{\infty} c_n e^{-\frac{i}{\hbar} E_n t}$$

For $t \rightarrow \infty$ this neither increases nor decreases but rather fluctuates perpetually, irrespective of the integrable or chaotic nature of the classical limit. This suggests that there exists no quantum chaos that manifests itself in the long-time behaviour of the dynamics.

Perhaps for this reason quantum mechanical studies of billiards, for example [27, 30, 39, 40, 42, 44, 49, 50, 52–54, 56–58, 60–66, 68, 69], concentrate on the energy level spectra of the dynamical system and largely omit consideration of the time evolution of the wave packet. Our study of the \mathcal{B}_\square is not restricted to chaotic dynamics so we present an investigation of wave packet dynamics for the \mathcal{B}_\square .

5.1 Dimensionless form of the Schrödinger equation

For computational purposes it is more convenient to deal with the dimensionless form of the Schrödinger equation. For the \mathcal{B}_\square the Schrödinger equation is:

$$i\hbar \frac{\partial \Psi}{\partial t} = \hat{H} \Psi \quad (5.1)$$

where we can make use of the dimensionless \hat{H} given in equation 4.3 on page 95.

Again a convenient characteristic time is \hbar/E_g , where E_g is the ground state energy of the stationary \mathcal{B}_\square (that is, the two dimensional infinite square well). Let $t = t' \hbar/E_g$ where t' is a dimensionless quantity, then we have the transformation

$$i\hbar \frac{\partial \Psi}{\partial t} \longrightarrow iE_g \frac{\partial \Psi}{\partial t'}$$

which leads to

$$\frac{\partial \Psi}{\partial t} = \left[\frac{2}{\pi^2} i \left(\frac{\partial^2}{\partial x^2} + \frac{\partial^2}{\partial y^2} \right) + \omega \left(x \frac{\partial}{\partial y} - y \frac{\partial}{\partial x} \right) \right] \Psi \quad (5.2)$$

or more conveniently for later purposes the dimensionless form of the Schrödinger equation for the \mathcal{B}_\square is

$$\frac{\partial \Psi}{\partial t} = -i \left[-\frac{2}{\pi^2} \left(\frac{\partial^2}{\partial x^2} + \frac{\partial^2}{\partial y^2} \right) + i\omega \left(x \frac{\partial}{\partial y} - y \frac{\partial}{\partial x} \right) \right] \Psi = -i\hat{H} \Psi \quad (5.3)$$

5.2 Numerical integration techniques

To convert equation 5.3 to a finite difference equation; let us designate time by a superscript n and spatial position by the subscripts j, k . The various x and y values become $j\epsilon$ and $k\epsilon$ where ϵ is the mesh width and $j = k = 0, 1, \dots, J$.

After formal integration of equation 5.3 from t to $t + \delta t$ we get

$$\Psi(x, y, t + \delta t) = e^{-i\hat{H}\delta t} \Psi(x, y, t) \quad (5.4)$$

which in terms of the discretisation yields:

$$\Psi_{j,k}^{n+1} = e^{-i\hat{H}\delta t} \Psi_{j,k}^n \quad (5.5)$$

which correct to terms of order δt becomes:

$$\Psi_{j,k}^{n+1} = (1 - i\delta t \hat{H}) \Psi_{j,k}^n = \Psi_{j,k}^n - i\delta t \hat{H} \Psi_{j,k}^n \quad (5.6)$$

5.2.1 Euler's method

Using equation 5.3 on the page before to evaluate $\hat{H}\Psi_{j,k}^n$ and substituting into equation 5.5 we obtain:

$$\Psi_{j,k}^n = e^{i\hat{H}\delta t}\Psi_{j,k}^{n+1} \quad (5.7)$$

which leads to the difference equation :

$$\Psi_{j,k}^{n+1} = \Psi_{j,k}^n - i\delta t \left[\begin{array}{l} -\frac{2}{\pi^2\epsilon^2} (\Psi_{j-1,k}^n + \Psi_{j+1,k}^n + \Psi_{j,k-1}^n + \Psi_{j,k+1}^n - 4\Psi_{j,k}^n) \\ +i\omega (j (\Psi_{j,k+1}^n - \Psi_{j,k-1}^n) - k (\Psi_{j+1,k}^n - \Psi_{j-1,k}^n)) \end{array} \right] \quad (5.8)$$

Equation 5.8 exhibits one especially attractive feature; it is an explicit differencing scheme, giving the wave function at time step $n+1$ directly in terms of the function at earlier time n . This permits a straightforward integration scheme and allows for an easy determination of Ψ for all n and j, k . Unfortunately, the scheme is unstable, round-off error and errors arising from dropping terms of order δt^2 and higher in the expansion of $e^{-i\delta t\hat{H}}$ can grow without bounds as the time integration proceeds from step to step.

5.2.2 Runge-Kutta method

The instability above can be eliminated by rewriting equation 5.4 on the preceding page in the form

$$\Psi_{j,k}^n = e^{i\hat{H}\delta t}\Psi_{j,k}^{n+1} \quad (5.9)$$

which leads to the difference equation :

$$\Psi_{j,k}^n = \Psi_{j,k}^{n+1} - i\delta t \left[\begin{array}{l} -\frac{2}{\pi^2\epsilon^2} (\Psi_{j-1,k}^{n+1} + \Psi_{j+1,k}^{n+1} + \Psi_{j,k-1}^{n+1} + \Psi_{j,k+1}^{n+1} - 4\Psi_{j,k}^{n+1}) \\ -i\omega (j (\Psi_{j,k+1}^{n+1} - \Psi_{j,k-1}^{n+1}) - k (\Psi_{j+1,k}^{n+1} - \Psi_{j-1,k}^{n+1})) \end{array} \right] \quad (5.10)$$

This stable equation is however implicit so Ψ^{n+1} is not given directly in terms of Ψ^n , requiring application of certain algebraic techniques in order to obtain Ψ^{n+1} from that at n .

However, equation 5.10 has a serious drawback (shared by equation 5.8) in that it is not unitary. Unitarity is a characteristic of the original wave function which maintains its normalisation over time. The operators $e^{\mp i\delta t\hat{H}}$ with \hat{H} Hermitian are clearly unitary, however, no approximation of these operators which involves expanding the exponential and retaining only a finite number of terms is unitary.

This problem can be overcome by renormalising the wave function after some appropriate number of time steps, but this in itself introduces errors and after many iterations the wave function becomes 'spiky', so is still unsatisfactory.

The integration technique we use (subject of the next subsection) is the two dimensional adaptation of the method used by [70, 71] for producing films of one dimensional quantum mechanical transmission and reflection phenomena. A relatively simple unitary approximation to $e^{-i\delta t\hat{H}}$ is provided by the Cayley form [72];

$$e^{-i\delta t\hat{H}} \approx \frac{(1 - i\delta t\hat{H}/2)}{(1 + i\delta t\hat{H}/2)}$$

which has an added desirable property of being correct to order δt^2 .

5.2.3 Unitary numerical integration technique

Operating on both sides of equation 5.4 on page 123 with the operator $e^{i\hat{H}\delta t/2}$ results in:

$$e^{i\hat{H}\delta t/2}\Psi_{j,k}^{n+1} = e^{-i\hat{H}\delta t/2}\Psi_{j,k}^n \quad (5.11)$$

and inserting the expression for \hat{H} from equation 5.3 on page 123 transforms the LHS of equation 5.11, after neglecting terms $\sim O(\delta t^2)$ into:

$$e^{i\hat{H}\delta t/2}\Psi_{j,k}^{n+1} = \left(1 - \frac{i}{\lambda}\Delta_x^2\right) \left(1 - \frac{i}{\lambda}\Delta_y^2\right) (1 - \gamma x D_y) (1 + \gamma y D_x) \Psi_{j,k}^{n+1} \quad (5.12)$$

and similarly for the RHS of equation 5.12:

$$e^{-i\hat{H}\delta t/2}\Psi_{j,k}^n = \left(1 + \frac{i}{\lambda}\Delta_x^2\right) \left(1 + \frac{i}{\lambda}\Delta_y^2\right) (1 + \gamma x D_y) (1 - \gamma y D_x) \Psi_{j,k}^n \quad (5.13)$$

where

$$\lambda = \frac{\pi^2}{\delta t}\epsilon^2, \quad \gamma = \frac{\omega\delta t}{4\epsilon}$$

and for some arbitrary function f

$$\Delta_x^2 f_{j,k} = f_{j-1,k} - 2f_{j,k} + f_{j+1,k}, \quad \Delta_y^2 f_{j,k} = f_{j,k-1} - 2f_{j,k} + f_{j,k+1}$$

$$D_x f_{j,k} = f_{j+1,k} - f_{j-1,k}, \quad D_y f_{j,k} = f_{j,k+1} - f_{j,k-1}$$

Equating equations 5.12 and 5.13 leads to:

$$\begin{aligned} & \left(1 - \frac{i}{\lambda}\Delta_x^2\right) \left(1 - \frac{i}{\lambda}\Delta_y^2\right) (1 - \gamma x D_y) (1 + \gamma y D_x) \Psi_{j,k}^{n+1} = \\ & \left(1 + \frac{i}{\lambda}\Delta_x^2\right) \left(1 + \frac{i}{\lambda}\Delta_y^2\right) (1 + \gamma x D_y) (1 - \gamma y D_x) \Psi_{j,k}^n \end{aligned} \quad (5.14)$$

Now introduce an inter-mediatory value Φ and split equation 5.14 on the page before into two equations:

$$\left(1 - \frac{i}{\lambda} \Delta_x^2\right) (1 + \gamma y D_x) \Phi_{j,k}^n = \left(1 + \frac{i}{\lambda} \Delta_y^2\right) (1 + \gamma x D_y) \Psi_{j,k}^n \quad (5.15)$$

$$\left(1 - \frac{i}{\lambda} \Delta_y^2\right) (1 - \gamma x D_y) \Psi_{j,k}^{n+1} = \left(1 + \frac{i}{\lambda} \Delta_x^2\right) (1 - \gamma y D_x) \Phi_{j,k}^n \quad (5.16)$$

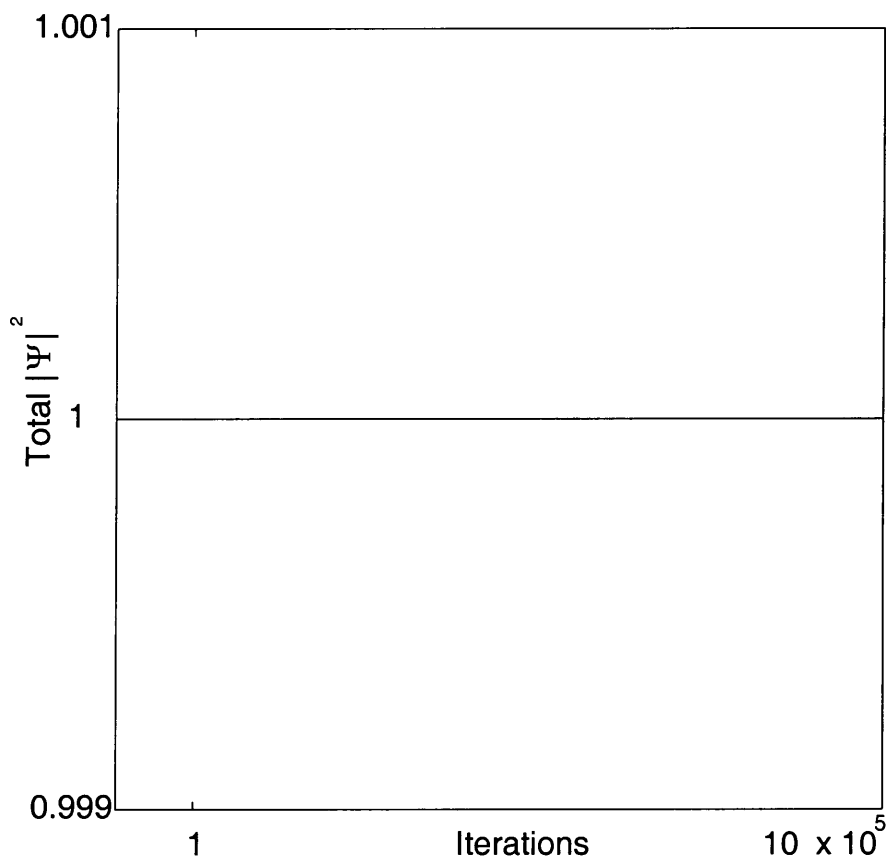


Figure 5.1: Unitarity of the Unitary Integration Method

Equations 5.15 and 5.16 are similar to the Peaceman-Rachford [73] solution of the heat equation. We show their numerical solution in Appendix H on page 175. Figure 5.1 illustrates just how well this method maintains the unitarity of the initial wavefunction, it follows the evolution of the initial wavefunction for time, $t = 10^6$ where, here and henceforth, t is in terms of δt .

5.3 Initial and boundary conditions

Generalising [70] to 2-dimensions the initial (normalised) wave packet is chosen to be Gaussian:

$$\Psi(\mathbf{r}, 0) = \frac{1}{\sqrt{\pi}\sigma_0} e^{i\mathbf{k}_0 \cdot \mathbf{r}} e^{-|\mathbf{r}-\mathbf{r}_0|^2/2\sigma_0^2} \quad (5.17)$$

This wave packet corresponds to a Gaussian position probability density $Q(\mathbf{r}, 0)$ centred at $\mathbf{r} = \mathbf{r}_0$ with a standard deviation of $\Delta\mathbf{r} = \sigma_0^2/2$:

$$Q(\mathbf{r}, 0) = |\Psi(\mathbf{r}, 0)|^2 = \frac{1}{\pi\sigma_0^2} e^{-|\mathbf{r}-\mathbf{r}_0|^2/\sigma_0^2} \quad (5.18)$$

The corresponding momentum space function (i.e. the Fourier transform of equation 5.17) at $t = 0$ is

$$\Phi(\mathbf{k}, 0) = \frac{\sigma_0}{\sqrt{\pi}} e^{(-i\mathbf{k} \cdot \mathbf{r}_0)} e^{-\sigma_0^2|\mathbf{k}-\mathbf{k}_0|^2/2} \quad (5.19)$$

Since we are quantising in a square box of length L at the edges of which the wave function must necessarily vanish places restrictions on \mathbf{r}_0 and σ_0 . For example choosing $\mathbf{r}_0 = (0, 0)$ and σ_0 to be 2.5% of L we find for \mathcal{B}_\square that $Q(1, 1, 0)$ is zero to the accuracy of the computer. Even choosing $\mathbf{r}_0 = (0.9, 0.9)$ then at the nearest point on the boundary to the initial Gaussian we get $Q(1, 0.9, 0) < 10^{-4}$. To approximate this to zero is clearly to incur no perceptible error, considering that $Q(0.9, 0.9, 0) \approx 84$. However, placing the initial Gaussian any closer to the boundary would incur error in setting Q to zero at the near boundary points.

The criteria for choice of initial conditions for the one dimensional square well of length L are as follows: if the spread in x is governed by the initial spread, σ_0 , then after time T the spread is given by

$$\sigma^2 = (\sigma_0^4 + T^2) = \left(\sigma_0^4 + \frac{16N^2\epsilon^4}{\lambda^2} \right)^{1/2} \quad (5.20)$$

where N is the number of time steps for the wave packet to move from $L/4$ to $3L/4$. For negligible spreading we must therefore have $16N^2\epsilon^4/\lambda^2$ reasonably small compared with σ^4 .

The replacement of the continuous variable x by the discrete index j places additional limitations: Consider a free particle; since the mesh width ϵ is the smallest interval in x which can be resolved by the differencing method, the largest wave number allowed is $k_{max} = \pi/\epsilon$. With the initial Gaussian wave packet given by

$$\psi(x, 0) = e^{ik_0x} e^{-(x-x_0)^2/2\sigma^2}, \quad (5.21)$$

the probability distribution in momentum space is

$$P(k) \sim e^{-\sigma_0^2(k-k_0)^2}. \quad (5.22)$$

Let k_m be the largest momentum present to any appreciable extent (e.g., with probability 10^{-5}). Then we must require that $k_m < k_{max}$. The eigenstates of the system are $\phi_k(x) = \sin kx$ and the second derivative of ϕ_k is

$$\frac{d^2 \phi_k}{dx^2} = -k^2 \phi_k, \quad (5.23)$$

whereas the second difference is

$$\begin{aligned} \frac{\Delta^2 \phi_k}{\epsilon^2} &= \frac{\phi_k(x+\epsilon) - 2\phi_k(x) + \phi_k(x-\epsilon)}{\epsilon^2} \\ &= -\frac{2(1 - \cos k\epsilon)}{\epsilon^2} \phi_k(x). \end{aligned} \quad (5.24)$$

Since $k\epsilon$ is presumed to be small, this may be approximated by

$$-k^2 \left(1 - \frac{k^2 \epsilon^2}{12}\right) \phi_k(x). \quad (5.25)$$

Thus, in order that equation 5.25 be an accurate approximation of equation 5.23 we must require that

$$\frac{k_m^2 \epsilon^2}{12} \ll 1. \quad (5.26)$$

For the two dimension case σ_0 and the wave vector \mathbf{k}_0 must be chosen so that each of its components satisfy the criteria for one dimension case:

$$\begin{aligned} k_{0x} &= k_{0y} = J\lambda/8N\epsilon \\ (\sigma_N/\sigma_0)^2 &= \left[1 + (4N\epsilon^2/\lambda\sigma_0^2)^2\right]^{1/2} \gtrsim 1 \\ (k_{mx}\epsilon)^2/12 &= (k_{my}\epsilon)^2/12 \ll 1 \\ k_{mx} &= k_{my} \ll \pi/\epsilon \end{aligned} \quad (5.27)$$

Where here N is the number of time steps for the wave packet to move from $(0.25, 0.25)$ to $(0.75, 0.75)$, σ_N is the width of the wave packet after time $N\delta t$ and k_{mx} is the value of the wave vector component for which $\exp[-(k_x - k_{0x})^2/\sigma^2] \leq 10^{-3}$. So with $J = 100$, $\epsilon = 10^{-2}$, $\delta t = 0.5\epsilon^2$ we get $N \cong 80$ and $k_{mx} = k_{my} \cong 1.5k_{0x}$.

5.4 Numerical simulations

5.4.1 Stationary table with initially stationary particle

For a stationary table we put $\omega = 0$ so $\gamma = \frac{\omega \delta t}{4\epsilon} = 0$ and the matrices A_x , A_y , B_x and B_y become tri-diagonal:

$$\begin{bmatrix} 1 \mp \frac{2i}{\lambda} & \pm \frac{i}{\lambda} & 0 & 0 & \cdots \\ \pm \frac{i}{\lambda} & 1 \mp \frac{2i}{\lambda} & \pm \frac{i}{\lambda} & 0 & \cdots \\ 0 & \pm \frac{i}{\lambda} & 1 \mp \frac{2i}{\lambda} & \pm \frac{i}{\lambda} & \cdots \\ \vdots & \vdots & \vdots & \vdots & \ddots \end{bmatrix}$$

Where taking the top signs gives the matrices A_x and B_y whilst taking the bottom signs gives A_y and B_x . Setting $\mathbf{k}_0 = \mathbf{0}$ in the initial Gaussian (equation 5.17 on page 127) we obtain an initially stationary particle.

Figures 5.3 on page 131, 5.4 on page 132, 5.5 on page 133 and 5.6 on page 134 are mesh and contour plots with initial conditions given in table 5.1 for various values of t and \mathbf{r}_0 .

$J(=K)$	σ_0	$\epsilon = 2/(J - 1)$	$\delta t = 2\epsilon^2$
101	5×10^{-2}	2×10^{-2}	4×10^{-4}

Table 5.1: Fixed initial conditions for all subsequent plots.

The symmetry of the initial stationary \mathcal{B}_\square is maintained throughout the integrations, the contour plots in figures 5.3 on page 131, 5.4 on page 132 and 5.5 on page 133 show the four-fold symmetry of the initial Gaussian wave packet at $\mathbf{r}_0 = (0, 0)$ whilst those in figure 5.6 on page 134 show symmetry in the $y = -x$ line of the initial Gaussian wave packet at $\mathbf{r}_0 = (-0.5, 0.5)$.

In the case of the one-dimensional infinite square well, [74], the bound-state wave packet, after deteriorating to a configuration in which it is spread almost uniformly across the full well, ultimately after reflections at the walls reforms into the initial $t = 0$ configuration. This reformation must occur periodically since the excited frequencies ω_n are commensurate with the ground state frequency, $\omega_n = E_n/\hbar = n^2\omega_1$. However, this behaviour is not observed in the case of the \mathcal{B}_\square , as the graphs show, the dispersing wave packet impinges on the mid-points of the four sides with the resultant reflections occurring long before the wave packet reaches the corners of the billiard. This destroys the periodic reformation found in the one-dimensional infinite square well.

For the figures mentioned above the maximum integration performed is for $t = 10^3$, we have, in fact, carried out integrations upto $t = 10^8$ and the wave packet maintains its initial symmetry and unitarity. Figure 5.2 is for $t = 90$ with the initial Gaussian wave packet at $\mathbf{r}_0 = (0, 0)$, showing rapid spatial oscillations at the $x = |1|$ walls. This reveals that the initial Gaussian wave packet is composed of highly excited states.

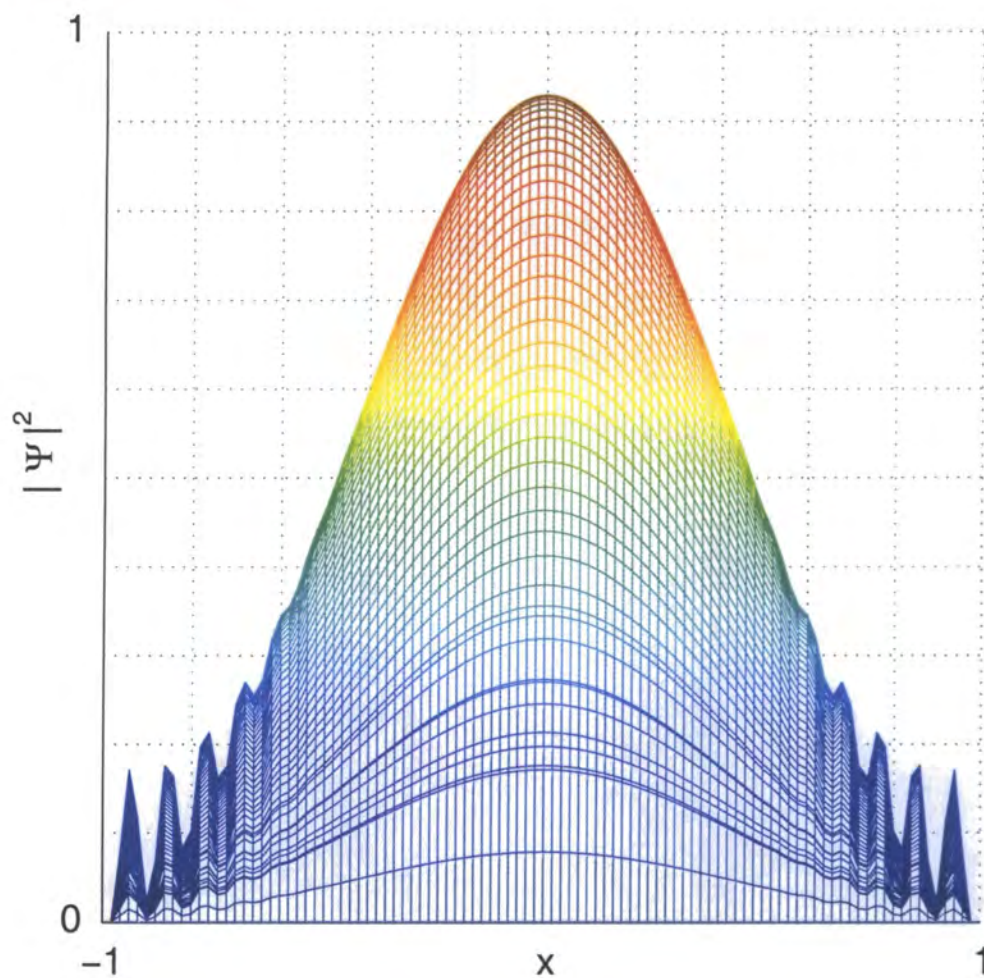
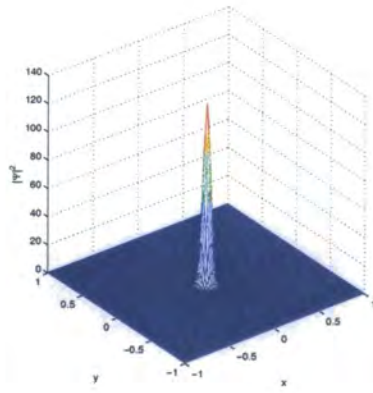
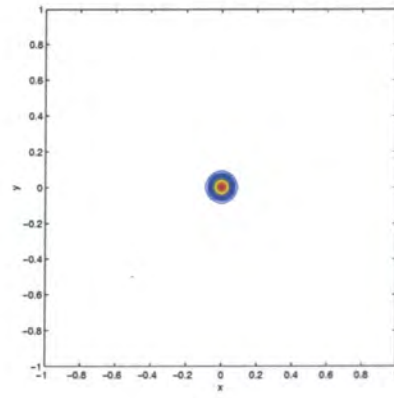


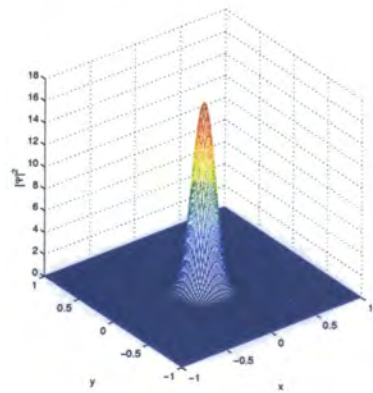
Figure 5.2: Mesh plot at $t = 90$ showing oscillations at the $x = |1|$ boundaries



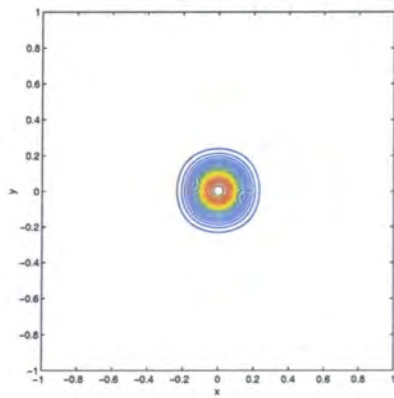
(a) Mesh plot at $t = 0$



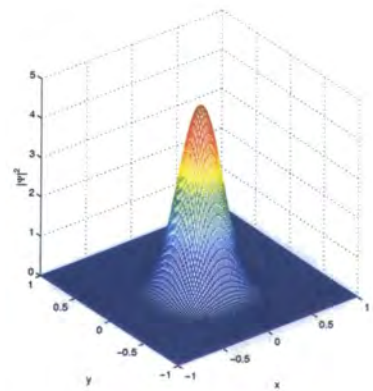
(b) Contour plot at $t = 0$



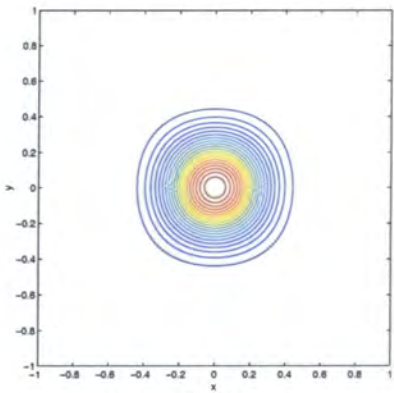
(c) Mesh plot at $t = 20$



(d) Contour plot at $t = 20$

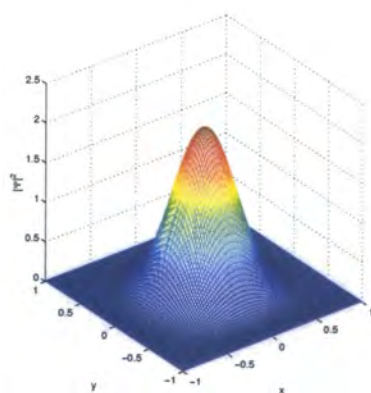


(e) Mesh plot at $t = 40$

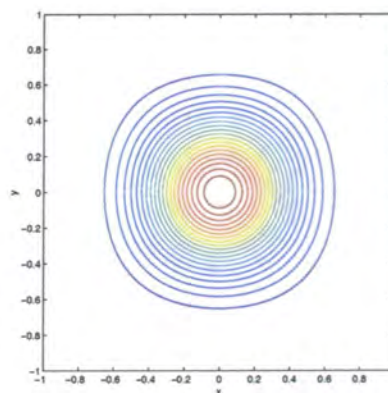


(f) Contour plot at $t = 40$

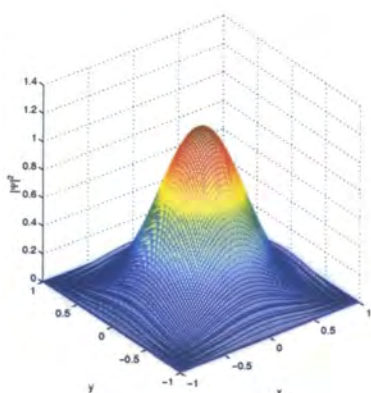
Figure 5.3: Mesh and contour plots of the Probability Densities at $t = 0, 20$ and 40 : $\omega = 0, \mathbf{r}=(0, 0)$



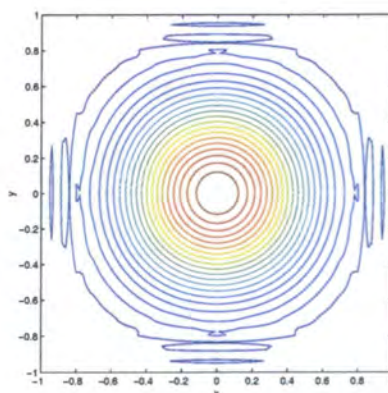
(a) Mesh plot at $t = 60$



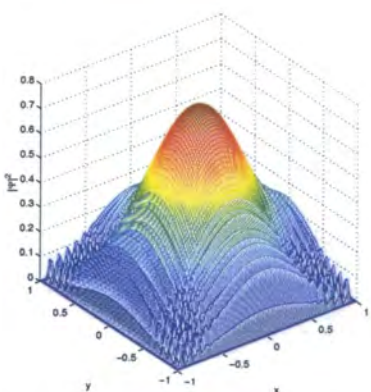
(b) Contour plot at $t = 60$



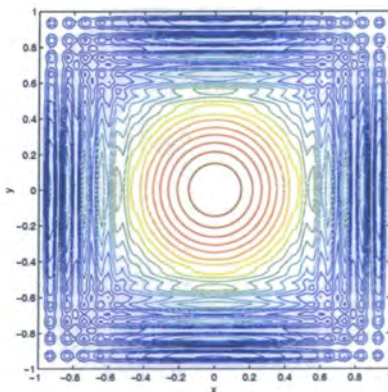
(c) Mesh plot at $t = 80$



(d) Contour plot at $t = 80$

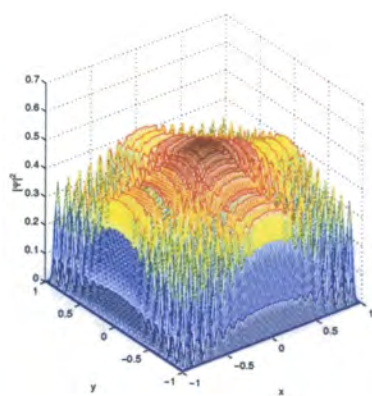


(e) Mesh plot at $t = 100$

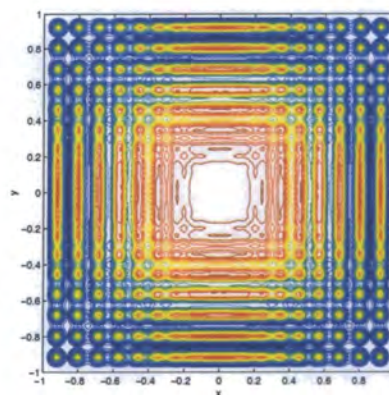


(f) Contour plot at $t = 100$

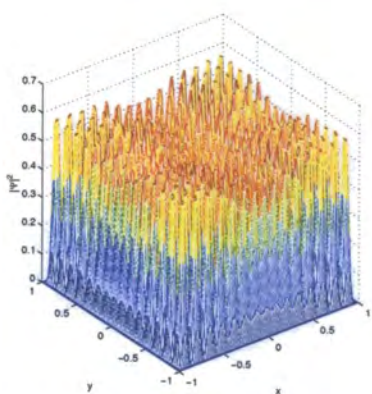
Figure 5.4: Mesh and contour plots of the Probability Densities at $t = 60, 80$ and 100 : $\omega = 0, \mathbf{r}=(0, 0)$



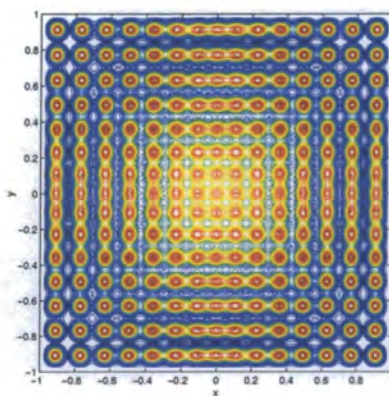
(a) Mesh plot at $t = 120$



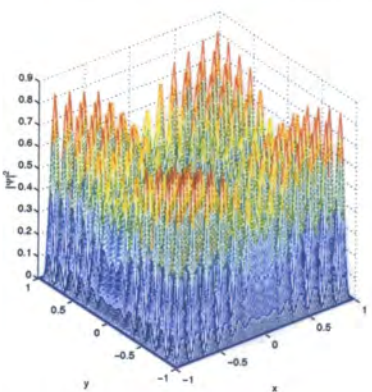
(b) Contour plot at $t = 120$



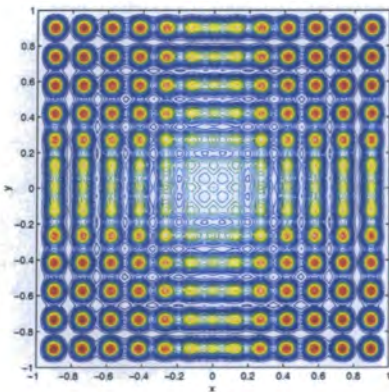
(c) Mesh plot at $t = 140$



(d) Contour plot at $t = 140$

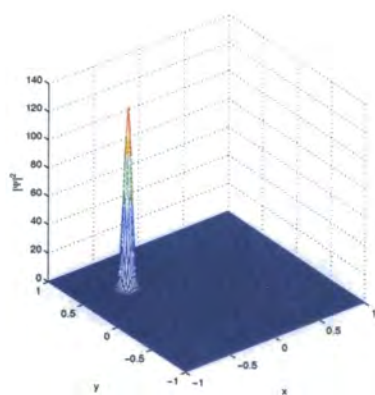


(e) Mesh plot at $t = 160$

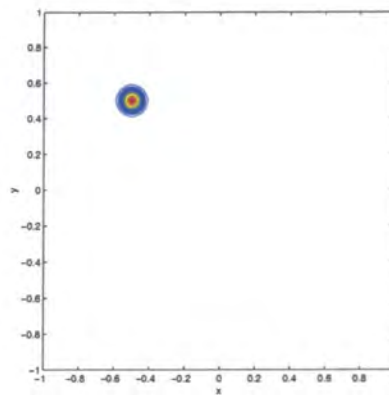


(f) Contour plot at $t = 160$

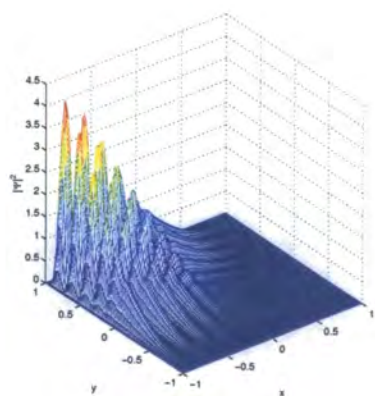
Figure 5.5: Mesh and contour plots of the Probability Densities at $t = 120, 140$ and 160 : $\omega = 0, \mathbf{r} = (0, 0)$



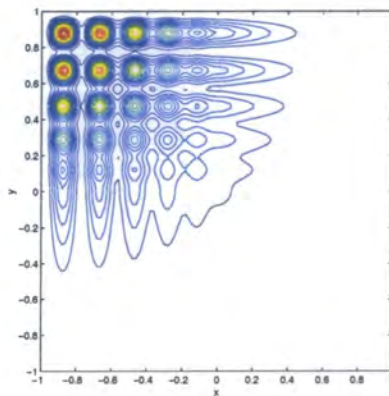
(a) Mesh plot at $t = 0$



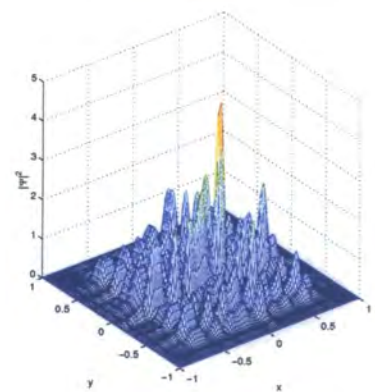
(b) Contour plot at $t = 0$



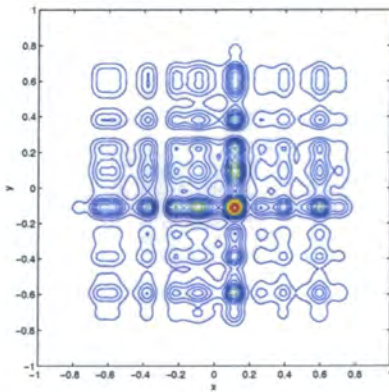
(c) Mesh plot at $t = 100$



(d) Contour plot at $t = 100$



(e) Mesh plot at $t = 1000$



(f) Contour plot at $t = 1000$

Figure 5.6: Mesh and contour plots of the Probability Densities at $t = 0, 100$ and 1000 : $\omega = 0, \mathbf{r} = (-0.5, 0.5)$

5.4.2 Stationary table with initially moving particle

Here again we have $\omega = 0$ for the stationary table but now put $\mathbf{k}_0 \neq 0$ to affect an initially moving particle. We also have θ as the angle of initial motion relative to the positive x -axis so we have $k_{0x} = k_0 \cos \theta$ and $k_{0y} = k_0 \sin \theta$.

Figure 5.7 shows the expectation values of position ($\langle \mathbf{r} \rangle$) of the moving wave packet (solid line) initially at $\mathbf{r}_0 = (0.5, -0.5)$ with $k_0 = 30\pi$ and $\theta = \frac{\pi}{4}$ for $t = 0$ to $t = 100$.

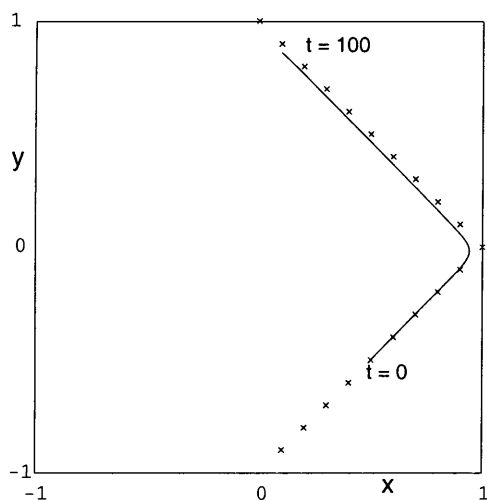
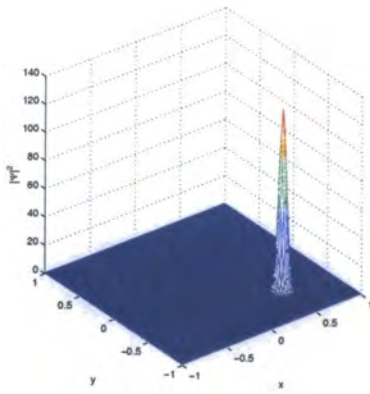


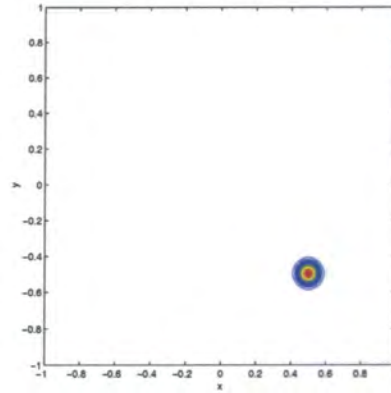
Figure 5.7: Plot of Expectation Values

Superimposed (crosses) is the trajectory of the particle in the classical system for the stationary \mathcal{B}_\square passing through \mathbf{r}_0 anticlockwise (in fact \mathbf{X}_+). Figures 5.7 and 5.8 on the following page show that until the wave packet impinges on the wall the motion of the $\langle \mathbf{r} \rangle$ of the wave packet and the classical trajectory are coincidental. After reflection (figures 5.7 and 5.9 on page 137) at the wall the $\langle \mathbf{r} \rangle$ are a little off-set, but nevertheless, follow the classical trajectory closely. This off-set is due to parts of

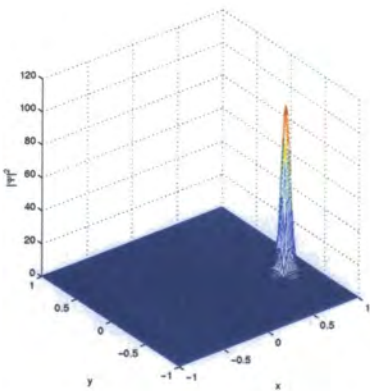
the wave function reaching the boundary before the rest and the reflected waves interfering with the incident waves. The figures demonstrate that on a small time scale the wave packet moves along the classical trajectory [75]. We were unable to determine the value of t when this is no longer the case due to the dispersive nature of the wave packet compounded by the fact that after a few reflections the wave packet is no longer localised and calculating the $\langle \mathbf{r} \rangle$ for this purpose does not make sense.



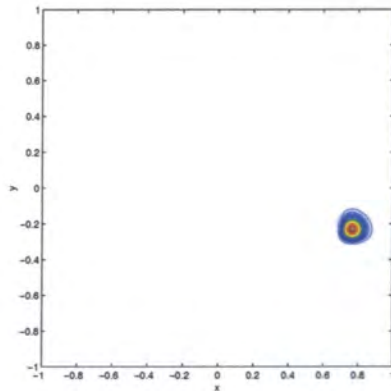
(a) Mesh plot at $t = 0$



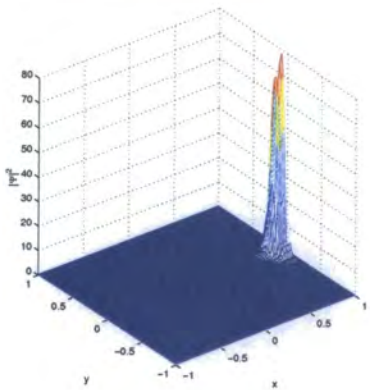
(b) Contour plot at $t = 0$



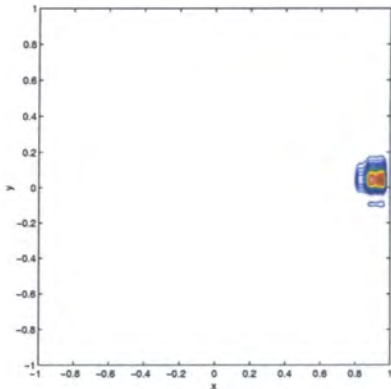
(c) Mesh plot at $t = 20$



(d) Contour plot at $t = 20$

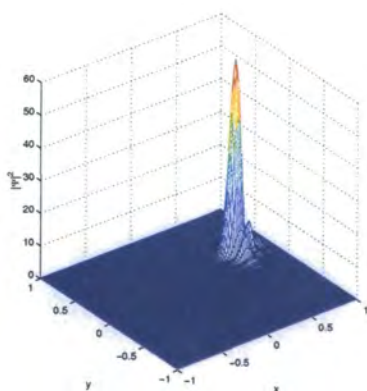


(e) Mesh plot at $t = 40$

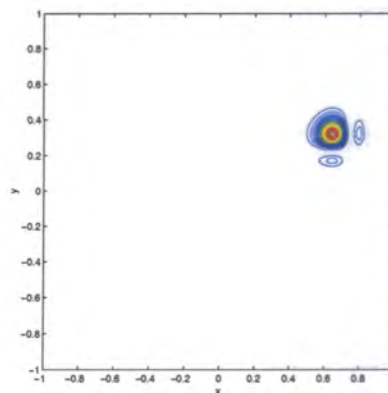


(f) Contour plot at $t = 40$

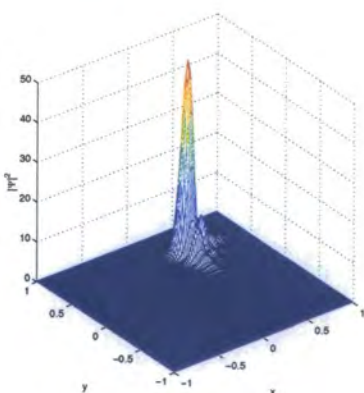
Figure 5.8: Mesh and contour plots of the Probability Densities at $t = 0, 20$ and 40 : $\omega = 0, K_r = 30\pi, \mathbf{r} = (0.5, -0.5)$



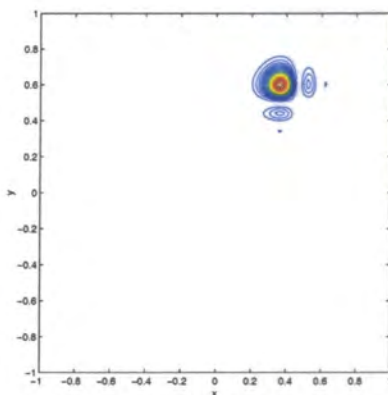
(a) Mesh plot at $t = 60$



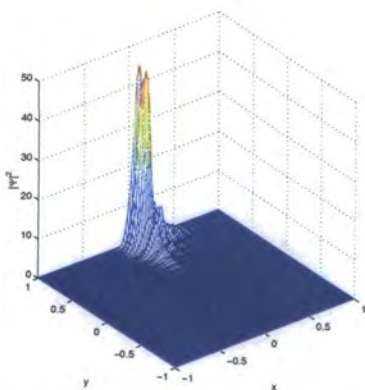
(b) Contour plot for at $t = 60$



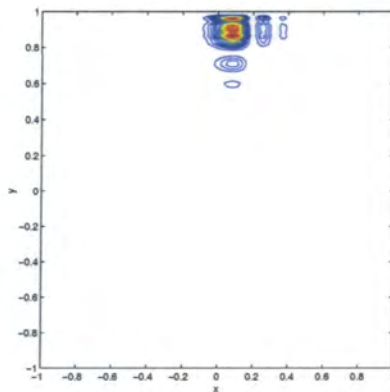
(c) Mesh plot at $t = 80$



(d) Contour plot for at $t = 80$



(e) Mesh plot at $t = 100$



(f) Contour plot at $t = 100$

Figure 5.9: Mesh and contour plots of the Probability Densities at $t = 60, 80$ and 100 : $\omega = 0, K_r = 30\pi, \mathbf{r}=(0.5, -0.5)$

5.4.3 Rotating table with initially stationary particle

Here we put $\omega \neq 0$ for the rotating table and $\mathbf{k}_0 = 0$ for the initially stationary particle. Figure 5.10 shows the $\langle \mathbf{r} \rangle$ of the stationary wave packet initiated from $\mathbf{r}_0 = (0.5, -0.5)$ on the rotating table, for $\omega = 1, 10$ and 100 , and for comparative purposes also the $\langle \mathbf{r} \rangle$ of the same wave packet for a stationary table, ($\omega = 0$), all for $t = 0$ to $t = 2000$.

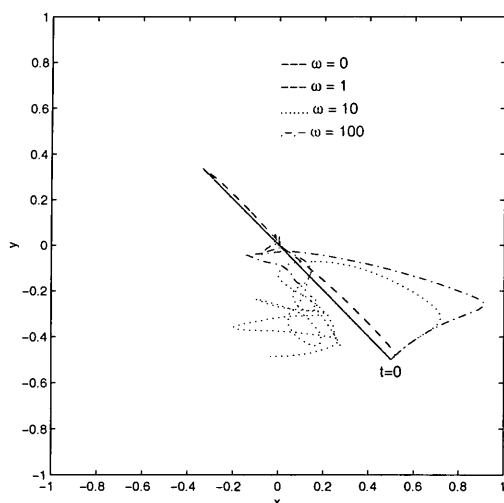


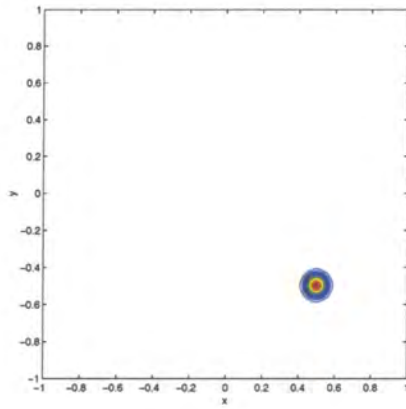
Figure 5.10: Plot of Expectation values for $\omega = 0, 1, 10$ and $\omega = 100$.

As indicated in figure 5.10 the $\langle \mathbf{r} \rangle$ do not move off this line.

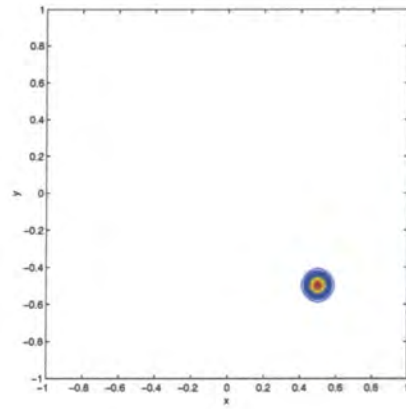
In contrast the symmetry of the initial Gaussian wave packet is immediately lost in the rotating case, as can be seen from figures 5.11(a), 5.11(c), 5.11(e) on the following page and figures 5.12(a), 5.12(c), 5.12(e) on page 140 for the $\omega = 10$ case. For $\omega = 1$ the $\langle \mathbf{r} \rangle$ move almost perpendicularly to the motion observed for $\omega = 0$ for a very short time, reaching $\mathbf{r} = (0.5174, -0.4805)$, and then follow it closely. For $\omega = 10$ the perpendicular motion of the $\langle \mathbf{r} \rangle$ lasts longer, reaching $\mathbf{r} = (0.7184, -0.3146)$, then curving to the left and eventually becoming completely tangled. The perpendicular motion of the $\langle \mathbf{r} \rangle$ lasts even longer for $\omega = 100$, reaching $\mathbf{r} = (0.9142, -0.2633)$, whereupon its behaviour is similar to that of $\omega = 10$.

For the $\omega = 0$ case the $\langle \mathbf{r} \rangle$ remain constant at \mathbf{r}_0 until the dispersing wave packet reaches the $x = 1, y = -1$ boundaries (figure 5.11(f) on the following page). Thereafter, due to the interference between the incident and reflected waves at the boundaries and dispersion the $\langle \mathbf{r} \rangle$ move along the $y = -x$ line, which is the symmetry line of the initial Gaussian wave packet.

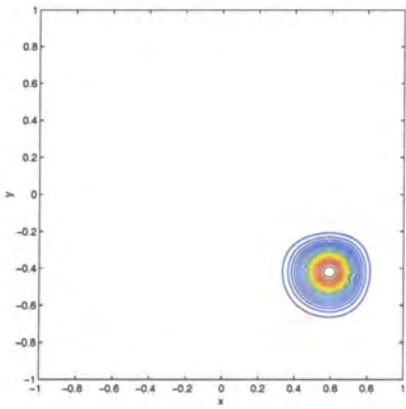
Figures 5.11(b), 5.11(d) and 5.11(f) on the next page and figures 5.12(b), 5.12(d) and 5.12(f) on page 140 clearly demonstrate this symmetry. As indi-



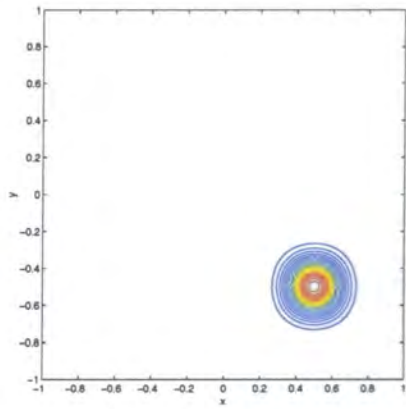
(a) Plot at $t = 0$ ($\omega = 10$)



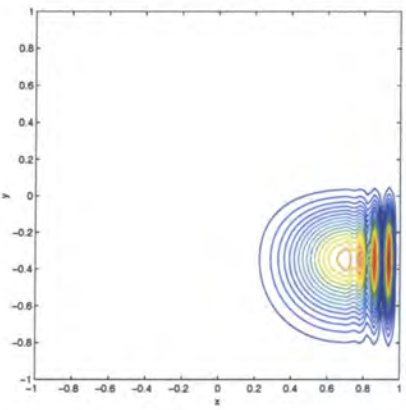
(b) Plot at $t = 0$ ($\omega = 0$)



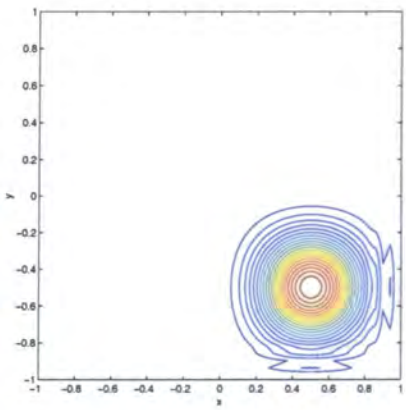
(c) Plot at $t = 20$ ($\omega = 10$)



(d) Plot at $t = 20$ ($\omega = 0$)

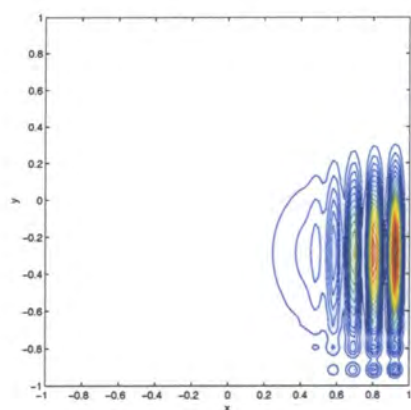


(e) Plot at $t = 40$ ($\omega = 10$)

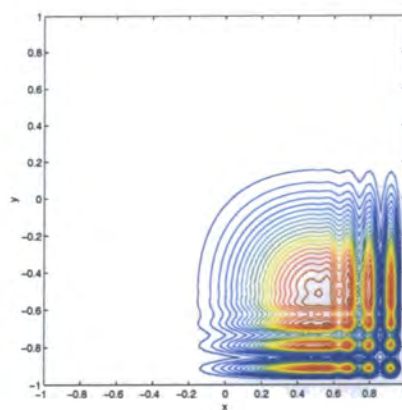


(f) Plot at $t = 40$ ($\omega = 0$)

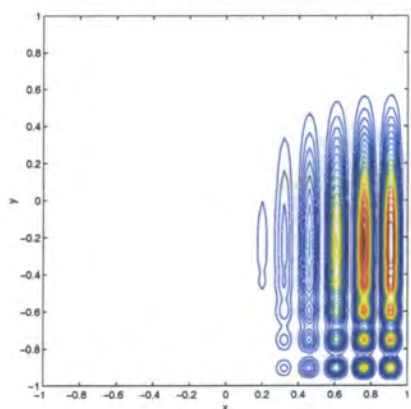
Figure 5.11: Contour plots of the Probability Densities, $\mathbf{r}=(0.5, -0.5)$



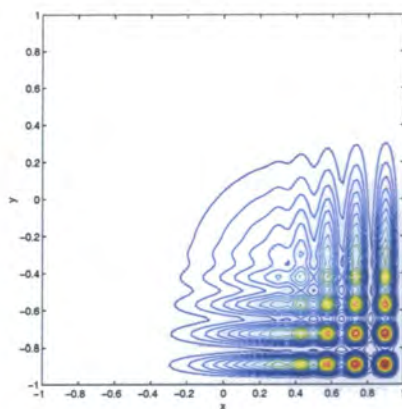
(a) Plot at $t = 60$ ($\omega = 10$)



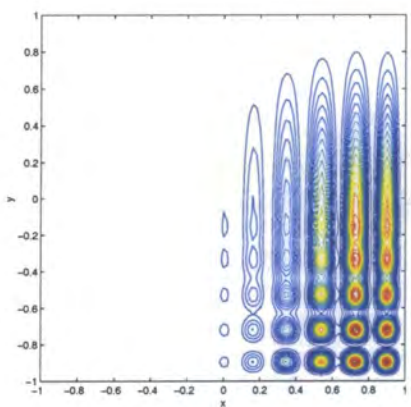
(b) Plot at $t = 60$ ($\omega = 0$)



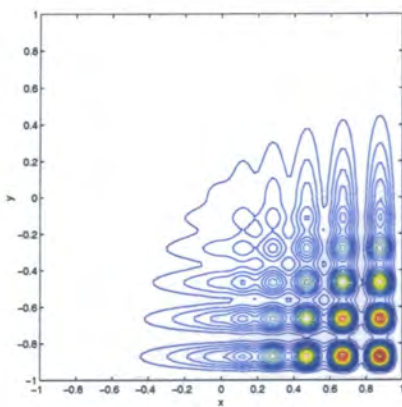
(c) Plot at $t = 80$ ($\omega = 10$)



(d) Plot at $t = 80$ ($\omega = 0$)



(e) Plot at $t = 100$ ($\omega = 10$)



(f) Plot at $t = 100$ ($\omega = 0$)

Figure 5.12: Contour plots of the Probability Densities, $\mathbf{r}=(0.5, -0.5)$

5.4.4 Rotating table with initially moving particle

Here we put $\omega \neq 0$ for the rotating table and $\mathbf{k}_0 \neq 0$ to obtain the initially moving particle. We set $k_0 = 30\pi, \theta = \pi/4, \mathbf{r}_0 = (0.5, -0.5)$ and $t = 100$ in all cases in this subsection. Figure 5.13 shows the motion of the $\langle \mathbf{r} \rangle$ for the values $\omega = 0, 20, 40, 60, 80, 100$.

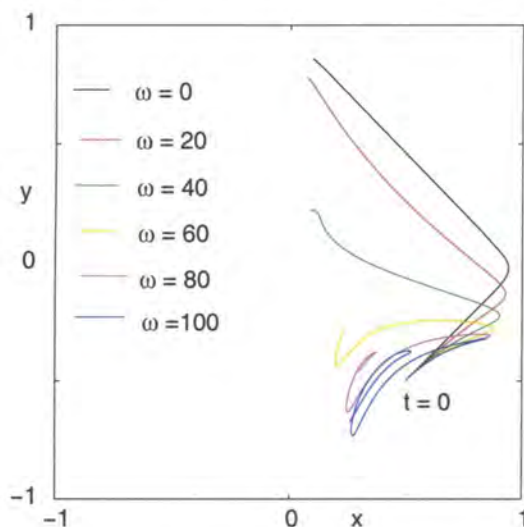


Figure 5.13: Expectation values for $\omega = 0, 20, 40, 60, 80, 100$.

As can be seen, with increasing ω the motion is reverting to that seen at lower ω values in figure 5.13 until the first impact. Thereafter, it resembles the motion of the higher ω values in the above figure, except that, now the wave packet reaches the origin and remains there. Figure 5.15 on the next page is for ω upto 2000, the motion (figure 5.15(a)) follows that exhibited at $\omega = 0$ until the first impact where upon it travels immediately to the origin. The wave packet remains at (figure 5.15(b)) the origin for all values of t in fact. The initial conditions used place a maximum limit on the value of ω that can be used ($\sim 10^4$),

Figure 5.14 shows the motion of the $\langle \mathbf{r} \rangle$ for values of ω increasing upto 1000. As can be seen, with increasing ω the motion is reverting to that seen at lower ω values in figure 5.13 until the first impact. Thereafter, it resembles the motion of the higher ω values in the above figure, except that, now the wave packet reaches the origin and remains there. Figure 5.15 on the next page is for ω upto 2000, the motion (figure 5.15(a)) follows that exhibited at $\omega = 0$ until the first impact where upon it travels immediately to the origin. The wave packet remains at (figure 5.15(b)) the origin for all values of t in fact. The initial conditions used place a maximum limit on the value of ω that can be used ($\sim 10^4$),

Here again we see that the motion of the $\langle \mathbf{r} \rangle$ for small values of $\omega < 30$ is the same as that observed for the classical trajectories in the case of the rotating \mathcal{B}_\square . The increase in curvature, to the right, of the motion of the $\langle \mathbf{r} \rangle$ with increasing ω corresponds to the increase in the curvature, to the right, of the classical trajectories with decreasing energy.

Above $\omega > 40$ we lose the above connection with classical trajectories in that the wave packet no longer remains fairly localised after impact with the

wall and travel to all parts of the \mathcal{B}_\square . Instead it remains in the bottom right quadrant of the \mathcal{B}_\square .

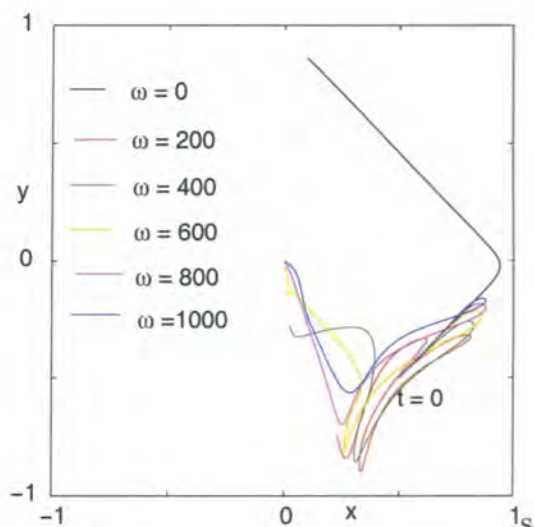
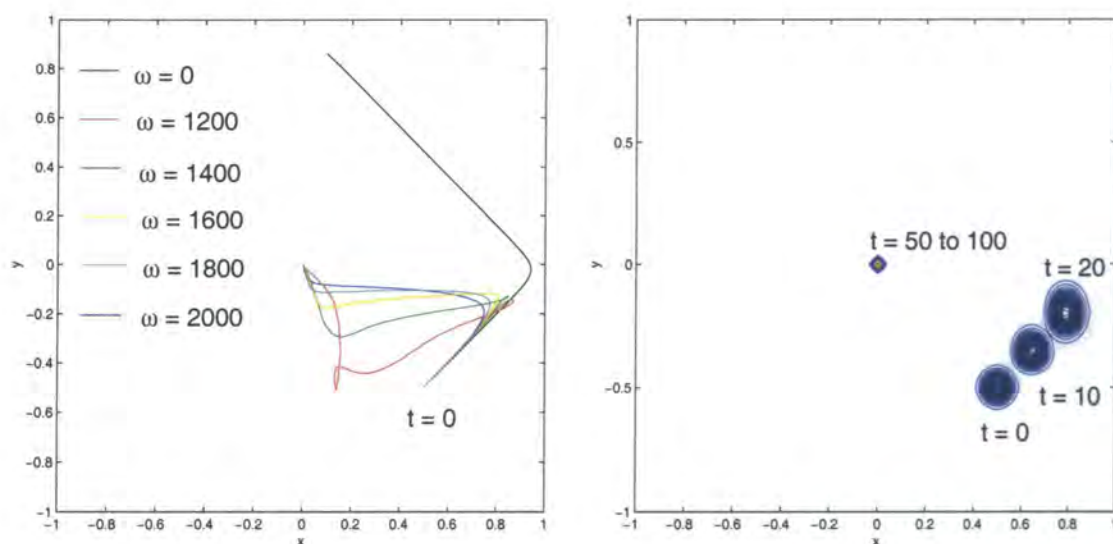


Figure 5.14: Expectation values for $\omega = 0, 200, 400, 600, 800, 1000$.

As can be seen, with increasing ω the motion is reverting to that seen at lower ω values in figure 5.13 until the first impact. Thereafter, it resembles the motion of the higher ω values in the above figure, except that, now the wave packet reaches the origin and remains there. Figure 5.15 on the next page is for ω upto 2000, the motion (figure 5.15(a)) follows that exhibited at $\omega = 0$ until the first impact where upon it travels immediately to the origin. The wave packet remains at (figure 5.15(b)) the origin for all values of t in fact. The initial conditions used place a maximum limit on the value of ω that can be used ($\sim 10^4$),



(a) Expectation values

(b) Contour plots

Figure 5.15: (a) Expectation values at $\omega = 0, 1200, 1400, 1600, 1800, 2000$. (b) Contour plots at $\omega = 1400$.

but computationally the value of ω that can be used is much lower as it swamps the other small values in the program.

Returning to lower values of ω , figures 5.16 on the following page and 5.17 on page 144 are the contours of the Probability Densities at various values of t , showing that with $\omega = 0$ (included for comparative purposes) the wave packet remains fairly localised in space, even after the reflection at the $x = 1$ boundary (figure 5.16(f) on the following page). On the other hand for the rotating case, ($\omega = 30$), the wave packet very quickly loses its Gaussian nature (fig 5.16(c) on the next page) and when it impinges on the $x = 1$ boundary (figure 5.16(e) on the following page) it is elongated in the y -direction. Thereafter, this elongation continues to the extent that by $t = 100$ (figure 5.17(e) on page 144) we have reflections and interferences on both the $y = -1$ and $y = 1$ boundaries. This figure is quite interesting, it is rather reminiscent of the cycle \mathbf{X}_+ which dominates phase space at the corresponding classical energy (> 10000), our interpretation being that it represents the particle bouncing between opposite walls.

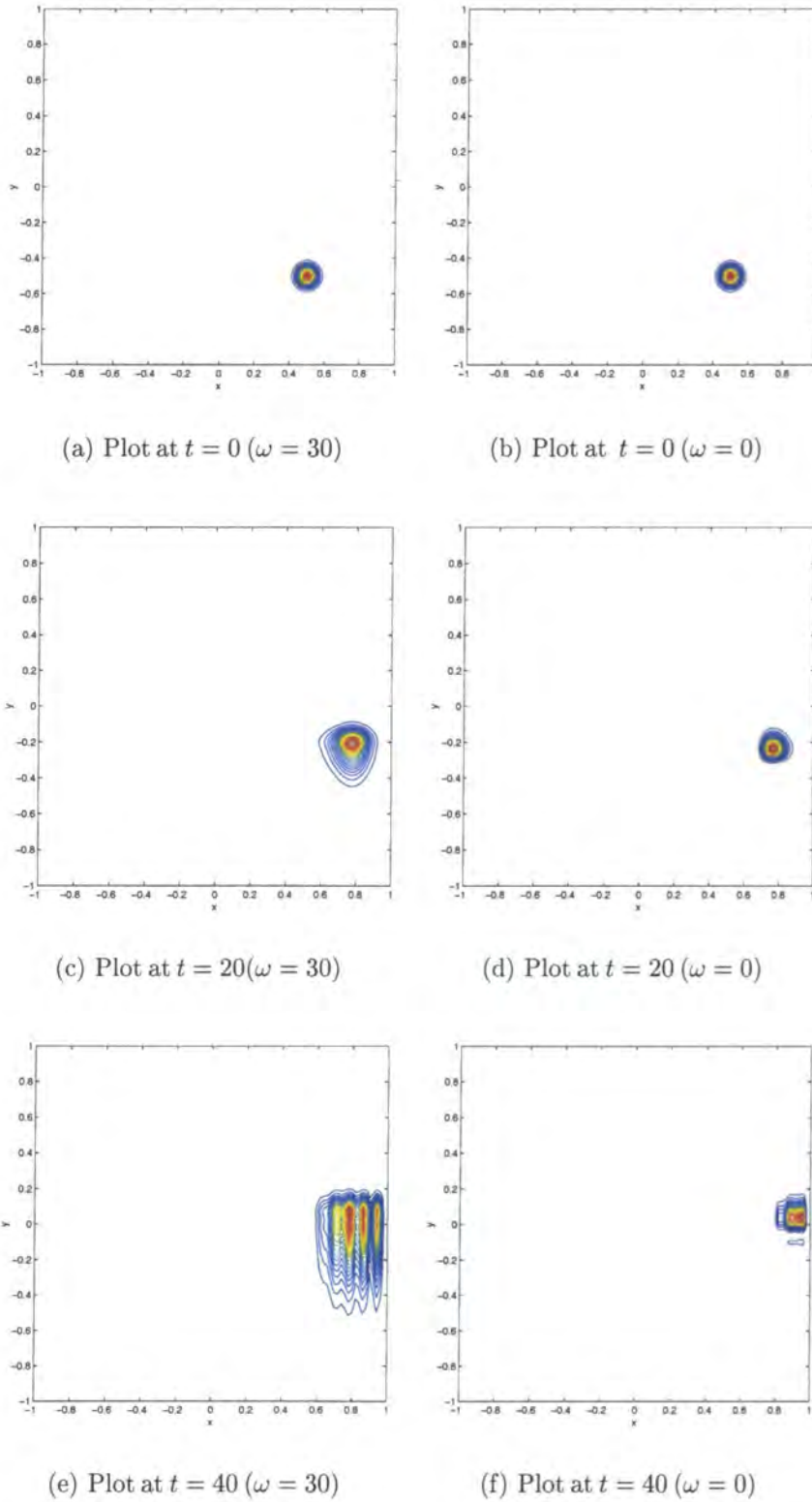
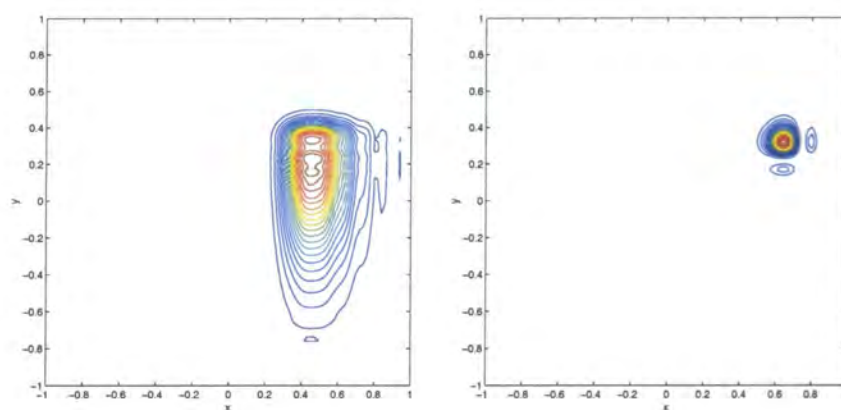
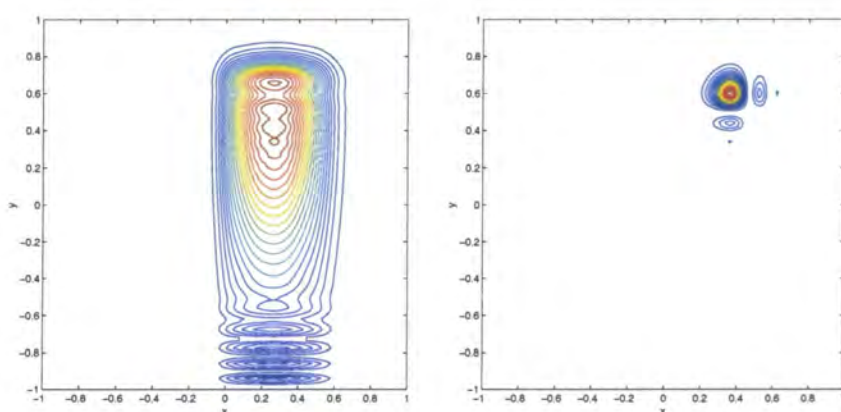


Figure 5.16: Contour plots of the Probability Densities, $\mathbf{r}=(0.5, -0.5)$



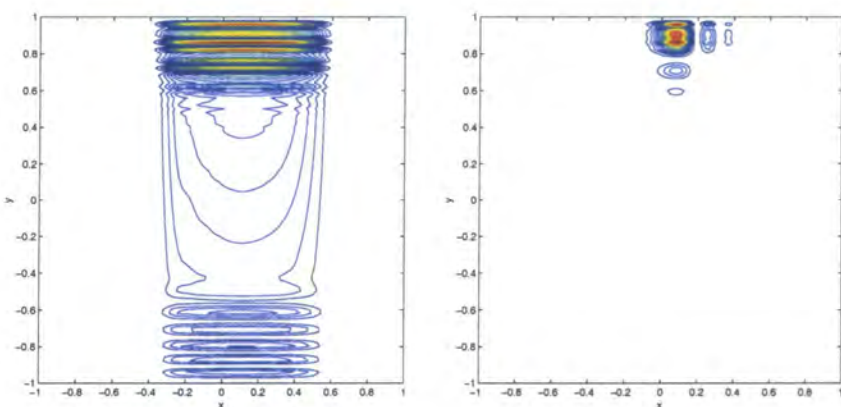
(a) Plot at $t = 60$ ($\omega = 30$)

(b) Plot at $t = 60$ ($\omega = 0$)



(c) Plot at $t = 80$ ($\omega = 30$)

(d) Plot at $t = 80$ ($\omega = 0$)



(e) Plot at $t = 100$ ($\omega = 30$)

(f) Plot at $t = 100$ ($\omega = 0$)

Figure 5.17: Contour plots of the Probability Densities, $\mathbf{r}=(0.5, -0.5)$

Chapter 6

Conclusions

6.1 Classical dynamics

The classical rotating \mathcal{B}_\square is seen to have the usual rich structure of KAM tori mixed with chaotic motion. The simplicity of the system has enabled us to delve deeper into the analysis of the cause of chaos than normally possible with more complex dynamical systems. We have found that order and disorder coexists for most values of the energy parameter E in its permitted range $(-2, \infty)$. There exist three sorts of ordered dynamics as E is decreased from ∞ to -2 , two being connected to these limits and the third being an intermediate transient.

At very high E numerous periodic cycles are present, connected to the stationary \mathcal{B}_\square , the most prominent being the hyperbolic (stable), \mathbf{X}_+ , and elliptical (unstable), \mathbf{X}_- , fixed points. As E is decreased we see the usual bifurcations of all these cycles, with the associated trajectories showing increased curvature. With further reduction only the persistent \mathbf{X}_+ remains amid a sea of chaos, diminishing in size and eventually vanishing at the lower fringe of phase space.

Before the disappearance of \mathbf{X}_+ , partial order is restored through the appearance of the transient cycles which owe their existence purely to rotational effects. The origin of these is the significant rightward trajectory curvature allowing an anticlockwise circulating particle to have one or more bounces on the same side of the billiard before a corner and a transit to the adjacent side, where the sequence repeats. These structures occupy small and decreasing proportion of phase space and die out after a 6-cycle at near $E = -0.54$.

At $E = -1.8$ the third type of stable cycle appears, as a precursor of the orderly limit $E = -2$. The associated trajectories include anti-clockwise segments that curve tightly rightward, sometime self-crossing, and there are also clockwise segments with leftward (centrifugal) curvature. Many orders of these ‘inverse KAM’ cycles coexist for $E = -1.95$, occupying an increasing proportion of the shrinking phase space as

$E \rightarrow -2$.

Flyaway was proposed as the origin of chaos in magnetic billiards [26] and identified as the mechanism for rotational chaos too [25]. We, in fact, find that this is not the case but rather that angular dispersion to be the source of disorder. Flyaway is an obvious candidate for the source of disorder, and it certainly implies a degree of sensitivity to initial conditions. However, it alone is not the main source of chaos, for several reasons.

- (i) With curved trajectories and piecewise linear walls (for example, polygon, stadium) flyaway is always present. In smooth convex boundaries, however, flyaway trajectories must curve more than the walls. Rotating circle [25] and ellipse [27] must be spinning fast enough, and magnetic billiards in an ellipse [26] must be in a strong enough field. The fact that these systems all show disorder even when the curvature is quite small implies that flyaway is not its only source.
- (ii) After a very-low-angle bounce the subsequent impact is still close to the direct impact of a nearby skimming trajectory. Unless some other mechanism operates, one trajectory simply has an extra bounce and continues thereafter still rather close to its neighbour.
- (iii) Flyaway evidently gives a line of discontinuity in the first-return map $\mathbf{X} \rightarrow \mathbf{X}'$, which is the inverse image of the lower edge of phase space, $\mathbf{X} \sim 0$. The line grows steadily as trajectories curve more and, in the rotating \mathcal{B}_\square , it ramifies too as E decreases and opportunities open for grazing bounces on more than one wall. Critical energies are $E = 12.098$ and $E = 2.968$ where respectively 2 and 3 other walls become accessible. However, these thresholds are not significant in the breakup of any KAM island and there is no change in the chaotic volume of phase space as they are crossed. This is unsurprising, since there is no necessary connection between such an isolated discontinuity and chaos.

Rather than flyaway, the main source of chaos is the first-return maps stretching of phase space which comes just from trajectory curvature itself. Its essence is in the analysis of small-rotation stability of \mathbf{X}_+ and \mathbf{X}_- cycles (equation 3.54 on page 62) - but it is ever present, as follows.

- * Particles on neighbouring trajectories generally make next boundary impacts at different positions and, because of trajectory curvature, inevitably do so with different angles too. This holds both for trajectories from the same point with

differing velocities and those from nearby points with the same velocity.

As a result there is further angular separation on the next transit - giving increased differences in both position and angle at the subsequent impact. So phase-space differences compound to grow exponentially, and chaos develops in the finite volume.

With a rotating billiard, the same mechanism can be viewed in the laboratory frame. Any differences δt in time of flight on linear trajectories, from separation in initial position or velocity, means an angular difference $\omega\delta t$ of the reflecting boundary due to rotation. With subsequent reflections both angular and positional dispersion accumulate.

* Trajectory separation per bounce by this mechanism is larger with greater curvature or faster rotation, predicting a leading Lyapunov exponent that increases with increasing ω or decreasing E . Figure 3.29 on page 89 shows confirmation for the rotating \mathcal{B}_\square .

* There is a further effect with the rotating \mathcal{B}_\square . Here time-of-flight discrepancy and the consequent defocussing clearly differ in magnitude between transits directly across the square to the opposite wall and transits angled away to an adjacent wall. This is for given separation of initial conditions, and the difference is between near-normal impacts and those at much lower angle. The latter give a larger δt , larger rate of defocussing, and hence larger positive Lyapunov exponent.

Figure 3.31 on page 91 shows examples of motion dominated by the two sorts of transits. For E of about 1200 and above Lyapunov exponents can be measured in separate parts of phase space, since a boundary of KAM islands prevents diffusion. The relative size of the positive exponents agree with expectation - for instance the opposite-wall and adjacent-wall values are respectively 0.11 and 0.14 at $E = 1200$, and 0.07 and 0.08 at $E = 2000$.

For E below about 1000 all lingering KAM reefs are broken. So trajectories diffuse freely in the chaotic part of phase space and a single leading Lyapunov exponent is measured - this is what figure 3.29 on page 89 records.

6.2 Quantum dynamics

In the spectral analysis we have compared three different theoretical distribution functions with the results obtained for the \mathcal{B}_\square :

- (i) The Brody distribution.
- (ii) The Berry-Robnik distribution.
- (iii) The Lopac-Brant-Paar distribution.

We have carried out Nearest Neighbour Spacing Distribution, Integral Transition Distribution and Spectral Rigidity calculations on the \mathcal{B}_\square and found that the Lopac-Brant-Paar distribution gave the closest fits to the data obtained. In all instances we have found the expected results, namely, as ω is increased from 0 we have a transition from the Poisson to the Wigner and back towards the Poisson statistics.

The Berry-Robnik distribution is very important as it introduces a parameter q (also incorporated into the Lopac-Brant-Paar distribution) which is the fraction of chaotic phase volume. We have utilised this parameter to make contact between the quantal and classical results for the \mathcal{B}_\square . We must point out that this has not been carried out in past studies of dynamical systems and it is a new feature in our research. Normally, the quantal and classical aspects of research on a particular system are treated in isolation.

By means of the classical chaotic volumes calculated we have been able, with the determined values of q , to associate the values of ω in the quantal analysis with the classical energy parameter E . We see that the increase in ω from 0 reflects quite well the classical dynamics as observed with decreasing E from ∞ . In the changing value of q with ω we see the births and subsequent destructions of the different periodic cycles. We do not, however, see the proliferation of cycles associated with the $E \rightarrow -2$ limit as the eigenvalues obtained with the required high values of ω are not accurate enough to justify performing any statistics upon them.

Study of the wave packet dynamics in the \mathcal{B}_\square does not, as expected, shed any light on the matter of quantum chaos. However, it has been a useful exercise for which we had to determine a unitary numerical integration technique for the 2-dimensional Schrödinger equation. We find that for small values of ω and for short time durations the motion of the expectation value follows closely the classical trajectory path. With higher values of ω this connection is lost as the wave packet no longer remains fairly localised after impact with a wall.

6.3 And there's more ...

We have by no means exhausted (due to the finite time available to complete the research) the studies that could be carried out on the \mathcal{B}_\square , particularly for the quantal case. Avenues for further research on the quantum \mathcal{B}_\square include:

- Investigating the wavefunctions of the Hamiltonian for the \mathcal{B}_\square , we would expect to see enhanced intensity in the pattern of each eigenstate associated with classical periodic orbits. This is the phenomena of scarring of the wavefunctions, [23], and it should be particularly clear in the case of \mathbf{X}_+ .
- Spectral analysis near $E = -2$ ($\omega = \infty$). This would require the term $1/\omega$ in the Hamiltonian and letting $\omega \rightarrow 0$; we are not certain how this could be achieved. The choice of basis is not obvious as they would need to give negligible values at the centre of the \mathcal{B}_\square and increase radially, considerably so for $(1, \sqrt{2})$, whilst taking into account the restrictions imposed by the square boundary conditions.
- Comparing the quantum particle motion with the classical particle motion at the same chaotic volume using the correspondence established between the classical energy parameter E and the quantum rotation parameter ω in Subsection 4.5.1 on page 109.
- More sophisticated methods of studying wave packet dynamics than the Gaussian wave packets used in Chapter 5 on page 122. Perhaps using coherent states or making use of the Bohm trajectory formulation employed in the study of quantum dots [100]. The latter seems a promising idea and should yield interesting and useful insights into wave packet dynamics. Nakamura's adiabatic-ansatz method offers alternative possibilities [101].

Appendix A

KAM Theorem

This Appendix is written with the aid of [5,6,31]. The Fundamental theorem proven at great length and depth in [5] is:

Let us consider a function H , a domain G_0 and positive numbers ρ, R, C . We suppose that the following four conditions are fulfilled:

1. The function $H(p, q)$ (where $p = p_0, p_1$; $q = q_0, q_1$; p_0 is a vector of dimension n_0 and p_1 is a vector of dimension n_1 , where $n_0 + n_1 = n$; q_0 are angular variables. $H(p_0, p_1, q_0 + 2\pi, q_1) = H(p_0, p_1, q_0, q_1)$) is analytic in the domain $F : P_0 \in G_0, |Imq_0| \leq \rho, |x_1| \leq R(x_1 = p_1, q_1)$ and depends on the parameter $\mu, 0 \leq \mu \leq \mu_0$.
2. H is of the form

$$H = H_0(p_0) + \mu H_1(p, q) + \mu^2 H_2(p, q), \quad (\text{A.1})$$

where

$$H_1(p, q) = \bar{H}_1(p_0, p_1, q_1) + \tilde{H}_1(p_0, q_0, p_1, q_1) \quad \int \tilde{H}_1 dq_0 = 0, \quad (\text{A.2})$$

with

$$\bar{H}_2(p_0, p_1, q_1) = \bar{\bar{H}}(p_0, \tau) + \tilde{\tilde{H}}(p_0, p_1, q_1) \quad (\text{A.3})$$

and

$$\bar{\bar{H}}(p_0, \tau) = \lambda_0 + \sum_{i=1}^{n_1} \lambda_i \tau_i + \sum_{i,j=1}^{n_1} \lambda_{ij} \tau_i \tau_j + \sum_{i,j,k=1}^{n_1} \lambda_{ijk} \tau_i \tau_j \tau_k, \quad (\text{A.4})$$

where $\lambda_0, \lambda_i, \lambda_{ij} = \lambda_{ji}$ and λ_{ijk} are functions of p_0 and

$$2\tau_i = p_{n_0+i}^2 + q_{n_0+i}^2 \quad (i = 1, \dots, n_1) \quad (\text{A.5})$$

3. In F the following inequalities are satisfied (for a certain $C \geq 1$):

$$|\mu^2 H_2| \leq \mu^2 C, \quad (\text{A.6})$$

$$|\tilde{H}_1| \leq C, |H_1| \leq C, |\bar{\bar{H}}| \leq C, \quad (\text{A.7})$$

$$|\tilde{\tilde{H}}| \leq C|x_1|^7. \quad (\text{A.8})$$

4. In G_0

$$\det \left\| \frac{\partial^2 H_0}{\partial p_0^2} \right\| \neq 0, \quad (\text{A.9})$$

$$\det |\lambda_{ij}(p_0)| \neq 0. \quad (\text{A.10})$$

On the assumptions (1) - (4), for any $\kappa > 0$ it is possible to find $\epsilon(\kappa; H_0, \bar{\bar{H}}, G_0; \rho_1, R, C; \mu_0) > 0$ such that, when $0 < \epsilon < \epsilon_0$ and $0 < \mu < \epsilon^4$, then:

(I) The domain $\text{Re } F_\epsilon$;

$$p_0 \in \text{Re } G_0 \quad |\text{Im } q_0| = 0, \quad 0 < \tau_i < \epsilon,$$

consists of two sets \mathbf{F}_ϵ and f_ϵ , of which one, \mathbf{F}_ϵ , is invariant with respect to the canonical equations with Hamiltonian (equation A.1 on the preceding page) and the other, f_ϵ , is small:

$$\text{meas } f_\epsilon < \text{meas } \kappa \mathbf{F}_\epsilon. \quad (\text{A.11})$$

(II) \mathbf{F}_ϵ consists of invariant n -dimensional analytic tori T_ω , given by the parametric equations

$$\begin{aligned} p_0 &= p_{0_\omega} + f_{0_\omega}(Q), & q_0 &= Q_0 + g_{0_\omega}, \\ p_1 &= \sqrt{2(\tau_\omega + f_{1_\omega}(Q))} \cos |Q_1 + g_{1_\omega}(Q)|, \\ q_1 &= \sqrt{2(\tau_\epsilon + f_{1_\omega}(Q))} \sin |Q_1 + g_{1_\omega}(Q)|, \end{aligned} \quad (\text{A.12})$$

where $Q = Q_0, Q_1$ are angular parameters and p_{0_ω} and τ_ω are constants depending on the number of the torus ω .

(III) The invariant tori T_ω differ little from the tori

$$p_0 = p_{0_\omega} = \text{constant} \quad \tau = \tau_\omega = \text{constant:}$$

$$|f_{1_\omega}(Q)| < \kappa\epsilon, \quad |g_{1_\omega}(Q)| < \kappa\epsilon. \quad (\text{A.13})$$

(IV) The motion determined by the Hamiltonian (A.1) on the torus T_ω is quasiperiodic with n frequencies ω :

$$\dot{Q}_0 = \omega_0, \dot{Q}_1 = \omega_1 \quad \left(\text{where } \omega_0 = \frac{\partial H_0}{\partial p_{0\omega}}, \quad \omega_1 = \mu \frac{\partial \bar{H}}{\partial \tau_\omega} \right). \quad (\text{A.14})$$

The KAM theorem guarantees that under certain assumptions, in the case of a perturbation $\epsilon H_1(\mathbf{J}, \theta)$ with small enough ϵ , the iterated series for the generator $W(\theta_i^0, J_i)$ converges and thus the invariant tori are not destroyed. The KAM theorem is valid for systems with two and more degrees of freedom, but only the former are dealt with here.

Let an integrable Hamiltonian system, $H_0(J_1, J_2)$, be perturbed by a term which depends on angle variables θ_i , $\epsilon H_1(J_1, J_2, \theta_1, \theta_2)$. Then the convergence of the various perturbation series is destroyed by the presence of the resonance condition $\sum_{i=1}^2 m_i \omega_i = 0$ in the denominators. Nevertheless, under certain conditions concerning the ratio of the unperturbed frequencies, numerous invariant tori ($J_i \theta_i$) survive a *moderate* perturbation, though somewhat deformed.

Parametrize these tori by $\boldsymbol{\eta}$, where the relationship between the unperturbed and perturbed tori is given by

$$\begin{aligned} \mathbf{J} &= \mathbf{J}_0 + \mathbf{v}(\boldsymbol{\eta}, \epsilon), \\ \boldsymbol{\theta} &= \boldsymbol{\eta} + \mathbf{u}(\boldsymbol{\eta}, \epsilon) \end{aligned} \quad (\text{A.15})$$

where $\boldsymbol{\eta}$ is a generalized angle variable. The perturbation terms \mathbf{u} and \mathbf{v} are periodic in $\boldsymbol{\eta}$ and vanish with $\epsilon \rightarrow 0$. $\dot{\boldsymbol{\eta}} = \boldsymbol{\omega}$ for $\epsilon \rightarrow 0$ are the unperturbed frequencies on the torus.

The conditions required to be fulfilled in order for invariant tori to survive a perturbation are:

1. Linear independence of the frequencies,

$$\sum_i m_i \omega_i(\mathbf{J}) \neq 0, \quad m_i \in \mathbb{Z} / \{0\}, \quad (\text{A.16})$$

over a certain region of \mathbf{J} . $\omega_i(J_i)$ are the components of $\boldsymbol{\omega} = \nabla_{\mathbf{J}} H_0(\mathbf{J})$, and the m_i are the components of the vector \mathbf{m} ; thus it should hold that $\mathbf{m} \cdot \boldsymbol{\omega}(\mathbf{J}) \neq 0$.

2. Existence of sufficiently numerous derivatives of H_1 ; that is, we require a certain *softness* of the perturbation.

3. *Sufficiently large distance* from the resonance:

$$|\mathbf{m} \cdot \boldsymbol{\omega}| \geq \gamma(\epsilon) |\mathbf{m}|^\tau, \quad \forall \mathbf{m}. \quad (\text{A.17})$$

Here, τ depends on the number of degrees of freedom and the softness of the perturbed term. γ depends on ϵ and the *nonlinearity* G of the unperturbed Hamiltonian H_0 .

Since condition (3) cannot be fulfilled if $\gamma(\epsilon)$ is too large, and grows with ϵ , the smallness of the perturbation is a condition for the existence of KAM tori.

The uncoupled harmonic oscillator (in two dimensions) is helpful in elucidating the terms *linear independence* and *moderate linearity*:

$$H_0(J_1, J_2) = H_0(J_1) + H_0(J_2) = \omega_1 J_1 + \omega_2 J_2$$

$H_0(J_1, J_2)$ is a linear function of the action variables, and ω_i is independent of the action J_i , so that the frequencies are indeed constants:

$$\frac{\partial H_0}{\partial J_1} = \omega_1 = \text{const.}, \quad \frac{\partial H_0}{\partial J_2} = \omega_2 = \text{const.}$$

Furthermore, it holds that

$$\frac{\partial^2 H_0}{\partial J_i^2} = \frac{\partial^2 H_0}{\partial J_i \partial J_k} = \frac{\partial \omega_i}{\partial J_k} = 0, \quad i, k = 1, 2.$$

Assuming the unperturbed frequencies of the two degrees of freedom,

$$\omega_i = \frac{\partial H_0(J_1, J_2)}{\partial J_i}, \quad i = 1, 2.$$

are functions of the action variables:

$$\omega_i = \omega_i(J_1, J_2).$$

Then assuming that between the two degrees of freedom of the unperturbed system commensurable frequencies $\sum_i m_i \omega_i(J_1, J_2) = 0, m_i \in \mathbb{Z}/\{0\}$ exists for a certain pair (J_1, J_2) ; for example, $\omega_1(J_1, J_2) = \omega_2(J_1, J_2)$, that is, $m_1 \omega_1 + m_2 \omega_2 = 0$, with $m_1 = -m_2 = 1$. Then according to KAM theorem, the invariant torus will be destroyed after turning on the interaction ϵH_1 . Only those invariant tori for which the ω_i are linear independent in the sense of condition (1) come into further consideration and have a chance (if ϵ is small enough) to survive a perturbation.

Letting $f(\omega_1, \omega_2) = 0$ be a general relation between the frequencies, we now need to establish the requirements regarding $\omega_i(J_i)$ in order to be led to the noncommensurate frequencies. We do not want a relation of the type $\sum_i m_i \omega_i(\mathbf{J}) = 0$ for all J_i . In other words, we are interested in finding a condition for the linear independence of the frequencies,

$$\sum_i m_i \omega_i(J_1, J_2) \neq 0 \tag{A.18}$$

This is achieved using the functional dependence $f = f|\omega_1(J_1, J_2), \omega_2(J_1, J_2)| = 0$ to construct

$$\begin{aligned} df &= \frac{\partial f}{\partial \omega_1} \left[\frac{\partial \omega_1}{\partial J_1} dJ_1 + \frac{\partial \omega_1}{\partial J_2} dJ_2 \right] + \frac{\partial f}{\partial \omega_2} \left[\frac{\partial \omega_2}{\partial J_1} dJ_1 + \frac{\partial \omega_2}{\partial J_2} dJ_2 \right] \\ &= \left(\frac{\partial f}{\partial \omega_1} \frac{\partial \omega_1}{\partial J_1} + \frac{\partial f}{\partial \omega_2} \frac{\partial \omega_2}{\partial J_1} \right) dJ_1 + \left(\frac{\partial f}{\partial \omega_1} \frac{\partial \omega_1}{\partial J_2} + \frac{\partial f}{\partial \omega_2} \frac{\partial \omega_2}{\partial J_2} \right) dJ_2 = 0 \\ &\quad \forall dJ_1, dJ_2 \end{aligned} \tag{A.19}$$

This gives the following pair of equations:

$$\begin{aligned} \frac{\partial f}{\partial \omega_1} \frac{\partial \omega_1}{\partial J_1} + \frac{\partial f}{\partial \omega_2} \frac{\partial \omega_2}{\partial J_1} &= 0, \\ \frac{\partial f}{\partial \omega_1} \frac{\partial \omega_1}{\partial J_2} + \frac{\partial f}{\partial \omega_2} \frac{\partial \omega_2}{\partial J_2} &= 0, \end{aligned} \tag{A.20}$$

or in matrix form:

$$\begin{pmatrix} \frac{\partial \omega_1}{\partial J_1} & \frac{\partial \omega_2}{\partial J_1} \\ \frac{\partial \omega_1}{\partial J_2} & \frac{\partial \omega_2}{\partial J_2} \end{pmatrix} \begin{pmatrix} \frac{\partial f}{\partial \omega_1} \\ \frac{\partial f}{\partial \omega_2} \end{pmatrix} = 0 \tag{A.21}$$

or,

$$\begin{aligned} \sum_{k=1}^2 \left(\frac{\partial}{\partial J_i} \omega_k \right) \frac{\partial f}{\partial \omega_k} &= \left(\frac{\partial}{\partial \mathbf{J}} \omega \right)_{ik} \frac{\partial f}{\partial \omega_k} \\ &= (\nabla_{\mathbf{J}} \omega) \cdot \nabla_{\omega} f(\omega) = 0. \end{aligned} \tag{A.22}$$

From $\det(\nabla_{\mathbf{J}} \omega) \neq 0$ follows, as only solution, $\nabla_{\omega} f = 0$; that is $\partial f / \partial \omega_1 = 0$ and $\partial f / \partial \omega_2 = 0$. Therefore, no valid relation for all J_i of the kind $f(\omega_1, \omega_2) = m_1 \omega_1 + m_2 \omega_2 = 0, m_i \neq 0$. Consequently, as necessary condition for the nonlinear dependence of the frequencies, we obtain

$$\det(\nabla_{\mathbf{J}} \omega(\mathbf{J})) = \det \left(\frac{\partial \omega_i}{\partial J_k} \right) = \det \left(\frac{\partial^2 H_0}{\partial J_i \partial J_k} \right) \neq 0. \tag{A.23}$$

Turning on the interaction ϵH_1 and assuming a particular resonance behaviour $f(\omega_1, \omega_2) \equiv r\omega_1 - s\omega_2 = 0$ in the Fourier decomposition of ϵH_1 also leads to the destruction of the torus. Thus it is necessary to formulate a nonlinearity condition for this case too, in order not to completely destroy the invariant torus. Here a weaker condition than (A.23) can be shown to prevail; requiring only that the frequency $\omega(\mathbf{J})$ not be zero along the direction of the actual change of \mathbf{J} . For proof consider the Hamiltonian

$$H = H_0(J_1, J_2) + \epsilon \sum_{l,m} H_{lm}^{(1)}(J_1, J_2) e^{i(l\theta_1 - m\theta_2)} \tag{A.24}$$

and choose a particular resonance $l = r, m = s$ and $\omega_2/\omega_1 = r/s$; in other words,

$$f(\omega_1, \omega_2)|_{res.} = r\dot{\theta}_1 - s\dot{\theta}_2 = r\omega_1 - s\omega_2 = 0,$$

which gives

$$\frac{\partial f}{\partial \omega_1} = r, \quad \frac{\partial f}{\partial \omega_2} = -s, \quad (\text{A.25})$$

At the point of resonance, using canonical equations, we get

$$\begin{aligned} \dot{J}_1 &= -\frac{\partial H}{\partial \theta_1} = ir\epsilon H_{rs}^{(1)} e^{i(r\theta_1 - s\theta_2)}, \\ \dot{J}_2 &= -\frac{\partial H}{\partial \theta_2} = is\epsilon H_{rs}^{(1)} e^{i(r\theta_1 - s\theta_2)}, \end{aligned}$$

from which is derived

$$\frac{\dot{J}_1}{\dot{J}_2} = \left. \frac{dJ_1}{dJ_2} \right|_{res.} = -\frac{r}{s} = -\frac{\omega_2}{\omega_1}. \quad (\text{A.26})$$

Thus in the (J_1, J_2) -diagram, the direction of \mathbf{J} at the location of the resonance is parallel to $\mathbf{m} = \{-r, s\} \sim \hat{\mathbf{J}}$, and by the assumption $\mathbf{m} \cdot \boldsymbol{\omega} = 0$, then $\hat{\mathbf{J}} \cdot \boldsymbol{\omega} = 0$. The unit vector $\hat{\mathbf{J}}$ is normalized according to

$$\hat{\mathbf{J}} = -\frac{r}{\sqrt{r^2 + s^2}} \hat{\mathbf{J}}_1 + \frac{s}{\sqrt{r^2 + s^2}} \hat{\mathbf{J}}_2.$$

So we obtain

$$\begin{aligned} 0 &= \hat{\mathbf{J}} \cdot \boldsymbol{\omega} = \hat{\mathbf{J}} \cdot \nabla H_0(\mathbf{J}) \\ &= \frac{-r}{\sqrt{r^2 + s^2}} \frac{\partial H_0}{\partial J_1} + \frac{s}{\sqrt{r^2 + s^2}} \frac{\partial H_0}{\partial J_2}. \end{aligned}$$

Together with $0 = f(\omega_1, \omega_2) = r\omega_1 - s\omega_2$, we then get for the frequencies:

$$\omega_1 = -\frac{1}{\sqrt{r^2 + s^2}} \frac{\partial H_0}{\partial J_1}, \quad \omega_2 = -\frac{1}{\sqrt{r^2 + s^2}} \frac{\partial H_0}{\partial J_2}. \quad (\text{A.27})$$

Using equation A.27 together with equation A.25 in equation A.21 on the page before gives,

$$r \frac{\partial^2 H_0}{\partial J_1^2} - s \frac{\partial^2 H_0}{\partial J_1 \partial J_2} = 0 \quad (\text{A.28})$$

$$r \frac{\partial^2 H_0}{\partial J_1 \partial J_2} - s \frac{\partial^2 H_0}{\partial J_2^2} = 0 \quad (\text{A.29})$$

Then $(r \times (A.28)) + (-s) \times (A.29)$ finally gives the sufficient condition for the *nonlinearity* as:

$$r^2 \frac{\partial^2 H_0}{\partial J_1^2} - 2rs \frac{\partial^2 H_0}{\partial J_1 \partial J_2} + s^2 \frac{\partial^2 H_0}{\partial J_2^2} \neq 0 \quad (A.30)$$

In canonical perturbation theory, the Hamiltonian describing the motion in the vicinity of a resonance is given by

$$\Delta \bar{H} = \frac{1}{2} G (\Delta \hat{J}_1)^2 - F \cos \hat{\theta}_1.$$

Where G is the nonlinearity parameter, that is the measure of the degree of linear independence above,

$$G(\hat{J}_{i0}) = \frac{\partial^2 \hat{H}_0}{\partial \hat{J}_{i0}^2},$$

and F is the product of the strength of the perturbation, ϵ , and the Fourier amplitude:

$$F = -2\epsilon H_{rs}^{(1)}(\hat{J}_{i0}).$$

To show that the nonlinearity condition can be derived from canonical perturbation theory: Apply the generating function

$$F_2(r\theta_1 - s\theta_2)\hat{J}_1 + \theta_2\hat{J}_2 \quad (A.31)$$

to the Hamiltonian

$$H = H_0(J_1, J_2) + \epsilon \sum_{l,m} H_{lm}^{(1)}(J_1, J_2) e^{i(l\theta_1 - m\theta_2)} \quad (A.32)$$

and obtain (in lowest order ϵ) in the new variables $r\hat{J}_1 = J_1, \dots$, after having expanded around the resonant value of the action and averaged over the fast variables:

$$\Delta \bar{H} = \frac{1}{2} \frac{\partial^2 \hat{H}_0}{\partial \hat{J}_1^2} (\Delta \hat{J}_1)^2 + 2\epsilon H_{rs}^{(1)} \cos \hat{\theta}_1. \quad (A.33)$$

Then again considering the case of the accidental degeneracy, $\partial^2 \hat{H}_0 / \partial \hat{J}_1^2 \neq 0$, we find

$$\begin{aligned}
 0 \neq \frac{\partial^2 \hat{H}_0}{\partial \hat{J}_1^2} &= \frac{\partial}{\partial \hat{J}_1} \left[\frac{\partial \hat{H}_0}{\partial J_1} \overbrace{\frac{\partial \hat{J}_1}{\partial \hat{J}_1}}{=r} + \frac{\partial \hat{H}_0}{\partial J_2} \overbrace{\frac{\partial \hat{J}_2}{\partial \hat{J}_1}}{=-s} \right] \\
 &= \frac{\partial}{\partial \hat{J}_1} \left[r \frac{\partial H_0}{\partial J_1} - s \frac{\partial H_0}{\partial J_2} \right] \\
 &= r \left[\frac{\partial^2 H_0}{\partial J_1^2} \overbrace{\frac{\partial \hat{J}_1}{\partial \hat{J}_1}}{=r} + \frac{\partial^2 H_0}{\partial J_1 \partial J_2} \overbrace{\frac{\partial \hat{J}_2}{\partial \hat{J}_1}}{=-s} \right] \\
 &\quad - s \left[\frac{\partial^2 H_0}{\partial J_1 \partial J_2} \overbrace{\frac{\partial \hat{J}_1}{\partial \hat{J}_1}}{=r} + \frac{\partial^2 H_0}{\partial J_2^2} \overbrace{\frac{\partial \hat{J}_2}{\partial \hat{J}_1}}{=-s} \right] \\
 &= r^2 \frac{\partial^2 H_0}{\partial J_1^2} - 2rs \frac{\partial^2 H_0}{\partial J_1 \partial J_2} + s^2 \frac{\partial^2 H_0}{\partial J_2^2} \neq 0 \tag{A.34}
 \end{aligned}$$

As to the question of *how far from zero* we must stay, then for a fixed ϵ -value, one can estimate the required nonlinearity in G by assuming the deviation in the action ΔJ_1 is much smaller than the unperturbed action $J_0(\epsilon = 0)$. Now $\Delta J_1 = r \Delta \hat{J}_1$. For the half-width of the separatrix, $|\Delta \hat{J}_1| = 2(2\epsilon H_{rs}/G)^{1/2}$, so that for the total we estimate

$$4r \left(\frac{2\epsilon H_{rs}}{G} \right)^{1/2} \ll J_0 \tag{A.35}$$

or

$$G \gg \frac{32r^2(\epsilon H_{rs})}{J_0^2}. \tag{A.36}$$

In this case, we find KAM curves.

For tori with sufficiently irrational frequency ratio and small enough perturbation, it has been made plausible that these are only deformed and remain otherwise stable (KAM curves). It would thus be natural to suspect that for rational $\alpha = r/s$, where the KAM theorem fails, all the tori would be destroyed. The circumstances of just how this happens are, however, more complicated, as a theorem going back to Poincare and Birkoff [6] shows.

Appendix B

Derivation of the equations of motion

The time rate of change of an arbitrary vector \mathbf{G} as seen by observers in the laboratory and the rotating frame is given by [102]:

$$\left(\frac{d\mathbf{G}}{dt}\right)_{lab} = \left(\frac{d\mathbf{G}}{dt}\right)_{rot} + \boldsymbol{\omega} \wedge \mathbf{G} \quad (\text{B.1})$$

This is the basic kinematic law upon which the dynamical equations of motion for a rigid body are founded. We can replace \mathbf{G} by \mathbf{r} , the radius vector of the particle and obtain:

$$\dot{\mathbf{r}}_{lab} = \dot{\mathbf{r}}_{rot} + \boldsymbol{\omega} \wedge \mathbf{r} \text{ or equivalently} \quad (\text{B.2})$$

$$\mathbf{v}_{lab} = \mathbf{v}_{rot} + \boldsymbol{\omega} \wedge \mathbf{r} \quad (\text{B.3})$$

Where \mathbf{v}_{lab} and \mathbf{v}_{rot} are the velocities of the particle relative to the laboratory and rotating set of axes, respectively, and $\boldsymbol{\omega}$ is the constant angular velocity of the boundary relative to the inertial frame. Applying (B.1) again gives the time rate of change of \mathbf{v}_{lab} :

$$\mathbf{a}_{lab} = \mathbf{a}_{rot} + 2\boldsymbol{\omega} \wedge \mathbf{v}_{rot} + \boldsymbol{\omega} \wedge (\boldsymbol{\omega} \wedge \mathbf{r}) \quad (\text{B.4})$$

Where \mathbf{a}_{lab} and \mathbf{a}_{rot} are the accelerations of the particle in the two systems. The equation of motion, which in the inertial frame is simply $\mathbf{F} = m\mathbf{a}_{lab}$ expands, when expressed in the rotating co-ordinates, into the equation:

$$\mathbf{F} - 2m(\boldsymbol{\omega} \wedge \mathbf{v}_{rot}) - m\boldsymbol{\omega} \wedge (\boldsymbol{\omega} \wedge \mathbf{r}) = m\mathbf{a}_{rot} \quad (\text{B.5})$$

Thus to an observer in the rotating frame it appears as if the particle is moving under the influence of an effective force, \mathbf{F}_{eff} :

$$\mathbf{F}_{eff} = \mathbf{F} - 2m(\boldsymbol{\omega} \wedge \mathbf{v}_{rot}) - m\boldsymbol{\omega} \wedge (\boldsymbol{\omega} \wedge \mathbf{r}) \quad (\text{B.6})$$

The last term in equation (B.6) is a vector normal to $\boldsymbol{\omega}$ and pointing outwards with magnitude $m\omega^2 r \sin \theta$ and so recognised as the familiar centrifugal force. When the particle is stationary in the rotating frame this is the only additional force in the effective force. However, when the particle is moving the middle term, known as the Coriolis force, comes into play. It differs from normal (non-dissipative) forces in its dependency on the particle velocity.

Appendix C

Lagrangian for a rotating billiard

Following [103] the Lagrangian and the equation of motion in a general non-inertial frame of reference can be derived from those in the inertial frame (subscripted by 0) as follows; The Lagrangian and the equation of motion in the inertial frame are respectively:

$$\mathcal{L}_0 = \frac{1}{2}m\mathbf{v}_0^2 - U \quad (\text{C.1})$$

$$m\frac{d\mathbf{v}_0}{dt} = m\mathbf{a} = -\frac{\partial U}{\partial \mathbf{r}} \quad (\text{C.2})$$

The basis of the transformation of these to the non-inertial frame is the principle of least action, whose validity does not depend on the frame of reference chosen. Lagrange's equations

$$\frac{d}{dt} \left(\frac{\partial \mathcal{L}}{\partial \mathbf{v}} \right) = \frac{\partial \mathcal{L}}{\partial \mathbf{r}} \quad (\text{C.3})$$

are likewise valid, but the Lagrangian is no longer of the form of equation (C.1) and to obtain the correct form requires an appropriate transformation of the function \mathcal{L}_0 , which is performed in two steps. First consider a frame of reference \mathbf{K}' which moves with a translational velocity $\mathbf{V}(t)$ relative to the inertial frame \mathbf{K}_0 . The respective velocities are related by

$$\mathbf{v}_0 = \mathbf{v}' + \mathbf{V}(t) \quad (\text{C.4})$$

Substitution of equation (C.4) into equation (C.1) gives the Lagrangian in \mathbf{K}' :

$$\mathcal{L}' = \frac{1}{2}m\mathbf{v}'^2 + m\mathbf{v}' \cdot \mathbf{V} + \frac{1}{2}m\mathbf{V}^2 - U \quad (\text{C.5})$$

Now, \mathbf{V}^2 is a given function of time, and can be written as the total derivative with respect to t of some other function, so the third term in \mathcal{L}' can be omitted. Also $\mathbf{v}' = d\mathbf{r}'/dt$, where \mathbf{r}' is the radius vector of the particle in the frame \mathbf{K}' . Hence

$$m\mathbf{V}(t) \cdot \mathbf{v}' = m \cdot \mathbf{V} \frac{d\mathbf{r}'}{dt} = \frac{d}{dt}(m\mathbf{V} \cdot \mathbf{r}') - m\mathbf{r}' \cdot \frac{d\mathbf{V}}{dt} \quad (\text{C.6})$$

Substituting equation (C.6) into the Lagrangian and again omitting the total time derivative gives the Lagrangian in \mathcal{L}' :

$$\mathcal{L}' = \frac{1}{2}mv'^2 - m\mathbf{W}(t) \cdot \mathbf{r}' - U \quad (\text{C.7})$$

Where $\mathbf{W}(t) = d\mathbf{V}/dt$ is the translational acceleration of the frame \mathbf{K}' . The Lagrange's equation derived from equation (C.7) is

$$m \frac{d\mathbf{v}'}{dt} = m\mathbf{a}' = -\frac{\partial U}{\partial \mathbf{r}'} - m\mathbf{W}(t) \quad (\text{C.8})$$

Secondly, introduce a further frame of reference \mathbf{K} , whose origin coincides with that of \mathbf{K}' but which rotates relative to \mathbf{K}' with angular velocity $\boldsymbol{\omega}(t)$. Thus \mathbf{K} executes both a translational and a rotational motion relative to the inertial frame \mathbf{K}_0 . The velocity \mathbf{v}' of the particle relative to \mathbf{K}' is composed of its velocity \mathbf{v} relative to \mathbf{K} and the velocity $\boldsymbol{\omega} \wedge \mathbf{r}$ of its rotation with \mathbf{K} :

$$\mathbf{v}' = \mathbf{v} + \boldsymbol{\omega} \wedge \mathbf{r} \quad (\text{C.9})$$

since the radius vectors \mathbf{r} and \mathbf{r}' coincide in the frames \mathbf{K} and \mathbf{K}' . Substituting equation (C.9) into equation (C.7) we obtain the general form of the Lagrangian in an arbitrary, not necessarily inertial, frame of reference:

$$\mathcal{L} = \frac{1}{2}mv^2 + m\mathbf{v} \cdot \boldsymbol{\omega} \wedge \mathbf{r} + \frac{1}{2}m(\boldsymbol{\omega} \wedge \mathbf{r})^2 - m\mathbf{W} \cdot \mathbf{r} - U \quad (\text{C.10})$$

This leads to the equation of motion:

$$m \frac{d\mathbf{v}}{dt} = m\mathbf{a} = -\frac{\partial U}{\partial \mathbf{r}} - m\mathbf{W} + m\mathbf{r} \wedge \dot{\boldsymbol{\omega}} + 2m\mathbf{v} \wedge \boldsymbol{\omega} + m\boldsymbol{\omega} \wedge (\mathbf{r} \wedge \boldsymbol{\omega}) \quad (\text{C.11})$$

Where again we have the centrifugal force, $m\boldsymbol{\omega} \wedge (\mathbf{r} \wedge \boldsymbol{\omega})$, and the Coriolis force, $2m\mathbf{v} \wedge \boldsymbol{\omega}$. The force $m\mathbf{r} \wedge \dot{\boldsymbol{\omega}}$ appearing in equation (C.11) is due solely to the non-uniformity of the rotation.

For the rotating billiard we have $U = 0$ inside the boundary, a uniformly rotating frame, so $\boldsymbol{\omega} = \text{constant}$, and no translational acceleration giving $\mathbf{W} = \mathbf{0}$. Thus we obtain the Lagrangian:

$$\mathcal{L} = \frac{1}{2}mv^2 + m\mathbf{v} \cdot \boldsymbol{\omega} \wedge \mathbf{r} + \frac{1}{2}m(\boldsymbol{\omega} \wedge \mathbf{r})^2 \quad (\text{C.12})$$

and the equation of motion derived from equation (C.12) is again equation (B.4) which leads to the equation of motion given by equation (3.2).

The energy of the particle in this case is obtained by substituting

$$\mathbf{p} = \frac{\partial \mathcal{L}}{\partial \mathbf{v}} = m\mathbf{v} + m\boldsymbol{\omega} \wedge \mathbf{r} \quad \text{into} \quad (\text{C.13})$$

$$\mathcal{E} = \mathbf{p} \cdot \mathbf{v} - \mathcal{L} \quad \text{which gives} \quad (\text{C.14})$$

$$\mathcal{E} = \frac{1}{2}mv^2 - \frac{1}{2}m(\boldsymbol{\omega} \wedge \mathbf{r})^2 \quad (\text{C.15})$$

The rotation of the frame adds to the energy a term depending only on the coordinates of the particle and proportional to the square of the angular velocity. This additional term is the centrifugal potential energy. The velocity \mathbf{v} of the particle is related to \mathbf{v}_0 by

$$\mathbf{v}_0 = \mathbf{v} + \boldsymbol{\omega} \wedge \mathbf{r} \quad (\text{C.16})$$

The momentum \mathbf{p} , in equation (C.14), of the particle in the frame \mathbf{K} is therefore the same as its momentum, $\mathbf{p}_0 = m\mathbf{v}_0$, in the frame \mathbf{K}_0 . The angular momenta $\mathbf{M}_0 = \mathbf{r}\mathbf{x}\mathbf{p}_0$ and $\mathbf{M} = \mathbf{r}\mathbf{x}\mathbf{p}$ are likewise equal. However, the energies of the particle in the two frames are not the same as can be seen by substituting \mathbf{v} from equation (C.16) into equation (C.15), we obtain

$$\mathcal{E} = \frac{1}{2}mv_0^2 - m\mathbf{v}_0 \cdot \boldsymbol{\omega} \wedge \mathbf{r} = \frac{1}{2}mv_0^2 - m\mathbf{r} \wedge \mathbf{v}_0 \cdot \boldsymbol{\omega} \quad (\text{C.17})$$

Using the angular momentum \mathbf{M} , we have

$$\mathcal{E} = \mathcal{E}_0 - \mathbf{M} \cdot \boldsymbol{\omega} \quad (\text{C.18})$$

Which gives the law of transformation of energy when we change to a uniformly rotating frame. With conditions given by equation (3.1), equation (C.17) becomes

$$\mathcal{E} = \frac{1}{2}m(\dot{x}^2 + \dot{y}^2) - m\omega(xy - y\dot{x}) \quad (\text{C.19})$$

and equation (C.12) becomes

$$\mathcal{L} = \frac{1}{2}((\dot{x}^2 + \dot{y}^2) + \omega^2(x^2 + y^2)) + \omega(xy - y\dot{x}) \quad \text{or} \quad (\text{C.20})$$

$$\mathcal{L} = |\dot{z}|^2 + |\omega z|^2 + i\omega^2(\dot{z}z - z\dot{z}) \quad (\text{C.21})$$

Appendix D

Energy conservation

Energy conservation in the rotating frame can be shown by writing equation (3.2) as

$$\ddot{x} + i\ddot{y} + 2i\omega(\dot{x} + i\dot{y}) - \omega^2(x + iy) = 0 \quad (\text{D.1})$$

and equating real and imaginary components leads to the following two equations:

$$\ddot{x} - 2\omega\dot{y} - \omega^2x = 0 \quad (\text{D.2})$$

$$\ddot{y} + 2\omega\dot{x} - \omega^2y = 0 \quad (\text{D.3})$$

Then equation (D.2) $\times \dot{x}$ + equation (D.3) $\times \dot{y}$ gives

$$(\dot{x}\ddot{x} - \omega^2x\dot{x}) + (\dot{y}\ddot{y} - \omega^2y\dot{y}) = 0 \quad \text{so} \quad (\text{D.4})$$

$$\frac{d}{dt}(\dot{x}^2 - \omega^2x^2) + \frac{d}{dt}(\dot{y}^2 - \omega^2y^2) = 0 \quad \text{hence} \quad (\text{D.5})$$

$$(\dot{x}^2 + \dot{y}^2) - \omega^2(x^2 + y^2) = \text{constant and} \quad (\text{D.6})$$

$$\mathcal{E} = \frac{1}{2}(|\dot{z}|^2 - |\omega z|^2) \quad \text{is conserved.} \quad (\text{D.7})$$

Energy conservation implies by (3.14) that

$$p_x^2 + p_y^2 = \text{constant} \quad (\text{D.8})$$

$$xp_y - yp_x = L = \text{constant} \quad (\text{D.9})$$

So both \mathbf{p} and L are independently conserved between reflections, and correspond to conservation of linear and angular momenta in the laboratory frame. However, they are not conserved on reflection, although their sum is.

Appendix E

Bounce maps

Let us assume the ball is starting from side 1, then using equations 3.5, 3.6, 3.16, 3.17 and 3.23 - 3.26 on page 50 we arrive at:

$$\begin{aligned}
 x' + iy' &= [(2X_1 - 1 + (\sqrt{E + 2\omega^2}(2X_2 - 1) + \omega)T) \cos(\omega T) \\
 &+ (-1 + (-2EW + \omega(2X_1 - 1))T) \sin(\omega T)] \\
 &+ i[(-1 + (-2EW + \omega(2X_1 - 1))T) \cos(\omega T) \\
 &+ (-2X_1 + 1 + (-\sqrt{E + 2\omega^2})(2X_2 - 1) - \omega)T) \sin(\omega T)] \\
 &\equiv A + iB
 \end{aligned} \tag{E.1}$$

$$\begin{aligned}
 \dot{x}' + i\dot{y}' &= [(\sqrt{E + 2\omega^2}(2X_2 - 1) + (-2\omega EW + \omega^2(2X_2 - 1))T) \cos(\omega T) \\
 &+ (-2EW + (-\omega\sqrt{E + 2\omega^2}(2X_2 - 1) - \omega^2)T) \sin(\omega T)] \\
 &+ i[-2EW + (-\omega\sqrt{E + 2\omega^2}(2X_2 - 1) - \omega^2)T) \cos(\omega T) \\
 &+ (-\sqrt{E + 2\omega^2}(2X_2 - 1) + (2\omega EW - \omega^2(2X_2 - 1))T) \sin(\omega T)] \\
 &\equiv C + iD
 \end{aligned} \tag{E.2}$$

Where $EW \equiv \sqrt{(E + 2\omega^2)X_2(1 - X_2) - \omega^2X_1(1 - X_1)}$ and $T \equiv T(E, X_1, X_2)$.
 Expressing $(x', y', \dot{x}'$ and $\dot{y}')$ in terms of (X'_1, X'_2) for the four sides leads to:

$$\left. \begin{aligned}
 -1 &= B \\
 X'_1 &= \frac{1}{2} + \frac{A}{2} \\
 X'_2 &= \frac{1}{2} + \frac{C}{2\sqrt{E+2\omega^2}} \\
 EW' &= -\frac{D}{2}
 \end{aligned} \right\} \text{For } B_{11} \tag{E.3}$$

$$\left. \begin{aligned} 1 &= A \\ X'_1 &= \frac{1}{2} + \frac{B}{2} \\ X'_2 &= \frac{1}{2} + \frac{D}{2\sqrt{E+2\omega^2}} \\ EW' &= \frac{C}{2} \end{aligned} \right\} \text{For } B_{12} \quad (\text{E.4})$$

$$\left. \begin{aligned} 1 &= B \\ X'_1 &= \frac{1}{2} - \frac{A}{2} \\ X'_2 &= \frac{1}{2} - \frac{C}{2\sqrt{E+2\omega^2}} \\ EW' &= \frac{D}{2} \end{aligned} \right\} \text{For } B_{13} \quad (\text{E.5})$$

$$\left. \begin{aligned} -1 &= A \\ X'_1 &= \frac{1}{2} - \frac{B}{2} \\ X'_2 &= \frac{1}{2} - \frac{D}{2\sqrt{E+2\omega^2}} \\ EW' &= -\frac{C}{2} \end{aligned} \right\} \text{For } B_{14} \quad (\text{E.6})$$

Where

$$EW' \equiv 2\sqrt{(E + 2\omega^2)X'_2(1 - X'_2) - \omega^2X'_1(1 - X'_1)}$$

knowing T , then with the above equations \mathbf{B} is defined implicitly.

Appendix F

Elements of the Jacobian, \mathbf{J} , matrix

The elements of \mathbf{J} for B_{11} are given by:

$$\begin{aligned}
 \frac{\partial X'_1}{\partial X_1} = & \frac{1}{2} \left\{ \left[2 + \left(\sqrt{E + 2\omega^2}(2X_2 - 1) + \omega \right) \frac{\partial T}{\partial X_1} \right] \cos(\omega T) \right. \\
 & - \left[2X_1 - 1 + \left(\sqrt{E + 2\omega^2}(2X_2 - 1) + \omega \right) T \right] \sin(\omega T) \omega \frac{\partial T}{\partial X_1} \\
 & + \left[\left(\frac{-\omega^2(2X_1 - 1)}{EW} + 2\omega \right) T \right. \\
 & \quad \left. + (-2EW + \omega(2X_1 - 1)) \frac{\partial T}{\partial X_1} \right] \sin(\omega T) \\
 & \left. + [-1 + (-2EW + \omega(2X_1 - 1))T] \cos(\omega T) \omega \frac{\partial T}{\partial X_1} \right\} \quad (\text{F.1})
 \end{aligned}$$

$$\begin{aligned}
 \frac{\partial X'_1}{\partial X_2} = & \frac{1}{2} \left\{ \left[2\sqrt{E + 2\omega^2}T \right. \right. \\
 & \quad \left. + \left(\sqrt{E + 2\omega^2}(2X_2 - 1) + \omega \right) \frac{\partial T}{\partial X_2} \right] \cos(\omega T) \\
 & - \left[2X_1 - 1 + \left(\sqrt{E + 2\omega^2}(2X_2 - 1) + \omega \right) T \right] \sin(\omega T) \omega \frac{\partial T}{\partial X_2} \\
 & + \left[\frac{(E + 2\omega^2)(2X_2 - 1)T}{-EW} + (2EW + \omega(2X_1 - 1)) \frac{\partial T}{\partial X_2} \right] \sin(\omega T) \\
 & \left. + [-1 + (-2EW + \omega(2X_1 - 1))T] \cos(\omega T) \omega \frac{\partial T}{\partial X_2} \right\} \quad (\text{F.2})
 \end{aligned}$$

$$\begin{aligned}
\frac{\partial X'_2}{\partial X_1} = & \frac{1}{2\sqrt{E+2\omega^2}} \{ \\
& \left[\left(-\frac{\omega^3(2X_1-1)}{EW} + 2\omega^2 \right) T + (-2\omega EW + \omega^2(2X_1-1)) \frac{\partial T}{\partial X_1} \right] \cos(\omega T) \\
& - \left[\sqrt{E+2\omega^2}(2X_2-1) + (-2\omega EW + \omega^2(2X_1-1))T \right] \sin(\omega T) \omega \frac{\partial T}{\partial X_1} \\
& + \left[-\frac{\omega^2(2X_1-1)}{EW} + (-\omega\sqrt{E+2\omega^2}(2X_2-1) - \omega^2) \frac{\partial T}{\partial X_1} \right] \sin(\omega T) \\
& + \left[-2EW + (-\omega\sqrt{E+2\omega^2}(2X_2-1) - \omega^2)T \right] \cos(\omega T) \omega \frac{\partial T}{\partial X_2} \} \quad (\text{F.3})
\end{aligned}$$

$$\begin{aligned}
\frac{\partial X'_2}{\partial X_2} = & \frac{1}{2\sqrt{E+2\omega^2}} \{ \\
& \left[2\sqrt{E+2\omega^2} + \frac{\omega(E+2\omega^2)(2X_2-1)T}{EW} \right. \\
& \quad \left. + (-2\omega EW + \omega^2(2X_1-1)) \frac{\partial T}{\partial X_2} \right] \cos(\omega T) \\
& - \left[\sqrt{E+2\omega^2}(2X_2-1) + (-2\omega EW + \omega^2(2X_1-1))T \right] \sin(\omega T) \omega \frac{\partial T}{\partial X_2} \\
& + \left[\frac{(E+2\omega^2)(2X_2-1)}{EW} - 2\omega\sqrt{E+2\omega^2}T \right. \\
& \quad \left. + (-\omega\sqrt{E+2\omega^2}(2X_2-1) - \omega^2) \frac{\partial T}{\partial X_2} \right] \sin(\omega T) \quad (\text{F.4}) \\
& + \left[-2EW + (-\omega\sqrt{E+2\omega^2}(2X_2-1) - \omega^2)T \right] \cos(\omega T) \omega \frac{\partial T}{\partial X_2} \}
\end{aligned}$$

For B_{12} we have:

$$\begin{aligned}
\frac{\partial X'_1}{\partial X_1} = & \frac{1}{2} \left\{ \left[\left(-\frac{\omega^2(2X_1 - 1)}{EW} + 2\omega \right) T \right. \right. \\
& \left. \left. + (-2EW + \omega(2X_1 - 1)) \frac{\partial T}{\partial X_1} \right] \cos(\omega T) \right. \\
& - [-1 + (-2EW + \omega(2X_1 - 1))T] \sin(\omega T) \omega \frac{\partial T}{\partial X_1} \\
& + \left[-2 + \left(-\sqrt{E + 2\omega^2}(2X_2 - 1) - \omega \right) \frac{\partial T}{\partial X_1} \right] \sin(\omega T) \\
& \left. + \left[-(2X_2 - 1) + \left(-\sqrt{E + 2\omega^2}(2X_2 - 1) - \omega \right) T \right] \cos(\omega T) \omega \frac{\partial T}{\partial X_1} \right\}
\end{aligned} \tag{F.5}$$

$$\begin{aligned}
\frac{\partial X'_1}{\partial X_2} = & \frac{1}{2} \left\{ \left[\frac{(E + 2\omega^2)(2X_2 - 1)T}{EW} \right. \right. \\
& \left. \left. + (-2EW + \omega(2X_1 - 1)) \frac{\partial T}{\partial X_2} \right] \cos(\omega T) \right. \\
& - [-1 + (-2EW + \omega(2X_1 - 1))T] \sin(\omega T) \omega \frac{\partial T}{\partial X_2} \\
& + \left[-2\sqrt{E + 2\omega^2}T + \left(-\sqrt{E + 2\omega^2}(2X_2 - 1) - \omega \right) \frac{\partial T}{\partial X_2} \right] \sin(\omega T) \\
& \left. + \left[-(2X_1 - 1) + \left(-\sqrt{E + 2\omega^2}(2X_2 - 1) - \omega \right) T \right] \cos(\omega T) \omega \frac{\partial T}{\partial X_2} \right\}
\end{aligned} \tag{F.6}$$

$$\begin{aligned}
\frac{\partial X'_2}{\partial X_1} = & -\frac{1}{2\sqrt{E + 2\omega^2}} \left\{ \right. \\
& \left[-\frac{\omega^2(2X_1 - 1)}{EW} + \left(-\omega\sqrt{E + 2\omega^2}(2X_2 - 1) - \omega^2 \right) \frac{\partial T}{\partial X_1} \right] \cos(\omega T) \\
& - \left[-2EW + \left(-\omega\sqrt{E + 2\omega^2}(2X_2 - 1) - \omega^2 \right) T \right] \sin(\omega T) \omega \frac{\partial T}{\partial X_1} \\
& + \left[\left(\frac{\omega^3(2X_1 - 1)}{EW} - 2\omega^2 \right) T \right. \\
& \quad \left. + (2\omega EW - \omega^2(2X_1 - 1)) \frac{\partial T}{\partial X_1} \right] \sin(\omega T) \\
& + \left[-\sqrt{E + 2\omega^2}(2X_2 - 1) \right. \\
& \quad \left. + (2\omega EW - \omega^2(2X_1 - 1))T \right] \cos(\omega T) \omega \frac{\partial T}{\partial X_1} \left. \right\}
\end{aligned} \tag{F.7}$$

$$\begin{aligned}
\frac{\partial X'_2}{\partial X_2} = & \frac{1}{2\sqrt{E+2\omega^2}} \left\{ \right. \\
& \left[\frac{(E+2\omega^2)(2X_2-1)}{EW} - 2\omega\sqrt{E+2\omega^2}T \right. \\
& \left. \left. + (-\omega\sqrt{E+2\omega^2}(2X_2-1) - \omega^2) \frac{\partial T}{\partial X_2} \right] \cos(\omega T) \right. \\
& - \left[-2EW + (-\omega\sqrt{E+2\omega^2}(2X_2-1) - \omega^2)T \right] \sin(\omega T) \omega \frac{\partial T}{\partial X_2} \\
& + \left[-2\sqrt{E+2\omega^2} - \frac{\omega(E+2\omega^2)(2X_2-1)T}{EW} \right. \\
& \left. \left. + (+2\omega EW - \omega^2(2X_1-1)) \frac{\partial T}{\partial X_2} \right] \sin(\omega T) \right. \\
& + \left[-\sqrt{E+2\omega^2}(2X_2-1) \right. \\
& \left. \left. + (+2\omega EW - \omega^2(2X_1-1))T \right] \cos(\omega T) \omega \frac{\partial T}{\partial X_2} \right\} \quad (\text{F.8})
\end{aligned}$$

For B_{13} we have:

$$\begin{aligned}
\frac{\partial X'_1}{\partial X_1} = & \frac{1}{2} \left\{ - \left[2 + \left(\sqrt{E+2\omega^2}(2X_2-1) + \omega \right) \frac{\partial T}{\partial X_1} \right] \cos(\omega T) \right. \\
& + \left[2X_2 - 1 + \left(\sqrt{E+2\omega^2}(2X_2-1) + \omega \right) T \right] \sin(\omega T) \omega \frac{\partial T}{\partial X_1} \\
& - \left[\left(-\frac{\omega^2(2X_1-1)}{EW} + 2\omega \right) T + (-2EW + \omega(2X_1-1)) \frac{\partial T}{\partial X_1} \right] \sin(\omega T) \\
& \left. - [-1 + (-2EW + \omega(2X_1-1))T] \cos(\omega T) \omega \frac{\partial T}{\partial X_1} \right\} \quad (\text{F.9})
\end{aligned}$$

$$\begin{aligned}
\frac{\partial X'_1}{\partial X_2} = & \frac{1}{2} \left\{ - \left[2\sqrt{E+2\omega^2}T \right. \right. \\
& \left. \left. + \left(\sqrt{E+2\omega^2}(2X_2-1) + \omega \right) \frac{\partial T}{\partial X_2} \right] \cos(\omega T) \right. \\
& + \left[2X_1 - 1 + \left(\sqrt{E+2\omega^2}(2X_2-1) + \omega \right) T \right] \sin \omega T \omega \frac{\partial T}{\partial X_2} \\
& - \left[\frac{(E+2\omega^2)(2X_2-1)T}{EW} + (-2EW + \omega(2X_1-1)) \frac{\partial T}{\partial X_2} \right] \sin(\omega T) \\
& \left. - [-1 + (-2EW + \omega(2X_1-1))T] \cos(\omega T) \omega \frac{\partial T}{\partial X_2} \right\} \quad (\text{F.10})
\end{aligned}$$

$$\begin{aligned}
\frac{\partial X'_2}{\partial X_1} = & -\frac{1}{2\sqrt{E+2\omega^2}} \left\{ \right. \\
& \left[\left(-\frac{\omega^3(2X_1-1)}{EW} + 2\omega^2 \right) T + (-2\omega EW + \omega^2(2X_1-1)) \frac{\partial T}{\partial X_1} \right] \cos(\omega T) \\
& - \left[\sqrt{E+2\omega^2}(2X_2-1) + (-2\omega EW + \omega^2(2X_1-1))T \right] \sin(\omega T) \omega \frac{\partial T}{\partial X_1} \\
& + \left[-\frac{\omega^2(2X_1-1)}{EW} + (-\omega\sqrt{E+2\omega^2}(2X_2-1) - \omega^2) \frac{\partial T}{\partial X_1} \right] \sin(\omega T) \\
& \left. + \left[-2EW + (-\omega\sqrt{E+2\omega^2}(2X_2-1) - \omega^2)T \right] \cos(\omega T) \omega \frac{\partial T}{\partial X_2} \right\} \quad (\text{F.11})
\end{aligned}$$

$$\begin{aligned}
\frac{\partial X'_2}{\partial X_2} = & -\frac{1}{2\sqrt{E+2\omega^2}} \left\{ \right. \\
& \left[2\sqrt{E+2\omega^2} + \frac{\omega(E+2\omega^2)(2X_2-1)T}{EW} \right. \\
& \quad \left. + (-2\omega EW + \omega^2(2X_1-1)) \frac{\partial T}{\partial X_2} \right] \cos(\omega T) \\
& - \left[\sqrt{E+2\omega^2}(2X_2-1) + (-2\omega EW + \omega^2(2X_1-1))T \right] \sin(\omega T) \omega \frac{\partial T}{\partial X_2} \\
& + \left[\frac{(E+2\omega^2)(2X_2-1)}{EW} - 2\omega\sqrt{E+2\omega^2}T \right. \\
& \quad \left. + (-\omega\sqrt{E+2\omega^2}(2X_2-1) - \omega^2) \frac{\partial T}{\partial X_2} \right] \sin(\omega T) \\
& \left. + \left[-2EW + (-\omega\sqrt{E+2\omega^2}(2X_2-1) - \omega^2)T \right] \cos(\omega T) \omega \frac{\partial T}{\partial X_2} \right\} \quad (\text{F.12})
\end{aligned}$$

For B_{14} we have:

$$\begin{aligned}
\frac{\partial X'_1}{\partial X_1} = & \frac{1}{2} \left\{ - \left[\left(-\frac{\omega^2(2X_1-1)}{EW} + 2\omega \right) T \right. \right. \\
& \quad \left. \left. + (-2EW + \omega(2X_1-1)) \frac{\partial T}{\partial X_1} \right] \cos(\omega T) \right. \\
& + [-1 + (-2EW + \omega(2X_1-1))T] \sin(\omega T) \omega \frac{\partial T}{\partial X_1} \\
& - \left[-2 + \left(-\sqrt{E+2\omega^2}(2X_2-1) - \omega \right) \frac{\partial T}{\partial X_1} \right] \sin(\omega T) \\
& \left. - \left[-(2X_2-1) + \left(-\sqrt{E+2\omega^2}(2X_2-1) - \omega \right) T \right] \cos(\omega T) \omega \frac{\partial T}{\partial X_1} \right\} \quad (\text{F.13})
\end{aligned}$$

$$\begin{aligned}
\frac{\partial X'_1}{\partial X_2} = \frac{1}{2} \left\{ - \left[\frac{(E + 2\omega^2)(2X_2 - 1)T}{EW} \right. \right. \\
\left. \left. + (-2EW + \omega(2X_1 - 1)) \frac{\partial T}{\partial X_2} \right] \cos(\omega T) \right. \\
+ [-1 + (-2EW + \omega(2X_1 - 1))T] \sin(\omega T) \omega \frac{\partial T}{\partial X_2} \\
- \left[-2\sqrt{E + 2\omega^2}T + (-\sqrt{E + 2\omega^2}(2X_2 - 1) - \omega) \frac{\partial T}{\partial X_2} \right] \sin(\omega T) \\
\left. - \left[-(2X_1 - 1) + (-\sqrt{E + 2\omega^2}(2X_2 - 1) - \omega)T \right] \cos(\omega T) \omega \frac{\partial T}{\partial X_2} \right\}
\end{aligned} \tag{F.14}$$

$$\begin{aligned}
\frac{\partial X'_2}{\partial X_1} = -\frac{1}{2\sqrt{E + 2\omega^2}} \left\{ \right. \\
\left[-\frac{\omega^2(2X_1 - 1)}{EW} + (-\omega\sqrt{E + 2\omega^2}(2X_2 - 1) - \omega^2) \frac{\partial T}{\partial X_1} \right] \cos(\omega T) \\
- \left[-2EW + (-\omega\sqrt{E + 2\omega^2}(2X_2 - 1) - \omega^2)T \right] \sin(\omega T) \omega \frac{\partial T}{\partial X_2} \\
+ \left[\left(\frac{+\omega^3(2X_1 - 1)}{EW} - 2\omega^2 \right) T \right. \\
\left. + (+2\omega EW - \omega^2(2X_1 - 1)) \frac{\partial T}{\partial X_1} \right] \sin(\omega T) \\
+ \left[-\sqrt{E + 2\omega^2}(2X_2 - 1) \right. \\
\left. + (2\omega EW - \omega^2(2X_1 - 1))T \right] \cos(\omega T) \omega \frac{\partial T}{\partial X_1} \left. \right\}
\end{aligned} \tag{F.15}$$

$$\begin{aligned}
\frac{\partial X'_2}{\partial X_2} = -\frac{1}{2\sqrt{E + 2\omega^2}} \left\{ \right. \\
\left[\frac{(E + 2\omega^2)(2X_2 - 1)}{EW} - 2\omega\sqrt{E + 2\omega^2}T \right. \\
\left. + (-\omega\sqrt{E + 2\omega^2}(2X_2 - 1) - \omega^2) \frac{\partial T}{\partial X_2} \right] \cos(\omega T) \\
- \left[-2EW + (-\omega\sqrt{E + 2\omega^2}(2X_2 - 1) - \omega^2)T \right] \sin(\omega T) \omega \frac{\partial T}{\partial X_2} \\
+ \left[-2\sqrt{E + 2\omega^2} - \frac{\omega(E + 2\omega^2)(2X_2 - 1)T}{EW} \right. \\
\left. + (2\omega EW - \omega^2(2X_1 - 1)) \frac{\partial T}{\partial X_2} \right] \sin(\omega T) \\
+ \left[-\sqrt{E + 2\omega^2}(2X_2 - 1) \right. \\
\left. + (2\omega EW - \omega^2(2X_1 - 1))T \right] \cos(\omega T) \omega \frac{\partial T}{\partial X_2} \left. \right\}
\end{aligned} \tag{F.16}$$

Appendix G

Bounce maps for the stationary \mathcal{B}_\square

From equations (E.1), (E.2) and (E.4) we have for B_{12} :

$$\begin{aligned}
 1 &= A|_{\omega=0} = (2X_1 - 1 + \sqrt{E}(2X_2 - 1)T) \quad \text{giving} \\
 T &= \frac{1 - X_1}{\sqrt{E}(X_2 - \frac{1}{2})} \quad \text{then} \\
 X'_1 &= \frac{1}{2} + \frac{1}{2}B|_{\omega=0} = \frac{1}{2} + \frac{1}{2} \left(-1 - 2\sqrt{EX_2(1 - X_2)}T \right) \\
 &= -\sqrt{E}\sqrt{X_2(1 - X_2)} \overbrace{\left(\frac{1 - X_1}{\sqrt{E}(X_2 - \frac{1}{2})} \right)}^{=T} \\
 &= -(1 - X_1) \left(\frac{\sqrt{X_2(1 - X_2)}}{(X_2 - \frac{1}{2})} \right) = -\frac{(1 - X_1)}{\tau} \\
 \frac{\partial X'_1}{\partial X_1} &= -\frac{1}{\tau} \frac{\partial(1 - X_1)}{\partial X_1} = \frac{1}{\tau} \\
 \frac{\partial X'_1}{\partial X_2} &= -(1 - X_1) \frac{\partial}{\partial X_2} \left(\frac{1}{\tau} \right) = \frac{(1 - X_1)}{(X_2 - \frac{1}{2})} \left(\tau + \frac{1}{\tau} \right) \\
 X'_2 &= \frac{1}{2} + \frac{1}{2\sqrt{E}}D|_{\omega=0} = \frac{1}{2} + \frac{1}{-2\sqrt{E}} \left(2\sqrt{EX_2(1 - X_2)} \right) \\
 &= \frac{1}{2} - \frac{(X_2 - \frac{1}{2})}{\tau} \\
 \frac{\partial X'_2}{\partial X_1} &= 0 \\
 \frac{\partial X'_2}{\partial X_2} &= -\frac{\partial}{\partial X_2} \left(\frac{X_2 - \frac{1}{2}}{\tau} \right) = \tau
 \end{aligned} \tag{G.1}$$

Where

$$\tau \equiv \frac{(X_2 - \frac{1}{2})}{\sqrt{X_2(1 - X_2)}}$$

is the cotangent of the angle between trajectory vector and positive sense of initial wall [29].

From equations (E.1), (E.2) and (E.5) we have for B_{13} :

$$\begin{aligned}
 1 &= B|_{\omega=0} = -1 + 2\sqrt{EX_2(1-X_2)}T \quad \text{giving} \\
 T &= \frac{1}{\sqrt{EX_2(1-X_2)}} \quad \text{then} \\
 X'_1 &= \frac{1}{2} - \frac{1}{2}A|_{\omega=0} = \frac{1}{2} - \frac{1}{2} \left(2X_1 - 1 + \sqrt{E}(2X_2 - 1)T \right) \\
 &= 1 - X_1 - \sqrt{E} \left(X_2 - \frac{1}{2} \right) \overbrace{\left(\frac{1}{\sqrt{EX_2(1-X_2)}} \right)}{=T} \\
 &= 1 - X_1 - \tau \\
 \frac{\partial X'_1}{\partial X_1} &= -1 \\
 \frac{\partial X'_1}{\partial X_2} &= -\frac{\partial \tau}{\partial X_2} = -\frac{1}{\sqrt{X_2(1-X_2)}}(1 + \tau^2) \\
 X'_2 &= \frac{1}{2} - \frac{1}{2\sqrt{E}}C|_{\omega=0} = \frac{1}{2} - \frac{1}{2\sqrt{E}} \left(\sqrt{E}(2X_2 - 1) \right) = 1 - X_2 \\
 \frac{\partial X'_2}{\partial X_1} &= 0 \\
 \frac{\partial X'_2}{\partial X_2} &= -1
 \end{aligned} \tag{G.2}$$

From equations (E.1), (E.2) and (E.6) we have for B_{14} :

$$\begin{aligned}
 -1 &= A|_{\omega=0} = 2X_1 - 1 + \sqrt{E}(2X_2 - 1)T \quad \text{giving} \\
 T &= \frac{-X_1}{\sqrt{E}(X_2 - \frac{1}{2})} \quad \text{then} \\
 X'_1 &= \frac{1}{2} - \frac{1}{2}B|_{\omega=0} = \frac{1}{2} - \frac{1}{2} \left(-1 + 2\sqrt{EX_2(1 - X_2)}T \right) \\
 &= 1 - \sqrt{EX_2(1 - X_2)} \overbrace{\left(\frac{-X_1}{\sqrt{E}(X_2 - \frac{1}{2})} \right)}^{=T} = 1 + \frac{X_1}{\tau} \\
 \frac{\partial X'_1}{\partial X_1} &= \frac{1}{\tau} \\
 \frac{\partial X'_1}{\partial X_2} &= X_1 \frac{\partial}{\partial X_2} \left(\frac{1}{i\tau} \right) = \frac{X_1}{(X_2 - \frac{1}{2})} \left(\tau + \frac{1}{\tau} \right) \\
 X'_2 &= \frac{1}{2} - \frac{1}{2\sqrt{E}}D|_{\omega=0} = \frac{1}{2} - \frac{1}{2\sqrt{E}} \left(2\sqrt{EX_2(1 - X_2)} \right) \\
 &= \frac{1}{2} - \frac{(X_2 - \frac{1}{2})}{\tau} \\
 \frac{\partial X'_2}{\partial X_1} &= 0 \\
 \frac{\partial X'_2}{\partial X_2} &= -\frac{\partial}{\partial X_2} \left(\frac{X_2 - \frac{1}{2}}{\tau} \right) = \tau
 \end{aligned} \tag{G.3}$$

Hence $\mathbf{B}_\infty : \mathbf{X} \rightarrow \mathbf{X}'$ is seen to be:

$$\begin{aligned}
 (X_1, X_2) &\rightarrow \left(\frac{(1 - X_1)}{\tau}, \frac{1}{2} + \frac{(X_2 - \frac{1}{2})}{\tau} \right) && \text{for } B_{12} \\
 &\rightarrow (1 - X_1 - \tau, 1 - X_2) && \text{for } B_{13} \\
 &\rightarrow \left(1 + \frac{X_1}{\tau}, \frac{1}{2} - \frac{(X_2 - \frac{1}{2})}{\tau} \right) && \text{for } B_{14}
 \end{aligned} \tag{G.4}$$

Appendix H

Unitary numerical integration technique

For equation 5.15 on page 126, $\Psi_{j,k}^n$ is known either from the initial conditions or from the previous iteration so that the RHS can be evaluated (where we use the boundary conditions $\Psi_{1,k}^n = \Psi_{2,k}^n = \Psi_{j,1}^n = \Psi_{j,2}^n = \Psi_{J,k}^n = \Psi_{J-1,k}^n = \Psi_{j,K}^n = \Psi_{j,K-1}^n = 0$; $J = K$ is the grid size):

$$\begin{aligned} & \left(1 + \frac{i}{\lambda} \Delta_y^2\right) (1 + \gamma x D_y) \Psi_{j,k}^n = -\frac{i}{\lambda} \gamma x \Psi_{j,k-2}^n + \left(-\gamma x + \frac{i}{\lambda} + 2i \frac{\gamma x}{\lambda}\right) \Psi_{j,k-1}^n \\ & + \left(1 - \frac{2i}{\lambda}\right) \Psi_{j,k}^n + \left(\gamma x + \frac{i}{\lambda} - 2i \frac{\gamma x}{\lambda}\right) \Psi_{j,k+1}^n + \frac{i}{\lambda} \gamma x \Psi_{j,k+2}^n \\ & \equiv \Gamma_{j,k}^n \end{aligned} \tag{H.1}$$

or

$$[\Gamma_{3,3}^n \quad \Gamma_{3,4}^n \cdots \Gamma_{3,K-2}^n] = [\Psi_{3,3}^n \quad \Psi_{3,4}^n \cdots \Psi_{3,K-2}^n] A_x \tag{H.2}$$

Where the pent-diagonal matrix A_x is given by:

$$\begin{bmatrix} 1 - \frac{2i}{\lambda} & A_{12} & -\frac{\gamma x i}{\lambda} & 0 & 0 & \cdots \\ A_{21} & 1 - \frac{2i}{\lambda} & A_{12} & -\frac{\gamma x i}{\lambda} & 0 & \cdots \\ \frac{\gamma x i}{\lambda} & A_{21} & 1 - \frac{2i}{\lambda} & A_{12} & -\frac{\gamma x i}{\lambda} & \cdots \\ 0 & \frac{\gamma x i}{\lambda} & A_{21} & 1 - \frac{2i}{\lambda} & A_{12} & \cdots \\ 0 & 0 & \frac{\gamma x i}{\lambda} & A_{12} & 1 - \frac{2i}{\lambda} & \cdots \\ \vdots & \vdots & \vdots & \vdots & \vdots & \ddots \end{bmatrix} \tag{H.3}$$

With $A_{12} = -\gamma x + \frac{i}{\lambda} + \frac{2\gamma x i}{\lambda}$ and $A_{21} = \gamma x + \frac{i}{\lambda} - \frac{2\gamma x i}{\lambda}$

For the discretised \mathcal{B}_\square the values of x in A_x are computed from $x = -1 + j\epsilon$. Then for the LHS of equation 5.15 on page 126:

$$\begin{aligned} \left(1 - \frac{i}{\lambda}\Delta_x^2\right) (1 - \gamma y D_x) \Phi_{j,k}^n &= -\frac{i}{\lambda} \gamma y \Phi_{j-2,k}^n + \left(\gamma y - \frac{i}{\lambda} + 2i \frac{\gamma y}{\lambda}\right) \Phi_{j-1,k}^n \\ &+ \left(1 + \frac{2i}{\lambda}\right) \Phi_{j,k}^n + \left(-\gamma y - \frac{i}{\lambda} - 2i \frac{\gamma y}{\lambda}\right) \Phi_{j+1,k}^n + \frac{i}{\lambda} \gamma y \Phi_{j+2,k}^n \\ &\equiv \Gamma_{j,k}^n \end{aligned} \quad (\text{H.4})$$

For a fixed k , j is changed from 3 to $J-2$ resulting in the following set of simultaneous linear equations:

$$A_y \begin{bmatrix} \Phi_{3,k}^n \\ \Phi_{4,k}^n \\ \vdots \\ \Phi_{J-2,k}^n \end{bmatrix} = \begin{bmatrix} \Gamma_{3,k}^n \\ \Gamma_{4,k}^n \\ \vdots \\ \Gamma_{J-2,k}^n \end{bmatrix} \quad (\text{H.5})$$

Where the matrix A_y is given by:

$$\begin{bmatrix} 1 + \frac{2i}{\lambda} & A_{12} & -\frac{\gamma x i}{\lambda} & 0 & 0 & \cdots \\ A_{21} & 1 + \frac{2i}{\lambda} & A_{12} & -\frac{\gamma x i}{\lambda} & 0 & \cdots \\ \frac{\gamma x i}{\lambda} & A_{21} & 1 + \frac{2i}{\lambda} & A_{12} & -\frac{\gamma x i}{\lambda} & \cdots \\ 0 & \frac{\gamma x i}{\lambda} & A_{21} & 1 + \frac{2i}{\lambda} & A_{12} & \cdots \\ 0 & 0 & \frac{\gamma x i}{\lambda} & A_{12} & 1 + \frac{2i}{\lambda} & \cdots \\ \vdots & \vdots & \vdots & \vdots & \vdots & \ddots \end{bmatrix} \quad (\text{H.6})$$

With $A_{12} = \gamma x - \frac{i}{\lambda} + \frac{2\gamma x i}{\lambda}$ and $A_{21} = -\gamma x - \frac{i}{\lambda} - \frac{2\gamma x i}{\lambda}$. Here for the discretised \mathcal{B}_\square the values of y in A_y are computed from $y = -1 + k\epsilon$. This pent-diagonal system is solved and the procedure is repeated for every k (requiring computation and inversion of A_y each time) giving the inter-mediatory Φ^n . We are now in a position to evaluate the RHS of equation 5.16 on page 126:

$$\begin{aligned} \left(1 + \frac{i}{\lambda}\Delta_x^2\right) (1 + \gamma y D_x) \Phi_{j,k}^n &= -\frac{i}{\lambda} \gamma y \Phi_{j-2,k}^n + \left(-\gamma y + \frac{i}{\lambda} + 2i \frac{\gamma y}{\lambda}\right) \Phi_{j-1,k}^n \\ &+ \left(1 - \frac{2i}{\lambda}\right) \Phi_{j,k}^n + \left(\gamma y + \frac{i}{\lambda} - 2i \frac{\gamma y}{\lambda}\right) \Phi_{j+1,k}^n + \frac{i}{\lambda} \gamma y \Phi_{j+2,k}^n \\ &\equiv \Xi_{j,k}^n \end{aligned} \quad (\text{H.7})$$

For a fixed k , j is changed from 3 to $J-2$ to give set of simultaneous linear equations:

$$B_y \begin{bmatrix} \Phi_{3,k}^n \\ \Phi_{4,k}^n \\ \vdots \\ \Phi_{J-2,k}^n \end{bmatrix} = \begin{bmatrix} \Xi_{3,k}^n \\ \Xi_{4,k}^n \\ \vdots \\ \Xi_{J-2,k}^n \end{bmatrix} \quad (\text{H.8})$$

Where the matrix B_y is given by:

$$\begin{bmatrix} 1 - \frac{2i}{\lambda} & B_{12} & -\frac{\gamma xi}{\lambda} & 0 & 0 & \cdots \\ B_{21} & 1 - \frac{2i}{\lambda} & B_{12} & -\frac{\gamma xi}{\lambda} & 0 & \cdots \\ \frac{\gamma xi}{\lambda} & B_{21} & 1 - \frac{2i}{\lambda} & B_{12} & -\frac{\gamma xi}{\lambda} & \cdots \\ 0 & \frac{\gamma xi}{\lambda} & B_{21} & 1 - \frac{2i}{\lambda} & B_{12} & \cdots \\ 0 & 0 & \frac{\gamma xi}{\lambda} & B_{12} & 1 - \frac{2i}{\lambda} & \cdots \\ \vdots & \vdots & \vdots & \vdots & \vdots & \ddots \end{bmatrix} \quad (\text{H.9})$$

With $B_{12} = -\gamma x + \frac{i}{\lambda} + \frac{2\gamma xi}{\lambda}$ and $B_{21} = \gamma x + \frac{i}{\lambda} - \frac{2\gamma xi}{\lambda}$

The procedure is repeated for every k to give Ξ^n , for use in the evaluation of the LHS of equation 5.16 on page 126:

$$\begin{aligned} \left(1 - \frac{i}{\lambda} \Delta_y^2\right) (1 + \gamma x D_y) \Psi_{j,k}^{n+1} &= \frac{i}{\lambda} \gamma x \Psi_{j,k-2}^{n+1} + \left(-\gamma x - \frac{i}{\lambda} - 2i \frac{\gamma x}{\lambda}\right) \Psi_{j,k-1}^{n+1} \\ &+ \left(1 + \frac{2i}{\lambda}\right) \Psi_{j,k}^{n+1} + \left(\gamma x - \frac{i}{\lambda} + 2i \frac{\gamma x}{\lambda}\right) \Psi_{j,k+1}^{n+1} - \frac{i}{\lambda} \gamma x \Psi_{j,k+2}^{n+1} \\ &\equiv \Xi_{j,k}^n \end{aligned} \quad (\text{H.10})$$

For each j , k is changed from 3 to $K-2$ to give the set of simultaneous linear equations:

$$[\Psi_{3,k}^{n+1} \quad \Psi_{4,k}^{n+1} \cdots \Psi_{J-2,k}^{n+1}] B_x = [\Xi_{3,k}^n \quad \Xi_{4,k}^n \cdots \Xi_{J-2,k}^n] \quad (\text{H.11})$$

Where the matrix B_x is given by:

$$\begin{bmatrix} 1 + \frac{2i}{\lambda} & B_{12} & -\frac{\gamma xi}{\lambda} & 0 & 0 & \cdots \\ B_{21} & 1 + \frac{2i}{\lambda} & B_{12} & -\frac{\gamma xi}{\lambda} & 0 & \cdots \\ \frac{\gamma xi}{\lambda} & B_{21} & 1 + \frac{2i}{\lambda} & B_{12} & -\frac{\gamma xi}{\lambda} & \cdots \\ 0 & \frac{\gamma xi}{\lambda} & B_{21} & 1 + \frac{2i}{\lambda} & B_{12} & \cdots \\ 0 & 0 & \frac{\gamma xi}{\lambda} & B_{12} & 1 + \frac{2i}{\lambda} & \cdots \\ \vdots & \vdots & \vdots & \vdots & \vdots & \ddots \end{bmatrix} \quad (\text{H.12})$$

With $B_{12} = \gamma x - \frac{i}{\lambda} + \frac{2\gamma xi}{\lambda}$ and $B_{21} = -\gamma x - \frac{i}{\lambda} - \frac{2\gamma xi}{\lambda}$

Finally this pent-diagonal system is solved and the procedure is repeated for every j (requiring computation and inversion of B_x each time) to give Ψ^{n+1} , the wave function at time step $n + 1$ from that at time step n .

Bibliography

- [1] S. Borgan and R. C. Johnson: Rotating square billiard. *Phys. Lett. A* **262**, 427 (1999).
- [2] S. Borgan and R. C. Johnson: Quantal square billiard. — In preparation.
- [3] Martin C. Gutzwiller: *Chaos in Classical and Quantum Mechanics* Springer-Verlag New York Inc., (1990).
- [4] M. V. Berry: *AIP Conference Proceedings*, **46**, 16 (1978).
- [5] V. I. Arnol'd: Small denominators in problems of stability of motion in classical and celestial mechanics. *Russ. Math. Survey* **18:6**, 85 (1963).
- [6] W. Dittrich and M. Reuter: *Classical and Quantum Dynamics* Springer-Verlag New York Inc., (1993).
- [7] J. L. Lebowitz and O. Penrose: Modern ergodic theory. *Physics Today* **26** (February), 91 (1981).
- [8] V. F. Lazutkin: The existence of caustics for a billiard problem in a convex domain. *Math. Izv. USSR.* **37**, 186 (1973).
- [9] J. B. Keller: Corrected Bohr-Sommerfeld Quantum Conditions for Nonseparable Systems. *Ann. Phys.* **4**, 180 (1958).
- [10] V. P. Maslov and M. V. Fedoriuk: *Semiclassical Approximation in Quantum Mechanics*. Reidal, Dordrecht (1981).
- [11] M. V. Berry and K. E. Mount: Semiclassical approximations in wave mechanics. *Rep. Prog. Phys.* **35**, 315 (1972).
- [12] P. A. M. Dirac: *The Principles of Quantum Mechanics*. Oxford University Press (1958).

- [13] E. Wigner: On the Quantum Correction For Thermodynamic Equilibrium. *Phys. Rev.* **40**, 749 (1932).
- [14] G. A. Baker: Formulation of Quantum Mechanics Based on the Quasi-Probability Distribution Induced on Phase Space. *Phys. Rev.* **109**, 2198 (1957).
- [15] H. J. Groenewold: On the principles of elementary Quantum Mechanics. *Physica.* **12**, 405 (1946).
- [16] M. V. Berry: Semi-Classical Mechanics in phase space: A study of Wigner's Function. *Phil. Trans. Roy. Soc.* **A287**, 237 (1977).
- [17] M. V. Berry and N. L. Balazs: Evolution of semiclassical quantum states in phase space. *J. Phys.* **A:12**, 625 (1979).
- [18] M. V. Berry: Regular and irregular semiclassical wavefunctions. *J. Phys.* **A:10**, 2083 (1977).
- [19] J. S. Hutchinson and R. E. Wyatt: Quantum ergodicity and the Wigner distribution. *Chem. Phys. Lett.* **72**, 378 (1980).
- [20] M. H. Mehta: On the statistical properties of the level spacings in nuclear spectra. *Nuc. Phys.* **18**, 395 (1960).
- [21] E. P. Wigner: Random matrices in Physics. *SIAM Rev.* **9**, 1 (1967).
- [22] F. J. Dyson: Statistical Theory of the Energy Levels of Complex Systems I. *J. Math. Phys.* **3**, 140 (1962).
- [23] E. J. Heller, P. W. O'Connor and J. Gehlan: The Eigenfunctions of Classically Chaotic Systems. *Physica Scripta* **40**, 354 (1989).
- [24] E. J. Heller: Quantum localization and the rate of exploration of phase space. *Phys. Rev.* **A35**, 1360 (1987).
- [25] D. B. Fairlie and D. K. Siegwart: Classical billiards in a rotating boundary. *J. Phys. A: Math. Gen.* **21**, 1157 (1988).
- [26] M. Robnik and M. V. Berry: Classical billiards in magnetic fields. *J. Phys. A: Math. Gen.* **18**, 1361 (1985).
- [27] H. Frisk and R. Arvieu: Rotating billiards. *J. Phys. A: Math. Gen.* **22**, 1765 (1989).

- [28] S. Wiggins: *Introduction to Applied Nonlinear Dynamical Systems and Chaos*, Springer-Verlag (1990).
- [29] R. C. Johnson - unpublished
- [30] M. V. Berry: Regularity and chaos in classical mechanics, illustrated by three deformations of a circular 'billiard'. *Eur. J. Phys.* **2**, 91 (1981).
- [31] M. V. Berry: Regular and irregular motion. *AIP Conference Proceedings* **46**, 16 (1978).
- [32] J. M. Greene, R.S. MacKay, F. Vivaldi and M. J. Feigenbaum: Universal behaviour in families of area-preserving maps. *Physica* **3D**, 486 (1981).
- [33] P. Richens and M. V. Berry: Pseudointegrable systems in classical and quantum mechanics. *Physica* **2D**, 495 (1981).
- [34] John M. Greene: A method for determining a stochastic transition. *Journal of Mathematical Physics* **20**, 1183 (1979).
- [35] D. F. Escande: Large-Scale Stochasticity in Hamiltonian Systems. *Physica Scripta* **T2/1**, 126 (1982).
- [36] R.S. MacKay: A renormalisation approach to invariant circles in area preserving maps. *Physica* **7D**, 283 (1983),
- [37] Charles F. F. Karney: Long-time correlations in the stochastic regime *Physica* **8D**, 360 (1983).
- [38] R. S. MacKay, J. D. Meiss and I. C. Percival: Transport in Hamiltonian systems. *Physica* **13D**, 55 (1984).
- [39] Suhan Ree and L. E. Reichl: Classical and quantum chaos in a circular billiard with a straight cut. Preprint: [chao-dyn/9807018](#).
- [40] Eduardo Canale, Roberto Markarian, Sylvie oliffson Kamphorst and Sonia Pinto de Carvalho: A lower bound for chaos on the Elliptical Stadium. Preprint: [chao-dyn/9704006](#).
- [41] N. Berglund and H. Kunz: Integrability and Ergodicity of Classical Billiards in a Magnetic Field. *J. Stat. Phys. Vol.* **83**, 1 (1996).
- [42] Vincent J. Daniels, Michel Vallières, Jian Min Yuan: Chaotic Scattering on a Billiard. Preprint: [chao-dyn/9706028](#).

- [43] R. C. Johnson: An example of chaotic dynamics. *Math. Gazette* **74**, 256 (1990).
- [44] D. K. Siegwart: Classical and quantum chaos of dynamical systems: Rotating billiards. *Ph.D Thesis* University of Durham (1990).
- [45] B. V. Chirikov: A universal instability of many-dimensional oscillator systems. *Physics Reports* **52**, 263 (1979).
- [46] J. Wisdom: Chaotic behaviour and the origin of the 3/1 Kirkwood gap. *Icarus* **56**, 51 (1983).
- [47] G. Benettin and J. M. Strelcyn: Numerical experiments on the free motion of a point mass moving in a plane convex region: Stochastic transition and entropy. *Phys. Rev. A* **17**, 773 (1978).
- [48] R. Aurich, J. Bolte and F. Steiner: Universal Signatures of Quantum Chaos. *Phys. Rev. Lett.* **73**, 1356 (1994).
- [49] Steven W. McDonald and Allan N. Kaufman: Wave chaos in the stadium: Statistical properties of short-wave solutions of the Helmholtz equation. *Phys. Rev.* **A37**, 3067 (1987).
- [50] Sunghwan Rim, Soo-Young Lee, Eui-Soon Yim and C. H. Lee: Transition to quantum chaos in a generic one-parameter family of billiards. Preprint: chaodyn/9808019.
- [51] Steven W. McDonald and Allan N. Kaufman: Spectrum and Eigenfunctions for a Hamiltonian with Stochastic Trajectories. *Phys. Rev. Lett.* **42**, 1189 (1979).
- [52] M. V. Berry: Quantizing a Classically Ergodic System: Sinai's Billiard and the KKR Method. *Ann. Phys.* **131**, 163 (1981).
- [53] Ya. M. Blanter, A. D. Mirlin and B. A. Muzykantskii: Quantum Billiards with Surface scattering: Ballistic Sigma-Model Approach. Preprint: cond-mat/9802169.
- [54] Baowen Li, Marko Robnik and Bambi Hu: Relevance of chaos in numerical solutions of quantum billiards. *Phys. Rev.* **E57**, 4095 (1998).

- [55] Gabriel Carlo, Eduardo Vergini and Alejandro J. Fendrik: Numerical Verification of Percival's Conjecture in a Quantum Billiard. Preprint: *chao-dyn/9804016*.
- [56] Tomaz Prosen: Berry-Robnik level statistics in a smooth billiard system. Preprint: *cond-mat/9803341*.
- [57] Debabrata Biswas: Periodic orbits and Spectral Statistics of Pseudointegrable Billiards. *Phys. Rev. E* **54**, 1044 (1996).
- [58] D. K. Siegwart: Quantum billiards in a rotating boundary. *J. Phys. A: Math. Gen.* **22**, 3537 (1989).
- [59] Soo-Young Lee, Sunghwan Rim, Eui-Soon Yim and C. H. Lee: Correspondence between classical dynamics and energy level spacing distribution in the transition billiard systems. Preprint: *chao-dyn/9809009*.
- [60] Fernando P. Simonotti, Eduardo Vergini and Marcos Saraceno: Quantitative study of scars in the boundary section of the stadium billiard. Preprint: *chao-dyn/9706024*.
- [61] Guillio Casati and Tomaz Prosen: The Quantum Mechanics of Chaotic Billiards. Preprint: *cond-mat/9803360*.
- [62] Martin Sieber, Nicolas Pavloff and Charles Schmit: Uniform approximation for diffractive contributions to the trace formula in billiard systems. Preprint: *chao-dyn/9610006*.
- [63] R. van Zon and Th. W. Ruijgrok: The Elliptic Billiard: Subtleties of Separability. Preprint: *chao-dyn/9702006*.
- [64] Marko Robnik and Tomaz Prosen: Comment on energy level statistics in the mixed regime. *J. Phys. A* **27**, 8787 (1997).
- [65] Benoit Gremaud and Sudhir R. Jain: Spacing distribution for rhombus billiards. Preprint: *chao-dyn/9807022*.
- [66] T. Shigehara and Taksu Cheon: Spectral Properties of Three-Dimensional Quantum Billiards with a Pointlike Scatterer. Preprint: *chao-dyn/9702009*.
- [67] Klaus M. Frahm and Dima L. Shepelyansky: Quantum localization in rough billiards. Preprint: *cond-mat/9612118*.

- [68] M. V. Berry
Semiclassical theory of spectral rigidity. *Proc. R. Soc. Lond. A* **400**, 229 (1985).
- [69] V. Lopac, I. Mrkonjic and D. Radic: Classical and quantum chaos in the generalized parabolic lemon-shaped billiard. *Phys. Rev. E* **59**, 303 (1999).
- [70] A. Goldberg, H. M. Schey and J. L. Schwartz: Computer-generated motion pictures of one-dimensional quantum-mechanical transmission and reflection phenomena. *Am. J. Phys.* **35**, 177 (1967).
- [71] A. Goldberg, H. M. Schey and J. L. Schwartz: One-Dimensional Scattering in Configuration Space and Momentum Space. *Am. J. Phys.* **36**, 454 (1968).
- [72] William H. Press, Saul A. Teukolsky, William T. Vetterling and Brian P. Flannery: *Numerical Recipes in C*, Cambridge University Press (1992).
- [73] A. R. Mitchell and D. F. Griffith: *The Finite Difference Method in partial differential equations*, Wiley, New York (1980).
- [74] Carlo U. Segre and J. D. Sullivan: Bound-state wave packets. *Am. J. Phys.* **44**, 279 (1975).
- [75] G. Djorgovski (Caltech): The Second ICRA Network Workshop, University of Rome, February 1 - 5, 1999.
- [76] E. Heller, H. Koppel and L. S. Cederbaum: On the statistical behaviour of molecular vibronic energy levels. *Chem. Phys. Lett.* **101**, 215 (1983).
- [77] R. Balian and C. Bloch: Distribution of Eigenfrequencies for the Wave Equation in a Finite Domain 1. Three-Dimensional Problem with Smooth Boundary Surface. *Ann. Phys.* **60**, 401 (1970).
- [78] R. Balian and C. Bloch: Asymptotic Evaluation of Green's Function for Large Quantum Numbers. *Ann. Phys.* **63**, 592 (1971).
- [79] M. V. Berry and M. Wilkinson: Diabolical points in the spectra of triangles. *Proc. R. Soc. Lond. A* **392**, 15 (1984).
- [80] J. B. French and S. S. M. Wong: Some random-matrix level and spacing distributions for fixed-particle-rank interactions. *Phys. Lett. B* **35**, 5 (1971).
- [81] S. Blumberg and G. E. Porter: Nuclear Fine Structure Widths and Spacings. *Phys. Rev.* **110**, 786 (1958).

- [82] M.V. Berry and M. Tabor: Level clustering in the regular spectrum. *Proc. R. Soc. Lond. A.* **356**, 375 (1977).
- [83] G. Casati, F. Valz-Griz and I. Guarneri: On the Connection between Quantization of Nonintegrable Systems and Statistical Theory of Spectra. *Lett. Nuovo Cimento* **28**, 279 (1980).
- [84] O. Bohigas, M. J. Giannoni and C. Schmit: Characterization of Chaotic Quantum Spectra and Universality of Level Fluctuation Laws. *Phys. Rev. Lett.* **52**, 1189 (1979).
- [85] T. A. Brody, J. Flores, J. B. French, P. A. Mello, A. Pandey and S. S. M. Wong: Random-matrix physics: spectrum and strength fluctuations. *Rev. Mod. Phys.* **53**, 385 (1981).
- [86] H. Friedrich and D. Wintgen: The Hydrogen atom in a uniform magnetic field - an example of chaos. *Phys. Rep.* **183**, 37 (1989).
- [87] D. Wintgen and H. Friedrich: Classical and quantum-mechanical transition between regularity and irregularity in a Hamiltonian system. *Phys. Rev. A* **35**, 1464 (1987).
- [88] D. Delande and J. Gay: Quantum Chaos and Statistical Properties of Energy Levels: Numerical Study of the Hydrogen Atom in a Magnetic Field. *Phys. Rev. Lett.* **57**, 2006 (1986).
- [89] D. C. Meredith, S. E. Koonin and M. R. Zirnbauer: Quantum chaos in a schematic shell model. *Phys. Rev. A* **37**, 3499 (1988).
- [90] T. H. Seligman, J. J. M. Verbaarschot and M. R. Zirnbauer: Quantum Spectra and Transition from Regular to Chaotic Classical Motion. *Phys. Rev. Lett.* **53**, 215 (1984).
- [91] T. Cheon and T. D. Cohen: Quantum Level Statistics of Pseudointegrable Billiards. *Phys. Rev. Lett.* **62**, 2769 (1989).
- [92] M. V. Berry and M. Robnik: Semiclassical level spacings when regular and chaotic orbits coexist. *J. Phys. A* **17**, 2413 (1984).
- [93] G. Casati, B. V. Chirikov and I. Guarneri: Energy-Level Statistics of Integrable Systems. *Phys. Rev. Lett.* **54**, 1350 (1985).

- [94] M. V. Berry: *Semiclassical Mechanics of Regular and Irregular Motion in Chaotic Behaviour of Deterministic Systems, Les Houches Lectures XXXVI.* ed G. Iooss, R. H. G. Hellman and R. Stora (North-Holland, Amsterdam (1983)).
- [95] T. A. Brody: A Statistical Measure for the Repulsion of Energy levels. *Lett. Nuovo Cimento* **7**, 482 (1973).
- [96] V. Lopac, S. Brant and V. Paar: Level density fluctuations and characterization of chaos in the realistic model spectra for odd-odd nuclei. *Z. Phys.* **A356**, 113 (1996).
- [97] T. Prosen and M. Robnik: Numerical demonstration of the Berry-Robnik level spacing distribution. *J. Phys.* **A27**, L459 (1994).
- [98] F. J. Dyson and M. L. Mehta: Statistical Theory of the Energy Levels of Complex Systems. IV *J. Math. Phys.* **4**, 701 (1963).
- [99] O. Bohigas and M. J. Giannoni: Level Density Fluctuations and Random Matrix Theory. *Ann. Phys.* **89**, 393 (1975).
- [100] J. R. Barker, R. Akis and D. K. Ferry: On the use of Bohm trajectories for interpreting quantum flows in quantum dot structures. Glasgow University Preprint.
- [101] K. Nakamura: *Quantum Chaos a new paradigm of nonlinear dynamics.* Cambridge University Press (1993)
- [102] Herbert Goldstein: *Classical Mechanics 2nd edition* Addison-Wesley Publishing Company, Inc., (1980).
- [103] L. D. Landau and E. M. Lifshitz: *Mechanics: Course of Theoretical Physics Vol. 1* Pergamon Press, Oxford (1976).

